The Pennsylvania State University

The Graduate School

Department of Mechanical and Nuclear Engineering

THRUST CHAMBER DYNAMICS AND PROPULSIVE PERFORMANCE OF AIRBREATHING PULSE DETONATION ENGINES

A Thesis in

Mechanical Engineering

by

Fuhua Ma

Submitted in Partial Fulfillment
of the Requirements
for the Degree of

Doctor of Philosophy

December 2003

The thesis of Fuhua Ma was received and approved* by the following:

Vigor Yang
Distinguished Professor of Mechanical Engineering
Thesis Advisor
Chair of Committee

Robert J. Santoro
Guillet Professor of Mechanical Engineering

John Mahaffy
Associate Professor of Mechanical Engineering

Robert F. Kunz
Associate Professor of Aerospace Engineering

Richard C. Benson
Professor of Mechanical Engineering
Head of Department of Mechanical Engineering

*Signatures are on file in the Graduate School.

Abstract

Pulse detonation engines (PDEs) have recently been recognized as a promising propulsion technology that offers potential advantages in thermodynamic cycle efficiency, hardware simplicity, and operation scalability. The present work studies the flow dynamics and system performance of airbreathing PDEs with a stoichiometric hydrogen/air mixture. The system includes a supersonic inlet, an air manifold, a rotary valve, a single-tube or multitube combustor, and a convergent-divergent nozzle. The flight condition involves an altitude of 9.3 km and a flight Mach number of 2.1.

The supersonic inlet dynamics is analyzed through axisymmetric two-dimensional simulations based on the Harten-Yee upwind total-variation-diminishing scheme. Turbulence closure is achieved by a two-equation model. In addition to the steady-state inlet flow dynamics, the response of the inlet shock system to downstream disturbances is studied by imposing periodic pressure oscillations at the exit plane. A wide range of fluctuation frequency and amplitude are investigated. In general, the acoustic response of the inlet flow increases with increasing amplitude of the imposed oscillation, but decreases with the frequency.

Both one- and two-dimensional simulations based on the recently developed Space-Time conservation element/solution element method are carried out for single-tube PDEs. The two-dimensional code is further parallelized using the message-passing-interface library and a domain decomposition technique for unstructured grid. The flow dynamics, the effects of the operation timing and nozzle configuration on the propulsive performance, and the various loss mechanisms are examined. Results show that an optimum cycle frequency exists for a given configuration. For a given frequency and purge time, a longer refilling period increases the specific thrust of PDEs considered. The nozzle studies indicate that the convergent-divergent nozzle significantly increases the propulsive performance. Moreover, the throat area of the convergent-divergent nozzle plays a more important role than the length.

Effort is also expended to study the flow dynamics and propulsive performance of multitube PDEs. Comparison with the single-tube results demonstrates that the multitube design improves the engine performance in terms of specific impulse, operation steadiness, and timing range. The effect of the system geometry is partially assessed by considering a free volume between the detonation tubes and the common nozzle. Results indicate that the free volume helps to reduce the imperfect nozzle expansion loss and improve the engine steadiness. However, it also induces more complicated shock waves and increases the internal flow loss. The overall effect is a decrease in the propulsive performance.

Table of Contents

List of Figures

List of Tables

Nomenclature

A_e	area of engine exit plane
c	speed of sound
c_p	constant-pressure specific heat
E_a	activation energy per unit mass of reactants
e_t	specific total energy
F	axial thrust
$\mathbf{F}$	thrust vector
F_{sp}	specific thrust (air-based)
f	fuel-to-air mass ratio of reactants
$\overline{f}$	fuel-to-air mass ratio of the mixture of reactants and purged air
g	gravitational acceleration
I_{sp}	specific impulse (fuel-based)
$\mathbf{i}$	unit vector in axial direction
K	pre-exponential factor
L	length of detonation tube
L_{driv}	length of driver gas region
M	Mach number
$\dot{m}_a$	mass flow rate of air delivered to the engine
$\dot{m}_f$	mass flow rate of fuel delivered to the combustor
$\mathbf{n}$	unit vector normal to surface

p	pressure
p_e	area-averaged pressure at engine exit plane
p_{t1}	total pressure at combustor entrance
q	heat release per unit mass of reactants
$\overline{q}$	heat release per unit mass of mixture of reactants and purged air
R	gas constant
s	specific entropy
T	temperature
T_{driv}	temperature of driver gas
T_{t1}	total temperature at combustor entrance
t	time
u	axial velocity
$\mathbf{u}$	velocity vector
u_e	mass-averaged axial velocity at engine exit plane
$\mathbf{u}_e$	mass-averaged velocity vector at engine exit plane
v	vertical velocity
x	axial coordinate
y	vertical coordinate
Z	mass fraction of reactants
β	purge-to-open time ratio
$\gamma=$	specific heat ratio
ρ	density

τ	time period
$\dot{\omega}$	mass production rate of reactants

Subscripts

close	stage during which valve is closed
cycle	PDE operation cycle
D	detonation wave
e	engine exit plane
i	engine entrance plane
open	stages during which valve is open
purge	purging stage
refill	refilling stage
∞	ambient condition
1	fresh reactant upstream of detonation wave front
2	Chapman-Jouguet state
3	uniform region between the head end and the rear of Taylor wave

Acknowledgements

With a deep sense of gratitude, first I wish to express my sincere thanks to my advisor, Dr. Vigor Yang, for kindly providing guidance throughout the development of this study. His support, encouragement, and comments have been of greatest help at all times.

Sincere thanks also go to Dr. Robert J. Santoro, Dr. John Mahaffy, and Dr. Robert F. Kunz for serving as my committee members. They monitored my work and took effort in reading and giving me with valuable suggestions on the earlier versions of this thesis.

This work was supported by the Department of Defense Multidisciplinary University Research Initiative under the Office of Naval Research Grant N00014-02-1-0589, with Gabriel Roy serving as the program manager. The financial support is greatly appreciated.

Sincere thanks also go to Dr. Jeong-Yeol Choi for his help on this research, and to Dr. Xiaoyen Wang and Dr. Yuhui Wu for their help on the space-time method.

I wish I would never forget the company I had from all the members of our research lab. In particular, I am thankful to Shanwu Wang, Danning You, Ying Huang, Nan Zong, and Yanxing Wang for their help.

I take this opportunity to express my love and sincere thanks to my parents for their endless love and support. My appreciation and love also go to my brother and sisters. They taught me the value of hard work by their own examples and provided me enormous support throughout my life.

Finally I wish to give a very special thank and all my love to my wife, Chunxia. Her support, love, and understanding have been invaluable to me.

Chapter 1
Introduction

1.1 Background and Motivation

The combustion process is a vital mechanism in most propulsion systems. A combustion process can be characterized as either a deflagration or a detonation. The deflagration is mainly governed by mass and thermal diffusion and has a flame speed of one or more meters per second. Usually, a deflagration process produces a slight decrease in pressure and can be modeled as a constant-pressure combustion process. Engines based on the deflagration process can be constructed to operate at steady state and are easy for design optimization with modular analyses of each subsystem. Most conventional engines, such as turbofans, turbojets, ramjets, and rocket engines, utilize a steady deflagration process.

In contrast to deflagration, the detonation process takes place much more rapidly and produces a supersonic combustion wave, or a detonation wave, propagating at around two thousand meters per second toward the unburned reactants. The detonation wave can be described as a strong shock wave coupled to a reaction zone. The shock wave compresses the reactants, acting like a valve between the reactants and products. The reaction thus takes place at a much higher pressure. Since there is not enough time for the pressure to reach its equilibrium, a detonation process closely approximates to a constant-volume combustion process. It is well known that an engine based on a constant-volume combustion process has higher thermodynamic efficiency than that based on a constant-pressure combustion process. The potential advantage in thermodynamic cycle efficiency becomes the primary reason that has been driving people's interests in developing engines that employ detonation processes. Examples of these engine concepts include those employing standing detonation waves, such as the detonation thrusters, the detonation ramjet (dramjet), and the oblique detonation wave engine (ODWE), or those employing intermittent traveling detonation waves, such as the pulse detonation engine (PDE). The engine concepts employing standing detonation waves are hampered by the difficulty in stabilizing the detonation wave. The PDE thus becomes a more practical candidate nowadays.

Early work on PDEs dates back to the 1940s (Hoffman, 1940; Nicholls et al., 1957; Dunlap et al., 1958; Krzycki, 1962) and was suspended possibly due to the lack of funding in the late 1960s. Interest in PDEs was reignited in the late 1980s by the work of Helman et al. (1986). Recently, the PDEs have been recognized worldwide as a promising propulsion technology that offers potential advantages in thermodynamic cycle efficiency, hardware simplicity, and operation scalability and reliability (Bussing and Pappas, 1996; Kailasanath, 2002; Wu et al., 2003). Several PDE concepts have been proposed and experimentally investigated in the past. The main challenges are to develop an ignition system for repetitive detonation initiation, to integrate the inlet with the unsteady-operated detonation chamber, and to choose an optimized nozzle to achieve high performance. Although substantial efforts have been made to overcome these challenges, a real PDE-based vehicle has not emerged yet.

One of the most important concerns is to estimate the propulsive performance of PDE concepts and to compare it with those of the conventional engines. In parallel to experimental investigations, attempts were made both theoretically and numerically to estimate the performance of PDEs. However, a general agreement on the performance has not been reached yet. Most previous numerical simulations were either limited to single-pulse operation with one- and two- dimensional models, or multicycle operation with only one-dimensional models. Very few efforts have been expended to simulate a PDE with multicycle operations using multidimensional models. On the other hand, since the unsteady nature of the PDE is dominated by the unsteady flow dynamics during a steady periodic cycle, it is thus very important to understand the flow dynamics prior to calculating the performance. Also, this understanding may help in improving the PDE designs. Unfortunately, none of the previous studies have ever presented the detailed multidimensional flow evolution within a whole cycle. Hence, the main motivation of this thesis is to establish a multidimensional numerical analysis to examine the flow dynamics involved in PDEs with multicycle operations, to provide a more convincible estimation of the propulsive performance of PDEs, and to investigate the effect of the various design parameters on the performance.

1.2 Detonation Physics

Studies of detonation phenomena date back to the end of the 19th century. The simplest theory was proposed by Chapman (1889) and Jouguet (1905), usually referred to as the CJ theory. It treats the detonation wave as a discontinuity plane in one dimension. This theory can be used to predict the detonation wave velocity without the need to know the details of the chemical reaction and the detonation wave structure. A significant advance in the understanding of the detonation wave structure was made independently by Zeldovich (1940) in Russia, von Neumann (1942) in the United States, and Döring (1943) in Germany. They considered the detonation wave as a leading planar shock wave with a chemical reaction zone behind the shock. Their treatment has come to be called the ZND model of detonation, and the corresponding detonation wave structure is called the ZND detonation wave structure. Although all the experimentally observed detonation waves have much more complex cellular three-dimensional structures resulting from the strong nonlinear coupling between gasdynamics and chemical kinetics (Glassman, 1996), the CJ theory and the ZND model, which assume a planar one-dimensional detonation wave, are still very useful. An overview of them is hence given in this subsection to provide some basic knowledge on detonation physics. More detailed and extended discussions about detonation physics and phenomena can be found from several textbooks (Fickett and David, 1979; Kuo, 1986; Glassman, 1996).

1.2.1 CJ Theory

For a steady, planar, one-dimensional detonation wave (see Fig. 1.1), with both the reactants and products modeled as the same perfect gas and the detonation wave modeled as a discontinuity plane at which heat addition occurs, the conservations of mass, momentum, and energy in a coordinate system fixed at the wave front give:

$$\rho_1 u_D = \rho_2 (u_D - u_2) \tag{1.1}$$

$$p_1 + \rho_1 {u_D}^2 = p_2 + \rho_2 (u_D - u_2)^2 \tag{1.2}$$

$$\frac{\gamma}{\gamma - 1}\frac{p_1}{\rho_1} + \frac{1}{2}{u_D}^2 + q = \frac{\gamma}{\gamma - 1}\frac{p_2}{\rho_2} + \frac{1}{2}(u_D - u_2)^2 \tag{1.3}$$

where the velocities relative to the wave front have already been expressed out with the velocities relative to the tube; u_D is the detonation wave velocity, q the heat release per unit mass of reactants due to chemical reaction, and γ the specific heat ratio; ρ, p, and u represent the density, pressure, and velocity, respectively; subscript 1 refers to the state of unburned gas or reactants and subscript 2 for the final state, i.e., the state of the burned gas immediately behind the detonation wave. Since there are only three equations, one extra equation is needed to solve for the four unknowns p_2, ρ_2, u_2 and u_D. This extra equation will be revealed through the following analysis.

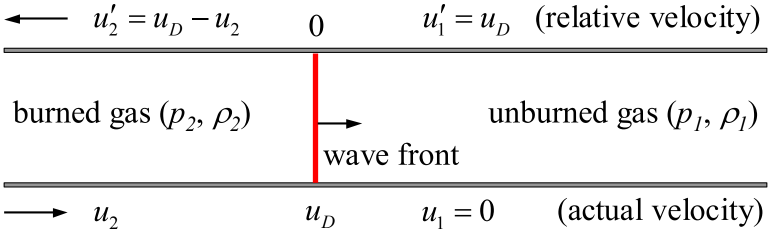

Fig. 1.1 Steady planar detonation wave in a tube

Combining the mass and momentum conservation equations leads to the so-called Rayleigh relation,

$$(p_2 - p_1)/(\frac{1}{\rho_2} - \frac{1}{\rho_1}) = -\rho_1^2 u_D^2 \tag{1.4}$$

Manipulations of Eqs. (1.1) – (1.3) yield the following Hugoniot relation,

$$\frac{\gamma}{\gamma - 1}(\frac{p_2}{\rho_2} - \frac{p_1}{\rho_1}) - \frac{1}{2}(p_2 - p_1)(\frac{1}{\rho_2} + \frac{1}{\rho_1}) = q \tag{1.5}$$

If these two relations are plotted in the $p_2 \sim 1/\rho_2$ plane, a Rayleigh line and a Hugoniot curve can be constructed. Figure 1.2 shows the schematic of the Hugoniot curve and the Rayleigh line. The point corresponding to the unburned gas state is denoted by A. Apparently, all the Rayleigh lines pass through point A. The possible final states are defined by the intersection of the Rayleigh line and the Hugoniot curve. Among all the straight lines passing through point A, there are two which are tangent to the Hugoniot curve. The corresponding tangent points are generally called as the CJ points, denoted in the figure by point U for the upper CJ point and L for the lower CJ point. The horizontal and vertical lines passing through point A correspond to a constant-pressure and a constant-volume process, respectively. The Hugoniot curve is divided into five regions, i.e., regions I~V, by the two tangent lines and the horizontal and vertical lines. Region V is unphysical since the Rayleigh lines defined by Eq. (1.4) cannot have positive slope. Regions I and II are called detonation branch, within which the velocity of the wave front is supersonic; regions III and IV are called deflagration branch, within which the velocity of the wave front is subsonic. The upper CJ point corresponds to a minimum detonation velocity, whereas the lower CJ point corresponds to a maximum deflagration velocity.

Through simple mathematical derivations, i.e., equating the slope of the Hugoniot curve to that of the Rayleigh line, the following relation, usually referred to as the CJ condition, can be obtained at the CJ points,

$$u_2' = u_D - u_2 = \sqrt{\gamma p_2 / \rho_2} = c_2 \quad \text{or} \quad M_2' = u_2' / c_2 = 1 \tag{1.6}$$

where c_2 is the sound speed of the burned gas, u_2' and M_2' the velocity and Mach number of the burned gas relative to the wave front, respectively. The flow velocity relative to the wave front at the CJ points equaling to the local sound speed is one of the notable characteristics of the CJ points. At the upper CJ point, since $u_2 + c_2 = u_D$, any rarefaction waves arising behind the wave front will not overtake the detonation wave and thus a self-sustained steady detonation wave can be established.

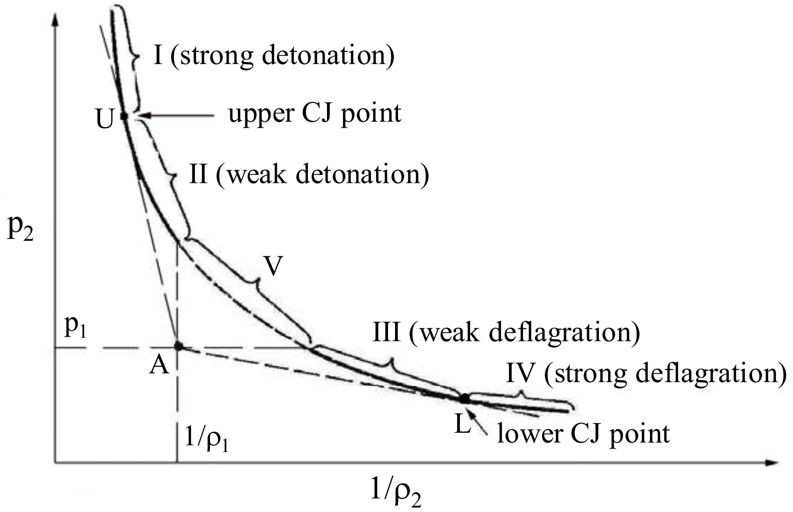

Fig. 1.2 Schematic of Rayleigh lines and Hugoniot curve in $p_2 \sim 1/\rho_2$ plane (adapted from Kuo, 1986)

Region I is called the strong-detonation region. In this region, the velocity of the burned gas relative to the wave front is subsonic, i.e., $u_2 + c_2 > u_D$, thus, any rarefaction waves arising behind the wave front will overtake and weaken the detonation wave. As a matter of fact, a strong detonation, also called overdriven detonation, is not stable and is thus seldom observed experimentally. It may, however, appear during a transient process or be generated with a driving piston.

Region II is called the weak-detonation region. In this region, the velocity of the burned gas relative to the wave front is supersonic, i.e., $u_2 + c_2 < u_D$. If the ZND detonation wave structure is adopted, the detonation wave can be considered as a shock wave and a following heat addition zone. The gas velocity immediately behind the shock relative to the wave front is known to be subsonic from classical shock dynamics theory. On the other hand, it is also well known that for a steady flow in a constant-area tube, the fluid cannot be accelerated from subsonic to supersonic by heat addition. This means that the velocity of the burned gas relative to the wave front cannot be supersonic. Thus, region II is physically impossible as long as the ZND detonation wave structure is assumed. Another discussion leading to the same conclusion can be found in the textbook of Glassman (1996).

Region III is called the weak-detonation region. The weak deflagration, or simply the deflagration, is often observed in experiments. A deflagration wave propagates toward the unburned gas at a subsonic velocity. Across a deflagration wave, the velocity of the gas relative to the wave front is accelerated within the subsonic regime, and the pressure is reduced.

Region IV is called the strong-deflagration region. Passing through a strong-deflagration wave, the gas velocity relative to the wave front is to be accelerated from subsonic to supersonic. Similar to the discussion for region II, this violates the common conclusion that for a steady flow in a constant-area tube, the fluid cannot be accelerated from subsonic to supersonic by heat addition. Thus, region IV is physically impossible, and a strong deflagration is never observed experimentally.

Based on the above discussions, the upper CJ point is the only possible state for a self-sustained steady detonation wave commonly observed. Thus, the CJ condition, Eq. (1.6), can be used as an additional equation along with Eqs. (1.1) ~ (1.3) to solve for the four unknowns aforementioned, i.e., p_2, ρ_2, u_2 and u_D. It is convenient to find the detonation wave Mach number M_D first and then express the other unknowns with respect to it. For concision, the corresponding mathematical manipulations are skipped, and the solutions for the unknowns as well as several other properties of the final state are listed as below.

$$M_D \equiv \frac{u_D}{c_1} = \sqrt{\frac{\gamma^2-1}{2\gamma}\frac{q}{RT_1}} + \sqrt{\frac{\gamma^2-1}{2\gamma}\frac{q}{RT_1}+1} \tag{1.7}$$

$$u_D = M_D\sqrt{\gamma RT_1} \tag{1.8}$$

$$u_2 = \frac{{M_D}^2-1}{(1+\gamma)M_D}\sqrt{\gamma RT_1} \tag{1.9}$$

$$c_2 = \frac{1+\gamma {M_D}^2}{(1+\gamma)M_D}\sqrt{\gamma RT_1} \tag{1.10}$$

$$M_2 = \frac{{M_D}^2-1}{\gamma {M_D}^2+1} \tag{1.11}$$

$$\frac{p_2}{p_1} = \frac{1+\gamma {M_D}^2}{1+\gamma} \tag{1.12}$$

$$\frac{\rho_2}{\rho_1} = \frac{(1+\gamma){M_D}^2}{1+\gamma {M_D}^2} \tag{1.13}$$

$$\frac{T_2}{T_1} \equiv \frac{p_2/(R\rho_2)}{p_1/(R\rho_1)} = \left(\frac{1+\gamma {M_D}^2}{(1+\gamma)M_D}\right)^2 \tag{1.14}$$

where R is the gas constant; T_1 and c_1 are the temperature and sound speed of the unburned gas, respectively; T_2, c_2, and M_2, are the temperature, sound speed, and Mach number of the unburned gas, respectively.

In most cases, the square of the detonation wave Mach number, ${M_D}^2$, is much larger than 1. Some of the above expressions can thus be approximately reduced to the following ones.

$$u_2 \cong \frac{1}{1+\gamma} u_D \tag{1.15}$$

$$c_2 \cong \frac{\gamma}{1+\gamma} u_D \tag{1.16}$$

$$M_2 \cong \frac{1}{\gamma} \tag{1.17}$$

$$\frac{p_2}{p_1} \cong \frac{\gamma}{1+\gamma} {M_D}^2 \tag{1.18}$$

$$\frac{\rho_2}{\rho_1} \cong \frac{1+\gamma}{\gamma} \tag{1.19}$$

$$\frac{T_2}{T_1} \cong \left(\frac{\gamma M_D}{1+\gamma} \right)^2 \tag{1.20}$$

1.2.2 ZND Detonation Wave Structure

The CJ theory brought great success in predicting the detonation wave velocity. It, however, gives no information about the details of the detonation wave structure. In the early 1940s, Zeldovich (1940), von Neumann (1942), and Döring (1943) independently extended the CJ theory to consider the detonation wave structure that has become the well-known ZND detonation structure. Their treatment is referred to as the ZND model. According to them, the detonation wave is interpreted as a strong planar shock wave propagating at the CJ detonation velocity, with a chemical reaction region followed and coupled to the shock wave. The shock wave compresses and heats the reactants to a temperature at which a reaction takes place at a rate high enough for the ensuring deflagration to propagate as fast as the shock wave. From the energy point of view, the shock wave provides activation energy to ignite reaction, whereas the energy released by reaction keeps the shock moving. Their assumption that no reaction takes place in the shock wave region was based on the fact that the width of the shock wave is in the order of a few mean free paths of the gas molecules, whereas the width of the reaction region is in the order of one centimeter (Kuo, 1986).

Figure 1.3 shows schematically the variation of physical properties through a ZND detonation wave. Plane 1 denotes the state of unburned gas. Plane 1' denotes the state immediately after the shock wave. Chemical reaction starts at plane 1' and finishes at plane 2, at which the CJ state reaches. If a single variable is used to represent the reaction progress or the degree of reaction, it will have a value of 0 at plane 1' and a value of 1 at plane 2. Generally, the reaction rate, such as that that follows the Arrhenius law, increases with temperature, and the chemical reaction region can be further divided into an induction and a heat addition zone. In the induction zone directly behind the shock wave where the temperature is not very high, the reaction rate is relatively slow and as a result, the temperature, pressure, and density profiles are relatively flat. In the heat addition zone behind the induction zone, the reaction rate increases drastically to high values along with a large amount of heat release from the reaction so that the gas properties change sharply.

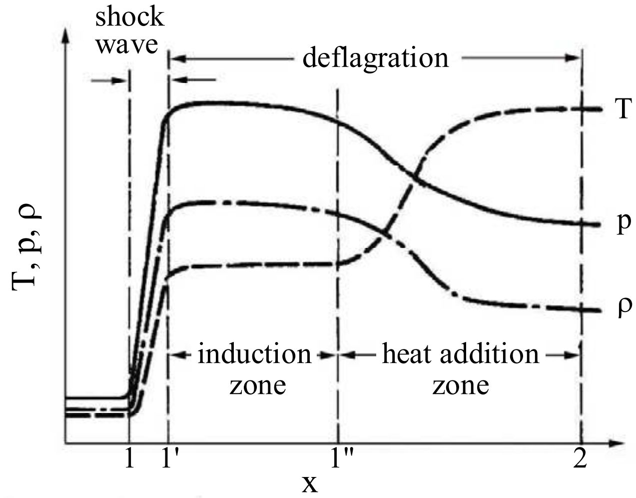

Fig. 1.3 Variation of physical properties through a ZND detonation wave (adapted from Kuo, 1986)

The ZND detonation wave structure can be also interpreted by Hugoniot curves shown in Fig. 1.4. There are many paths, such as a, b, c, and d, by which a reacting mixture may pass through the detonation wave from the unburned state to the burned state (Kuo, 1986). In the limit of zero chemical-energy release in the shock, a path will reach point s, the intersection of the shock Hugoniot curve and the Rayleigh line, and then the upper CJ point. The point s is referred to as the von Neumann spike. The von Neumann spike pressure can be determined from a normal shock relation:

$$\frac{p_s}{p_1} = \frac{2(1+\gamma M_D{}^2)}{1+\gamma} - 1 \tag{1.21}$$

Using Eq. (1.12), the von Neumann spike pressure relates to the CJ pressure as follows:

$$\frac{p_s}{p_1} = 2\frac{p_2}{p_1} - 1 \tag{1.22}$$

Hence, the von Neumann spike pressure is about twice of the CJ pressure.

The ZND model marks a great advance from the CJ theory in recognizing the detonation wave structure. However, all the experimentally observed detonation waves exhibit much more complex cellular three-dimensional structures. The smoked-foil record of a detonation shown in Fig. 1.5 displays the typical cellular structure (Strehlow, 1968). More detailed discussions about these structures can be obtained from the textbooks of Kuo (1986) and Glassman (1996).

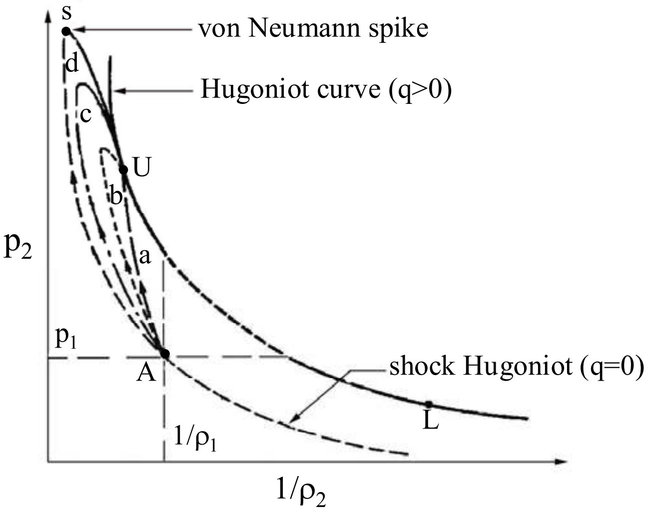

Fig. 1.4 Schematic of ZND detonation structure in $p_2 \sim 1/\rho_2$ plane (adapted from Kuo, 1986)

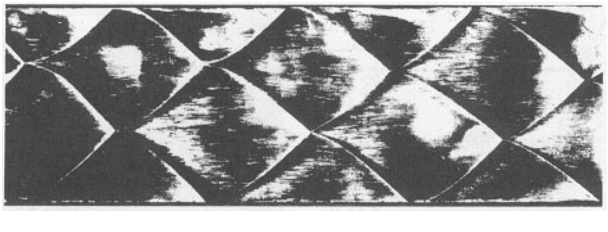

Fig. 1.5 Smoked-foil record of a detonation (Strehlow, 1968)

1.2.3 ZND Detonation Wave Propagation in a Tube

This subsection considers the ZND detonation propagation in a constant-area tube that is closed at one end and open at the other, as shown schematically in Fig. 1.6. The tube is initially filled with a static premixed detonable mixture. Detonation is initiated at the closed end and propagates downstream toward the open end. Following the detonation wave is a centered rarefaction wave, known as the Taylor wave, emanating from the closed end to satisfy the stationary boundary condition there. After the passage of the Taylor wave, a uniform region forms. The corresponding wave diagram in the space-time plane is given in Fig. 1.7. Figure 1.8 schematically shows the pressure profile within the tube. The width of the detonation wave is enlarged for visualization. The states 1, s, 2, and 3 denote the unburned gas state, the von Neumann spike state, the CJ state, and the uniform region state, respectively. The von Neumann spike state and the CJ state can be readily determined using the equations derived in the previous subsection. The focus of this subsection is hence on the solution of the Taylor wave and uniform regions.

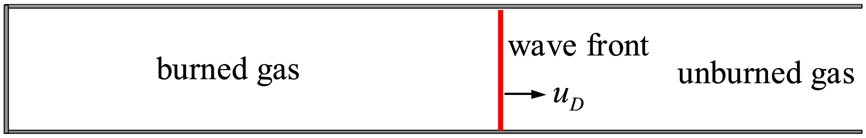

Fig. 1.6 ZND detonation propagation in a tube closed at one end

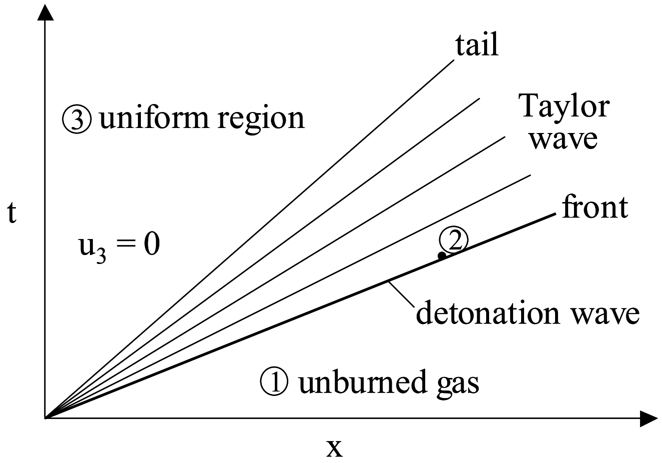

Fig. 1.7 Space-time wave diagram for a ZND detonation wave propagation in a tube

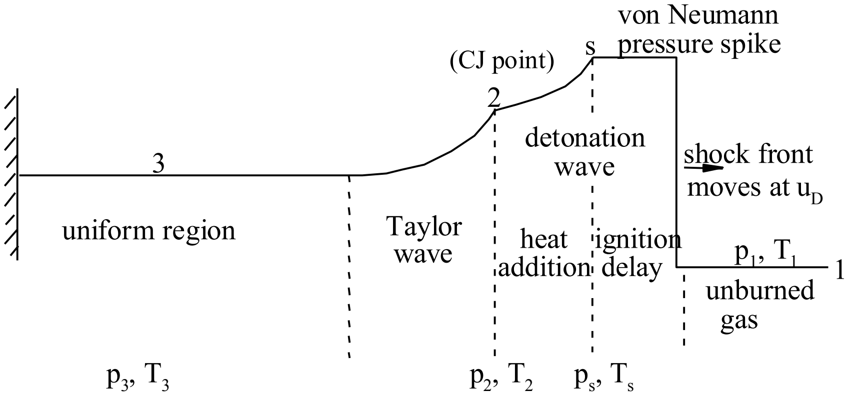

Fig. 1.8 Schematic of pressure profile for a ZND detonation propagation in a tube closed at one end. (adapted from Bussing and Pappas, 1994)

The properties of the uniform region can be obtained as follows. Applying the Riemann invariant relation along the characteristic line passing through the Taylor wave from state 2 to state 3 gets

$$u_3 - \frac{2}{\gamma - 1} c_3 = u_2 - \frac{2}{\gamma - 1} c_2 \tag{1.23}$$

where u_3 and c_3 are the velocity and sound speed in the uniform region, respectively. Since $u_3 = 0$, the above equation yields,

$$\frac{c_3}{c_2} = 1 - \frac{\gamma - 1}{2} \cdot \frac{u_2}{c_2} = 1 - \frac{\gamma - 1}{2} M_2 = 1 - \frac{\gamma - 1}{2} \frac{{M_D}^2 - 1}{\gamma {M_D}^2 + 1} \tag{1.24}$$

where M_2 is the Mach number of the gas at state 2 expressed with Eq. (1.11). Consequently, the temperature in the uniform region is

$$\frac{T_3}{T_2} = \left(1 - \frac{\gamma - 1}{2} \frac{{M_D}^2 - 1}{\gamma {M_D}^2 + 1} \right)^2 \tag{1.25}$$

Through an isentropic relation from state 2 to state 3, the pressure can be determined as:

$$\frac{p_3}{p_2} = \left(1 - \frac{\gamma - 1}{2} \frac{{M_D}^2 - 1}{\gamma {M_D}^2 + 1} \right)^{\frac{2\gamma}{\gamma - 1}} \tag{1.26}$$

The relation of the sound speed c_3 with the detonation wave velocity u_D can be obtained by combining Eqs. (1.24), (1.10), and (1.8):

$$\frac{c_3}{u_D} = \frac{{M_D}^2 + 1}{2{M_D}^2} \tag{1.27}$$

With the sound speed c_3 available, the length of the uniform region, L_{const}, at a particular instant of time t, can also be determined. Since the rear of the Taylor wave propagates at c_3, thus,

$$L_{const} = c_3 t \tag{1.28}$$

Similar to the previous subsection, considering that the square of the detonation wave Mach number, ${M_D}^2$, is much larger than 1, the above expressions, Eqs. (1.24)~(1.27) can be further simplified with approximation:

$$\frac{c_3}{c_2} \cong \frac{\gamma+1}{2\gamma} \tag{1.29}$$

$$\frac{T_3}{T_2} \cong \left(\frac{\gamma+1}{2\gamma}\right)^2 \tag{1.30}$$

$$\frac{p_3}{p_2} \cong \left(\frac{\gamma+1}{2\gamma}\right)^{\frac{2\gamma}{\gamma-1}} \tag{1.31}$$

$$\frac{c_3}{u_D} \cong \frac{1}{2} \tag{1.32}$$

The length of the uniform region can thus be approximated as:

$$L_{const} = c_3 t \cong \frac{1}{2} u_D t \tag{1.33}$$

It indicates that the length of the uniform region is about halfway between the detonation wave front and the head end (Fickett and Davis, 1979).

The flow properties within the Taylor wave region, $c_3 t \le x \le u_D t$, can also be derived. The Riemann invariant relation along the characteristic line from state 3 to the point (x, t) gives:

$$0 - \frac{2}{\gamma-1} c_3 = u - \frac{2}{\gamma-1} c \tag{1.34}$$

where *u* and *c* are the velocity and sound speed at point (x, t). On the other hand, since the forward characteristic lines are straight, thus,

$$\frac{x}{t} = u + c \tag{1.35}$$

Combination of the above two equations leads to the following solutions of *u* and *c*.

$$\frac{u}{c_3} = \frac{2}{\gamma + 1} \cdot \frac{x}{c_3 t} - \frac{2}{\gamma + 1} \tag{1.36}$$

$$\frac{c}{c_3} = \frac{\gamma - 1}{\gamma + 1} \cdot \frac{x}{c_3 t} + \frac{2}{\gamma + 1} \tag{1.37}$$

Other properties such as the temperature and pressure at point (x, t) are:

$$\frac{T}{T_3} = \left(\frac{\gamma - 1}{\gamma + 1} \cdot \frac{x}{c_3 t} + \frac{2}{\gamma + 1} \right)^2 \tag{1.38}$$

$$\frac{p}{p_3} = \left(\frac{\gamma - 1}{\gamma + 1} \cdot \frac{x}{c_3 t} + \frac{2}{\gamma + 1} \right)^{\frac{2\gamma}{\gamma - 1}} \tag{1.39}$$

1.3 Pulse Detonation Engine Concept

The pulse detonation engine (PDE) is an unsteady propulsion device that produces periodic impulse by utilizing repetitive detonations. Based on whether or not to use the ambient air as working fluid, it can be classified as an airbreathing version referred to as the airbreathing PDE and a rocket version referred to as the pulse detonation rocket engine (PDRE). The PDE differs from the conventional engines by its two distinguishing characteristics: unsteady operation and detonation process. It is noteworthy that the PDE concept is also different from the widely known pulsejets, such as the German V-1 "buzz bomb" used in World War II. These pulsejets employ a deflagration combustion process although they are unsteady engines. A comparison of the PDE with the existing engines is briefly summarized in Fig. 1.9. The cycle operation, potential advantages, and typical structure of the PDE are discussed in detail in the following paragraphs.

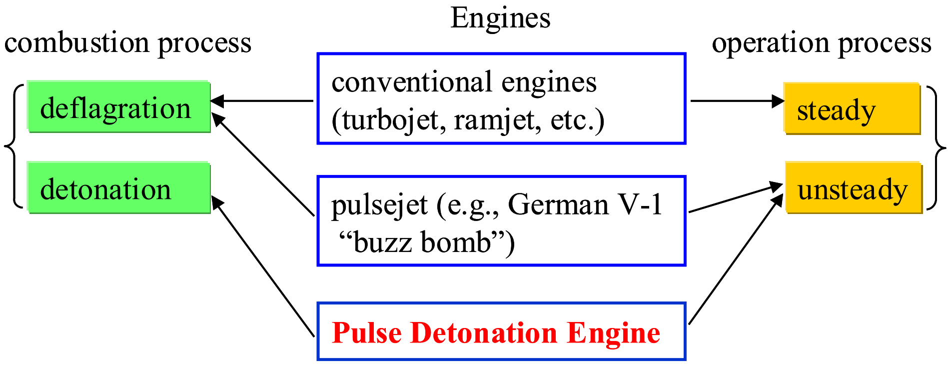

Fig. 1.9 Conceptual comparison of PDEs with other engines

1.3.1 Cycle Operation of PDE

A typical PDE cycle operation includes four basic processes: initiation of detonation wave, propagation of detonation wave, exhaust of combustion products or the blowdown process, and refilling of fresh reactants (Bussing and Pappas, 1994). These four processes are schematically shown in Fig. 1.10 for an idealized PDE which involves a straight detonation tube along with a valve located at the head end.

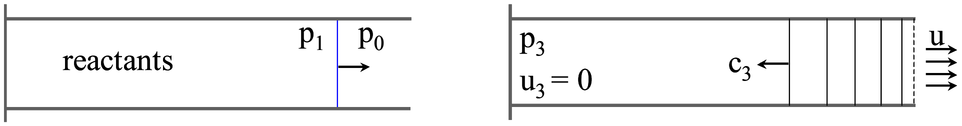

a. valve closed

d. blowdown

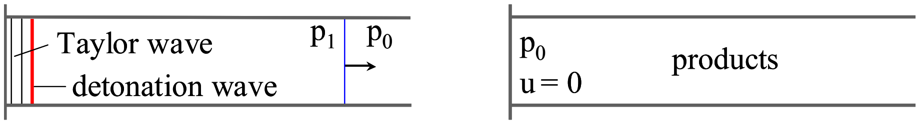

b. detonation initiation

e. blowdown finished

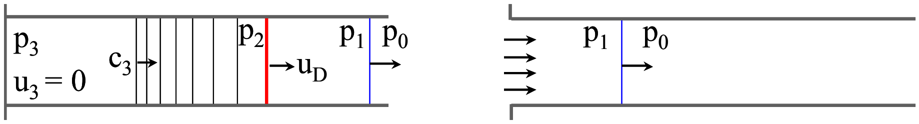

c. detonation propagation

f. refilling

Fig. 1.10 Schematic of cycle operation for idealized PDE

The cycle begins as the tube is filled with reactants at pressure p_1. The valve is then closed and the detonation is initiated either directly or after a deflagration-to-detonation transition (DDT) by an ignition source near the closed end. The detonation wave propagates toward the open end at the CJ detonation velocity u_D, usually in the order of 2000 m/s. Following the detonation wave is a set of rarefaction waves known as the Taylor wave emanating from the closed end to ensure the zero velocity condition at the closed end. The tail of the Taylor wave propagates toward the open end at the local sound speed c_3 which is in the order of 1000 m/s. Between the tail of the Taylor wave and the closed end is a uniform region, as discussed in Section 1.2.3. The Taylor wave reduces the CJ pressure (p_2) immediately behind the detonation wave to a relatively lower level (p_3) in the uniform region. This pressure, usually referred to as the plateau pressure, is still much higher than the ambient pressure (p_0) so that thrust is produced on the closed end.

When the detonation wave exits the tube, another set of rarefaction waves are generated and propagate back into the tube to reduce the pressure thereby, marking the beginning of the blowdown process. The reflection of these rarefaction waves off the closed end forms another set of rarefaction waves propagating downstream toward the open end, further reducing the chamber. The unsteady blowdown process is characterized by a series of compression and rarefaction waves which are alternately generated from the closed and open ends (Bussing and Pappas, 1994). Eventually, the chamber pressure decays to the ambient level and the blowdown process is finished.

Upon the end of the blowdown process, the valve opens to allow for the fresh reactants to be charged into the tube. The valve timing is controlled so that no fresh reactants escape from the open end to the ambient. This requires that the leading fresh reactants should be caught by the detonation wave of the next cycle somewhere within the detonation tube, or ideally, at the exit plane of the detonation tube. After the refilling process finishes, the valve closes and the next cycle begins.

In a more practical cycle operation, the refilling process may start when the closed-end pressure decays to a prespecified pressure level instead of the ambient value, to avoid the very low or even negative thrust produced on the closed end during the later period of the blowdown process. In addition, the temperature of the products near the closed end may be still very high and ignite the refilling fresh reactants if they contact directly. This kind of preignition may cause engine unstart. Thus, a purging process, i.e., filling a little inert gas or cold air before filling the reactants, would be necessary to prevent the preignition.

1.3.2 Potential Advantages of PDE

Due to the much more rapid burning or material conversion rate of a detonation process than a deflagration process, PDEs possess several potential advantages over those conventional engines based on the deflagration process. The first and also the most attractive one is the higher thermodynamic cycle efficiency, which is attributed to the facts that a detonation process approximately closes to a constant-volume combustion process (Kailasanath, 2002) and that a constant-volume combustion based engine cycle (the Humphrey cycle) has higher thermodynamic cycle efficiency than a constant-pressure combustion based engine cycle (the Brayton cycle). The thermodynamic cycle efficiencies of the Brayton, Humphrey, and ideal PDE cycle are given in Appendix A. It has been noted that the Humphrey cycle efficiency may be 30% to 50% higher than that of Brayton cycle for stoichiometric hydrogen/air mixture (Bussing and Pappas, 1994). The potentially higher thermodynamic cycle efficiency of PDEs directly translates to their potentially higher specific impulse. Figure 1.11, provided by Adroit System Inc., shows the anticipated specific impulse and operational envelope of various airbreathing engines including PDEs, turbojets, ramjets, and scramjets using hydrogen or hydrocarbon fuels (Roy, 1999). Clearly from this figure, PDEs have a performance advantage over their counterpart ramjet within their mutual flight regime. The lower performance of PDEs than turbojets within the regime of flight Mach number less than 2 is due to the fact that the turbojets utilize an additional compressor for precompression of the incoming air.

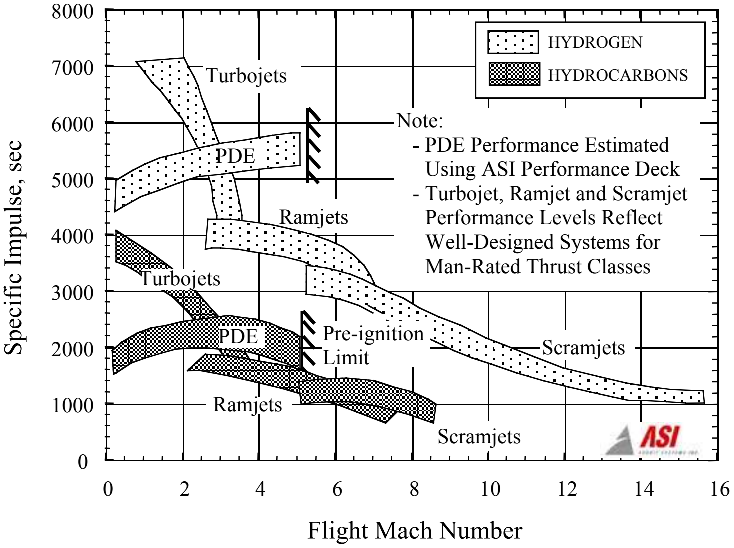

Fig. 1.11 Anticipated specific impulses of airbreathing engines (Roy, 1999)

In addition to their potentially higher thermodynamic cycle efficiency and specific impulse, PDEs have a wider operation range in terms of flight Mach number. The turbojets used nowadays in most commercial and military aircrafts are suitable for subsonic and low supersonic flight speed because of their high performance resulting from the precompression of the incoming air by the compressor. They become expensive and inefficient as the flight Mach number increases and cannot be used at a flight Mach number of greater than about 3 due to the cooling problem of the compressor blade. Ramjets, on the other hand, are designed for supersonic operation with a flight Mach number greater than 2. They usually require solid propellant rocket boosters for accelerating to the ramjet take over speed. PDEs, however, can produce thrust at static conditions and thus have the potential to operate in both subsonic and supersonic flight regimes with competitive efficiencies.

Other desirable features of PDEs over current propulsion systems include hardware simplicity and configuration scalability. PDEs do not necessarily require compressors to precompress the incoming air, nor turbines to produce work, nor boosters to produce thrust at static condition, thus significantly reducing the hardware complexity and design cost of the engine. Unlike pulsejets, which are tuned to the acoustical resonances of the combustion chamber, PDEs are uncoupled from the acoustical chamber resonance (Eidelman et al., 1990). It is theoretically possible to construct PDEs of a large range of sizes and thrust levels. In addition, the detonation frequency is physically restricted by the filling velocity of the fresh reactants into the detonation tube and is thus also scalable.

In summary, PDEs offer the potential advantages of higher thermodynamics cycle efficiency and specific impulse, wider operating region, hardware simplicity, and operation scalability over other existing propulsion systems. However, it should be mentioned that, in spite of these advantages, PDEs have also encountered a lot of challenging design issues such as the low-energy repetitive detonation initiation, inlet integration, nozzle optimization, and so forth. A real PDE-powered vehicle will not emerge until all these challenging issues are resolved.

1.3.3 Typical Structure of PDE

Figure 1.12 shows schematically the typical structure of an airbreathing PDE, which includes the following components (Bussing and Pappas, 1996): inlet, fuel and/or oxidizer sources, distribution manifolds, mixer, initiator, detonation tube, nozzle, and interfaces. The incoming air delivered by the inlet is distributed by the air manifold and mixes with the fuel distributed by the fuel manifold from the fuel source. The resultant mixture is fed into the detonation tube for detonation. The detonation products exhaust through the nozzle to generate thrust.

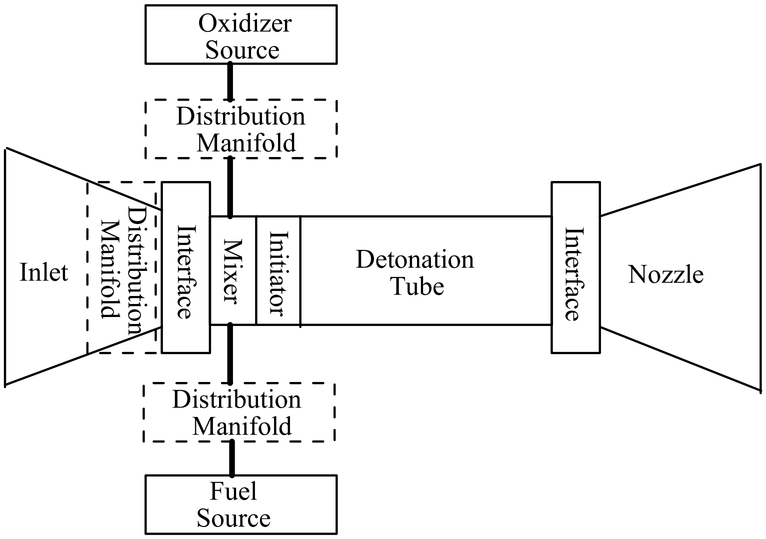

Fig. 1.12 Typical structure of airbreathing PDE (Bussing and Pappas, 1996)

All conventional airbreathing engines require an inlet to compress the air from the freestream velocity and pressure to lower velocity and higher pressure for further processing by other engine components. So do the airbreathing PDEs. The inlet of conventional airbreathing engines is designed to provide stable airflow to the combustor with the highest possible recovery of total pressure and lowest possible external drag and weight (Yang and Cappuccio, 1991). In airbreathing PDEs, because of the strong pressure waves arising from the unsteady operation of the detonation tube, additional concerns should be placed in the inlet design. Several approaches have been proposed. The first is to design an inlet manifold large enough to dampen the pressure waves. It is, however, not practical for volume-limited applications (Bussing and Pappas, 1996). The second approach is to bleed excess air between detonation cycles through a well-designed inlet/detonation tube manifold (Bussing and Pappas, 1996). A more practical approach would be to utilize a combustor consisting of multiple detonation tubes that operate out of phase to enable continuous airflow to the combustor (Bussing and Pappas, 1996) so that the pressure waves propagating to the inlet are significantly reduced to a level within the stable margin of the inlet.

The inlet/detonation tube interface serves both to isolate the detonation tube flowfield from the inlet flowfield during the detonation initiation and propagation and the blowdown processes, and to allow for the air and reactants to be delivered to the detonation tube during the purging and refilling processes. An example of this interface is a mechanical valve located at the head end of the detonation tube as mentioned in Section 1.3.1. Another way to achieve the same purpose would be through some kind of aerodynamic means.

The fuel source supplies fuel to the mixer through the fuel distribution manifold. In some cases, a separate oxidizer source and oxidizer manifold may be required to reduce the time and physical distance required for detonation initiation. The mixer is to provide efficient mixing of fuel and air, and/or fuel and oxidizer for further detonation.

The initiator is used to initiate the detonation wave in the detonation tube. The detonation can be initiated either directly through a large amount of energy deposition, or indirectly through a low-energy deposition along with a deflagration-to-detonation transition (DDT) process. In general, the energy required for a direct initiation of fuel/air mixture is impractical for repetitive operation. On the other hand, the DDT length associated with the indirect initiation might be quite large. One of the possible ways to reduce the DDT length is to fill the initiator section with the fuel/oxidizer mixture which is known to be more detonable than its corresponding fuel/air mixture. The detonation is first initiated in the initiator section, usually referred to as the predetonator, and then propagates into the detonation tube to initiate the detonation in the fuel/air mixture.

The detonation tube is the kernel part designed to sustain and confine the detonation process. Since the tube wall is exposed periodically to high-temperature, high-pressure detonation products and low-temperature, low-pressure reactants, the selection of proper material and the cooling of the detonation tube are two major design considerations. In addition, the size of the detonation tube should be scaled to satisfy the performance requirement such as the thrust level and the operation frequency.

The nozzle plays an important role in determining the PDE performance. In conventional steady engines, the nozzle is simply optimized by matching the exhaust pressure with the ambient pressure. This approach is, however, not available for PDEs since the exhaust flow is unsteady and the exit pressure is not constant. The situation is further compounded by the presence of the strong shock waves arising from the detonation process. Therefore, the nozzle design of PDEs represents a challenging task.

1.4 Literature Survey on PDE Studies

Studies of PDEs have been conducted for several decades. The first reported work on intermittent or pulse detonation engines is attributed to Hoffman (1940) in Germany. The device involved no valves. Holes were bored in a long detonation tube to allow gas jets to escape. The heights of the gas jets escaping through the holes were used to indicate the progress of the combustion wave and the onset of the detonation. Both gaseous acetylene and liquid benzene fuels were employed with oxygen in his experiments. He found that a continuous injection of the combustible mixture leads to only a narrow range of ignition frequencies that produce an intermittent detonation cycle. He also pointed out the importance of the spark plug location with respect to the tube length. World Wall II prevented further work by Hoffmann and colleagues.

A substantial effort was made by Nicholls et al. (1957) at the University of Michigan in the United States. They performed a series of single- and multiple-cycle detonation experiments with hydrogen/oxygen, hydrogen/air, acetylene/oxygen, and acetylene/oxygen mixtures in a stainless-steel detonation tube mounted on a pendulum platform suspended by support wires. The tube has a length of 182.9 cm (6 feet) and an internal diameter of 2.54 cm (1 inch). Fuel and oxidizer were injected coannually from the head end of the tube and ignited by a spark plug located 25.4 cm (10 inches) downstream. A maximum frequency of 35 Hz was obtained in their tests. The most promising results were demonstrated for the hydrogen/air mixture, where fuel-based specific impulses up to 2100 s were reached and agreed well with the predictions from their simplified theoretical analyses. However, the agreement was partly fortuitous since the measured thrust-time history was significantly different from the theoretical results. Moreover, because a low-energy spark ignitor was used in their experiments and no deflagration-to-detonation transition (DDT) augmentation device was utilized, it is not clear whether full detonation waves were realized.

In a setup similar to Nicholls', Krzycki (1962) performed experimental investigations of PDEs at the US Naval Ordinance Test Station. A gaseous propane/air mixture was continuously injected at the head end of the detonation tube through a reverse-flow injector and ignited by an automobile spark plug at frequencies up to 60 Hz. The power output of the spark plug varied inversely with the ignition frequency and was only 0.65 J at the frequency of 60 Hz. This fact implies that a substantial part of the combustion process occurring in the detonation tube was deflagration. Krzycki also used the method of characteristics to calculate the pressure history at the head end of the detonation tube, with the effect of the blowdown process taken into account. Based on his well-documented experimental results, Krzycki concluded that the PDEs are not promising for propulsion application. Possibly due to this conclusion, most experimental works related to the PDE concept were stopped in the late 1960's.

A different design concept was proposed by Nicholls et al. (1966). They examined the feasibility of a rocket motor that utilized a rotating detonation wave propagating in an annular combustor chamber. Both hydrogen/oxygen and methane/oxygen mixtures were employed in their experiments. A unidirectional detonation wave was created after transition from a deflagration wave. However, multicycle operations were not achieved. Their experiments and accompanying analyses indicated that the ideal performance of such a rocket motor is essentially the same as that of a conventional rocket engine.

Applications of the pulse detonation devices to fields rather than propulsion were reported in Russia in the 1980s. Korovin et al. (1981) examined the efficiency of thermal oxidation of nitrogen in a detonation reactor involving intermittent detonation waves with initiation frequencies from 2 to 16 Hz. The reactor was reported to be able to operate without significant changes for 2000 hours. Smirnov and Boichenko (1986) studied intermittent detonations of a gasoline/air mixture in a 3-m-long tube with frequencies up to 8 Hz, aiming at improving the efficiency of a commercial rock-crushing apparatus.

In the late 1980s, Helman and colleagues (1986) reexamined the PDE concept at the US Naval Postgraduate School. They carried out a series of experiments with an ethylene/air mixture, showing the first successful self-aspirating airbreathing PDE. The system was operated at frequencies up to 25 Hz, the maximum frequency allowed by the solenoid valve that was used to control the gas flow. An important new idea employed in their experiments is the use of a predetonator to overcome the energy requirement for detonation initiation. The detonation was first initiated in the predetonator, a small tube containing an ethylene/oxygen mixture, and then transmitted to the primary detonation tube. The volume of the predetonator is only 2% of that of the primary detonation tube. Based on the experimental results, they suggested that frequencies of 150 Hz and specific impulse in the range of 1000-1400 s might be obtained in a practical PDE.

Since the renewed work of Helman et al., there has been a growing interest in the PDE as an advanced propulsion system. A number of reviews can be obtained from the literature. Eidelman et al. (1991) reviewed some of the early research as well as that done in the late 1980s. Bussing and Pappas (1996) discussed the basic theory and design concepts. Kailasanath (2000) reviewed the applications of detonations to propulsion. A comprehensive review of the more recent progress in PDE research was provided by Kailasanath (2003). Wu, Ma, and Yang (2003) summarized the experimental work up to date. For clarity, the research on PDEs since 1986 is divided into three categories: experimental, numerical, and analytical studies, and is reviewed in the following subsections.

1.4.1 Experimental Studies on PDEs

Much effort has been expended in studying various important aspects of PDEs experimentally. These studies can be divided into single-pulse and multicycle experiments and are briefly summarized in Tables 1.1 and 1.2. Single-pulse experiments involve only the detonation initiation and propagation and the blowdown processes, whereas multicycle experiments include the additional purging and refilling processes. Single-pulse experiments can be used to determine the detonation initiation energy required for a given mixture, to measure the detonation wave properties, and to validate the concepts, serving as the basis for the more complex multicycle experiments. Both hydrogen and hydrocarbon fuels were involved in the experiments. The hydrocarbon fuels include both gaseous fuels such as ethylene (C_2H_4) and propane (C_3H_8) and liquid fuels such as JP10 ($C_{10}H_{16}$). Ethylene (C_2H_4) was selected by many researchers because of its well-documented detonation properties and as a common decomposition of some typical heavy hydrocarbon fuels.

Table 1.1 Survey of single-pulse experimental investigations of PDEs

reference	propellants	tube length	ignitor energy	DDT augmentation	impulse measurement
Hinkey et al. (1995)	H_2/air H_2/O_2	unknown	1.7 J	Shchelkin spiral	pressure history load cell
Sterling et al. (1996)	H_2/air	175.9 cm	N/A	unspecified device	N/A
Broda et al. (1999)	C_2H_4/air	182.9 cm	3.5 J	half-disk protrusion	N/A
Daniau et al. (2000)	C_2H_4/O_2	6.5~10 cm	30 J	direct initiation Shchelkin spiral	ballistic pendulum
Sanders et al. (2000)	C_2H_4/air C_2H_4/O_2	135 cm	N/A	Shchelkin spiral	N/A
Sinibaldi et al. (2000)	$C_2H_4/O_2/N_2$	190.5 cm	0.33~8.31 J	none	N/A
Litchford (2001)	H_2/O_2	90 cm	0.11 J	Shchelkin spiral	load cell
Sinibaldi et al. (2001)	C_2H_4/air C_2H_4/O_2 C_3H_8/O_2	120 cm	N/A	N/A	N/A
Cooper et al. (2002)	$C_2H_4/O_2/N_2$ $C_3H_8/O_2/N_2$	60.9~150 cm	0.03 J	Shchelkin spiral blockage plate orifice plate	ballistic pendulum
Lieberman et al. (2002)	$C_3H_8/O_2/N_2$	100 cm	0.03 J	hot jet initiation	ballistic pendulum
Meyer et al. (2002)	H_2/air	91.4 cm	N/A	Shchelkin spiral extended cavity coannulus	N/A
Cooper et al. (2003)	C_2H_4/O_2	105.7 cm	0.03 J	none	ballistic pendulum

Table 1.2 Survey of multicycle experimental investigations of PDEs

reference	propellants	tube length	ignitor energy	DDT augmentation	impulse measurement	frequency
Aarnio et al. (1996)	H_2/air	121.9 cm	1.7 J	N/A	pressure history load cell	5 Hz
Sterling et al. (1996)	H_2/O_2 C_2H_4/O_2	15.2 cm 50.8 cm	N/A	unspecified device	N/A	33 Hz 100 Hz
Stuessy and Wilson (1996)	H_2/O_2	53.3 cm	N/A	N/A	N/A	10~12 Hz
Hinkey et al. (1997)	H_2/air	91.4 cm	1.5 J	N/A	N/A	10 Hz
Stuessy and Wilson (1997)	C_3H_8/O_2	53.3 cm	N/A	N/A	N/A	20.4~28.5 Hz
Brophy et al. (1998)	JP10/O_2	15.2~76.2 cm	1.4 J	N/A	N/A	5 Hz
Schauer et al. (1999)	H_2/air	91.4 cm (1~4 tubes)	N/A	Shchelkin spiral	N/A	0.5~100 Hz (per tube)
Broda et al. (1999)	C_2H_4/air	182.9 cm	4~8 J	obstacle	N/A	8~10 Hz
Brophy and Netzer (1999)	JP10/O_2	29 cm	0.5 J	N/A	N/A	10 Hz
Zitoun and Desbordes (1999)	C_2H_4/O_2	6.1~43.6 cm	35 J	none	pressure history	1~15 Hz
Schauer et al. (2000)	H_2/air	91.4 cm	N/A	Shchelkin spiral	pressure history	14~40 Hz
Watts et al. (2000)	C_2H_4/air	N/A	25 J	obstacle	N/A	10 Hz
Falempin et al. (2001)	C_2H_4/O_2	5.0~42.6 cm	N/A	N/A	N/A	80 Hz
Litchford (2001)	H_2/O_2	90 cm	0.11 J	Shchelkin spiral	load cell	5 Hz
McManus et al. (2001)	H_2/air	25.4 cm	0.02 J	N/A	load cell	10~35Hz
Frankey et al. (2002)	H_2/air	182.88 cm	N/A	Shchelkin spiral	pressure history	11~21 Hz
Shimo et al. (2002)	C_2H_4/air	82.2 cm	N/A	Shchelkin spiral	N/A	15 Hz
Brophy et al. (2002)	C_2H_4/air JP10/O_2	25 cm	N/A	N/A	pressure history	80 Hz 30 Hz
Farinaccio et al. (2002)	C_3H_8/O_2	40 cm	N/A	N/A	load cell	10~25 Hz
Brophy et al. (2003)	C_2H_4/air C_3H_8/air	100 cm	N/A	obstacle	N/A	30 Hz
Meyers et al. (2003)	C_3H_8/O_2	7.62~30.5 cm	N/A	Shchelkin spiral	pressure history	4.4~20 Hz
Rasheed et al. (2003)	H_2/air	100 cm	N/A	orifice plate	spring-damper	10 Hz
Shehadeh et al. (2003)	$C_2H_4/O_2/N_2$	184 cm	N/A	N/A	spring-damper	10 Hz

1.4.1.2 Impulse Measurements

Impulse is one of the key performance measures of a PDE. Several techniques have been proposed for the impulse measurement. The most straightforward one is to integrate the pressure history at the closed end of the detonation tube. This technique doesn't require complex measurement setup but can be implemented only to a simple detonation tube without internal obstacles. Another popular technique used in single-pulse experiments is known as ballistic pendulum technique, in which the detonation tube is suspended as a pendulum by support wires and the impulse is determined by measuring the maximum horizontal deflection of the tube (Cooper et al., 2003). In multicycle experiments, the load cell technique is often used. In this technique, the force history is directly measured by the load cell attached to the detonation tube through a load cell cage (Hinkey et al., 1995). Since the negative thrust cannot be recorded, the impulse may be overestimated in this technique. In addition, the response of the structure must be taken into account. Other reported techniques include using damped thrust stand (Schaller et al., 2001) and spring-damper system (Shehadeh et al., 2003). Due to the limitation of each technique, a combination of these techniques may be required to obtain reliable impulse measurements. Hinkey et al. (1995) measured the impulse in their single-pulse experiments using both the pressure history and load cell techniques and found that the impulse from the pressure history is about 20% lower than that from the load cell data.

With the measured impulse and the weight of fuel to generate this impulse, the propulsive performance parameter such as the specific impulse can be readily obtained. It should be mentioned that the specific impulse calculated from these direct-connect experiments doesn't represent the specific impulse of PDEs at flight condition, under which the engine inlet and the momentum of the incoming air must be taken into account. On the other hand, because the purging and refilling processes are not included in the single-pulse experiments and the negative thrust may appear during these two processes, the impulses from single-pulse experiments are usually lower than those from multicycle experiments.

1.4.1.3 Detonation Initiation

Detonation initiation is one of the major challenges in the PDE design. A detonation can be initiated either directly through a large amount of energy deposition or indirectly through a low-energy deposition along with a deflagration-to-detonation (DDT) process. Typical values for direct initiation energy for hydrocarbon fuel/air mixtures are of the order of Kilo-Joules to Meg-Joules (Benedick et al., 1986). The deposition of such high initiation energies is impractical for repetitive initiations. Most PDE experiments have thus relied on a DDT process for detonation initiation.

According to the literature (Oppenheim, 1963; Lee and Moen, 1980; Kuo, 1986), a DDT process consists of the following sequence of events: 1) deflagration initiation — a deflagration combustion is initiated by a low-energy deposition; 2) shock wave formation — the energy released by the deflagration increases the volume of the products and generates a train of weak compression waves that propagate into the reactants ahead of the flame and finally merge into a shock wave; 3) onset of "an explosion in an explosion" — the shock wave heats and compresses the reactants ahead of the flame, creates a turbulent reaction zone within the flame front, and eventually cause one or more explosive centers formed behind the shock front; 4) overdriven detonation formation —

strong shock waves are produced by the explosions and couple with the reaction zone to form a overdriven detonation; 5) stable detonation establishment — the overdriven detonation wave decreases to a steady speed at around the CJ detonation velocity.

The distance from the ignition to the detonation formation point is referred to as the DDT length, which is in general a function of the fuel and oxidizer, the tube diameter and geometry, the tube wall surface roughness, and the method used to ignite the mixture. Sinibaldi et al. (2000) investigated the dependence of the DDT length on the ignition energy, ignition location, and mixture stoichiometry for a $C_2H_4/O_2/N_2$ mixture. They found that ignition energies above 0.28 J had little effect on DDT lengths. The ignition location tests revealed that when the ignitor was placed 1.33 tube diameter from the head wall, the DDT length could be reduced by up to 32%. Their results also showed that the mixture equivalence ratio significantly affects the DDT length. The minimum DDT length of around 7.5 cm for the C_2H_4/O_2 mixture was obtained with an equivalence ratio of 1.2. A drastic increase in DDT length was observed when the equivalence ratio is less than 0.75.

In general, the DDT length could be large compared to the tube length used in PDE experiments. Hinkey et al. (1995) carried out a series of tests with H_2/O_2 mixtures of various equivalence ratios and found that the DDT lengths are on the order of 30 to 100 cm. They thus suggested using some DDT augmentation devices to enhance the DDT process and reduce the DDT length, which was adopted in most late PDE experiments. In the early multicycle experimental work of Nicholls (1957) and Krzycki (1962), it is not clear whether full detonation waves were realized because a low-energy spark ignitor was used in their experiments and no DDT augmentation devices were implemented.

A classical approach for DDT enhancement is to place a spiral, known as the Shchelkin spiral (Shchelkin, 1940), into the detonation tube. Hinkey et al. (1995) first applied this approach to their single-pulse PDE experiments with H_2/O_2 mixture and found that the Shchelkin spiral reduced the DDT length by a factor of about 3. In addition to the Shchelkin spirals, other internal obstacles such as half-disk protrusions (Broda et al., 1999), blockage plates and orifice plates (Cooper et al., 2002), and coannulus (Mayer et al., 2002) have also been used by various researchers. It should be noted, however, while enhancing the DDT processes, all these obstacles result in significant total pressure loss and degrade the propulsive performance. Cooper et al. (2002) reported that the DDT lengths could be reduced by an average of 65% in various $C_3H_8/O_2/N_2$ and $C_2H_4/O_2/N_2$ mixtures using obstacles with a blockage ratio of 0.43, whereas the impulse was reduced by up to 25%.

Another traditional detonation initiation concept involves using a predetonator (Helman et al., 1986), which is in essence a detonation-to-detonation initiator. A detonation is initiated in a more easily detonable mixture called as the driver gas and then propagates into and initiates a detonation in the primary mixture. A simple example of this concept is to fill a fuel/oxygen mixture or the driver gas in an initiation section near the closed end of the detonation tube (Hinkey et al., 1995; Sanders et al., 2000). The minimum length of the initiation section is the DDT length of the driver gas. The aforementioned DDT augmentation devices can be further implemented within the initiation section to achieve more rapid initiation. A disadvantage of this concept is the need to carry an additional driver gas or oxygen generator, which increases the system weight. The additional driver gas also lowers the specific impulse since the weight flow rates of both the fuel and the driver gas should be taken into account in calculating the specific impulse. To mitigate this disadvantage, the amount of the driver gas or the volume of the driver gas region must be as small as possible. A practical way to reduce the volume of the driver gas region is to utilize an additional smaller tube for the driver gas. This additional tube, usually with a volume on the order of 1% of that of the main detonation tube, is called a predetonator. The detonation transmission from the predetonator to the main detonation tube is thus a key issue in the predetonator applications (Sinibaldi et al., 2001; Santoro et al., 2003).

Diffraction of detonation from a small tube into an unconfined space has been extensively investigated in the past (Lee, 1984; Desbordes, 1988). According to the literature, a successful detonation transmission happens if the tube diameter is larger than the critical diameter. This critical diameter is usually expressed in terms of the detonation cell size of the mixture. It is now commonly accepted that the critical diameter is about thirteen times of the detonation cell size for smooth circular tubes. The detonation transmission from the predetonator to the main detonation tube has also been investigated recently (Sinibaldi et al., 2001; Santoro et al., 2003; Brophy, et al., 2003). Successful detonation transmission from the predetonator to the main detonation tube could be achieved at predetonator tube diameters less than the critical diameter because of the confinement of the transition region and main detonation tube (Santoro et al., 2003).

Other techniques proposed for promptly achieving detonation initiation include hot jet initiation, detonation wave focusing, etc. Hot jet initiation was observed by Knystautas et al. (1979) for sensitive fuel-oxygen mixtures. Lieberman et al. (2002) recently demonstrated the possibility of using a hot jet to initiate a detonation in a short detonation tube filled with the $C_3H_8/O_2/N_2$ mixture. The idea of the detonation wave focusing is to initiate the detonation in the main detonation tube through the merging of the detonation waves from a bunch of small tubes (Jackson and Shepherd, 2002).

1.4.2 Numerical Studies on PDEs

In addition to experimental investigations, substantial attempts were made to numerically study the single-pulse and multicycle operations of various PDEs consisting of single or multiple detonation tubes with or without nozzles and ejectors. Based on the spatial dimensions used, these numerical studies can be classified into one-dimensional or quasi-one-dimensional and two-dimensional or axisymmetric simulations, as summarized in Tables 1.3 and 1.4, respectively.

In contrast to experiments in which ethylene (C_2H_4) is often used as the fuel, most numerical studies use hydrogen (H_2) as the fuel because of its relatively simpler chemical kinetics. Another significant difference between experiments and simulations is the detonation initiation. In experiments, as discussed in Sec. 1.4.1.3, the detonation is usually initiated indirectly through a low-energy deposition along with a DDT process since the direct initiation with high-energy deposition is not practical. In numerical simulations, however, a small spark region with high temperature and pressure is commonly implemented to directly initiate the detonation. In addition, because of the lack of the DDT process and because there is no frequency limitation arising from the hardware such as the solenoid valves, the operating frequencies are much higher in numerical simulations than those that can be achieved in experiments. In spite of many simplifications used in the numerical simulation, its capabilities in providing the detailed unsteady flowfield make it a practical and efficient methodology for PDE performance and flow dynamic analyses.

Table 1.3 Survey of one-dimensional numerical simulations of PDEs

reference	exit B.C.	propellants	chemical kinetics	tube length	spark length	nozzle	frequency (cycles)
Cambier and Adelman (1988)	N/A	H_2/air	16-step 7-species	50 cm	2 cm	divergent	667 Hz (3 cycles)
Bussing (1994)	N/A	H_2/O_2 H_2/air	18-step 7-species	20 cm	0.2 cm	none	single pulse
Sterling et al. (1995)	constant pressure	H_2/air	equilibrium chemistry	100 cm	0.5 cm	none	≈220 Hz (6 cycles)
Cambier and Tegner (1998)	N/A	H_2/air	N/A	10 cm	0.4 cm	divergent	1000~2600 Hz
Kailasanath et al. (1999)	relaxing pressure	H_2/air	48-step 8-species	20 cm	0.2 cm	none	single pulse
Fong and Nalim (2000)	constant pressure	H_2/air	N/A	10.2 cm	N/A	none	30~150Hz
Mohanraj and Merkle (2000)	constant pressure	H_2/O_2	1-step 2-species	50 cm	0.12 cm	divergent CD	≈230 Hz
Ebrahimi and Merkle (2002)	constant pressure	H_2/O_2	16-step 8-species	20 cm	0.2 cm	none	≈400 Hz (3 cycles)
Ebrahimi et al. (2002)	varying pressure with 2D correction	H_2/O_2	1-step 2-species	10.2 cm	0.1 cm	none	200~1000 Hz
Wu, Ma, and Yang (2003)	zero-gradient	H_2/air	1-step 2-species	60 cm	0.02cm	CD	200~400 Hz

Table 1.4 Survey of two-dimensional numerical simulations of PDEs

reference	num. of tubes	propellants	chemical kinetics	tube length	spark length	nozzle	cycles/ frequency
Eidelman et al. (1990)	1	C_2H_4/air	energy release behind detonation	8cm 16 cm	N/A	none	single pulse
Lynch and Edelman (1996)	1	H_2/air	7-step 6-species	8cm 16 cm	1~2 cm	none	single pulse
Cambier and Tegner (1998)	1	H_2/air	N/A	10 cm	0.4 cm	divergent	single pulse
Eidelman and Yang (1998)	1	C_2H_2/air	1-step	16 cm	N/A	convergent divergent	single pulse
Li et al. (2000)	1	C_2H_4/air	2-step induction-parameter	50 cm	1.25 cm	none	single pulse
Li and Kailasanath (2001)	1	C_2H_4/O_2	2-step induction-parameter	135 cm	2 cm	none	single pulse
Allgood et al. (2002)	1	H_2/O_2/Ar	2-step induction-parameter	50.8 cm	N/A	ejector	single pulse
Ebrahimi et al. (2002)	1	H_2/O_2	16-step 8-species	10.2 cm	0.1 cm	none	single pulse
Kawai and Fujiwara (2002)	1	H_2/O_2/Ar	2-step induction-parameter	10~40 cm	N/A	none	2 cycles
Li and Kailasanath (2002)	1	C_2H_4/O_2	2-step induction-parameter	10~500 cm	1 cm	none	single pulse
Yungster and Perkins (2002)	1	H_2/O_2	19-step 9-species	182.9 cm	N/A	ejector	5 cycles (≈122 Hz)
Li and Kailasanath (2003)	1	C_2H_4/O_2 C_2H_4/air	2-step induction-parameter	50 cm	jet initiation	none	single pulse
Povinelli and Yungster (2003)	1	C_2H_4/air	36-step 20-species	100 cm	0.5~1 cm	none	single pulse
Tangirala et al. (2003)	1	H_2/air C_2H_4/O_2	23-step 7-species 38-step 21-species	100 cm	0.5 cm	none	single pulse
Wu, Ma, and Yang (2003)	1	H_2/air	1-step 2-species	60 cm	0.02 cm	none	200~400 Hz
Yungster (2003)	1	H_2/O_2 H_2/air	19-step 9-species	100 cm	0.5 cm	divergent	3 cycles (≈110Hz)
Ebrahimi et al. (2001)	2	H_2/O_2	16-step 8-species	10 cm	N/A	CD	single pulse
Ebrahimi and Merkle (2002)	2	H_2/O_2	16-step 8-species	10 cm	N/A	CD	single pulse
Ebrahimi et al. (2003)	1~3	H_2/O_2	16-step 8-species	10~30 cm	N/A	CD	single pulse
Ma et al. (2003)	1; 3	H_2/air	1-step 2-species	60 cm	0.02 cm	CD	250~333 Hz

1.4.2.2 One-Dimensional Numerical Simulations

One of the first numerical studies on PDE reported in the literature was attributed to Cambier and Adelman (1988). Quasi-one dimensional simulations with multi-step finite rate chemical kinetics were carried out for a 50-cm-long detonation tube attached to a 43-cm-long diverging nozzle with stoichiometric H_2/air mixture. The detonation was initiated at the closed end by a 2-cm-long spark region with a temperature of 1500 K. The refilling process started when the head-end pressure fell to 3.5 atm. The fresh reactants moved at speeds up to 350 m/s. The engine reached steady cyclic operation by the third cycle with a cycle frequency of about 667 Hz. Specific impulses up to 6507 s were reported. These very high specific impulses may be due to the facts that their calculations were based on the gross thrust from the exit plane and that the contribution from the spark region on the impulse was not accounted for.

Sterling et al. (1995) also conducted one-dimensional simulations with H_2/air mixture. The detonation tube is 100 cm long. The spark region has a length of 0.5 cm with a temperature of 3000 K and a pressure of 50 atm. The refilling process began when the head-end pressure decayed to the atmospheric pressure. They calculated the specific impulse for the sixth cycle based on the head-end pressure history and obtained a value of 5152 s, which is much smaller than that of Cambier and Adelman (1988).

Cambier and Tegner (1998) examined the effect of the spark region on the performance in their quasi-one-dimensional and two-dimensional simulations with H_2/air mixture for a 10-com-long detonation tube with various divergent nozzles. The spark region spans 0.4 cm, with a temperature of 2500 K and a pressure of 50 atm. They observed that the contribution from the spark region on the single-pulse peak impulse ranges from 17% to 27%. After subtracting this contribution, they obtained specific impulses of 3500 s ~ 4100 s based on the head-end pressure history of their quasi-one-dimensional multicycle results.

In addition to the differences in the operation conditions and in the calculation methods for the specific impulse, the exit boundary condition plays another important factor that cause the differences in the reported specific impulses from one-dimensional simulations (Kailasanath et al., 1999). Choosing appropriate exit boundary conditions represents a major challenge in the one-dimensional simulations for PDEs. In general, if the outflow is supersonic, extrapolation of the condition from the inside can be used. However, for subsonic outflow, the flow inside the domain near the exit relates to the flowfield outside the domain, which is unknown from the one-dimensional simulations. The situation is further compounded by the existence of the unsteady detonation waves and other associated waves. Strictly, there are no accurate exit boundary conditions for this kind of complex unsteady subsonic outflow.

Most one-dimensional simulations have relied on a fixed-pressure boundary condition for the outflow (Cambier and Adelman, 1988; Starling, 1995). Ebrahimi et al. (2002) used the fixed-boundary condition as well as a varying-pressure condition based on corrections from two-dimensional simulations. They found that with the fixed-pressure condition, the flow chokes as soon as the detonation wave arrives at the exit, whereas the varying-pressure result shows a duration of a subsonic outflow before choking. Kailasanath et al. (1999) utilized a relaxing-pressure boundary condition. The pressure is set to reach the ambient value in a relaxation length from the end of the detonation tube. A larger value of the relaxation length implies a slower relaxation of pressure to ambient. Based on single-pulse operation, they observed that the specific impulse is larger for slower relation cases. They then concluded that the variations in specific impulses reported in the literature could be explained on the basis of exit boundary conditions used.

1.4.2.3 Two-Dimensional Numerical Simulations

In spite of the computational efficiency of the one-dimensional simulations for performance predictions, the difficulty in specifying the exit boundary condition makes them less attractive. Multi-dimensional simulations with computation domain including both the detonation tube and the external region are required in order to faithfully describe the system dynamics, especially in the near field of the tube exit where the flow is intrinsically multi-dimensional, and to provide more accurate performance predictions. This subsection will provide a brief review on some of the two-dimensional simulations. Issues related to nozzle and multitube will be discussed in other subsections.

Eidelman et al. (1990) carried out two-dimensional axisymmetric simulations for a valveless PDE with C_2H_4/air mixture. Both internal and external flowfields were included in their computational domain. The system simulated consisted of a cylindrical detonation tube with a length of 8 or 16 cm. Its operation is a little different from that described in Sec. 1.3.1. The detonation is initiated at the aft open end and travels toward the head end where the thrust wall, fuel injector, and air inlet are located, ejecting burned gases through both the open end and the air inlet. Air is entrained into the detonation tube when the pressure falls below the atmospheric pressure during part of the cycle. Since no valves are required to separate the air inlet and the detonation tube, this kind of

PDE is self-aspirating and is called valveless PDE. From a scaling study based on single-pulse operation, they concluded that the thrust of the detonation tube increases linearly with the detonation tube length when the other parameters are kept constant. This conclusion, however, is incorrect or misleading, since the thrust they calculated was based on only a portion of a cycle.

Lynch and Edelman (1996) conducted two-dimensional axisymmetric simulations with multi-step finite rate chemical kinetics for H_2/air mixture for a valveless PDE similar to that analyzed by Eidelman et al. (1990). They investigated the flow dynamics with two types of air inlet. In the straight inlet case, a large recirculation zone is formed behind the thrust surface upon the inflow of the fresh air. This recirculation zone may cause an increase in the time required to entrain the air and to purge the products. By using a scoop inlet, the recirculation zone is reduced. They suggested additional inlet shaping and viscous entrainment effects to obtain optimizing design.

Most of the recent two-dimensional studies focused on single-tube PDEs with detonation initiated at the closed end. Ebrahimi et al. (2002) carried out two-dimensional simulations with a H_2/O_2 mixture to provide exit boundary condition corrections for their one-dimensional simulations. Li and Kailasanath (2001) looked at the single-pulse flowfield evolution under full or partial fills for a C_2H_4/O_2 mixture. The two-step induction-parameter chemical kinetic model was adopted, in which combustion radicals are formed in the first step, which is represented by an induction parameter, and the energy is released in the second step. This model has also been used by other researchers for H_2/O_2 mixtures (Allgood et al., 2002; Kawai and Fujiwara, 2002). In a later work of Li and Kailasanath (2002), they further investigated the effect of partial filling on the propulsive performance and observed that the fuel-based specific impulse increases as the partial filling ratio decreases for single-pulse operation. A scaling relation of the specific impulses between the partial and full fillings was then proposed.

Many of the two-dimensional simulations are limited to single-pulse operations. However, significant differences exist between single-pulse and multicycle computations and the conclusions from single-pulse studies may not be applied to multicycle cases directly (Cambier and Tegner, 1998; Yungster, 2003; Wu, Ma, and Yang, 2003). To date, two- dimensional simulations with multicycle operations are rather sparse. Kawai and Fujiwara (2002) carried out two-dimensional simulations for the first two cycles of a straight tube PDE containing an Ar-diluted stoichiometric H_2/O_2 mixture, with attention paid to the injection behavior during the 2nd cycle. Yungster and Perkins (2002) conducted multicycle simulations of various PDE-ejector configurations utilizing H_2/O_2 mixture. The thrust and mass flow rate over five cycles are presented. They stated that more cycles might be required to establish some kind of limit cycle or steady periodic cycle. Up to now, two-dimensional simulations with steady periodic cycle attained have been reported only by Ma and colleagues (Wu, Ma, and Yang, 2003; Ma et al., 2003).

1.4.2.4 Effect of Nozzles

The detonation products exhausting from the detonation tube carry a large amount of internal energy. A nozzle is thus needed to convert this internal energy to kinetic energy to improve the performance. In conventional steady engines, the nozzle is optimized by matching the exit pressure with the ambient pressure. The nozzle designs for PDEs, however, are complicated by the unsteady nature of the PDEs, especially the complex shock waves resulting from the repetitive detonations. To date, no theory for PDE nozzle designs has been developed. Several numerical and experimental studies that focused on the effect of nozzles on the PDE performance are reviewed in the following paragraphs.

Cambier and Adelman (1988) considered a 43-cm-long divergent nozzle attached to a 50-cm-long detonation tube in their quasi-one-dimension multicycle simulations with a H_2/air mixture. They stated that other designs with a convergent section and throat cause the detonation waves to reflect as shock waves from the converging section. The reflected shock waves elevate the head-end pressure, interfere with the refilling process, and lower the cycle frequency. On the other hand, a divergent nozzle causes reflected rarefaction waves that propagate back into the tube to allow rapid refilling processes. A cycle frequency of as high as 667 Hz was reported in their studies with a divergent nozzle. However, they didn't compare the propulsive performance numbers between the divergent nozzle and other nozzles. It is thus unclear which kind of nozzle is better for achieving higher propulsive performance.

Cambier and Tegner (1998) investigated the effects of five different divergent nozzles on the performance based on quasi-one-dimensional multicycle simulations and two-dimensional single-pulse simulations. The lengths of the detonation tube and the nozzle are 10 cm and 5 cm, respectively. Both the tube and nozzles were initially filled with a H_2/air mixture. Their single-pulse results indicate that the divergent nozzles can increase the impulse and that the bell-shaped nozzle produces a higher impulse than those with shapes of positive curvatures. In addition, significant differences were observed between single-pulse and multicycle results, and between quasi-one-dimensional and two-dimensional results.

Eidelman and Yang (1998) also considered different nozzle shapes, i.e. three divergent and three convergent nozzles, in their two-dimensional single-pulse simulations. The detonation tube was filled with a C_2H_2/air mixture, whereas the nozzle was filled with air. Their results showed that both the convergent and divergent nozzles drastically increase the PDE performance. Convergent nozzles lead to significant increases in impulse generation time and rapid changes in thrust due to shock wave reflections and relative later times in attaining the peak impulses. Divergent nozzles tend to generate impulse rapidly during detonation product expansion due to the increase in effective thrust wall area so that the peak impulses are reached earlier. These peak impulses, however, are followed by rapid reductions due to the negative thrust generated during the overexpansion of the detonation products. Among the three divergent nozzles, the bell-shaped nozzle produces the highest peak impulse.

Mohanraj and Merkle (2000) used quasi-one-dimension multicycle simulations to study the effects of the divergent and convergent-divergent (CD) nozzles at different back pressures. The injection pressure is fixed at one atmosphere. They found that both types of nozzles provide performance benefit at low back pressures, while the divergent nozzle causes performance deterioration at high back pressures. Their results also showed that divergent nozzles lead to higher cycle frequency.

More recently, Yungster (2003) examined the effect of divergent nozzles on PDE performance in his two-dimensional simulations with operations up to 3 cycles. Both H_2/O_2 and H_2/air mixtures were employed. The detonation tube and nozzles are 100 cm and 40 cm long, respectively. In the single-pulse operation, the nozzles can utilize some of the energy carried by the detonation products to significantly augment the impulse obtained from the detonation tube alone. Impulse augmentation ratios of up to 2.34 and 1.41 were obtained with the bell-shaped nozzle for H_2/O_2 and H_2/air mixtures, respectively. In multicycle operation, however, the performance augmentation is very limited or even negative because of the nozzle flow overexpansion during most of the purging and refilling periods. He stated that in order for the nozzle to remain effective after the first cycle, the combustion products must be purged from the nozzle before the next cycle is started. This will, however, reduce the cycle frequency.

The effect of nozzles was also investigated in several experiments. Stuessy and Wilson (1997) conducted multicycle experiments with and without conical exhaust nozzles. They noted that the inclusion of the nozzle improves the performance. Daniau et al. (2000) investigated the effects of divergent nozzles of different shapes and lengths on the performance of a PDE based on single-pulse experiments. They also observed that bell-shaped nozzles are especially efficient. Cooper et al. (2002) carried out single-pulse experiments and investigated the effect of a 30-cm-long divergent nozzles attached to a 101.6-cm-long detonation tube. They found that the divergent nozzle had a negligible effect, increasing the specific impulse by an average of 1% which is within the experimental uncertainty.

The observations and conclusions reported in these previous numerical and experimental studies indicate the nozzle effect on the PDE performance is far from mature. More studies based on multicycle operations need to be conducted.

1.4.2.5 Multitube PDEs

In addition to the nozzle, another way that may improve the PDE performance is the use of multiple detonation tubes (Ma et al., 2003). The concept of multitube designs is not new. In as early as 1950, Goddard considered a valved multiple combustor deflagration-based pulse jet engine (Goddard, 1950). Bussing proposed a rotary valve multitube pulse detonation engine concept in 1995 by combining some aspects of the Goddard design and the detonation process (Bussing, 1995). It consists of several detonation tubes coupled to an air inlet and fuel source via a rotary valve. The rotary valve isolates the steady operation of the air inlet and fuel system from the unsteady operation of the detonation tubes and allows the filling of some of the detonation tubes while detonation occurs in other tubes. A simple performance model, including the contributions from the inlet, the mixer, the combustor, and the nozzle, was proposed by Bratkovich and Bussing (1995) to examine the aforementioned multitube PDE performance characteristics over a wide range of flight regime. Recently, an in-house four-detonation-tube research PDE was built at the US Air Force Research Laboratory, serving as a test-bed for detonation initiation concept, high frequency operation, heat transfer studies, multitube detonation engine operation, and pulse jet research (Schauer, 2001). It used a valve system based on the “Quad-4”, a sixteen-valve, four-cylinder automobile engine from General Motors. A rotary position sensor was adapted to the intake camshaft to provide both an index of the valve timing sequence and the relative position of the valves. Each detonation tube can operate at frequencies of up to 100 Hz.

Numerical investigations on multitube PDEs also commenced recently. Mohanraj et al. (2001) presented an approximate model for a PDE with five detonation tubes. Time accurate one-dimensional solution of the flowfield was obtained for only one tube. Time delayed versions of this solution were used to model the other tubes. Their results showed that the filling process in a multitube PDE can be markedly different from that in a single-tube PDE. For example, increasing the fill time does not affect the fill fraction in the tubes at some conditions. They also observed that the number of cycles needed to attain steady periodic operation in a multitube configuration is typically larger. Although this approach saves computational effort, the resultant error due to the model approximation is difficult to estimate and may likely be quite large.

Ebrahimi et al. (2001) conducted two-dimensional simulations for a dual-tube PDE, but with only the first-pulse operation. They found that the pressure induced by the detonation in the neighboring tube is nearly as large as that produced by the detonation itself and that the shock wave produced by the detonation is sufficient to initiate combustion in the adjacent tube filled with fresh reactants. In a more recent work (Ebrahimi et al., 2003), the effects of the number of tubes and the tube length on the flowfield interaction among tubes were investigated based on the first-pulse operation. The results indicate that the flowfield interaction among three tubes is approximately a factor of three smaller than that between two tubes, but that increased tube length has no significant effect. The first multidimensional numerical study on multitube PDEs involving multicycle operations was conducted by Ma et al. (2003).

1.4.3 Analytical Studies on PDEs

The intrinsic unsteady nature of the PDE operation process makes the theoretical analyses rather difficult or even impossible. On the other hand, it is desirable to develop simple analytical models that can be used to rapidly and reliably predict the PDE performance and to conduct parametric studies. Several analytical models have been proposed in the past and are summarized in Table 1.5. Based on how the impulse is obtained, these models fall into two classes. One class employs unsteady gasdynamic analysis to determine the instantaneous pressures and forces acting on the thrust wall and calculate the impulse as the integration of them (Nicholls, et al., 1957; Wintenberger et al., 2002; Wintenberger and Shepherd, 2003). The other class, without the need to consider the unsteady wave process within the detonation tube, obtains the impulse or specific impulse of the engine by deriving the flow properties at the exit plane (Talley and Coy, 2002; Heiser and Pratt, 2002; Wu, Ma, and Yang, 2003).

Table 1.5 Survey of analytical studies on PDEs

classification based on impulse calculation	reference	remarks
head-end pressure	Nicholls et al. (1957)	Only constant pressure portion was considered.
	Wintenberger et al. (2003)	Decaying pressure portion was modeled through dimensional analysis and experimental calibration.
	Wintenberger and Shepherd (2003)	Filling process was incorporated.
exit-plane properties	Talley and Coy (2002)	The cycle consists of a constant-volume combustion, a constant-volume blowdown, and a constant-pressure filling process.
	Heiser and Pratt (2002)	Classical thermodynamic cycle analysis was applied to an ideal PDE cycle to predict the upper limit of the PDE performance.
	Wu, Ma, and Yang (2002)	The Heiser and Pratt (2002) approach was extended to accommodate property variations across the detonation wave front.

The most simplified model was reported by Nicholls et al. (1957) in conjunction with their straight-tube experiments. The pressure at the head end remains constant until the arrival of the first rarefaction wave generated as the detonation wave emerges from the open end. The head-end pressure then decays due to the continuing arriving of more rarefaction waves. Only the contribution of the constant pressure portion was considered and the contribution of the decaying pressure period was neglected. Consequently, this model underpredicted the impulse.

Recently, Wintenberger et al. (2003) presented a semi-analytical model for a single-pulse detonation tube. Both the constant pressure and decaying pressure portions are considered. The duration and amplitude of the constant pressure portion is determined by analyzing the gasdynamics of the self-similar flow behind a steadily moving detonation wave within the tube. The decaying pressure portion is analyzed using dimensional analysis, leaving a nondimensional parameter to be obtained through experimental calibrations. Wintenberger and Shepherd (2003) later extended this model to multicycle operations by accommodating the refilling process. These models, however, are only useful for predicting the impulse from a simple straight detonation tube.

The constant volume limit model proposed by Talley and Coy (2002) is based on a cycle consisting of a constant-volume combustion process, a constant-volume blowdown process, and a constant-pressure filling process. The characteristic wave transit times are assumed to be much shorter than the blowdown time. During the blowdown process, the gases in the chamber are modeled as being time varying but spatially uniform while venting occurs through an infinitely thin nozzle with quasi-steady flow. When the chamber pressure reaches the fill pressure, the filling process begins and is modeled as a constant-pressure process.

Heiser and Pratt (2002) applied the classical thermodynamic cycle analysis to an ideal PDE thermodynamic cycle. The detonation wave converts the reactants to the products with CJ properties. These products are then assumed to isentropically expand to the atmospheric pressure. They recognized that no simple device can fulfill this unsteady isentropic expansion process but the upper limit of the performance can be established through this assumption. After the thermodynamic cycle efficiency is obtained, the specific impulse can be readily determined through the control-volume energy balance. This model was later extended by Wu, Ma, and Yang (2003) to accommodate property variations across the detonation wave front. The advantage of this model over that proposed by Tally and Coy (2002) is that the detonation combustion is considered. However, since all thermodynamic cycle analyses are based on an assumption that all the fluid elements experience the same processes at same sequence, the purging and refilling processes involved in a PDE can thus not be incorporated. Moreover, comparisons with more accurate numerical simulations should be made in order to judge its accuracy in predicting the upper performance limit.

1.5 Research Objectives

The primary objective of this research is to evaluate the concept of airbreathing PDEs, to investigate their flow dynamics, to determine their performance, to identify the various loss mechanisms, and to examine the effects of the operation timing and system geometry.

Figure 1.13 schematically shows the airbreathing PDE studied herein. It includes a supersonic inlet with mixed compression, an air manifold/acoustic cavity, a rotary valve, a combustion chamber containing single or multiple detonation tubes, and a convergent-divergent nozzle. Hydrogen is used as the fuel. As a specific example, the flight condition with a flight altitude of 9.3 km and a flight Mach number of 2.1 is considered. The static pressure and temperature are 0.29 atm and 228 K, respectively, corresponding to a total pressure of 2.65 atm and a total temperature of 428 K.

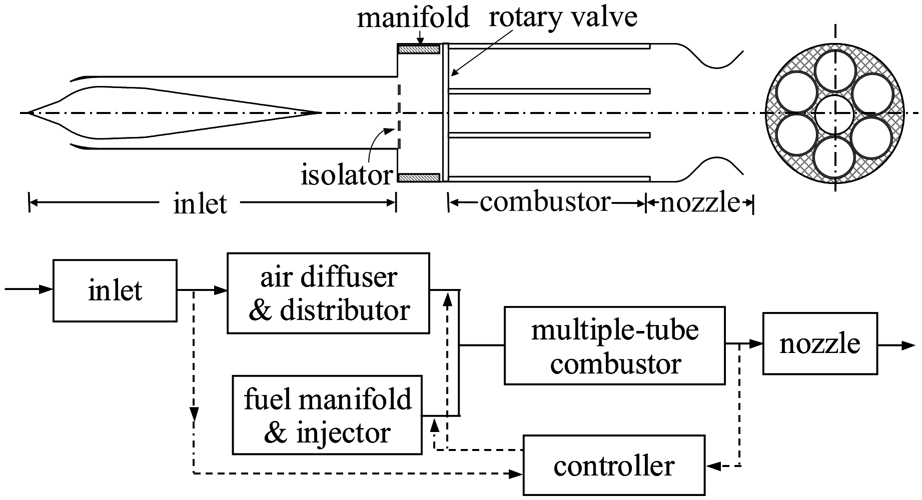

Fig. 1.13 Supersonic airbreathing pulse detonation engine

In Chapter 2, the supersonic inlet dynamics is studied. The time-dependent Favre-averaged Navier-Stokes equations along with a two-equation turbulence model are solved by a finite-volume method, with a four-stage Runge-Kutta time integration technique for temporal discretization and the Harten-Yee upwind TVD scheme for spatial discretization. The steady-state inlet flow dynamics and the response of the inlet shock system to downstream pressure disturbance are investigated.

Chapter 3 introduces the recently developed space-time conservation element/solution element method and utilizes it to the quasi-one-dimensional study of a single-tube PDE. Chemical kinetics is simulated using a simple one-progress-variable model for a stoichiometric hydrogen/air mixture. The flow dynamics is examined through numerically obtained x-t diagrams. The effects of operating frequency and valve close-up time on the propulsive performance are investigated.

In Chapter 4, two-dimensional analyses are carried out for single-tube PDEs with or without CD nozzles under multicycle operations. The two-dimensional code is efficiently parallelized by implementing the message-passing-interface (MPI) library and a domain decomposition technique. The flow dynamics involved in the PDE operation is examined in detail. A flow-path based performance prediction model is proposed to estimate the upper performance limit of the current PDE system. The various performance loss mechanisms are identified. The effects of operation timing including the cycle time or frequency, valve close-up time, and purge time on the propulsive performance are comprehensively studied. Moreover, the effects of nozzle configurations in terms of the nozzle length and throat area are examined.

In Chapter 5, multitube airbreathing PDEs with repetitive operations are studied by means of two-dimensional simulations. The combustor consists of three detonation tubes. The flow evolution and tube interactions are carefully examined and the various loss mechanisms are identified. The effects of operating timing such as the cycle time and the valve close-up time were investigated systematically. Comparisons with the single-tube results are made. The effect of the system geometry is partially assessed by considering a free volume between the detonation tubes and the common nozzle.

Finally, Chapter 6 summarizes the present work and provides several recommendations for the future work.

Chapter 2

Supersonic Inlet Dynamics

The inlet and its interaction with combustor represent a crucial aspect in the development of any airbreathing engine, including PDEs. The inlet is designed to capture and supply stable airflow at a rate demanded by the combustor, and to maintain high pressure recovery and stability margin at various engine operating conditions. The overall vehicle performance depends greatly on the energy level and flow quality of the incoming air. A small loss in inlet efficiency may translate to a substantial penalty in engine thrust. Moreover, any change in the inlet flow structure may modify the downstream combustion characteristics and subsequently lead to undesirable behaviors, such as flame blow-off and flashback. Thus, matching inlet behavior to engine requirements is of fundamental importance to designers (Yang and Cappuccio, 1990).

In addition to its primary function of supplying air, an inlet has a determining influence on the dynamics of the entire system through its intrinsic unsteadiness and interactions with the combustion chamber. Typically, pressure waves are produced in the combustion chamber and propagate upstream to interact with the inlet flow through a manifold where mixing of air and fuel occurs. The resultant flow oscillations in the inlet diffuser then either propagate downstream in the form of acoustic waves or are convected downstream with the mean flow in the form of vorticity and entropy waves, and further reinforce the unsteady motions in the combustor. A feedback loop is thus established between the inlet and combustor. The situation is much more complicated in a supersonic airbreathing PDE due to its pulsed operation.

2.1 Problem Description

In this chapter, axisymmetric two-dimensional simulations are conducted for a mixed-compression supersonic inlet as shown in Fig 2.1. The cowl radius is $R_c = 3.4$ cm. This inlet is designed for a flight Mach number of 2.1 and a flight altitude of 9.3 km. The static pressure and temperature of the freestream are 0.29 atm and 228 K, respectively. The corresponding total pressure and temperature are 2.65 atm and 428 K, respectively. The time-dependent Favre-averaged Navier-Stokes equations are solved by a finite-volume method, with a four-stage Runge-Kutta time integration technique for temporal discretization and the Harten-Yee upwind TVD scheme (Harten, 1983; Yee, 1989) for spatial discretization. The specific objectives of this work are: 1) to understand the overall shock and flow structures in a realistic supersonic inlet, 2) to examine the effects of downstream disturbances on inlet dynamics, 3) to investigate the influences of the viscous boundary layer and flow separations downstream of the terminal shock, and 4) to provide entrance information for further combustor simulations.

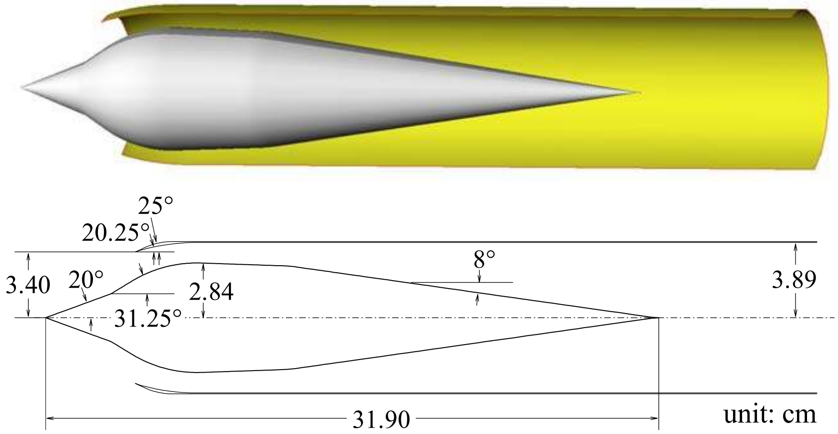

Fig. 2.1 Configurations of a mixed-compression supersonic inlet

2.2 Governing Equations

The analysis for the supersonic inlet flows is based on the axisymmetric, Favre-averaged conservation equations of mass, momentum, and energy. In a vector notation, this set of equations becomes

$$\frac{\partial \mathbf{Q}}{\partial t}+\frac{\partial}{\partial x}(\mathbf{E}-\mathbf{E}_v)+\frac{\partial}{\partial r}(\mathbf{F}-\mathbf{F}_v)=\mathbf{H} \tag{2.1}$$

where x and r stand for the axial and radial coordinates, respectively. The conserved variable vector **Q**, convective flux vectors **E** and **F**, diffusion flux vectors $\mathbf{E}_v$ and $\mathbf{F}_v$, and source vector **H** are defined as

$$\mathbf{Q}=r[\rho,\rho u,\rho v,\rho e_t]^T \tag{2.2}$$

$$\mathbf{E}=r[\rho u,\rho u^2+p,\rho uv,(\rho e_t+p)u]^T \tag{2.3}$$

$$\mathbf{F}=r[\rho v,\rho uv,\rho v^2+p,(\rho e_t+p)v]^T \tag{2.4}$$

$$\mathbf{E}_v=r[0,\tau_{xx},\tau_{xr},u\tau_{xx}+v\tau_{xr}-q_x]^T \tag{2.5}$$

$$\mathbf{F}_v=r[0,\tau_{xr},\tau_{rr},u\tau_{xr}+v\tau_{rr}-q_r]^T \tag{2.6}$$

$$\mathbf{H}=r[0,0,p-\tau_{\theta\theta},0]^T \tag{2.7}$$

In the above equations, standard notations in fluid mechanics are used. The stress tensor τ and the heat flux vector $\boldsymbol{q}$ are given by

$$\tau_{xx}=\mu(2\partial u/\partial x-2/3\nabla\cdot\mathbf{u}) \tag{2.8}$$

$$\tau_{rr}=\mu(2\partial v/\partial r-2/3\nabla\cdot\mathbf{u}) \tag{2.9}$$

$$\tau_{xr}=\mu(\partial v/\partial x+\partial u/\partial r) \tag{2.10}$$

$$\tau_{\theta\theta}=\mu(2v/r-2/3\nabla\cdot\mathbf{u}) \tag{2.11}$$

$$q_x = -\lambda \partial T / \partial x \tag{2.12}$$

$$q_r = -\lambda \partial T / \partial r \tag{2.13}$$

The divergence in cylindrical coordinates is defined as

$$\nabla \cdot \mathbf{u} = \frac{\partial u}{\partial x} + \frac{1}{r}\frac{\partial (rv)}{\partial r} \tag{2.14}$$

The pressure p and temperature T are obtained through the equation of state for a perfect gas as

$$p = (\gamma - 1)[\rho e_t - \frac{1}{2}\rho(u^2 + v^2)] \tag{2.15}$$

$$T = p/(\rho R) \tag{2.16}$$

where γ and R are the specific heat ratio and gas constant, respectively. These two parameters are taken as: $\gamma = 1.4$ and $R = 287 \text{ J/kg} \cdot \text{K}$ for air.

The viscosity μ and thermal conductivity λ contain both laminar and turbulent components,

$$\mu = \mu_l + \mu_t, \quad \lambda = \lambda_l + \lambda_t \tag{2.17}$$

The laminar component of viscosity μ_l is obtained from the Sutherland law (White, 1974),

$$\frac{\mu_l}{\mu_0} = \frac{T_0 + S}{T + S}\left(\frac{T}{T_0}\right)^{1.5} \tag{2.18}$$

where μ_0 is the Sutherland law reference viscosity, T_0 the Sutherland law reference temperature, and S the Sutherland law temperature. For the current problem, these constants are: $T_0 = 300 \text{ K}$, $\mu_0 = 1.8464 \times 10^{-5} \text{ kg/m} \cdot \text{s}$, $S = 110 \text{ K}$.

The turbulent viscosity μ_t is evaluated with a two-layer model of Rodi (1991). This model combines the standard high-Reynolds-number k-ε model in the bulk flow region with a one-equation model near the wall. In the bulk flow region, the distributions of the turbulent kinetic energy k and its dissipation rate ε are calculated from the turbulence transport equations. In the viscosity-affected near-wall region, the turbulent kinetic energy is still determined from the transport equation, but the dissipation rate is determined from a prescribed length-scale distribution. The details of the application of this model can be obtained from the thesis of Oh (1994).

The laminar and turbulent thermal conductivities λ_l and λ_t are calculated as

$$\lambda_l = \frac{C_p \mu_l}{\Pr_l}, \quad \lambda_t = \frac{C_p \mu_t}{\Pr_t} \tag{2.19}$$

where C_p is the specific heat at constant pressure. The laminar Prandtl number $\Pr_l$ and the turbulent Prandtl number $\Pr_t$ are taken to be 0.73 and 0.9, respectively.

2.3 Numerical Procedures and Validations

The governing equations outlined above are solved numerically by means of a finite-volume methodology. Temporal discretization is obtained using a four-stage Runge-Kutta integration method. The spatial discretization employs an upwind total-variation-diminishing (TVD) scheme developed by Harten (1983) and Yee (1989) in generalized coordinates for the convective terms and second-order central-differencing method for the diffusion terms. Specific details of the numerical algorithm can be obtained from Oh (1994).

The boundaries encountered in the internal and external flowfields of an axisymmetric supersonic inlet include inflow, outflow, symmetry, wall, and far-field conditions. Since the inflow is supersonic along the boundary, the flow variables are fixed at their corresponding free stream values. At the exit boundary of the inlet duct, a constant back pressure is prescribed with other flow variables deduced from the interior points for the steady-state calculations. For the unsteady calculations, a sinusoidal pressure fluctuation is applied at the outflow boundary of the inlet duct, with the implementation of the non-reflective boundary conditions proposed by Watson and Myers (1991). For the symmetry boundary, the normal velocity and the normal gradients of the axial velocity, pressure, and temperature are set to zero. A non-slip boundary condition is applied along the wall, together with zero normal gradients of pressure and temperature. Finally, the flow variables at the far-field boundary are extrapolated from the interior along the characteristic lines based on the solution of a simple wave (Roache, 1982) to avoid shock reflections.

In order to assess the accuracy of the aforementioned numerical method, a wide variety of flow problems were tested by Oh (1994). A calculation was carried out for a supersonic flow over a cone with a semi-vertex cone angle of 20 degrees. The free stream Mach number and pressure is 2.1 and 0.29 atm, respectively. Both Mach number and pressure distributions agree very well with the exact numerical solution of the ordinary differential equation derived by Taylor and Maccoll (1929). The turbulence model is tested for a turbulent boundary layer on a flat plate. The calculated velocity profile at $\mathrm{Re}_\theta = 1410$ agrees very well with the DNS data (Spapart, 1988).

2.4 Steady-State Flow Analysis

The steady-state flowfields are first studied to understand the overall flow structures in a realistic supersonic inlet and to provide a baseline for studying the response of the inlet flow to downstream disturbances.

The computational domain, as shown in Fig. 2.2, comprises the internal flow region (inner domain) that contains most of the essential flow structure, and the external flow region (outer domain), which becomes important when flow spillage over the cowl lip occurs at subcritical operating conditions. Two sizes of grids are used in order to obtain grid independent solution. The fine grid consists of 601×101 points for the inner domain and 201×81 points for the outer domain, while the coarse grid consists of 401×81 points for the inner domain and 161×81 points for the outer domain. Both grids are stretched toward the walls to provide sufficient resolution of turbulent boundary layer. Results from the steady-state calculations using these two grids show that the relative difference in terms of the terminal shock position is less than 2%, which demonstrates that grid independence is satisfied. To save CPU time, the coarse grid will be used in the later unsteady-flow calculations. A more strict grid-independent study may be conducted based on the Richardson extrapolation (Roache, 1997).

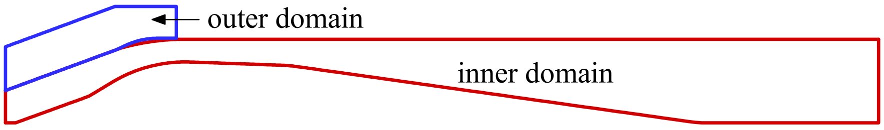

Fig. 2.2 Computational domain for inlet study

Figure 2.3 presents the Mach-number, pressure, and vorticity contours at two different back pressures (p_b = 2.1 and 2.2 atm), which are carefully chosen such that the engine operates at a supercritical condition to provide a sufficient shock stability margin. Under these conditions, the two leading conical shocks generated by the double-cone centerbody compress the airflow externally, merge slightly above the cowl lip, and form a strong oblique shock, which extends into the external-flow region. In addition, a shock stemming from the cowl inner surface continues downstream, hitting and reflecting from both cowl and centerbody walls, and finally leading to a terminal normal shock. The flow in this region undergoes a compression-expansion cycle, being compressed by reflecting shocks and expanded by expansion waves. The wavy Mach number and pressure distributions along the middle line of the inlet duct for the case of p_b = 2.1 atm, as shown in Fig. 2.4, clearly depict this feature. The flow finally becomes subsonic after passing through the normal shock located in the divergent section of the diffuser. During this process, the inlet recovers a high percentage of the free stream total pressure by decelerating the air flow through the shock train. The total pressure recovery coefficients are 84% for the case of p_b = 2.1 atm and 88% for the case of p_b = 2.2 atm, and the Mach number immediately in front of the terminal shock are 1.42 and 1.32, respectively. At the same time, the flow direction, which is originally deflected away by the leading shocks, is adjusted back to the axial direction.

Due to the viscous effect, boundary layers exist on both the cowl and centerbody walls. The growth of the boundary layer and shock-wave/boundary-layer interactions play important roles in dictating the inlet flow structure. The presence of the boundary layer prohibits a discontinuous change in pressure across the shock near the wall since the flow in the inner part of the boundary layer is subsonic. The overall pressure rise across the shock is partly transmitted upstream through the boundary layer, causing the streamlines in that region to diverge (Green, 1970). Consequently, the boundary layer thickens and may be separated from the wall if the pressure rise across the shock is sufficiently large. Due to its interaction with the boundary layer, the terminal shock is no longer a strictly normal shock. An oblique shock is formed due to the abrupt thickening of the boundary layer and runs into the terminal shock. If the flow deflects away enough after the leading oblique shock, a rear oblique shock may be formed from the intersection of the leading oblique shock and the main shock to form the lambda-shock (Dyke, 1997).

On the other hand, the flow passing through the stronger normal shock will be slower than that passing through the oblique shock systems. Thus, vortex sheets emanate from the shock bifurcation points, convect downstream, and maybe interact with each other. This phenomenon is clearly depicted in the vorticity contours in Fig. 2.3.

Furthermore, the vorticity displays more complicated structure due to the different compression histories of the flow just upstream of the terminal shock. However, the pressure distribution in the transverse direction behind the terminal shock is quite uniform, in order to satisfy the condition of equal static pressure in that direction. This implies a non-uniformity of total pressure in the transverse direction.

The abrupt thickening of the boundary layer downstream of the normal shock acts like a convergent nozzle by reducing the effective duct area, accelerating the subsonic flow after the shock with an associated pressure drop. The sudden decrease in pressure (or sudden increase in Mach number) after the terminal shock in the core flow region, as shown in Fig. 2.4, is attributed to this effect.

Mach-number Contours

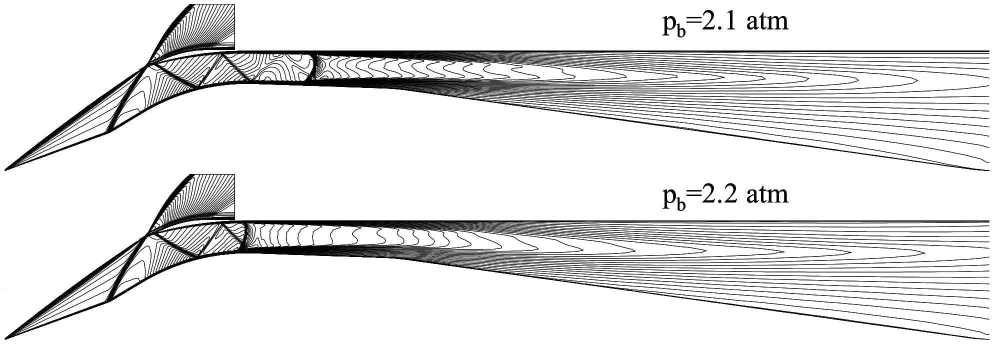

Pressure Contours

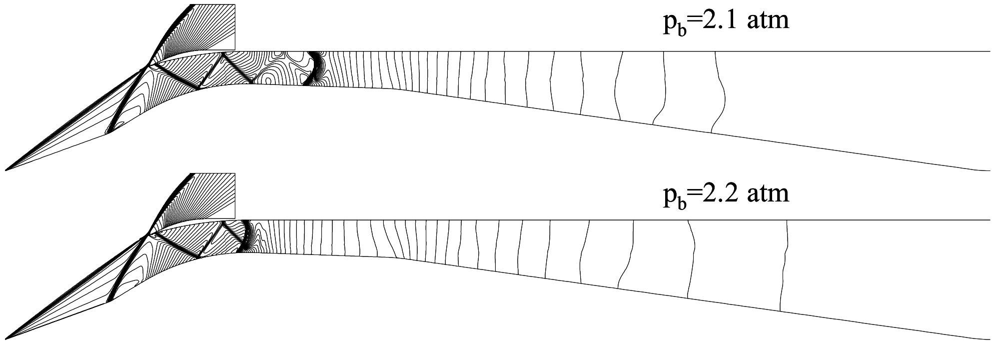

Vorticity Contours

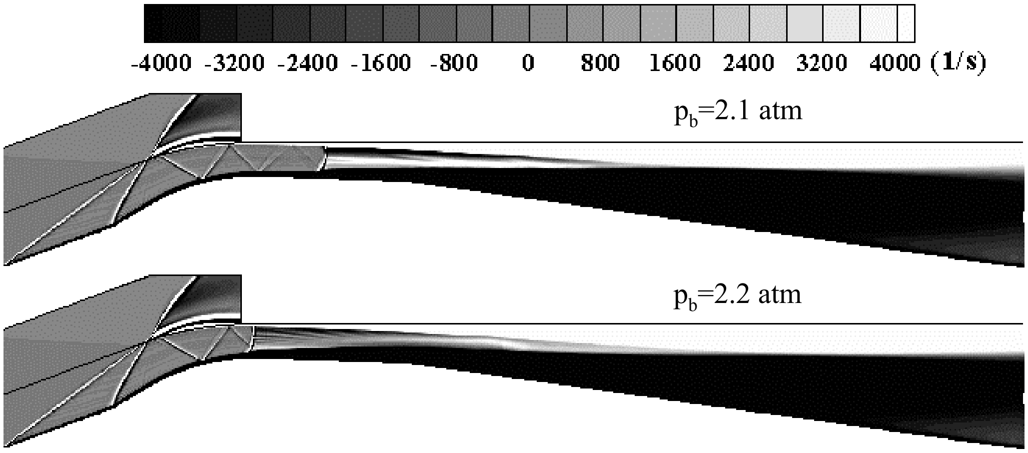

Fig. 2.3 Mach-number, pressure, and vorticity contours with different back pressures under steady-state condition

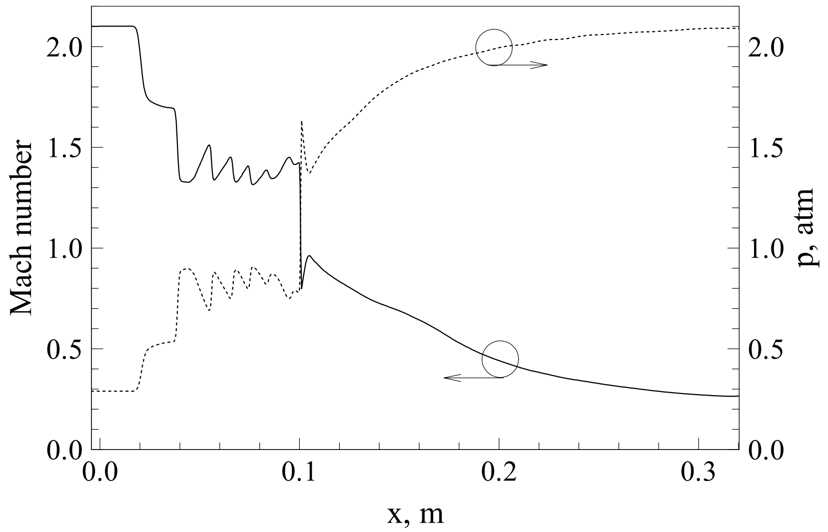

Fig. 2.4 Mach-number and pressure distributions along midline under steady-state condition (p_b = 2.1atm)

2.5 Shock/Acoustic-Wave Interactions

The steady-state flowfields with back pressure of 2.1 atm are used to initialize the unsteady flow calculations, considering that the terminal shock in this case is further downstream, which means it has a larger stability margin. The downstream disturbance is simulated by imposing a sinusoidal pressure oscillation at the exit plane:

$$p' = Ap_b \sin(\omega t) \tag{2.20}$$

where ω is the angular frequency, $2\pi f$, with f the frequency. A wide range of A and f are considered with A = 0.05 and f = 500 Hz as the baseline case.

Figure 2.5 shows the pressure distributions along both cowl and centerbody walls and the midline over one cycle of oscillation for the baseline case. The corresponding Mach-number contours near the terminal shock are also presented. Different time intervals are chosen in order to display more key structures of the unsteady flowfield. The oscillation cycle begins when the terminal shock is at its steady-state position. As the terminal shock progresses upstream, the Mach number before the shock decreases. However, that does not necessarily mean that the terminal shock weakens. It is the relative Mach number with respect to the terminal shock that determines the strength of the shock. The numerical results indicate that the moving shock has a velocity as large as 40 m/s as it moves upstream for the baseline case. With this in consideration, the terminal shock may strengthen first and weaken then. The terminal shock reverses its direction after it reaches the farthest upstream position by the time of about $\omega t = \pi$. Similarly, as the terminal shock moves downstream, it first strengthens but soon becomes weaker, now that it has a larger downstream moving velocity and the relative Mach number becomes smaller. As the velocity of the shock increases, the shock may finally turns into a pressure pulse. On the other hand, a strong adverse pressure gradient wave gradually forms farther downstream and eventually steepens into a secondary shock. This secondary shock becomes stronger as it moves upstream and finally combines into the primary shock (or pressure pulse) to form a stronger shock. The shape of the terminal shock also changes as it moves upstream or downstream. The ‘S’ in Fig. 2.5 stands for the separation point on the centerbody wall. It can be seen that the terminal shock will always induce boundary layer separation as long as it reaches certain strength. It is worth mentioning that in the last plot of Fig. 2.5, two separation points can be found, the first one is induced by the terminal shock, and the second one is induced by the pressure gradient resulting from the acoustic wave and area changing.

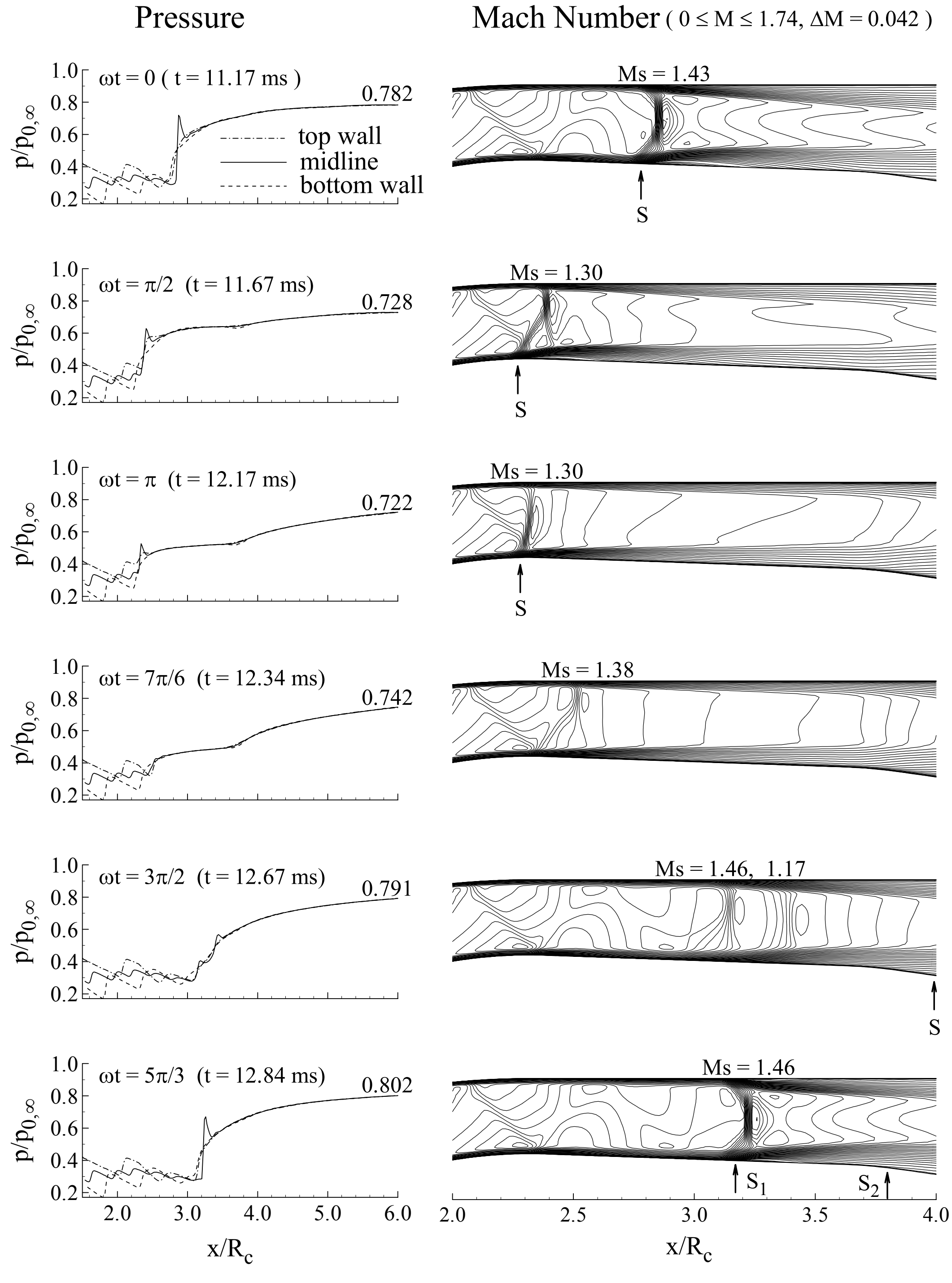

Fig. 2.5 Pressure distributions along walls and midline of inlet and Mach-number contours within one cycle of oscillation ($A = 0.05, f = 500$ Hz)

Figure 2.6 shows the instantaneous terminal shock locations for several cases. The shock location is determined by finding a position with Mach number equal to 1. The terminal shock begins to respond after the time required for the disturbance to travel upstream to it. It then may oscillate around its mean position and be stabilized after one or two cycles, or be disgorged out of the inlet as for the case of $A = 0.1$ and $f = 500$ Hz. It is evidently shown that the shock exhibits larger upstream and downstream excursions for lower frequency and higher amplitude disturbance. It can also be seen that the farthest upstream excursion of the shock moves gradually from upstream to downstream during the initial response stage, which can be rationalized as follows. When the acoustic pressure wave (left-running) hits the normal shock, part of the pressure wave is absorbed by the shock and the remainder is reflected as a right-running wave. This reflected wave could either strengthen the left-running wave or weaken it, depending on the phase angle difference between the two. Thus, for the first few cycles in which the reflected wave does not fully interact with the left-running wave in the entire subsonic diffuser section, the shock responds primarily to the left-running wave at first, and then gradually responds to the combined left- and right-running waves. In the present study, the reflecting wave seems to weaken the left-running wave, causing the phenomena aforementioned. The shock oscillation displays a nearly sinusoidal shape for the cases with small disturbance, and the mean position of the terminal shock is very close to the steady-state position. However, when the disturbance becomes larger, many nonlinear phenomena emerge. The oscillation of the terminal shock is no longer sinusoidal. The shock moves faster downstream than upstream. A significant characteristic is that a secondary shock forms and the primary shock disappears sometime within the cycle. The discontinuous line sections in Fig. 2.6(b) are due to this phenomenon. In the extreme case, say, for the case of $A = 0.1$ and $f = 500$ Hz, the terminal shock is disgorged out of the inlet, and engine unstart (Seddon and Goldsmith, 1999) may happen.

In Fig. 2.7, the position ranges of the terminal shock are given. For the cases with $A = 0.05$, the upmost point is the farthest downstream position of the secondary shock. It is quite clear that the range decreases as the frequency increases. The amplitude of the shock oscillation has been derived by Culick and Rogers (1983) under one dimensional, linear, and inviscid assumption. In the present study, the flowfield displays multi-dimensional effects as mentioned before, however, the motion of the terminal shock is mainly determined by the pressure wave behind it, which is nearly one dimensional. Figure 2.8 displays good agreements of the amplitudes of terminal shock oscillations with the analytical results.

Air flow matching is an important issue for the inlet. The mass flow rate entering the inlet does not change during the supercritical operating conditions, but oscillations of mass flow rate do change at the exit of inlet due to shock motion. Figure 2.9 presents the ratio of relative mass flow rate fluctuation to the relative amplitude of pressure oscillation. It is observed that the oscillation of pressure causes larger oscillation of mass flow rate. For an engine with constant fuel injection rate, this implies that the equivalence ratio would fluctuate more severely, perhaps enhancing combustion instability. The phase angle differences between the mass and pressure oscillations are 1.16π, 1.06π, 0.95π, and $0.97\ \pi$ for the four cases given in Fig. 2.9, respectively.

Total pressure recovery is another important issue of inlet. A small loss of inlet total pressure may cause considerable loss in engine thrust. Figure 2.10 presents the mass averaged total pressure at exit over one cycle of oscillation for several cases. It is found that the averaged total pressures appear nearly sinusoidal oscillations. The main effect on the averaged total pressures is from the amplitude of pressure oscillation, while the frequency has a minor effect. The flow distributions at the exit plane of the inlet provide the coupling between the inlet and combustor. Figure 2.11 shows the axial velocity and total pressure profile at the exit plane over one cycle of oscillation for the baseline case. The steady-state results are also plotted for comparison. It can be seen that the unsteady profiles have similar shapes with the steady ones. However, the pressure oscillations cause very large velocity oscillations, which can reach 60% near the centerbody wall. This may exert substantial influence on the combustor environments. Figure 2.12 compares the time-averaged axial velocity and stagnation pressure profiles with those of steady-state, indicating that they are very close.

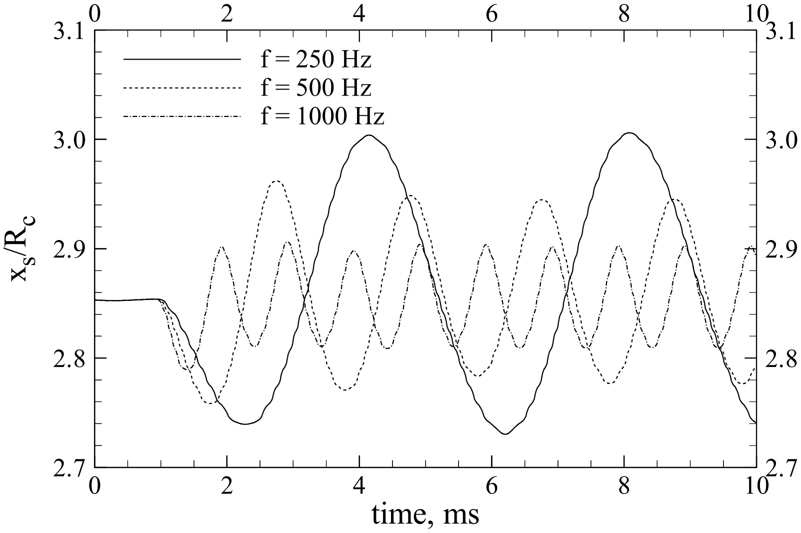

(a) *A* = 0.01

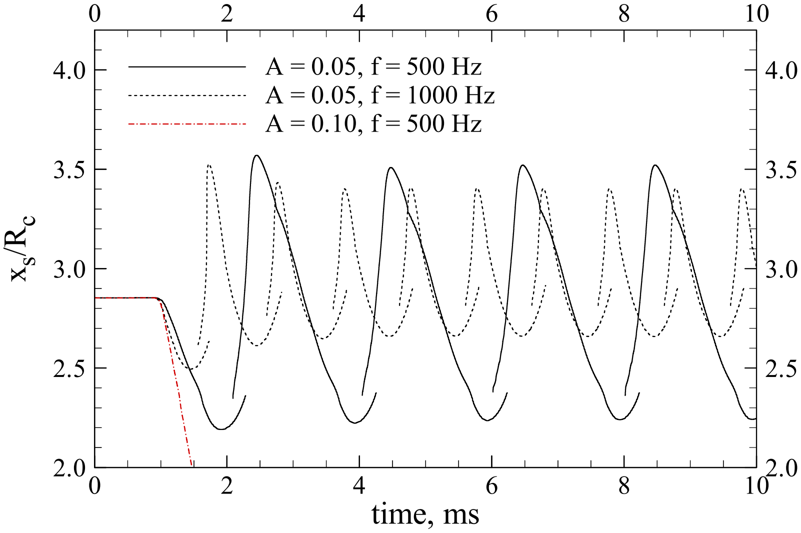

(b) *A* = 0.05, 0.10

Fig. 2.6 Instantaneous shock locations for different cases

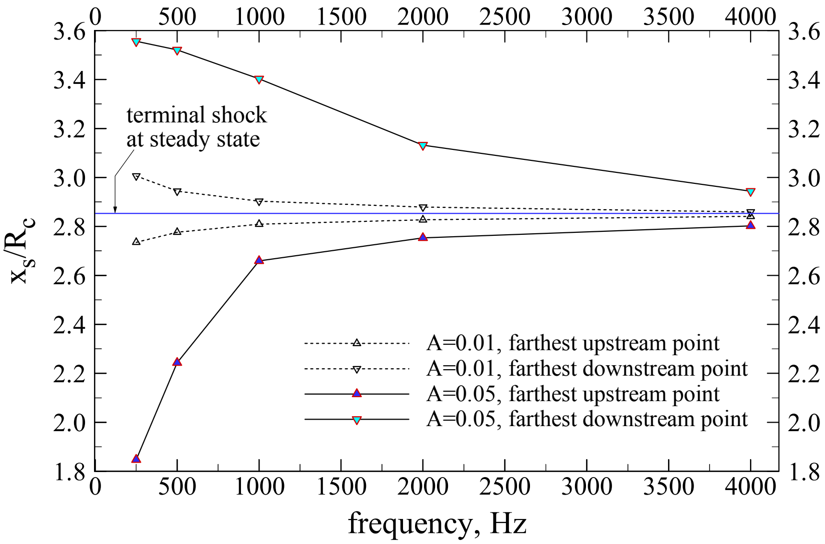

Fig. 2.7 Shock position ranges with different frequencies

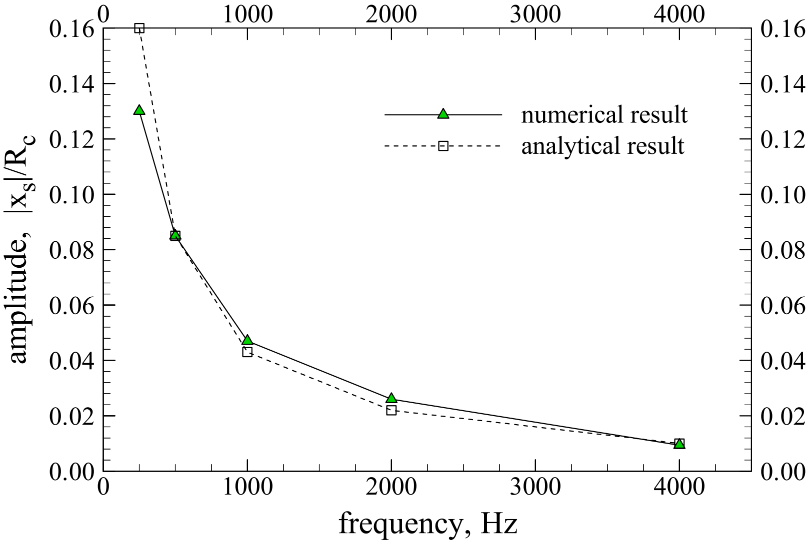

Fig. 2.8 Comparison of the amplitude of terminal shock oscillation with analytical result ($A = 0.01$)

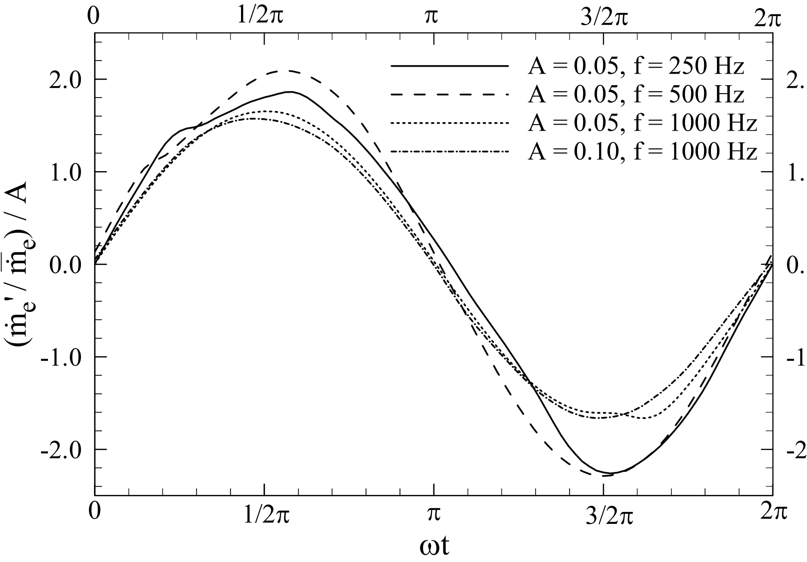

Fig. 2.9 Mass response to the pressure oscillation at exit over one cycle

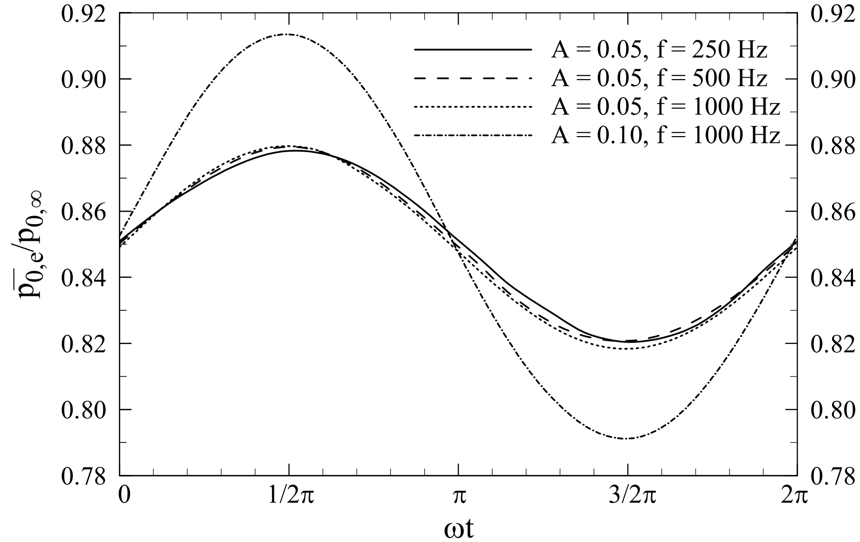

Fig. 2.10 Mass averaged stagnation pressure at exit over one cycle

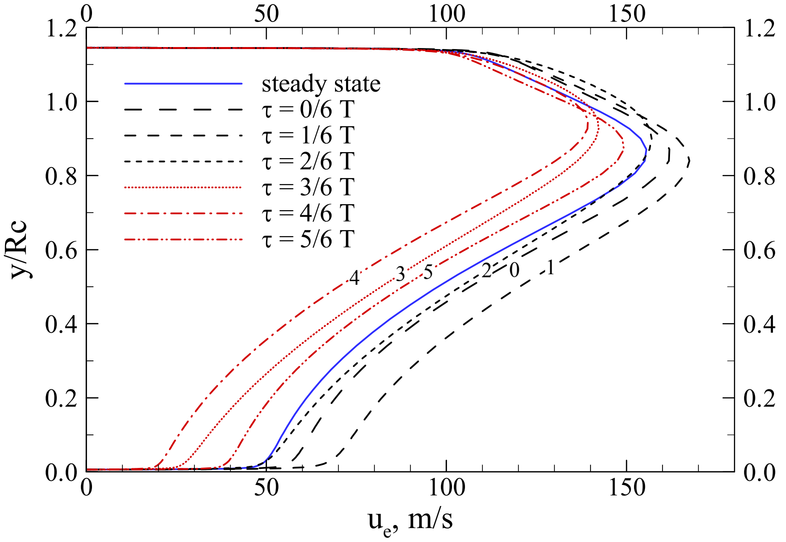

(a) Axial velocity

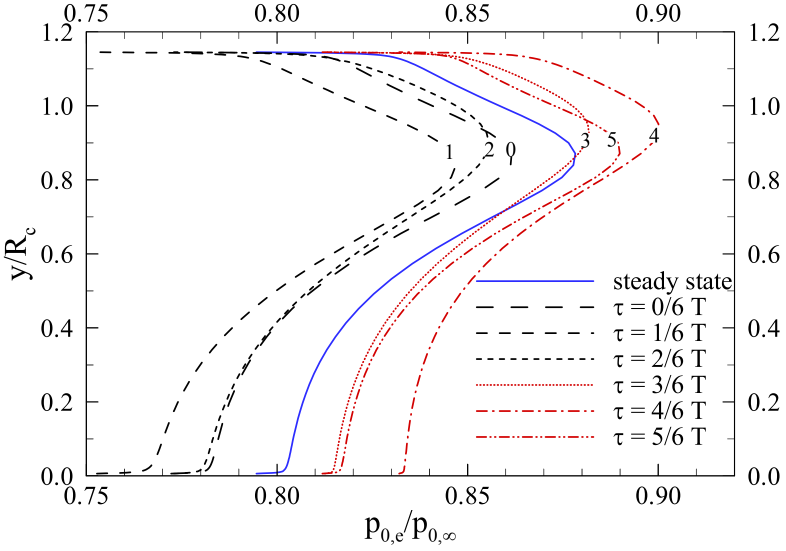

(b) Stagnation pressure

Fig. 2.11 Axial velocity, stagnation pressure profiles at exit plane ($A = 0.05$, $f = 500$ Hz)

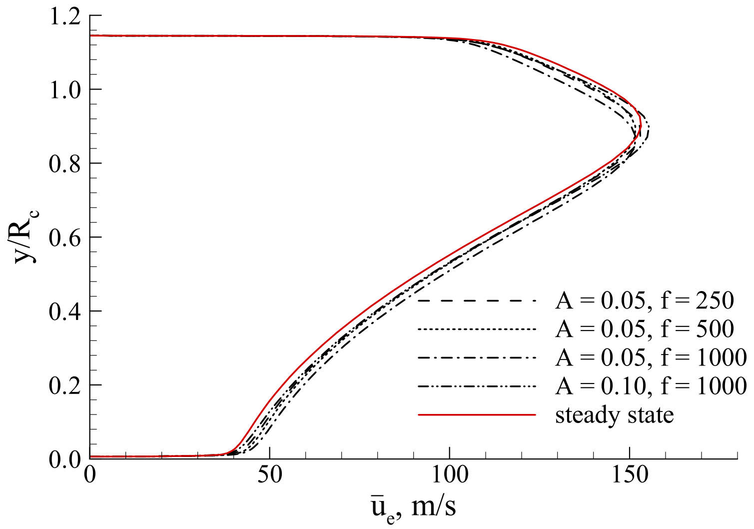

(a) Axial velocity

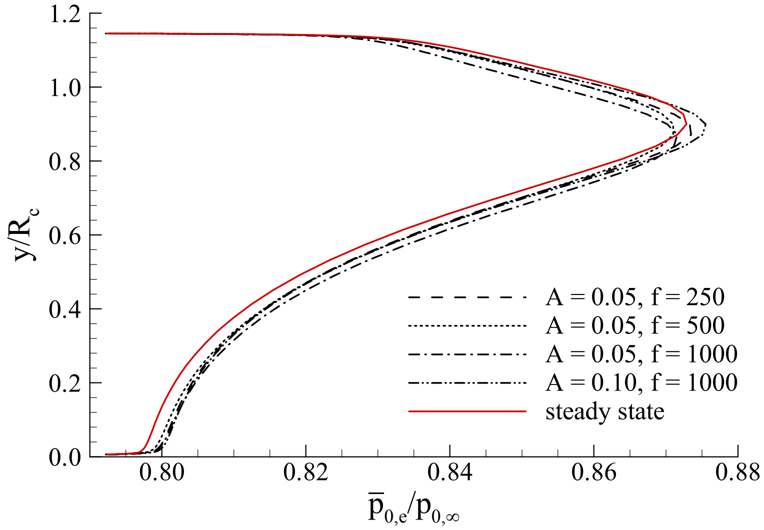

(b) Stagnation pressure

Fig. 2.12 Comparison of time averaged axial velocity and stagnation pressure profiles at exit plane

2.6 Conclusions

Interactions between the shock waves and pressure waves were numerically investigated for a viscous flowfield in an axisymmetric, mixed-compression supersonic inlet diffuser by solving the unsteady Navier-Stokes equations with a two-equation turbulence model in cylindrical coordinates. A 500 Hz sinusoidal pressure disturbance with amplitude of 5% of the mean static pressure was applied to the exit plane as a baseline case. A number of notable features observed in this study are given below.

1) The acoustic response of the inlet flow increases with increasing amplitude of the imposed oscillation, but decreases with frequency.

2) For a relatively large pressure oscillations (such as the case of A=5%), the adverse pressure gradient farther downstream of the terminal shock can steepen to form a secondary shock, while the primary shock may turn into a pressure pulse. Under an extreme case, the terminal shock may be disgorged out of the inlet to cause engine unstart.

3) Vorticities generated from the intersection points of the terminal shock and oblique shocks change their position in both axial and transverse directions as the terminal shock moves, resulting in a significant multi-dimensional effect.

4) Shock-induced flow-separation pockets on both walls form and disappear as the terminal shock moves.

5) The pressure oscillation causes a larger mass flow rate oscillation and severe axial velocity oscillation, which may exert strong influence on the combustor flowfield.

Chapter 3

Quasi-One-Dimensional Analyses of PDEs

It has been pointed out that one-dimensional or quasi-one-dimensional simulations are not enough for the PDE analysis since they cannot correctly account for the effect of the exit boundary conditions. However, for a PDE with a convergent-divergent (CD) nozzle, the exhaust flow may exhibit supersonic behavior during most of the cycle period. Therefore, quasi-one-dimensional simulations are still acceptable and are conducted in this chapter as a preliminary step. Two-dimensional analyses will be considered in next chapters.

The recently developed space-time conservation element/solution element (CE/SE) method is implemented because it circumvents the deficiencies of existing numerical methods for treating detonation waves and shock discontinuities. Chemical kinetics is modeled by a one-progress-variable scheme which is calibrated with NASA CEA code. The diffusive transport is neglected in the current study because of its minor role in determining detonation dynamics and system performance.

3.1 Space-Time CE/SE Method

3.1.1 Introduction to Space-Time CE/SE Method

The space-time conservation element and solution element (CE/SE) method was originally developed by S.C. Chang at NASA Glenn Research Center and was first published out in 1995 (Chang, 1995). It is a high-resolution and genuinely multidimensional numerical method for solving conservation laws. This method differs substantially in both concept and methodology from other well-established methods, such as finite-difference, finite-volume, finite-element, and spectral methods. It has many nontraditional features, such as a unified treatment of space and time, enforcement of flux conservation in the space-time domain, introduction of solution and conservation elements to construct simple stencil, treatment of independent variables and their spatial derivatives as unknowns to be solved simultaneously, and no interpolation or extrapolation required to evaluate fluxes at cell interfaces.

The development of the CE/SE method was motivated by the fact that physical conservation laws are actually a collection of statements of flux conservation in space-time. Mathematically, these laws are represented by a set of integral equations, and the differential form of these laws is obtained from the integral form by assuming that the physical solution is smooth. For a physical solution in a region with rapid variations, this smoothness assumption is difficult to be realized by a numerical approximation that uses only a limited number of discrete variables. The situation becomes even worse in the presence of large gradients or discontinuities. Thus, a method designed to obtain numerical solutions to the differential form without enforcing flux conservation is a fundamental disadvantage in modeling physical phenomena with steep gradients. In contrast, a numerical solution obtained from a method that enforces flux conservation both locally and globally will always retain the basic physical reality of flux conservation even in a region involving discontinuities (Chang, 1995).

With this consideration, the CE/SE method was designed to treat space and time as a single entity, and the integral form of the conservation laws are solved to ensure both local and global flux conservation in space and time. In comparison, finite-difference, finite-element, and spectral methods deal with the differential form of the conservation laws. The traditional finite-volume method attempts to enforce flux conservation in space and/or time, but it treats space and time separately in the sense that flux conservation cells are defined only in the space domain. In the finite-volume method, a flux must be assigned at any interface separating two neighboring cells, and the flux is typically evaluated by extrapolating or interpolating the mesh values at the neighboring cells. This evaluation generally requires ad hoc techniques such as flux limiters or slope limiters. These ad hoc techniques usually involve the calculation of the eigenvector matrices of the Jacobian matrices, which may complicate the coding and increase the computational time.

The CE/SE method introduces two types of cells in the space-time domain: conservation elements (CEs) and solution elements (SEs). The union of the CEs covers the whole computational domain. Physical conservation laws are enforced on each CE. The SEs are designed to facilitate the evaluation of the fluxes at interfaces separating neighboring CEs. Several unique features are adopted for this purpose. (1) Each SE is chosen to cover some interfaces of neighboring CEs. (2) A solution point is defined within each SE to hold both the basic independent variables and their spatial derivatives as unknowns to be solved simultaneously, while the time derivatives are obtained by satisfying the differential form of the governing equations at the solution point. (3) Each physical flux vector is approximated in terms of some simple smooth functions within each SE. With the above strategies, the CE/SE method is able to enforce both local and global flux conservation in space and time with flux evaluation being an integral part of the solution procedure and requiring no interpolation or extrapolation. As a result, the CE/SE method is more efficient than the traditional finite-volume method in terms of coding complexity and computational burden.

A distinguished feature of the Space-Time CE/SE method is that it can fully control numerical dissipation, even down to zero if necessary. This is important in simulating flows involving small disturbances such as sound waves. Relatively large numerical dissipation introduced by numerical schemes can lead to the annihilation of small disturbances. Unexpected numerical dissipation may overwhelm physical dissipation, causing a complete distortion of the solution. Thus, a solver that can fully control its numerical dissipation is desirable. For conventional methods, numerical dissipation is adjusted by varying the magnitude of added artificial dissipation terms. With a few exceptions, numerical dissipation in almost every traditional scheme cannot be reduced to zero even without artificial dissipation terms. A study of finite-difference analogues of a simple convection equation shows that a numerical analogue is free of numerical dissipation only if it does not violate certain space-time invariant properties of the convection equation (Chang, 1992). In other words, numerical dissipation may be considered as a result of symmetry-breaking by a numerical scheme. An ideal scheme must be able to reserve this symmetry property in order to avoid numerical dissipation. Because of the intrinsic nature of space-time unity, the Space-Time CE/SE method is perfectly suited to constructing such schemes. Its ability to accurately simulate both small disturbances and strong shock waves has been proven in treating various problems involving interactions between shock waves and sound waves (Loh *et al.*, 1996).

3.1.2 Space-Time CE/SE Method for One-Dimensional Problems

This subsection, adopted from Wu (2002) with minor modifications, describes the solution procedure of the Space-Time CE/SE method for one-dimensional systems governed by

$$\frac{\partial Q}{\partial t}+\frac{\partial E}{\partial x}=H \tag{3.1}$$

Since the Space-Time CE/SE method treats space and time as a single entity, the computational domain for spatially one-dimensional problems becomes a two-dimensional Euclidean space $E_2=(x,t)$. Define $\mathbf{h}=(E,Q)$ as the current vector in E_2. The Gaussian divergence theorem in E_2 leads to the integral form, which is a more physically basic form:

$$\oint_{s(V)}\mathbf{h}\cdot d\mathbf{s}=\int_{V}HdV \tag{3.2}$$

The second step is to construct the CEs and SEs. The computational domain E_2 is discretized equally in space and time, and the dimension of each cell is assumed to be Δx by Δt. Following the suggestion of Yu and Chang (1997), the conservation element CE(*j, n*) and the solution element SE(*j, n*) are both defined to cover the rectangular area $\overline{ABCDEFA}$ with a line segment $\overline{AG}$ sticking out on top of the rectangle, as shown in Fig. 3.1. Each CE(*j, n*) can be divided into two sub-elements: $\text{CE}_-(j,n)$ and $\text{CE}_+(j,n)$. The boundaries of $\text{CE}_-(j,n)$ are $\overline{AB}$, $\overline{BC}$, $\overline{CD}$, and $\overline{DA}$, while $\text{CE}_+(j,n)$ is enclosed by $\overline{FA}$, $\overline{AD}$, $\overline{DE}$, and $\overline{EF}$. Note that the line segments $\overline{BC}$ and $\overline{CD}$ belong to the solution element SE(*j*-1/2, *n*-1/2) and the line segments $\overline{DE}$ and $\overline{EF}$ to SE(*j*+1/2, *n*-1/2).

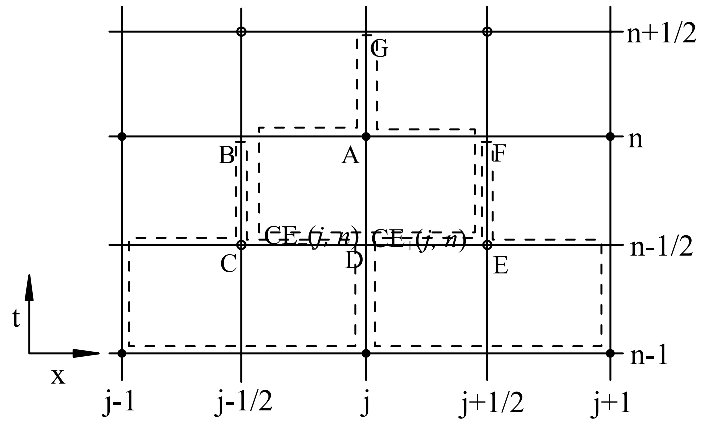

Fig. 3.1 Mesh system and CEs/SEs in Space-Time CE/SE method (adopted from Wu, 2002).

For any point $(x, t) \in \mathrm{SE}(j, n)$, the dependent variable vector $Q(x, t)$, flux vector $E(x, t)$, and source term vector $S(x, t)$ are approximated by $Q^*(x, t; j, n)$, $E^*(x, t; j, n)$, and $H^*(x, t; j, n)$, respectively, whose definitions are given below.

$$Q^*(x,t;j,n) = Q_j^n + (Q_x)_j^n(x - x_j) + (Q_t)_j^n(t - t^n) \tag{3.3}$$

$$E^*(x,t;j,n) = E_j^n + (E_x)_j^n(x - x_j) + (E_t)_j^n(t - t^n) \tag{3.4}$$

$$H^*(x,t;j,n) \ = H_j^n + (H_x)_j^n(x - x_j) + (H_t)_j^n(t - t^n) \tag{3.5}$$

where the label $(\,)_j^n$ denotes the corresponding quantities evaluated at mesh point (j, n) whose coordinate is (x_j, t^n). $Q^*(x, t; j, n)$, $E^*(x, t; j, n)$, and $H^*(x, t; j, n)$ are actually first-order Taylor's expansions of $Q(x, t)$, $E(x, t)$, and $H(x, t)$ at point (j, n), respectively. Moreover, all terms on the right-hand sides in the above approximations are only functions of Q_j^n, $(Q_x)_j^n$, and $(Q_t)_j^n$ because 1) both E_j^n and H_j^n are only functions of Q_j^n, and 2) $(E_x)_j^n$, $(H_x)_j^n$ $(E_t)_j^n$, and $(H_t)_j^n$ are only functions of Q_j^n, $(Q_x)_j^n$, and $(Q_t)_j^n$ due to the following relations:

$$(E_x)_j^n = A_j^n\ (Q_x)_j^n, \qquad (H_x)_j^n = D_j^n\ (Q_x)_j^n \tag{3.6}$$

$$(E_t\ )_j^n = A_j^n\ (Q_t)_j^n, \qquad (H_t)_j^n = D_j^n\ (Q_t)_j^n \tag{3.7}$$

where $A_j^n \equiv (\frac{\partial E}{\partial Q})_j^n$ and $D_j^n \equiv (\frac{\partial H}{\partial Q})_j^n$ are the Jacobian matrices of the convective flux vector *E* and source term vector *H* at (x_j, t^n) , respectively.

The Space-Time CE/SE method further requires the above solution approximations to satisfy the following differential form of the governing equations within SE(*j, n*) except the line segment $\overline{AG}$ that sticks out on the top of the solution element.

$$\frac{\partial Q^*}{\partial t} + \frac{\partial E^*}{\partial x} = H^* \tag{3.8}$$

Substitution of equations (3.3)-(3.5) into the above equation leads to

$$(Q_t)_j^n + (E_x)_j^n = H_j^n \tag{3.9}$$

From which $(Q_t)_j^n$ can be expressed as function of Q_j^n and $(Q_x)_j^n$.

Define $\mathbf{h}^*(x,t;j,n) \equiv (E^*(x,t;j,n), Q^*(x,t;j,n))$ as the approximation of the current density vector $\mathbf{h} = (E,Q)$ within the conservation element CE(*j, n*). Then the fluxes at $\overline{AB}$ and $\overline{FA}$ can be evaluated in terms of Q_j^n and $(Q_x)_j^n$. Similarly, the fluxes at other boundaries of CE(*j, n*) (i.e., $\overline{BC}$, $\overline{CD}$, $\overline{DE}$, and $\overline{EF}$) can be obtained by applying equations (3.3)-(3.9) to the solution elements SE(*j*±1/2, *n*-1/2).

With the fluxes at all the boundaries of CE(*j, n*) being evaluated, the integral form of the conservation laws, equation (3.2), can be readily enforced on CE(*j, n*).

$$Q_j^n - \frac{1}{\Delta x}\int_{CE(j,n)} H dV = \frac{1}{2}\left[Q_{j-1/2}^{n-1/2} + Q_{j+1/2}^{n-1/2} + R_{j-1/2}^{n-1/2} - R_{j+1/2}^{n-1/2}\right] \equiv RHS \tag{3.10}$$

where R is defined as

$$R_j^n \equiv \frac{\Delta x}{4}(Q_x)_j^n + \frac{\Delta t}{\Delta x}E_j^n - \frac{(\Delta t)^2}{4\Delta x}A_j^n(E_x)_j^n \tag{3.11}$$

After Q_j^n are solved from equation (3.10), $(Q_x)_j^n$ can be evaluated using the following oscillation-suppressing procedure. First, the solutions at point (j±1/2, n) are approximated using the first-order Taylor series expansions as shown below.

$$(Q_{x\pm}^+)_j^n \equiv \pm\frac{Q'^n_{j\pm 1/2} - Q_j^n}{\Delta x/2} \tag{3.12}$$

$$Q'^n_{j\pm 1/2} = Q_{j\pm 1/2}^{n-1/2} + \frac{\Delta t}{2}(Q_t)_{j\pm 1/2}^{n-1/2} \tag{3.13}$$

where $(Q_{x+}^+)_j^n$ and $(Q_{x-}^+)_j^n$ are two numerical analogues of $(Q_x)_j^n$ at point (j, n) evaluated from the right and left sides, respectively. Define function W as

$$W(x_+, x_-;\alpha) = \frac{|x_+|^\alpha x_- + |x_-|^\alpha x_+}{|x_+|^\alpha + |x_-|^\alpha} \tag{3.14}$$

Then $(Q_x)_j^n$ can be calculated using

$$(Q_x)_j^n = W((Q_{x+}^+)_j^n, (Q_{x-}^+)_j^n;\alpha) \tag{3.15}$$

Usually, α is chosen as an integer of 2.

Before closing this section, there are two points to be emphasized. First, even though numerical dissipation has been introduced into the scheme during the above oscillation-suppressing procedure, conservation laws are strictly enforced on CE(j, n). Moreover, since the union of all conservation elements covers the entire computational domain, global conservation is also enforced strictly. Second, although the order of the accuracy of the solution approximations, equations (3.3)-(3.5), is second order, the actual accuracy of the above scheme is comparable to that of 4-6th order compact difference schemes when nonlinear Euler problems are modeled. This is because second order is its nominal order of accuracy, and is only meaningful for linearized equations. For non-linear problems, the flux conservation property ensures that the space-time method possesses an order of accuracy much higher than its nominal one. In addition, the space-time method has surprisingly small dispersive errors in nonlinear calculations, which also contributes to the enhancement of its accuracy (Wang, *et al.*, 1994).

3.2 Governing Equations

The conservation equations of mass, momentum, energy, and species concentration in a quasi-one-dimensional system can be written in the following vector form.

$$\frac{\partial \mathbf{Q}}{\partial t}+\frac{\partial \mathbf{E}}{\partial x}=\mathbf{H} \tag{3.16}$$

The conserved variable vector **Q**, convective flux vector **E**, and source vector **H** are defined as

$$\mathbf{Q}=\begin{bmatrix}\rho\\ \rho u\\ \rho e_t\\ \rho Z\end{bmatrix},\quad \mathbf{E}=\begin{bmatrix}\rho u\\ \rho u^2+p\\ u(\rho e_t+p)\\ \rho u Z\end{bmatrix},\quad \mathbf{H}=-\frac{1}{A}\frac{dA}{dx}\begin{bmatrix}\rho u\\ \rho u^2\\ u(\rho e_t+p)\\ \rho u Z\end{bmatrix}+\begin{bmatrix}0\\ 0\\ 0\\ \dot{\omega}\end{bmatrix} \tag{3.17}$$

In the above equations, ρ, u, e_t, Z and A represent the density, velocity, specific total energy, mass fraction of reactant, and area of cross section, respectively. The pressure p is obtained through the equation of state for a perfect gas as,

$$p = (\gamma - 1)\rho[e_t - u^2/2 - Zq] \tag{3.18}$$

with γ the specific heat ratio, q the heat release per unit mass of reactant. The mass production rate $\dot{\omega}$ is obtained using the Arrhenius expression,

$$\dot{\omega} = -K\rho Z \exp(-E_a / RT) \tag{3.19}$$

with K the pre-exponential reaction rate factor, Ea the activation energy per unit mass of reactant, R the gas constant, and T the temperature which can be obtained using perfect gas state equation:

$$T = p / \rho R \tag{3.20}$$

It is noted that there are five parameters (γ, R, q, Ea and K) associated with the above governing equations. Determination of these parameters is discussed in the following section. The Jacobian matrices of the flux and source vectors are given in Appendix B.

3.3 Parameter Calibration and Code Validation

3.3.1 Parameter Calibration

Among the five parameters γ, R, q, Ea, and K, the first three are thermodynamic parameters that determine the detonation wave properties such as the CJ state and wave speed. These three parameters are calibrated with the NASA CEA code (McBride and Gordon, 1996) for a stoichiometric H_2/air mixture, as described below.

Two sets of CJ detonation solutions, one from the CEA code and the other from analytical formulation given in Sec. 1.2.1, are first obtained for a series of different unburned pressures and temperatures: p_1 = 1, 2 atm, T_1 = 300, 350, 400, 450, 500 K. The simulated annealing (SA) optimization algorithm (Belegundu and Chandrupatla, 1999) is then applied to find the optimum values of γ, R, and q by minimizing the relative difference in terms of T_{CJ}/T_1, p_{CJ}/p_1 and u_D between these two sets of solutions. The following values are obtained.

$$\gamma = 1.290,\ R = 368.9 \text{ J/(kg·K)},\ q = 2.720\times10^6 \text{ J/kg} \tag{3.21}$$

The analytical CJ detonation velocity and CJ state based on these parameters are compared with those from CEA code and shown in Fig. 3.2. It is observed that both the CJ temperature and pressure agree with the CEA results very well, with a maximum relative error less than 8%, and have the same trends as T_1 increases. The detonation velocity differs in the trend. For example, the analytical CJ detonation velocity increases with T_1, while the detonation velocity from CEA code decreases with T_1. Although the trend is different, the relative errors for the detonation velocity are still small, e.g., less than 3%. These small relative errors indicate that the current one-progress-variable model represents a good approximation in predicting the detonation wave properties.

The other two parameters, Ea and K, are chemical kinetic parameters. Their primary influence appears in the internal structure of a detonation wave front, and the effect on the overall flow evolution and propulsion performance are relatively minor. The following values, adopted from Mohanraj and Merkle (2000), are used for these two parameters.

$$Ea = 4.794\times10^6 \text{ J/kg},\ K = 7.5\times10^9 \text{ s}^{-1} \tag{3.22}$$

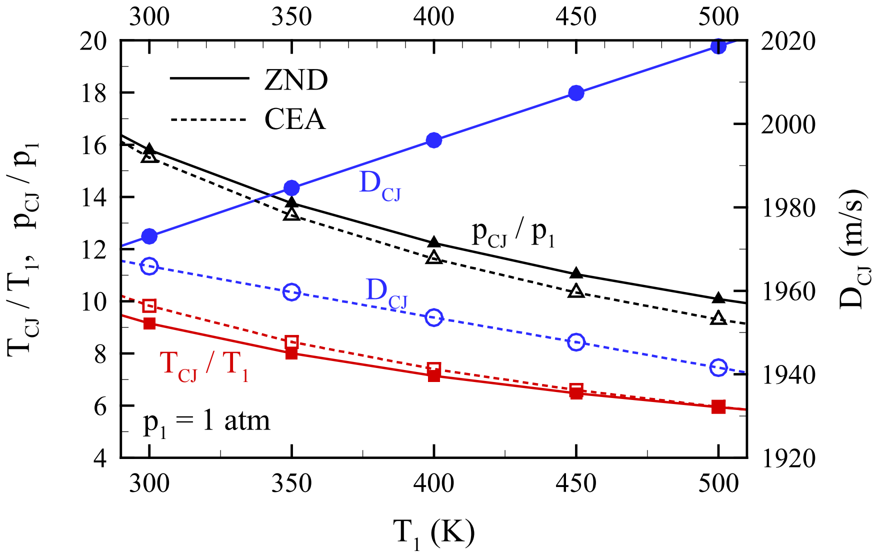

(a) p_1 = 1 atm

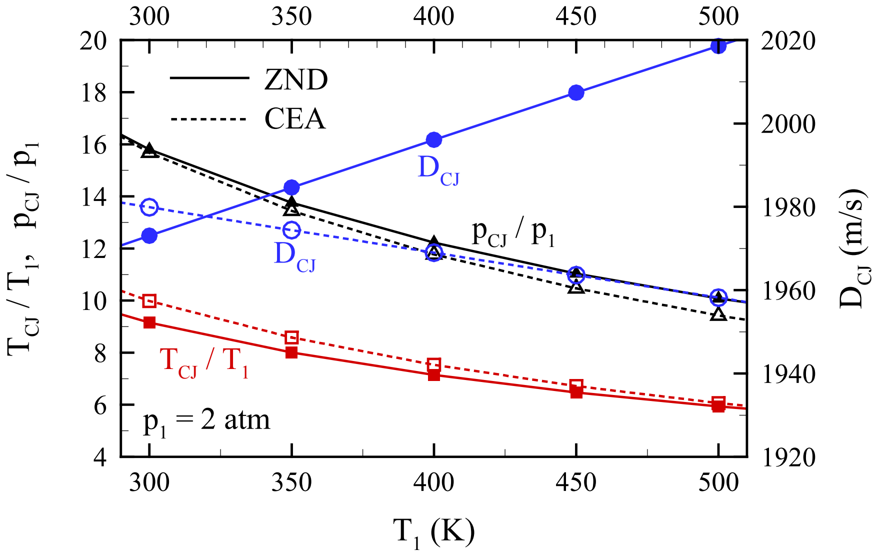

(b) p_1 = 2 atm

Fig. 3.2 Comparison of detonation velocity and CJ state between ZND model and CEA

3.3.2 ZND Detonation in a One-Dimensional Tube

The code is first validated for a ZND detonation in a one-dimensional tube as discussed in Sec. 1.2.3. Figure 3.3 shows the schematic of the physical problem. The 20 cm-long tube is closed at the head end and open at the other. Initially, it is filled with static, premixed stoichiometric hydrogen/air at temperature $T_1 = 300$ K and pressure $p_1 =$ 1 atm. A small energetic spark region spanning 0.02 cm with temperature $T_i = 2000$ K and pressure $p_i = 30$ atm is placed at the head end to initiate detonation.

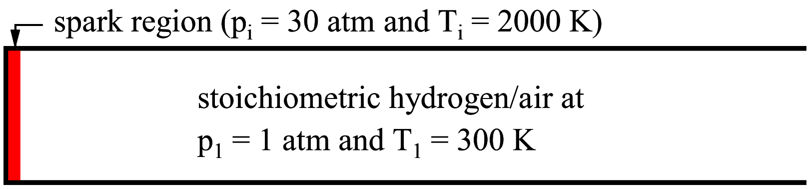

Fig. 3.3 Schematic of detonation tube with spark region at closed end

A series of calculations are carried out with five different grid resolutions to conduct grid-dependence study as well as validation. The grid points of these grids are 1000, 2000, 4000, 8000, 16000, respectively. Figures 3.4~3.7 show the time evolutions of pressure, temperature, mass fraction and velocity, respectively, for the case of grid points of 2000. These figures clearly depict the propagation of a self-sustained and fully-developed detonation wave. The leading shock, the rarefaction wave region, and the uniform region can also be observed. The small non-uniform region of temperature near the head end is due to the remaining effect of the initial spark.

Figure 3.8 shows the snapshots of pressure profiles at t = 80 μs with different grid resolutions. These profiles collapse into a single one, demonstrating nearly perfect satisfaction of grid dependence. The only exception is that the pressure immediately after the shock (spike pressure) increases with grid resolution. This is due to the fact that the higher the resoltuion, the less the degree of reaction across the shock front, thus leading to a higher spike pressure. Theoretically, the von Neummann spike pressure can be reached by using tremendously high resolution grid. However, significant round-errors appear with high reslolution grid, leaving the spike pressure unreachable in practice. In a worst case, too fine grid may cause unphysical soltutions. It is found that the detonation is not ignited with the finest grid (grid points = 16000). Similar phenomenon was also reported by Ebrahimi et al. (1999).

Table 3.1 compares the numerical solutions of different grid resolutions in terms of detonation velocity, von Neummann spike pressure, CJ state, and head-end pressure. The analytical solutions, obtained from the formulation given in Sections 1.2.1~1.2.3, are also listed for comparison. All these values are in perfect agreement with each other except for the von Neumann spike pressure.

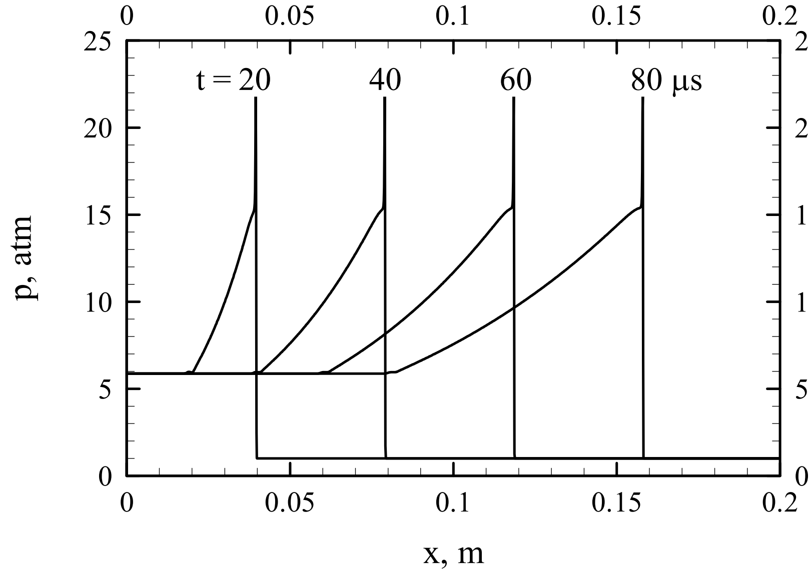

Fig. 3.4 Time evolution of pressure field for ZND problem (grid points = 2000)

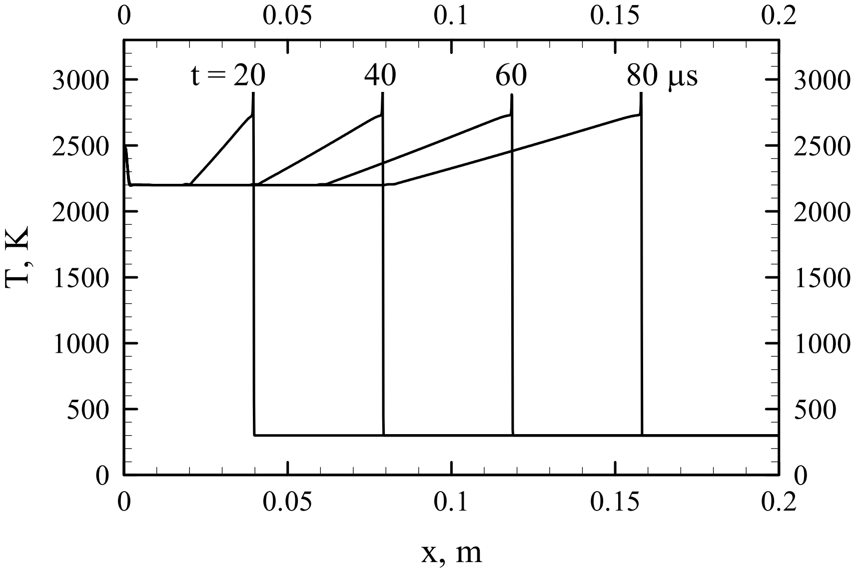

Fig. 3.5 Time evolution of temperature field for ZND problem (grid points = 2000)

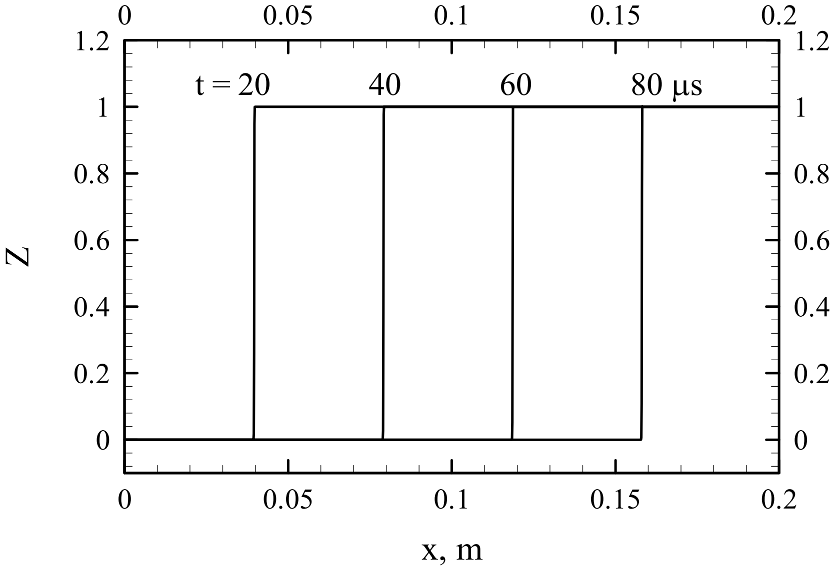

Fig. 3.6 Time evolution of reactant mass ratio field for ZND problem (grid points = 2000)

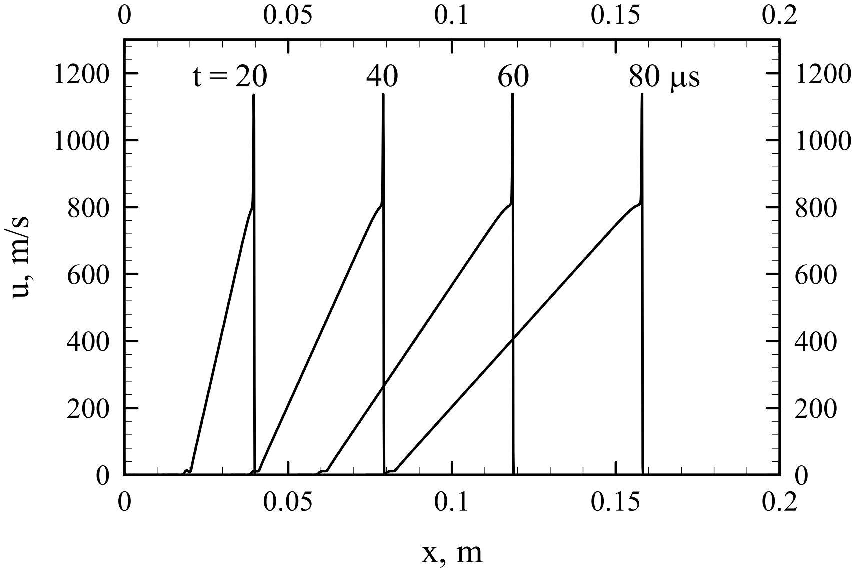

Fig. 3.7 Time evolution of velocity field for ZND problem (grid points = 2000)

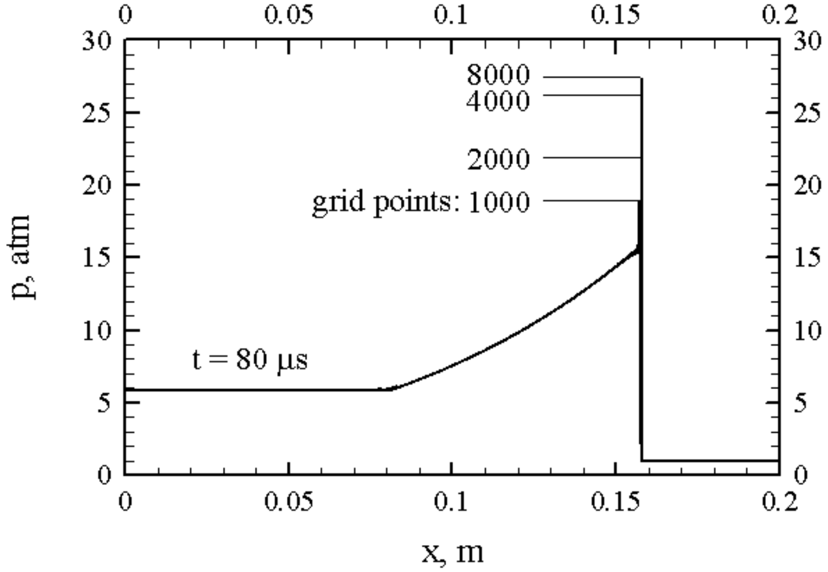

Fig. 3.8 Snapshots of pressure field for ZND problem with different grid points

Table 3.1 Comparison of numerical results of different grid resolutions with analytical solutions for the ZND problem

grid points	u_D, m/s	p_s, atm	p_{CJ}, atm	T_{CJ}, K	u_{CJ}, m/s	p_3, atm
analytical	1973	30.60	15.80	2746	830.0	5.871
1000	1975	18.8±0.1	15.80	2746	829.9	5.872
2000	1974	22.1±0.4	15.78	2745	830.0	5.872
4000	1974	25.6±0.8	15.79	2745	830.0	5.872
8000	1973	29.2±1.0	15.79	2745	830.0	5.872
16000	detonation can not be initiated					

3.3.3 Flow Through a Convergent-Divergent Nozzle

A calculation is carried out for a non-reacting flow through a nozzle with a length of 1 m and a cross-section area of $A(x) = 1 + (2x-1)^2$, as shown in Fig 3.9. The stagnation pressure (P_0), stagnation temperature (T_0) and back pressure (p_b) are 2 atm, 400 K, and 1.5 atm, respectively. Specific heat ratio γ is taken as 1.4. The analytical solution can be easily obtained from the classical gasdynamics. Figure 3.10 compares the pressure distribution with the analytical solution and perfect agreement is observed.

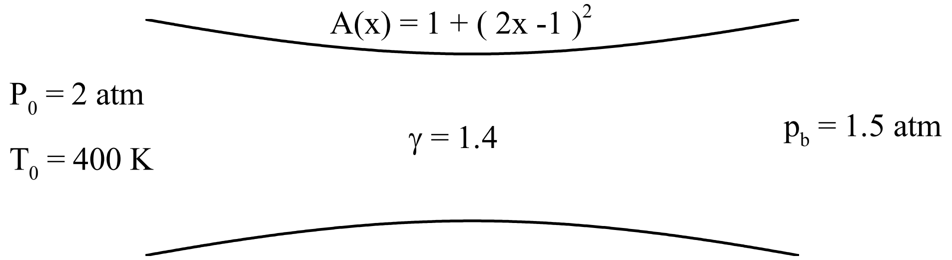

Fig. 3.9 Schematic of convergent-divergent nozzle in the validation case

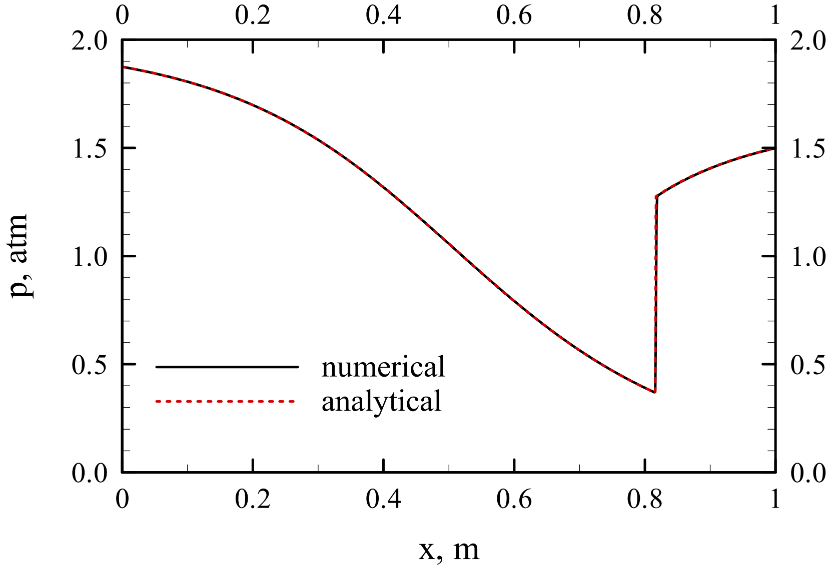

Fig. 3.10 Comparison of pressure distributuion with analytical results

3.4 Flow Dynamics

The validated quasi-one-dimensional code is then used to study the flow dynamics and system performance of an airbreathing PDE with a convergent-divergent (CD) nozzle. The reason for choosing a CD nozzle is that other types of nozzles such as convergent, divergent and plug nozzles have been studied by many researchers and limited performance improvements on the performance were found. On the other hand, the CD nozzle results in a supersonic exit flow during most of the cycle period, thus reducing the error induced by the exit boundary condition.

The tube has a length of 60 cm and a diameter of 16 cm, with a valve located at the head end as shown in Fig. 3.11. The valve is supposed to be either fully closed or fully open. The nozzle has a length of 20 cm, with a 45° convergent angle and a 15° divergent angle. The diameters of the nozzle throat and exit are 12 cm and 20 cm, respectively.

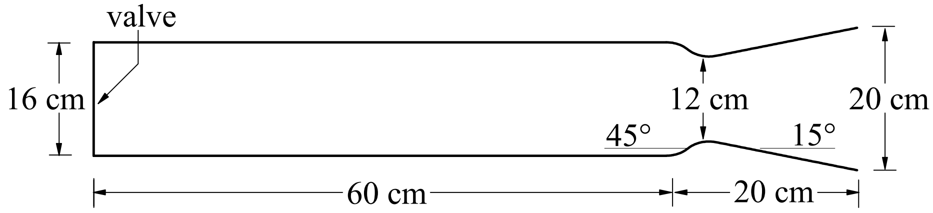

Fig. 3.11 Configuration of the single tube and CD nozzle in the current study

As a specific example, the flight condition involving an altitude of 9.3 km and a Mach number of 2.1 is considered. The free stream static pressure and temperature are 0.29 atm and 228 K, respectively, corresponding to a total pressure of 2.65 atm and a total temperature of 428 K. The supersonic inlet at this flight condition has been studied in Chapter 2. Based on the inlet analyses, the exit flow of the inlet has a total temperature of 428 K and a total pressure of 2.23 atm. By assuming 5% loss of the total pressure within the manifold, the total pressure at the entrance of the combustor becomes 2.12 atm, where the total temperature is still 428K.

The cyclic operation of the PDE is controlled by a valve located at the entrance of the combustor. Generally, there are two modes of valve operation (Mohanraj and Merkle, 2000). One is external mode, i.e., the timing of the valve opening and closing is specified externally. The other is internal mode. In this mode, the opening and closing procedures are controlled by the flow condition inside the detonation tube, e.g., using a pre-specified threshold pressure for valve open and a chemical sensor in the detonation tube for valve close. In the present study, the first mode is chosen and the valve response time is neglected for simplicity, i.e., the valve is either fully closed or fully open. Furthermore, the valve open area is equal to that of the detonation tube. The engine operation sequence, as shown schematically in Fig. 3.12, is thus controlled by three time periods: the valve close-up period (τ_{close}) during which the valve is closed and the tube undergoes detonation initiation and propagation and blowdown processes, the purging period (τ_{purge}) during which a small amount of cold air is injected into the tube to prevent preignition of fresh reactants, and the refilling period (τ_{refill}) during which the combustible mixture is delivered to the tube. The sum of these three periods equals the operation cycle time (τ_{cycle}), that is, $\tau_{cycle} = \tau_{close} + \tau_{purge} + \tau_{refill}$.

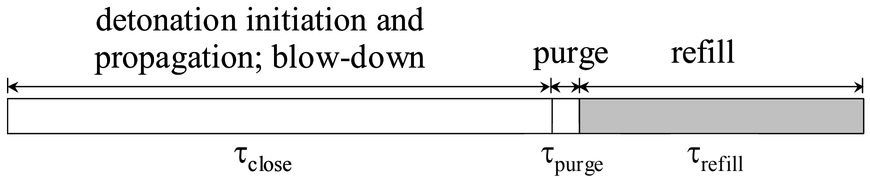

Fig. 3.12 Time periods during one cycle of operation

The boundary conditions at the head end of the detonation tube are specified according to the engine operation. During the valve close-up stage, the head end is modeled as a rigid wall. During the purging stage, the total temperature and total pressure are specified as 428 K and 2.12 atm, respectively, as mentioned in Section II. The axial velocity is obtained with extrapolation, and the reactant mass fraction is set to zero. During the refilling stage, the same conditions are used except that the reactant mass fraction is set to unity. At the exit of the nozzle, the boundary conditions are determined from the flow condition at exit. If the flow is supersonic, all flow variables are extrapolated from inside. If the flow is subsonic, the exit pressure is specified as the ambient pressure and other flow variables are extrapolated.

A series of calculations are conducted for various operation parameters. A particular case with $\tau_{cycle} = 3$ ms, $\tau_{close} = 2.1$ ms, and $\tau_{purge} = 0.1$ ms is first studied in detail to investigate the flow dynamics of the airbreathing PDE. The detonation tube is initially filled with a stoichiometric H_2/air mixture at ambient pressure and temperature. It takes about 6 cycles to reach a stable operation. Figure 3.13 presents the temporal evolution of the pressure field within one cycle of operation. Detonation is initiated immediately after the valve is closed. The detonation wave moves downstream and catches the leading fresh reactant at about x = 36 cm. It then degenerates to a non-reactive shock wave. Expansion waves from the interface reduce the pressures on both sides. When the shock wave reaches the convergent section of the nozzle, a reflected shock wave is formed and travels upstream. This reflected shock is reflected again when it reaches the head end of the combustor. On the other hand, the average chamber pressure decreases as the mass flows out of the combustor and nozzle. As the purging stage begins, a shock wave is generated due to the pressure difference across the valve. It is observed that the nozzle throat remains choked during most of the cycle period.

A more clear and detailed wave pattern is numerically obtained through the Eulerian approach as detailed in Appendix C. Figure 3.14 shows the x-t diagram during the first cycle. The time history of the flow properties at head end is also presented. The detonation wave is ignited in a very short time and propagates at a uniform CJ velocity of 1935 m/s in the unburned region (region 1), followed by the Taylor expansion waves (region 2) to satisfy the stationary condition at head end. A uniform region (region 3) is then formed behind the tail of Taylor waves. At t = 0.310 ms, the detonation wave arrives the reactant-product interface (point A), which is also the nozzle inlet, and transits to a non-reactive shock wave continuing to the nozzle exit. At the same time, expansion waves are generated from the interface. However, these expansion waves are soon overridden by the later formed compression waves from the convergent section of the nozzle. A shock wave is eventually formed due to the coalescence of the compression waves. This shock wave arrives at the head end at t = 0.949 ms (point B) and reflects again, causing an abrupt increase of the head-end pressure, which can be clearly observed in the time history of head-end pressure. This leads to a significant difference in the head-end pressure history from that of Wintenberger et al. (2003) which was based on an ideal modeling. Expansion waves are also emanated from the nozzle throat, result in a non-simple wave region when interacting with the Taylor waves, form a simple wave region (region 5) after passing through the tail of the Taylor waves, and cause a gradual decrease of head-end pressure. Inside the nozzle, flow chokes shortly after the primary shock passing through the throat. A secondary shock is then generated due to the interaction of the supersonic flow later induced by flow expansion from the divergent section and the subsonic flow immediately following the primary shock. The flow within the divergent section becomes fully supersonic after this secondary shock moves out of the nozzle. When the purging stage begins at $t = 2.1$ ms, the head-end pressure increases suddenly and two discontinuities appear: a shock wave caused by the pressure difference across the valve and a contact surface caused by the temperature difference between the hot product and the cold air. It can be clearly seen that the left-traveling characteristics deflect when passing through these two discontinuities. The refilling stage begins 0.1 ms later, causing a third discontinuity, i.e., a contact surface between reactant and air. This contact surface travels to $x = 32$ cm at the end of the first cycle, representing a partial filling for the next cycle.

Under the effects from the previous cycle, the wave pattern becomes much more complicated during later cycles. Figure 3.15 shows the x-t diagram and time history of head-end properties for a stable cycle. A significant difference from the first cycle is the absence of the pressure plateau due to the effects of the shock waves and expansion waves from the previous cycle. However, many phenomena are still similar, such as the propagation of detonation wave, Taylor expansion waves, choked throat, contact surfaces induced by purging and refilling, and so on.

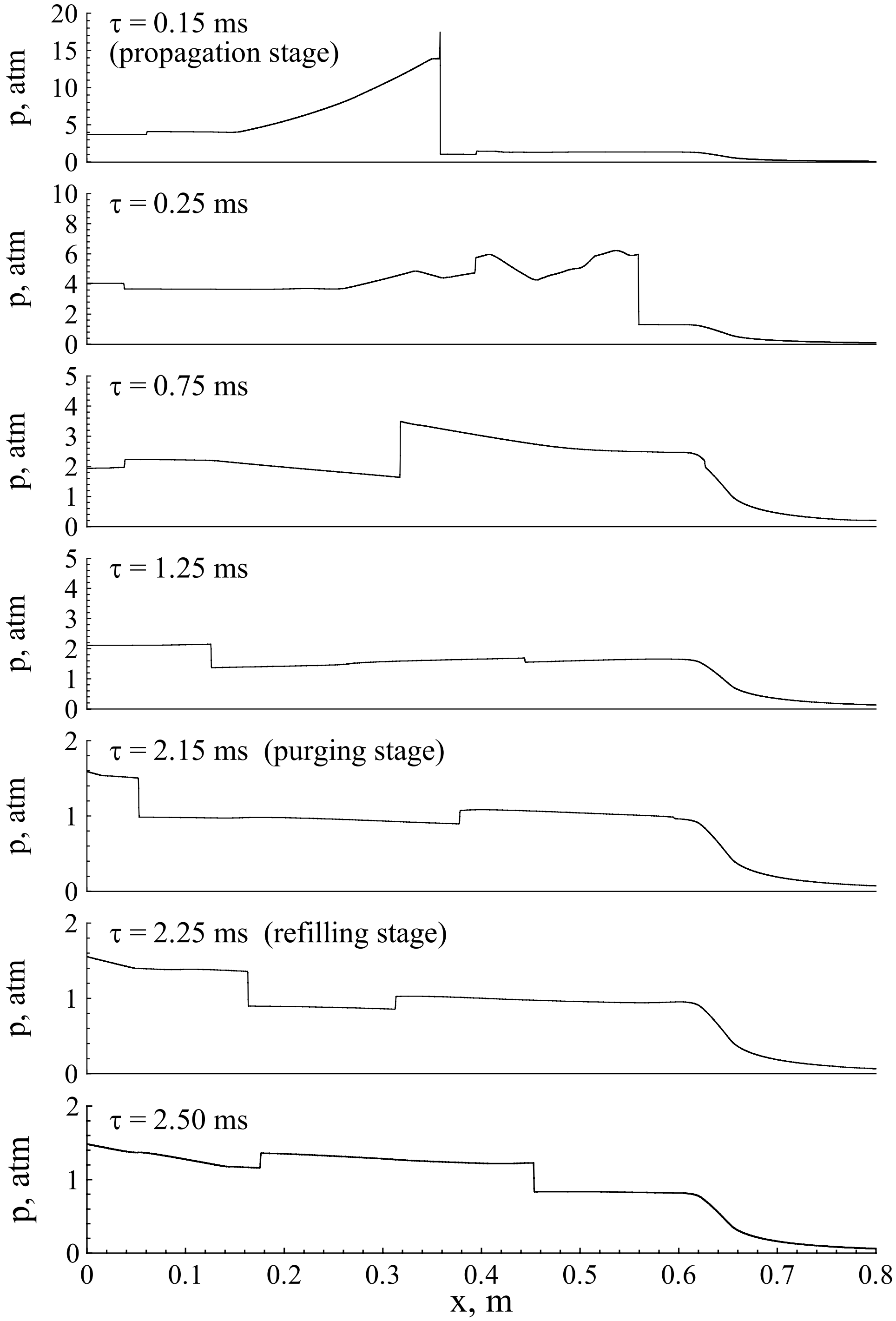

Fig. 3.13 Temporal evolution of pressure field within one cycle of operation ($\tau_{cycle} = 3$ ms, $\tau_{close} = 2.1$ ms, $\tau_{purge} = 0.1$ ms)

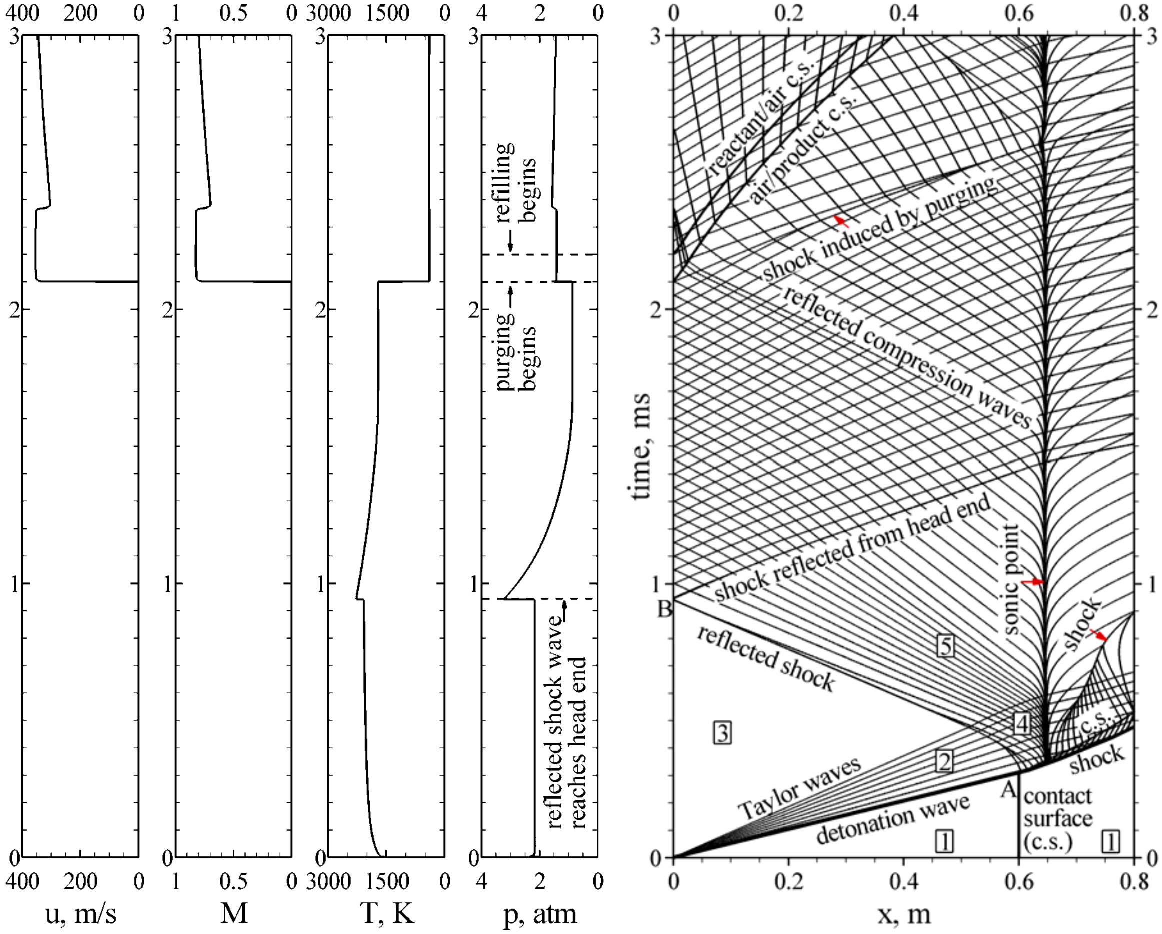

Fig. 3.14 x-t diagram for the first cycle and time histories of flow properties at head end under typical PDE operation with CD nozzle (stoichiometric H_2/air mixture, $\tau_{cycle} = 3$ ms, $\tau_{close} = 2.1$ ms, $\tau_{purge} = 0.1$ ms). 1 = uniform unburned region, 2 = Taylor expansion waves, 3 = uniform region, 4 = non-simple wave region, 5 = simple wave region.

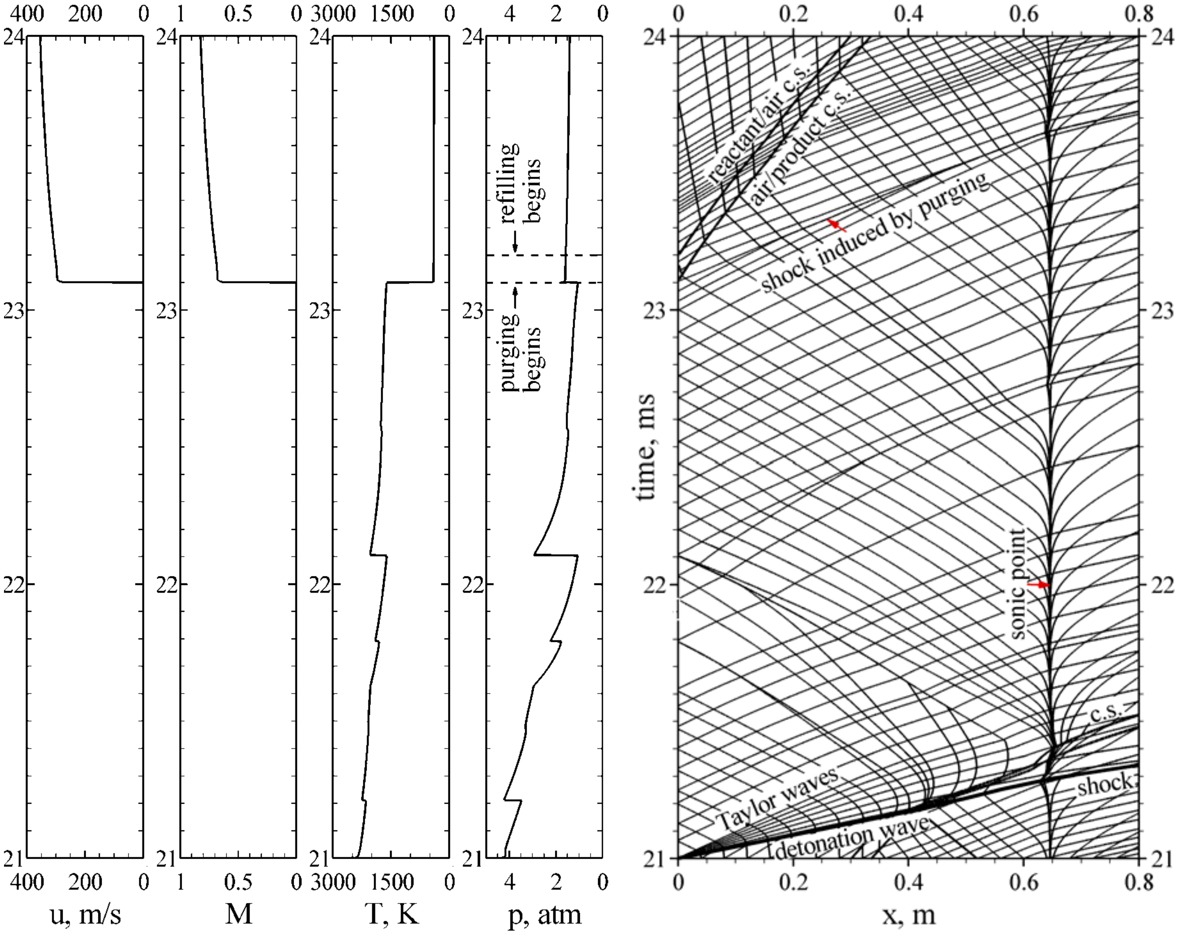

Fig. 3.15 x-t diagram for the eighth cycle and time histories of flow properties at head end under typical PDE operation with CD nozzle (stoichiometric H_2/air mixture, $\tau_{cycle} = 3$ ms, $\tau_{close} = 2.1$ ms, $\tau_{purge} = 0.1$ ms).

3.5 Parametric Study

3.5.1 Effect of Valve Timing

A parametric study is conducted to study the timing effect on system performance by varying τ_{cycle} and τ_{close}. The purge time τ_{purge} is fixed at 0.1 ms. Figure 3.16 shows the effect of τ_{close} on the specific thrust F_{sp}, defined as the cycle-averaged thrust per unit of air mass flow rate, and the fuel-based specific impulse, I_{sp}, at four different cycle frequencies of 200, 250, 333, and 400 Hz. The corresponding cycle periods are 5, 4, 3, and 2.5 ms, respectively.

The specific thrust increases as τ_{close} decreases for all of the frequencies considered herein. This can be explained as follows. For a given τ_{cycle} and $\tau_{purge,}$ a smaller τ_{close} translates to a shorter blow-down process. The resultant higher chamber pressure during the refilling stage increases the loading density of fresh reactants. The increased refilling period also enhances the amount of reactants delivered to the chamber. Combined, these two factors result in a higher cycle-averaged chamber pressure and consequently a higher specific thrust. It should be noted, however, that the lower bound of τ_{close} is subject to three practical constraints. The first is concerned with inlet over-pressurization. The head-end pressure must not exceed the stagnation pressure of the inlet air to allow for purging and refilling when the valve is open. The second is related to chamber over-filling. The fresh reactants should not flow out of the nozzle to the external region before being burned completely unless after-burning is considered. The third constraint, although commonly satisfied in practical cases, is that τ_{close} should be sufficiently long to cover at least the time required for detonation initiation and propagation throughout the entire chamber. The upper bound of τ_{close} (or the lower bound of τ_{refill}) is based on the requirement that an appropriate amount of fresh reactants be delivered to the chamber to produce thrust.

The effect of τ_{close} on the fuel-based specific impulse follows the same trend as that of the air-based specific thrust, except for a small range of τ_{close} close to its lower bound. The specific impulse and specific thrust satisfy the following relation,

$$I_{sp} = \frac{F_{sp}(1 + \tau_{\text{purge}} / \tau_{\text{refill}})}{f\,g} \tag{3.23}$$

As τ_{close} decreases, the factor $(1 + \tau_{\text{purge}/}\tau_{\text{refill}})$ decreases and may override the increase of F_{sp}, consequently leading to a decrease in I_{sp}, as shown in Fig. 3.16b.

For a given cycle period, τ_{close} determines the filling length of fresh reactants. A larger τ_{close} (or smaller τ_{refill}) leads to a smaller filling length in most cases and consequently decreases the specific impulse. This result, however, is in contrast to the previous experimental (Cooper and Shepherd, 2002) and numerical (Li and Kailasanath, 2002) observations for single-pulse operations, which concluded that the specific impulse increases as the filling length decreases. One factor contributing to this discrepancy is that in single-pulse studies, the pressure and temperature of reactants are preconditioned to ambient values, while in the present multicycle study, the flow conditions of the refilled mixture depend on the timing of the engine operation. The use of a choked CD nozzle also exerted a substantial influence on the chamber dynamics. Significant differences thus exist between single-pulse and multicycle operations. The conclusions from single-pulse studies may not be applied to multicycle cases directly.

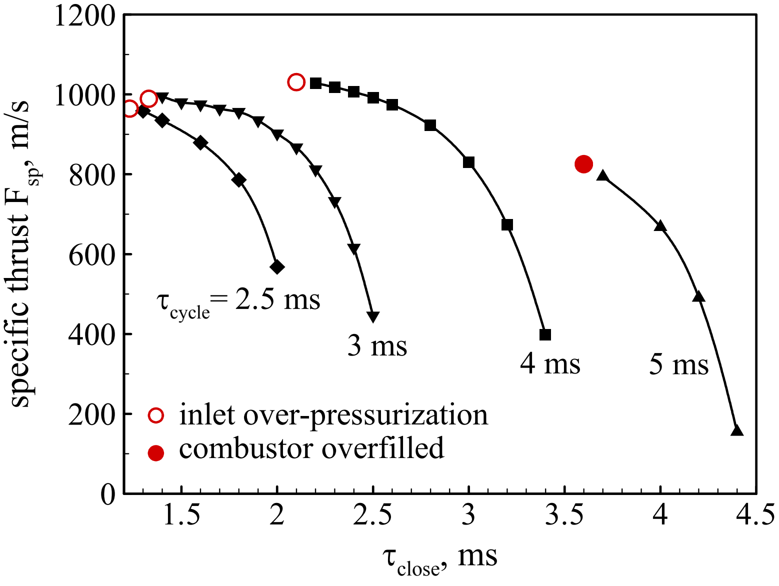

(a) specific thrust

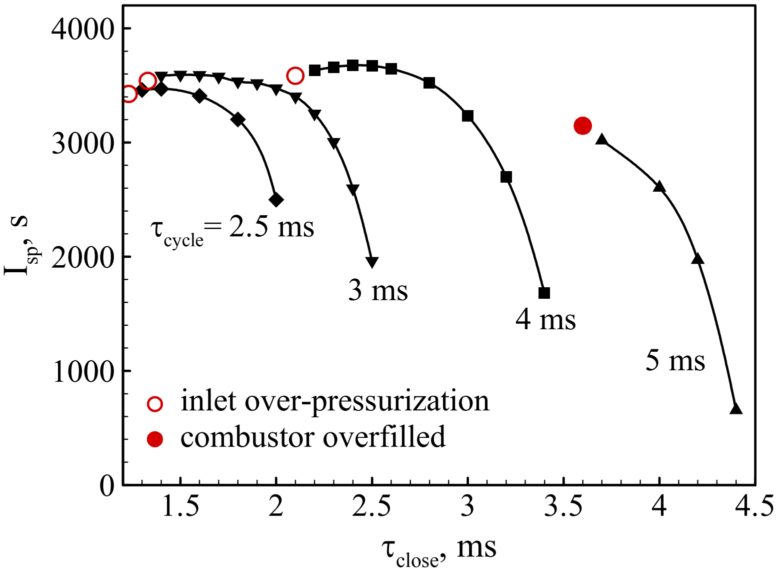

(b) specific impulse

Fig. 3.16 Effect of valve close-up time on (a) specific thrust and (b) specific impulse at four different operation frequencies; straight tube with CD nozzle; stoichiometric H_2/air mixture, h = 9.3 km, $M_\infty = 2.1$.

Figure 3.16 also demonstrates the existence of an optimum frequency for achieving a maximum performance. At a low cycle frequency, more reactants can be recharged into the detonation tube. As a consequence, a higher chamber pressure can be reached and the engine efficiency improves. However, a large refilling time associated with low-frequency operation may cause chamber over-filling and thus degrade the performance. These two conflicting effects result in an optimum frequency. In the present study, the operating frequency of 250 Hz (τ_{cycle} = 4 ms) offers the best performance. The highest specific impulse is 3676 s, slightly lower than its ramjet counterpart of 3866 s with optimum nozzle flow expansion (Wu, Ma, and Yang, 2003).

3.5.2 Effect of Nozzle Throat Area

The effect of the nozzle throat area was also studied. Figure 3.17 compares the performances between the aforementioned CD nozzle and another CD nozzle with a smaller throat diameter of 10 cm. A smaller throat implies higher chamber pressure, therefore, performance gains are observed for those τ_{close} that are larger than their corresponding optimums. A smaller throat also leads to an earlier inlet over-pressurization. Apparently, the operating ranges for τ_{close} are narrower with the smaller throat under frequencies of 333 Hz and 250 Hz. For the 200 Hz case, however, the operating range becomes wider, since the lower limit is determined by combustor overfilling for the larger throat under this frequency while a smaller throat can postpone the combustor overfilling. An even smaller throat with a diameter of 8 cm was also tested. A too small throat is not beneficial because of the inlet over-pressurization.

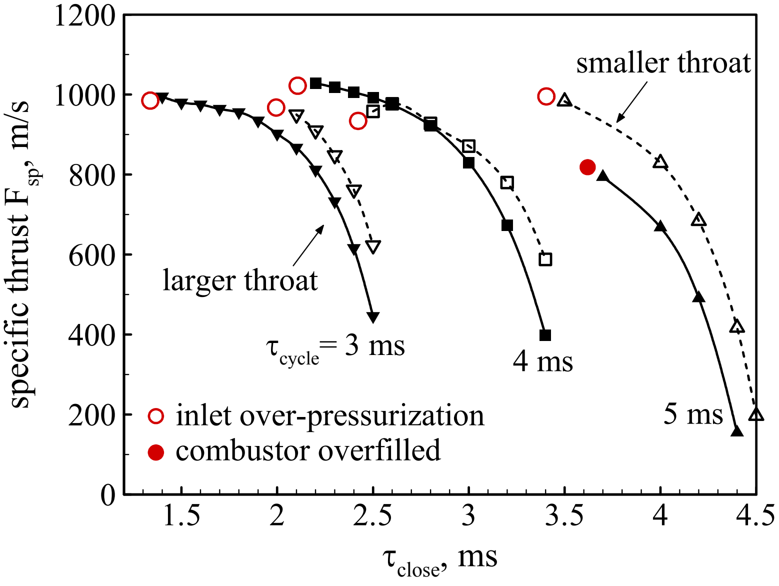

(a) specific thrust

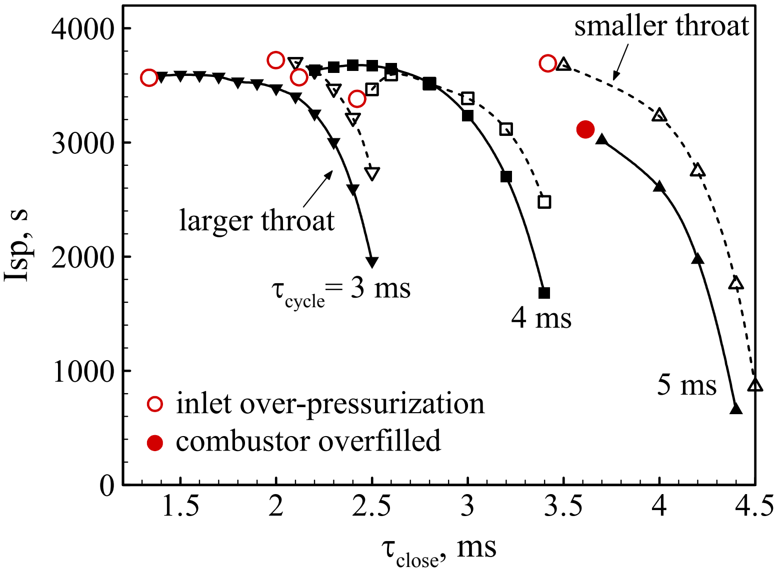

(b) specific impulse

Fig. 3.17 Effects of τ_{close} on (a) specific thrust and (b) specific impulse at three different frequencies for two CD nozzles with different throat areas. The larger one has a diameter of 12 cm and the smaller one 10 cm.

Chapter 4

Two-Dimensional Analyses of Single-Tube PDEs

One-dimensional simulations are computationally efficient. Nevertheless, they cannot provide detailed multidimensional flow dynamics and cannot be applied to a PDE involving multiple detonation tubes. Multidimensional simulations with computation domain including both the detonation tube and the external region are required in order to faithfully describe the system dynamics, especially in the near field of the tube exit where the flow is intrinsically multidimensional, and to provide more accurate performance predictions. However, the difficulties of using very fine grid to resolve the significant flow structure and running many time steps to reach steady periodic operation have limited previous multidimensional simulations of PDEs. Two-dimensional multicycle simulations, to the knowledge of the author, has not been reported elsewhere in the literature. In the current study, an efficient parallel computing technology coupling to the high fidelity Space-Time CE/SE method is implemented to overcome these difficulties.

4.1 Governing Equations

The analysis is based on the two-dimensional conservation equations of mass, momentum, and energy and takes into account finite-rate chemical kinetics. Diffusive effects are neglected in the current study because of their minor roles in determining the overall flow dynamics and propulsive performance of PDEs. If the chemical reaction rate is expressed with a single progress variable, the resultant governing equations can be written in the following vector form:

$$\frac{\partial \mathbf{Q}}{\partial t} + \frac{\partial \mathbf{E}}{\partial x} + \frac{\partial \mathbf{F}}{\partial y} = \mathbf{H} \tag{4.1}$$

where the dependent variable vector, **Q**, convective flux vectors, **E** and **F**, and source vector, **H**, are defined as:

$$\mathbf{Q} = \begin{bmatrix} \rho \\ \rho u \\ \rho v \\ \rho e_t \\ \rho Z \end{bmatrix}, \quad \mathbf{E} = \begin{bmatrix} \rho u \\ \rho u^2 + p \\ \rho uv \\ u(\rho e_t + p) \\ \rho uZ \end{bmatrix}, \quad \mathbf{F} = \begin{bmatrix} \rho v \\ \rho uv \\ \rho v^2 + p \\ v(\rho e_t + p) \\ \rho vZ \end{bmatrix}, \quad \mathbf{H} = \begin{bmatrix} 0 \\ 0 \\ 0 \\ 0 \\ \dot{\omega} \end{bmatrix} \tag{4.2}$$

In the above equations, ρ, u, v, e_t, and Z represent the density, axial velocity, vertical velocity, specific total energy, and progress variable (i.e., mass fraction of reactant), respectively. The pressure p is obtained through the equation of state,

$$p = (\gamma - 1)\rho[e_t - (u^2 + v^2)/2 - Zq] \tag{4.3}$$

where γ is the specific heat ratio and q the heat release per unit mass of reactant. For a one-step, irreversible reaction, the mass production rate of reactant $\dot{\omega}$ is

$$\dot{\omega} = -K\rho Z \exp(-E_a / RT) \tag{4.4}$$

where K is the pre-exponential factor, T the temperature, E_a the activation energy per unit mass of reactant, and R the gas constant. The five parameters involved in the above equations remain the same as those in Chapter 3. The Jacobian matrices of the flux and source vectors of Eq. (4.1) are given in Appendix B.

4.2 Numerical Treatment and Parallel Implementation

A two-dimensional unstructured triangular mesh non-reacting Euler solver based on the space-time CE/SE method has been developed by Wang and Chang (1999). The ideas and solution procedure are identical to the one-dimensional version described in Chapter 3. The details of the space-time CE/SE method for two-dimensional problems are given in Appendix D. In the current study, a two-dimensional code is developed and efficiently parallelized by implementing the message-passing-interface (MPI) library and the domain decomposition technique. The parallel code is then executed on an in-house Beowulf cluster.

Beowulf is a multi-computer architecture for parallel computations. A Beowulf system is a cluster of PCs (or workstations) including server nodes and client nodes connected through network such as switch (http://www.beowulf.org). This system has only a history of several years. The first Beowulf Cluster was built by NASA in 1994. The current in-house Beowulf cluster was built up in 1997 and has been extended to a large parallel system consisting of 350 workstations and several high-speed switches.

Parallel virtual machine (PVM) and message passing interface (MPI) are software systems for writing message-passing parallel programs that run on a cluster. PVM used to be the de facto standard until MPI appeared. The MPI is standardized by the MPI Forum and available on all massively parallel supercomputers.

To effectively use the Beowulf system, the task should be properly distributed among the processors. A common approach is to decompose the computational domain into sub-domains and assign each sub-domain to a different processor. The objective of domain decomposition is to balance the computational workload and memory occupancy of processing nodes while keeping the inter-node communication as small as possible. In the current work, a software package, METIS, which is a family of programs for partitioning unstructured graphs and hypergraphs and computing fill-reducing orderings of sparse matrices (Karypis and Kumar, 1998), is used for domain decomposition.

4.3 Model Validation

As part of the model validation effort, a series of single-pulse calculations were conducted for a straight tube of 60 cm in length initially filled with a stoichiometric mixture of hydrogen and air at preconditioned pressure p_1 and temperature T_1. A spark region spanning 0.2 mm near the head end with a temperature of 2,000 K and a pressure of 30 atm was employed to directly initiate the detonation wave. Four different numerical grids with the sizes of 0.2, 0.1, 0.05, and 0.025 mm were used to check the solution accuracy in terms of grid independence. All of the calculated pressure profiles collapsed onto a single curve, with the CJ properties matching the analytical values exactly. As a result, the 0.2 mm grid was chosen for the entire study to alleviate the computational burden. For a single-pulse operation, the head-end pressure remains at a plateau value p_3 for certain period soon after the detonation initiation, and then decays gradually to a level lower than the ambient state. The impulse on the thrust wall can be determined by integrating temporally the force exerted on the head end from t = 0 to the instant when the head-end pressure reaches the ambient value. The contribution to the impulse from the ignition source is estimated to be less than 0.5%. Figure 4.1 shows the impulse per unit cross-sectional area as a function of the plateau pressure p_3 and the detonation residence time τ_D (defined as the tube length L divided by the detonation wave velocity u_D, i.e., $\tau_D \equiv L/u_D$). Results can be correlated well in the following form

$$I / A = 4.1(p_3 - p_1)\tau_D \tag{4.5}$$

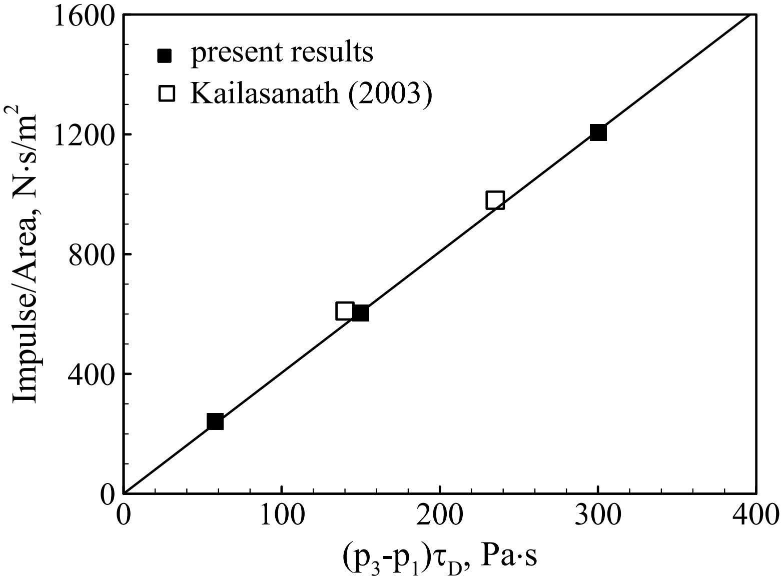

Fig. 4.1 Generalized impulse curve for single-pulse detonation in straight tube with stoichiometric H_2/air mixture.

This expression is quite similar to those obtained from the semi-analytical analysis of Wintenberger et al. (2003) and the experimental work of Falempin et al. (2001). The constants of proportionality differ slightly in the various studies, suggesting dependence on the details of experimental procedure and operating conditions. The generalized formula proposed by Kailasanath (2003) based on his numerical simulations for hydrogen/air, ethylene/oxygen, and propane/oxygen mixtures has a larger constant of proportionality of 4.65. One factor contributing to this disparity may be differences in ignition source. The width of the detonation initiation region used by Kailasanath (2003) is 20 mm, as opposed to 0.2 mm in the present simulations. Nonetheless, the above parametric study demonstrates the capacity and fidelity of the present approach for the PDE performance analysis.

4.4 Calculation of Propulsive Performance

The propulsive performance of the PDE must be calculated appropriately. There are several ways to experimentally measure the impulse, such as integrating the pressure force on the thrust wall, using the ballistic pendulum, load cell, damped thrust stand, and spring-damper system, as discussed in Sec. 1.4.1.1. In numerical simulations, the impulse or thrust can be obtained either by integrating the pressure force on the thrust wall or through a momentum balance fro the entire system. The latter is more practical for PDEs including both inlet and nozzle and is detailed as below.

Considering a control volume that contains the fluid within the entire engine, the momentum conservation gives:

$$\int_{CV} \frac{\partial \rho \mathbf{u}}{\partial t} dV + \oint_{CS} [\rho \mathbf{u}\mathbf{u} \cdot \mathbf{n} + (p - p_\infty)\mathbf{n}] dS = 0 \tag{4.6}$$

where *CV* represents the control volume and *CS* the control surface which can be further divided into three parts: the entrance plane S_i, the exit plane S_e, and the remaining surface S_w. Defining $\dot{m}_e$, $\mathbf{u}_e$, and p_e as

$$\dot{m}_e = \int_{S_e} \rho \mathbf{u} \cdot \mathbf{n} dS \tag{4.7}$$

$$\mathbf{u}_e = \frac{1}{\dot{m}_e} \int_{S_e} \rho \mathbf{u}\mathbf{u} \cdot \mathbf{n} dS \tag{4.8}$$

$$p_e = \frac{1}{A_e} \int_{S_e} p dS \tag{4.9}$$

the instantaneous thrust, in a vector form, can thus be derived:

$$\mathbf{F} = -\left\{ [\dot{m}_e \mathbf{u}_e - \dot{m}_a u_\infty \mathbf{i}] + [(p_e - p_\infty) A_e \mathbf{i}] \right\} - \int_{CV} \frac{\partial \rho \mathbf{u}}{\partial t} dV \tag{4.10}$$

The second term on the right-hand side is arisen from the unsteady effect. For a steady periodic operation, the cycle average of this term becomes zero, and the cycle-averaged thrust becomes

$$\langle \mathbf{F} \rangle = -\left[\langle \dot{m}_e \mathbf{u}_e \rangle - \dot{m}_a u_\infty \mathbf{i} \right] - \left[\left(\langle p_e \rangle - p_\infty \right) A_e \mathbf{i} \right] \tag{4.11}$$

where the bracket denotes the cycle-averaged quantities. Because of the symmetric property of the system, the vertical component of the cycle-averaged thrust is zero, and the axial component is

$$\langle F \rangle = \left[\langle \dot{m}_e u_e \rangle - \dot{m}_a u_\infty \right] + \left[\left(\langle p_e \rangle - p_\infty \right) A_e \right] \tag{4.12}$$

This formulation is identical to the conventional one obtained for steady engines, except for the averaging symbol. The two terms on the right-hand side are referred to as momentum thrust and pressure thrust, respectively. The air-based specific thrust and fuel-based specific impulse are then calculated as

$$F_{sp} = \frac{\langle F \rangle}{\dot{m}_a} \tag{4.13}$$

$$I_{sp} = \frac{\langle F \rangle}{\langle \dot{m}_f \rangle g} \tag{4.14}$$

It should be pointed out that, since the valve timing, the total pressure, and the total temperature in front of the valve are prespecified, the air mass match between the combustor and the inlet is achieved either by adjusting the width of the combustor, which is a free parameter in two-dimensional simulations, or by changing the size of the inlet. Otherwise, the computational domain should be extended more upstream to cover a choked section so that the mass flow rate instead of the total pressure is specified at the entrance boundary.

4.5 Straight-Tube PDE

As a first approach, a single straight tube is considered to provide direct insight into the chamber dynamics without complications arising from the nozzle.

4.5.1 Problem Setup

The computational domain is shown schematically in Fig. 4.2. The detonation tube measures 60 cm in length and 16 cm in height, which are similar to the dimensions of contemporary ramjet combustors for air defense applications. An external region is included to circumvent the difficulty of specifying boundary conditions at the tube exit. The computational domain is discretized into 421590 unstructured triangular grid cells, with 320000 for the detonation tube and 101590 for the external region. This dense grid resolves the detailed detonation propagation in the axial direction and was selected after performing a grid independence analysis of the computed solution such as pressure profile along the axial direction. The cell size near the head end is about 0.4 mm in the axial direction and 2 mm in the vertical direction. It increases to about 5 mm at the external boundary.

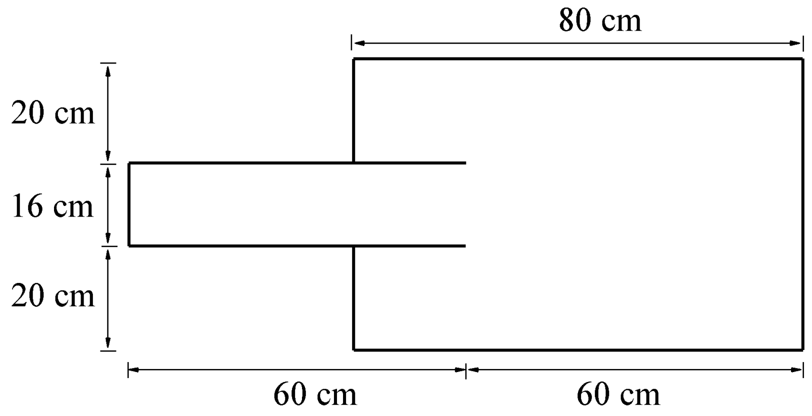

Fig. 4.2 Computational domain for straight-tube PDE

4.5.1.2 Domain Decomposition

The computational domain is decomposed into 64 sub-domains using the METIS software (Karypis and Kumar, 1998) for parallel computing. This domain decomposition technique allows for the balance of the computational workload and memory occupancy of processors, while keeping the inter-processor communications as low as possible, and thus obtaining a high parallel efficiency. With METIS, each cell is marked with a number to which sub-domain (or sub-grid) it belongs. A user code is then needed to gather this information and write out sub-grid data into different grid files. Figure 4.3 schematically shows the computational domain that decomposed into 64 sub-domains. The number of cells for each sub-domain is given in Fig. 4.4, demonstrating a quite evenly decomposition of grid cells.

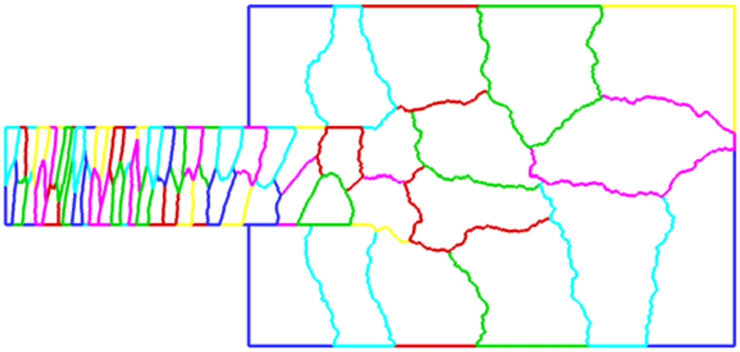

Fig. 4.3 Schematic of the computational domain decomposed into 64 sub-domains

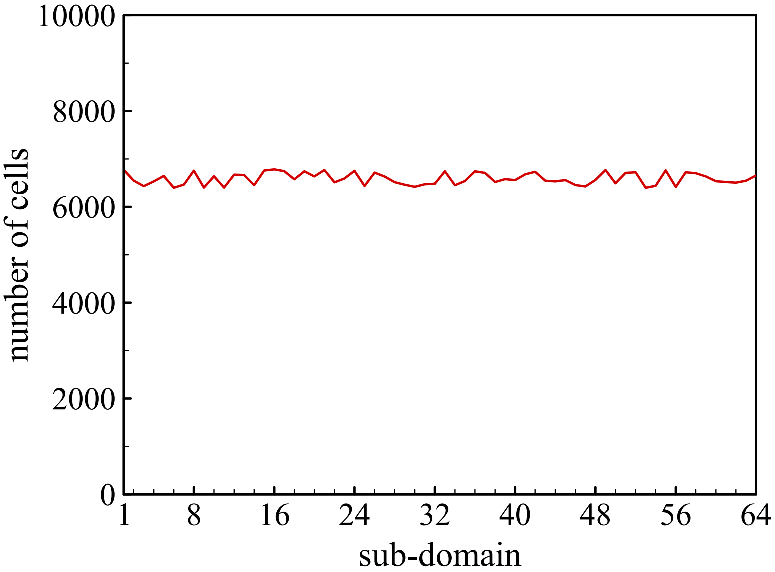

Fig. 4.4 Number of cells of sub-domains

4.5.1.3 Boundary Conditions

The boundary conditions at the head end of the detonation tube are specified according to the engine operation. During the valve close-up stage, the head end is modeled as a rigid wall. During the purging stage, the total temperature and total pressure are specified as 428 K and 2.12 atm, respectively. The axial velocity is obtained with extrapolation, and the reactant mass fraction is set to zero. During the refilling stage, the same conditions are used except that the reactant mass fraction is set to unity. At the open boundary of the external region, a non-reflecting boundary condition is implemented (Wang and Chang, 1999). The slip wall boundary conditions are detailed in Appendix E.

4.5.1.4 Initial Conditions

The detonation tube is initially filled up with a stoichiometric hydrogen/air mixture at the ambient pressure (0.29 atm) and temperature (228 K), whereas the other region is filled with the ambient air.

4.5.1.5 Detonation Initiation

Detonation initiation is assured by a small driver region near the head end that extends across the entire tube cross section. The temperature and pressure of the driver gas are 2,000K and 30 atm, respectively. Because of the high energy density associated with the driver gas, its effect on the propulsive performance could be quite large. Cambier and Tegner reported an effect of 17 to 27% on the single-pulse impulse for a PDE system with a 10-cm-long detonation tube and a 5-cm-long divergent nozzle

(Cambier and Tegner, 1998). In the present study, several lengths of the driver region were tested and the smallest one of 0.2 mm was selected to minimize the effect of the initiation source on the propulsive performance. The thermal energy per unit area of this initiation source is approximated as

$$c_p T_{driv} \rho_{driv} L_{driv} = [\gamma/(\gamma-1)] p_{driv} L_{driv} \approx 0.27 J/cm^2 \tag{4.15}$$

Its effect on the propulsive performance can be estimated by comparing the thermal energy of the initiation source with the heat that could be released from the detonation of the reactant within the tube:

$$\frac{c_p T_{driv} \rho_{driv} L_{driv}}{q \rho L} = \frac{[\gamma/(\gamma-1)] p_{driv} L_{driv}}{[q/(RT)] p L} \approx 0.5\% \tag{4.16}$$

The net effect appears to be limited.

4.5.2 Results

A series of analyses are conducted over a wide range of operation parameters. The CFL number used is 0.5, whereas the corresponding time step is about 5×10^{-5} ms. The typical turn-around time for one cycle of calculation is about 10 hours on an in-house PC cluster consisting of 64 Pentium II processors.

The baseline case has τ_{cycle} of 3 ms and τ_{close} of 2.4 ms. It takes about 5 cycles to reach steady cyclic operation. Figure 4.5 shows the x-t diagram for the first cycle of operation, obtained by tracing the characteristic lines of the flowfield along the centerline of the tube. The time histories of the flow properties at the head end are also presented. Procedures for building the x-t diagram are given in Appendix C.

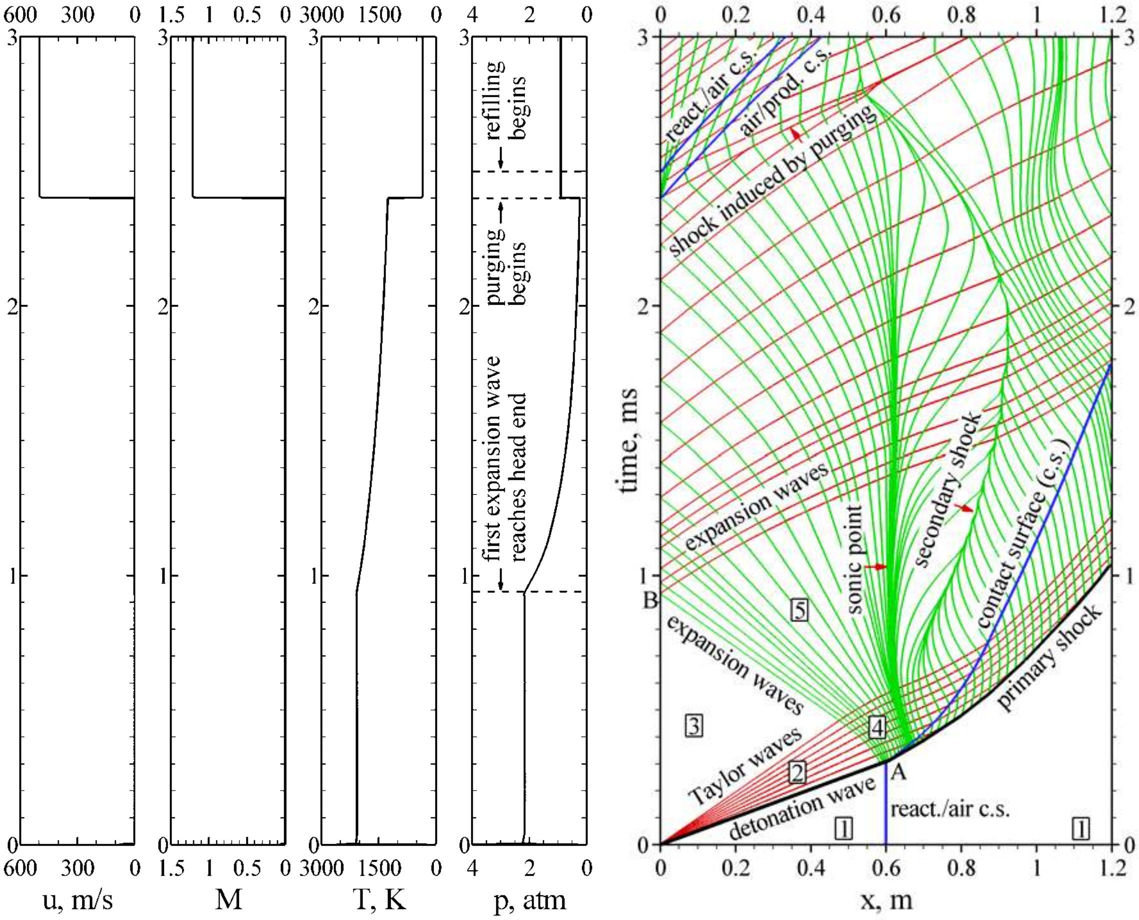

Fig. 4.5 x-t diagram for first cycle and time histories of flow properties at head end under typical PDE operation (stoichiometric H_2/air mixture, $\tau_{cycle} = 3$ ms, $\tau_{close} = 2.4$ ms, $\tau_{purge} = 0.1$ ms). 1 = unburned region, 2 = Taylor expansion waves, 3 = stationary region, 4 = non-simple wave region, 5 = simple wave region.

The detonation wave is directly initiated by a hot driver gas and propagates downstream at the CJ detonation velocity toward the unburned mixture (region 1). It then induces the Taylor expansion waves (region 2) in order to satisfy the stationary condition at the head end, causing a uniform region (region 3) with constant flow properties in the upstream.

The detonation wave reaches the reactant/air interface at the tube exit at t = 0.305 ms (point A), which deviates slightly from the following analytical prediction by 0.6% due to the effect of the externally imposed ignition source.

$$\tau_{\mathrm{D}} = \frac{L}{u_D} = \frac{0.6\ \mathrm{m}}{1956\ \mathrm{m/s}} = 0.307\ \mathrm{ms} \tag{4.17}$$

The wave then degenerates to a non-reactive shock (i.e., the primary shock wave) proceeding further downstream into the external region, followed by a contact surface separating the ambient air and combustion products. A sonic region is gradually formed near the tube exit due to the local flow expansion, as evidenced by the clustered characteristic lines in the x-t diagram. Downstream of the sonic region, the flow is expanded to become supersonic and finally leads to the formation of a secondary shock to match with the subsonic flow behind the primary shock. This secondary shock wave moves further downstream, meeting with expansion waves originating from the primary shock wave. These complicated flow structures can be also observed in Fig. 4.6, which shows the instantaneous pressure and density and their gradient fields at t = 0.7 ms. Many salient features are clearly examined, including the expansion fans, vortices, and the rolled-up slip lines developed as the shock diffracts over the edge of the tube exit.

As the detonation wave catches the reactant/air interface and the resultant primary shock wave travels outside the tube, a series of expansion waves are generated and propagate upstream, resulting in a non-simple wave region (region 4) when interacting with the incoming Taylor waves. A simple wave region (region 5) is recovered after passing through the Taylor waves. The first expansion wave reaches the head end at t = 0.935 ms (point B), which can be determined by considering the interaction between the expansion and the Taylor waves and the sound speed in region 3. A similarity solution has been derived by Wintenberger et al. (2003) and is detailed in Appendix F. The analytical solution gives

$$\mathrm{t} = \frac{L}{u_D} + \alpha \frac{L}{c_3} \tag{4.18}$$

where α is function of γ and M_D and can be calculated as,

$$\alpha = \frac{1}{2}\left(1 + \frac{1}{{M_D}^2}\right) \cdot \left\{ 2\left[\frac{2(\gamma {M_D}^2 + 1)}{(\gamma + 1)({M_D}^2 + 1)} \right]^{\frac{\gamma+1}{2(\gamma-1)}} - 1 \right\} \tag{4.19}$$

Application of Eqs. (4.18) and (4.19) gives rise to an analytical value of 0.958 ms. The slight difference between the numerical and the analytical solutions may be attributed to the numerical resolution and dissipation near the tube exit.

On the arrival of the first expansion wave at the head end, the pressure begins to decay gradually. These expansion waves reflect off the head end and form another series of expansion waves, further reducing the chamber pressure. The downstream-traveling expansion waves weaken the secondary shock, and eventually cause it to move upstream.

The head-end pressure decays to 0.23 atm at t = 2.4 ms, at which point the purging stage begins. The head-end temperature is 1258 K at this instant. Because of the pressure difference across the entrance plane, a right-running shock wave is established, along with a series of central expansion waves and a contact surface between the burned gas and the cold air. Another contact surface forms between the fresh reactants and purging air when the refilling stage commences 0.1 ms later. The corresponding refilling pressure, velocity, and Mach number are about 0.91 atm, 500 m/s, and 1.2, respectively.

The time evolution of the pressure distribution along the centerline during the first cycle of operation is shown in Fig. 4.7.

The flow evolution during a steady operation cycle is examined. Figure 4.8 shows the x-t diagram and time histories of flow properties at the head end for the fifth cycle. The main flow features remain qualitatively the same as those in the first cycle. However, the secondary shock wave disappears, since the flow behind the primary shock wave is already supersonic. In addition, the head-end pressure and temperature begin to decay earlier relative to the first cycle, due to the rarefaction waves produced from the previous cycle. It should also be noted that the detonation wave catches the leading fresh reactant at x = 51.2 cm instead of at the tube exit.

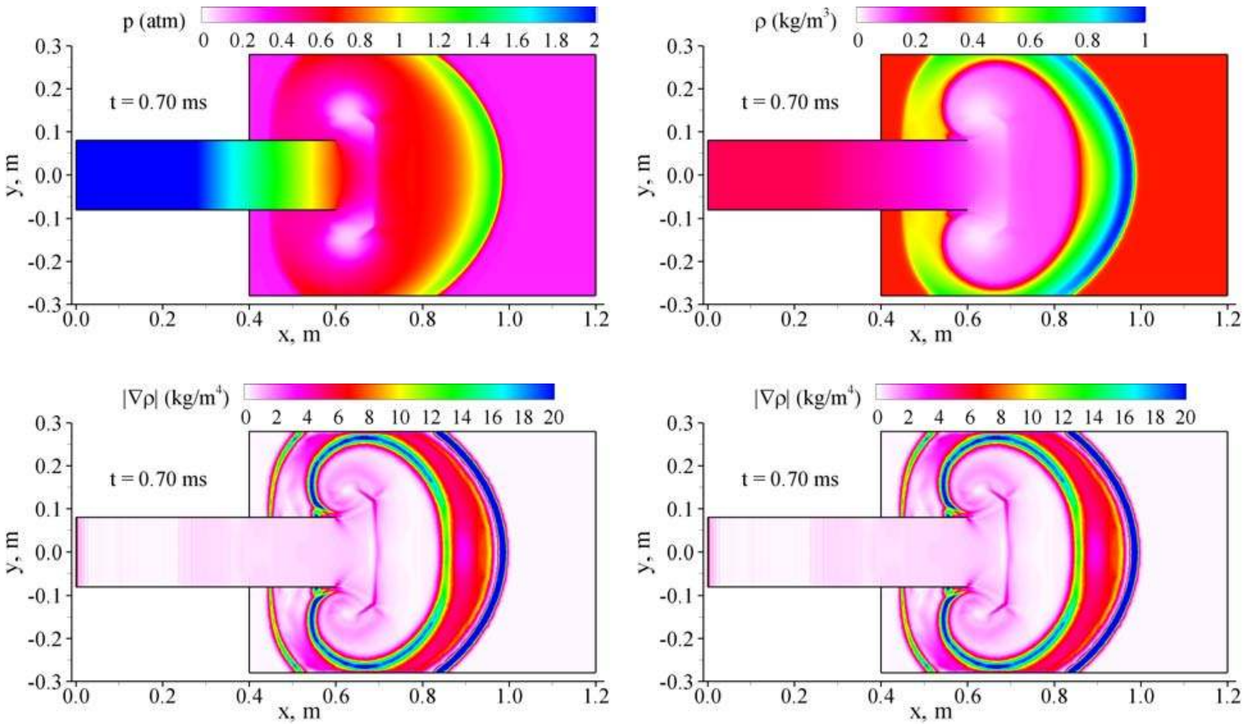

Fig. 4.6 Snapshots of pressure, density and their gradients fields at t = 0.7 ms.

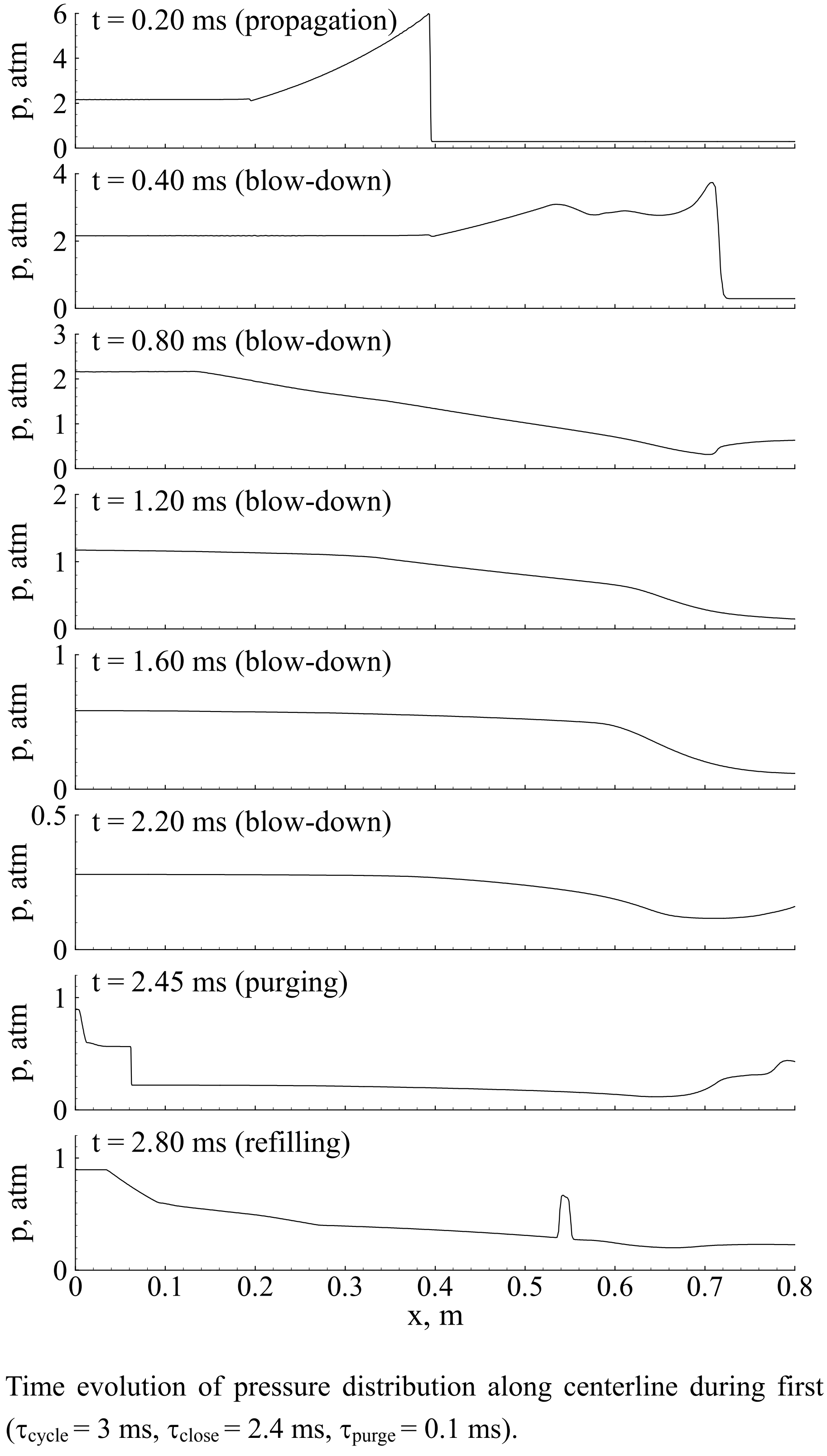

Fig. 4.7 Time evolution of pressure distribution along centerline during first cycle of operation ($\tau_{cycle} = 3$ ms, $\tau_{close} = 2.4$ ms, $\tau_{purge} = 0.1$ ms).

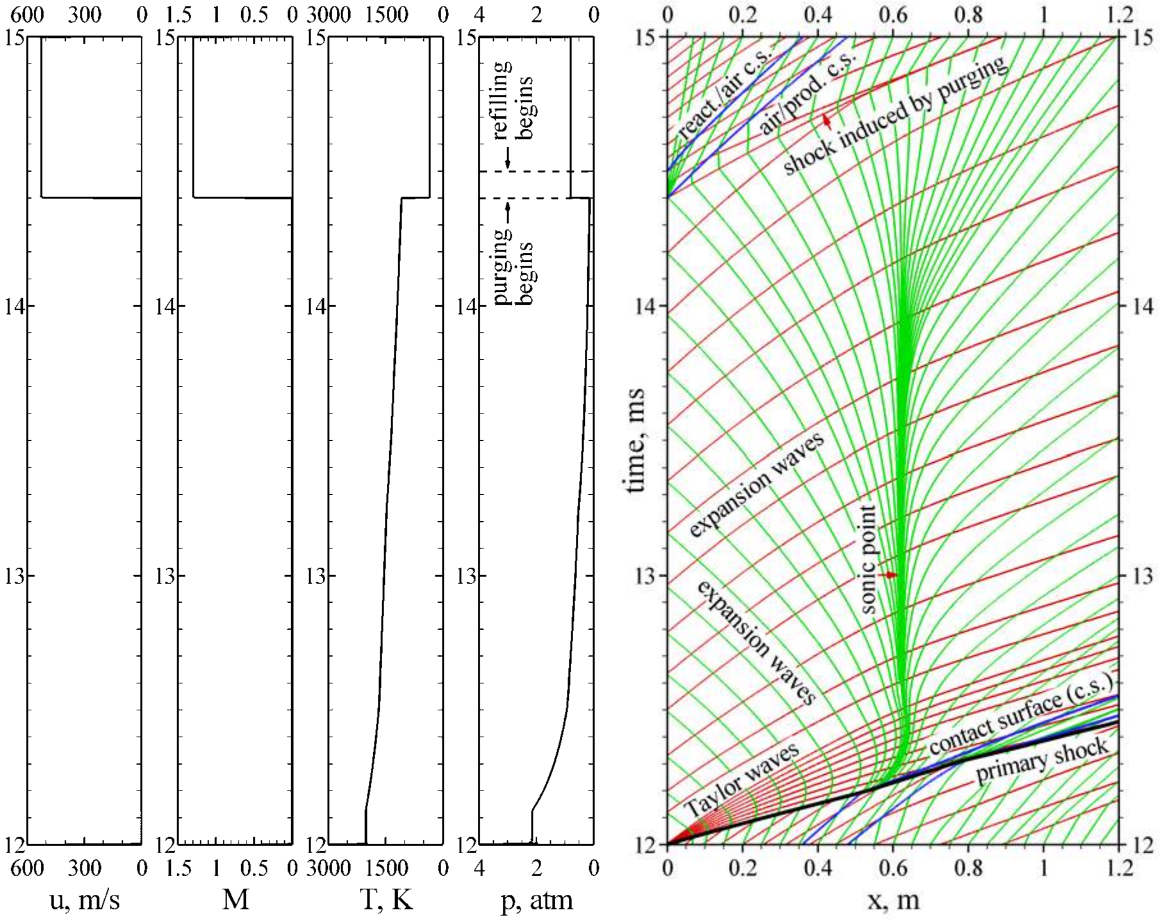

Fig. 4.8 x-t diagram for fifth cycle and time histories of flow properties at head end under typical PDE operation (stoichiometric H_2/air mixture, $\tau_{cycle} = 3$ ms, $\tau_{close} = 2.4$ ms, $\tau_{purge} = 0.1$ ms).

The impulse of each cycle is calculated by considering the momentum balance over a control volume enclosing the entire engine. The cycle-averaged specific thrust (air-based) and specific impulse (fuel-based) are then obtained by dividing the impulse by the air mass and fuel weight for each cycle, respectively. For the baseline case, the fuel-based specific impulse is 2328 s.

For comparison, the performance parameters and flow conditions of a corresponding ramjet engine with perfect nozzle flow expansion are given in Fig. 4.9, which has a specific impulse of about 3866 s. Thus, with the straight-tube configuration, the PDE performs even worse than the ramjet engine.

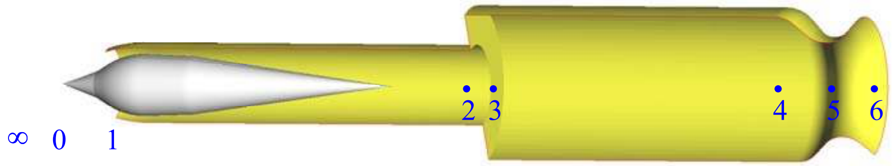

- <u>freestream conditions:</u>
  $M_\infty = 2.1$, $h = 9.3$ km
  $T_{0,\infty} = 428$ K, $p_{0,\infty} = 2.65$ atm
  $T_\infty = 228$ K, $p_\infty = 0.29$ atm
- <u>inlet exit conditions:</u>
  $M_2 = 0.29$, $\dot{m} = 1.01$ kg/s
  $T_{0,2} = 428$ K, $p_{0,2} = 2.23$ atm
  $T_2 = 422$ K, $p_2 = 2.10$ atm
- <u>combustor conditions:</u>
  $M_3 = 0.1$, $M_4 = 0.26$, $\Phi = 1.0(H_2)$
  $T_{0,4} = 2472$ K, $p_{0,4} = 2.05$ atm
  $T_4 = 2458$ K, $p_4 = 1.97$ atm
- <u>engine performance:</u>
  F = 1105 N (248 lbf)
  $I_{sp} = 3866$ s

Fig. 4.9 Performance parameters of ramjet engine for stiochiometric H_2/air mixture

A parametric study was carried out to examine the effect of various operating times on the system performance. Figure 4.10 shows the result as a function of τ_{close}. The highest specific impulse obtained is 2906 s. This is far lower than its theoretical limit of 5263 s (Wu, Ma, and Yang, 2003), which assumes isentropic flow processes in the inlet and nozzle. Although the calculated specific impulse can be improved by optimizing the operation frequency and timing, the net gain appears to be limited with the current design. Several fundamental mechanisms responsible for such an unacceptable performance have been identified. First, at high altitudes, the straight-tube design fails to preserve the chamber pressure during the refilling stage at a level sufficient to meet the requirements for the mass loading density of fresh reactants. Second, the low chamber pressure in the refilling stages causes a high-speed reactant stream in the tube, and subsequently results in a large performance loss. It is well established that the stagnation pressure drop due to energy addition is proportional to the square of the Mach number. In the present case, the local Mach number may reach a value of up to 1.2 during the refilling process. The ensuing loss of thermodynamic efficiency becomes exceedingly large compared with conventional propulsion systems with subsonic combustions. Third, the lack of an appropriate flow expansion device downstream of the detonation tube gives rise to an extremely complicated flow structure near the tube exit. The internal energy of the exhaust flow cannot be effectively converted to the kinetic energy for thrust generation, further deteriorating the situation.

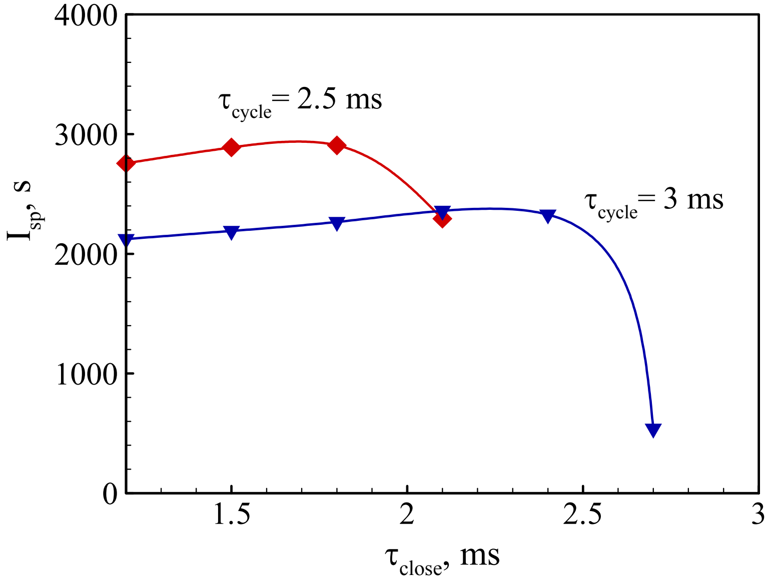

Fig. 4.10 Effect of valve close-up time on specific impulse ($\tau_{cycle} = 3$ ms, $\tau_{purge} = 0.1$ ms); straight tube with stoichiometric H_2/air mixture, h = 9.3 km, $M_\infty = 2.1$

4.6 Single-Tube PDE with CD Nozzle

In light of the limited performance of the straight-tube design, much effort was expended to study the effect of nozzle configuration on the system propulsive performance. The nozzle design for PDEs poses a serious challenge because of the intrinsically unsteady nature of the pulse detonation process. Recent studies on the nozzle effect, as been reviewed in Chapter 1, indicate that the nozzle configuration may significantly change the thrust delivered by an engine. In addition to its influence on specific impulse through modification of the gas expansion process, the nozzle affects the chamber flow dynamics and, consequently, the timing of various phases of the engine operation cycle, especially for high-altitude and space applications. The present work focuses on a choked convergent-divergent (CD) nozzle because of its effectiveness in preserving the chamber pressure during the blowdown and refilling stages. In contrast, divergent and plug nozzles do not possess such an advantage, especially under high-altitude conditions, in spite of their superior performance for a single-pulse operation at sea level.

Figure 4.11 shows schematically the computational domain. The detonation tube remains the same as in Sec. 4.5. The CD nozzle has a length of 20 cm and a throat height of 12 cm, with a 45° convergent angle and a 15° divergent angle. The computational domain is discretized into 554228 unstructured triangular grid cells, with 320000 for the detonation tube, 88080 for the nozzle, and 146168 for the external region. Figures 4.12 and 4.13, respectively, show the decomposed sub-domains and the number of cells of the sub-domains.

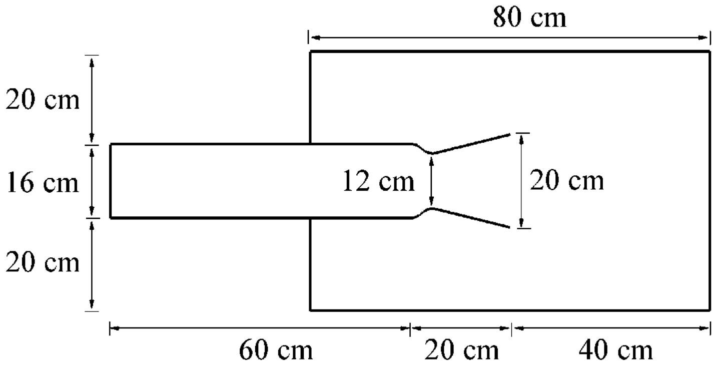

Fig. 4.11 Computational domain for single-tube PDE

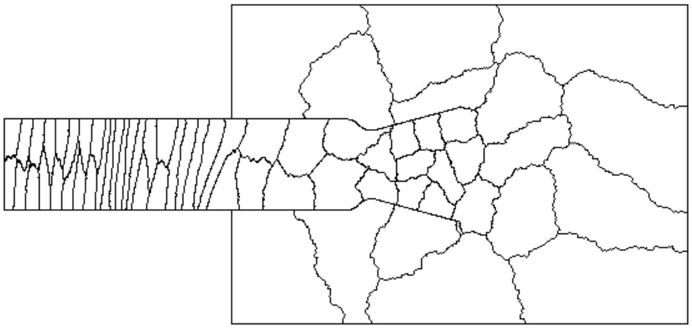

Fig. 4.12 Schematic of the computational domain decomposed into 64 sub-domains

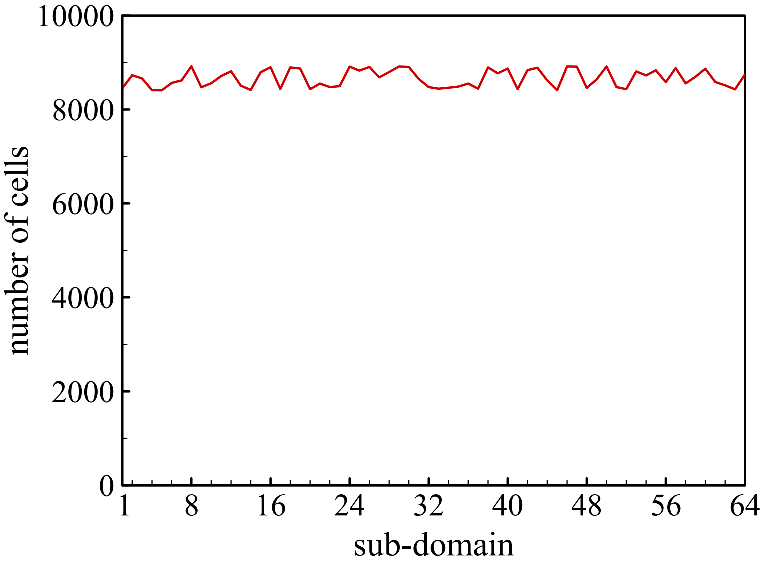

Fig. 4.13 Number of cells of sub-domains

4.6.1 Flow Evolution

A series of analyses are conducted over a wide range of operation parameters. The baseline case has an operation cycle period (τ_{cycle}) of 3 ms, a valve close-up time (τ_{close}) of 2.1 ms, and a purge time (τ_{purge}) of 0.1 ms. The ambient flow is treated as stationary. Figures 4.14 and 4.15 show the time evolution of the Mach number and density-gradient fields during the first cycle of operation, respectively. The corresponding pressure and Mach-number distributions along the centerline of the computational domain are displayed in Fig. 4.16. Figure 4.17 shows the time histories of pressure and Mach number at the midpoints of the head end, nozzle throat, and nozzle exit.

Initially, the detonation tube is filled with a stoichiometric hydrogen/air mixture at the ambient pressure and temperature. The cycle begins with the valve closed. Detonation is then initiated by the driver gas near the head end and propagates downstream toward the unburned mixture. It is immediately followed by a centered rarefaction wave known as the Taylor wave (Taylor, 1950; Fickett and Davis, 2000), which decreases the pressure and brings the flow to rest in order to satisfy the stationary condition at the head end. Between the head end and the rear of the Taylor wave is a uniform region with constant flow properties. These wave structures have also been presented in detail in Sec. 4.5 by means of a numerically obtained x-t diagram. The detonation wave speed, u_D, Mach number, M_D, and the flow properties at CJ point can be obtained analytically based on the standard CJ theory. The flow properties of the uniform region can be derived through the Riemann invariant relation and the isentropic

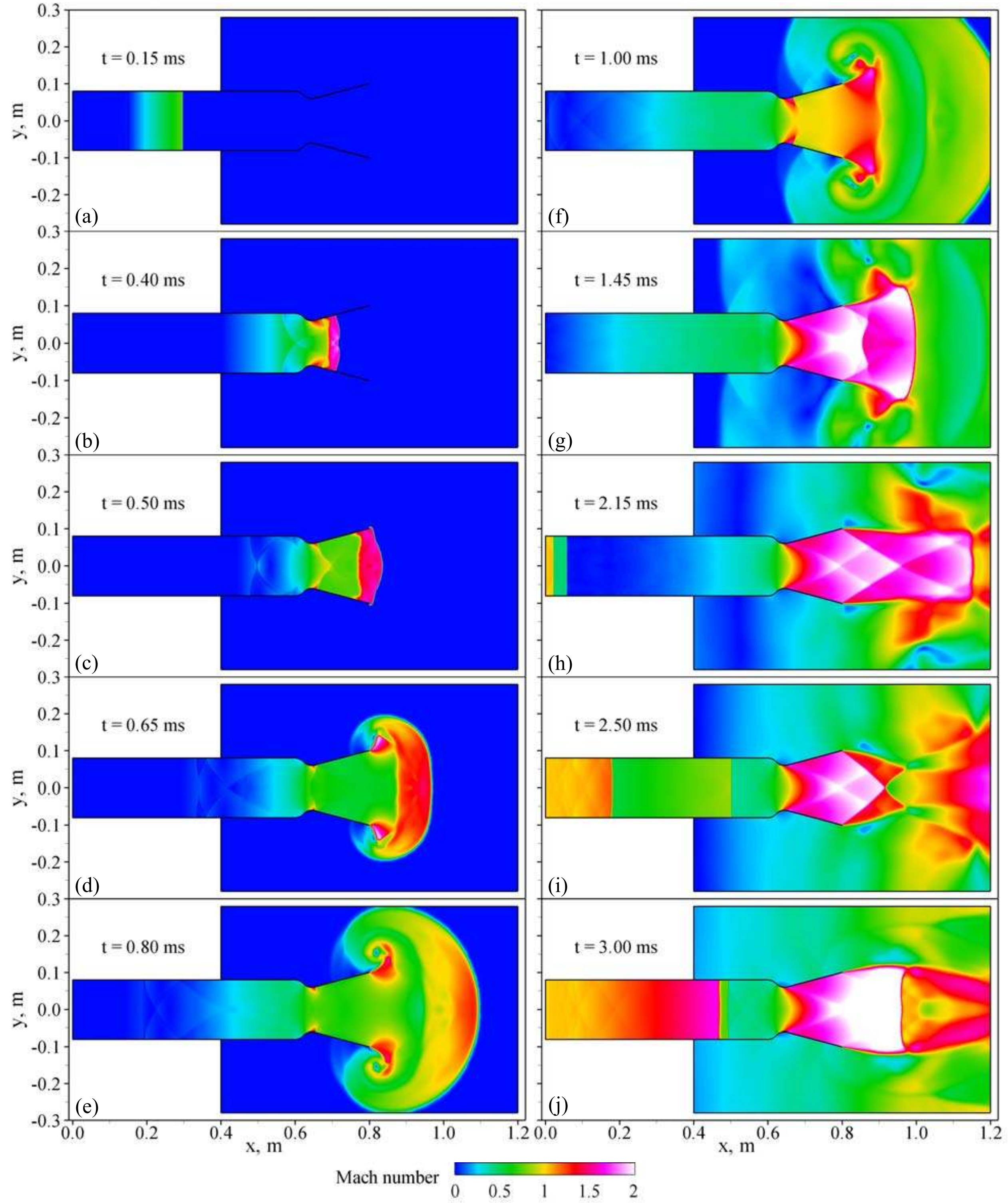

Fig. 4.14 Time evolution of Mach number field during the first cycle of operation (τ_{cycle} = 3 ms, τ_{close} = 2.1 ms)

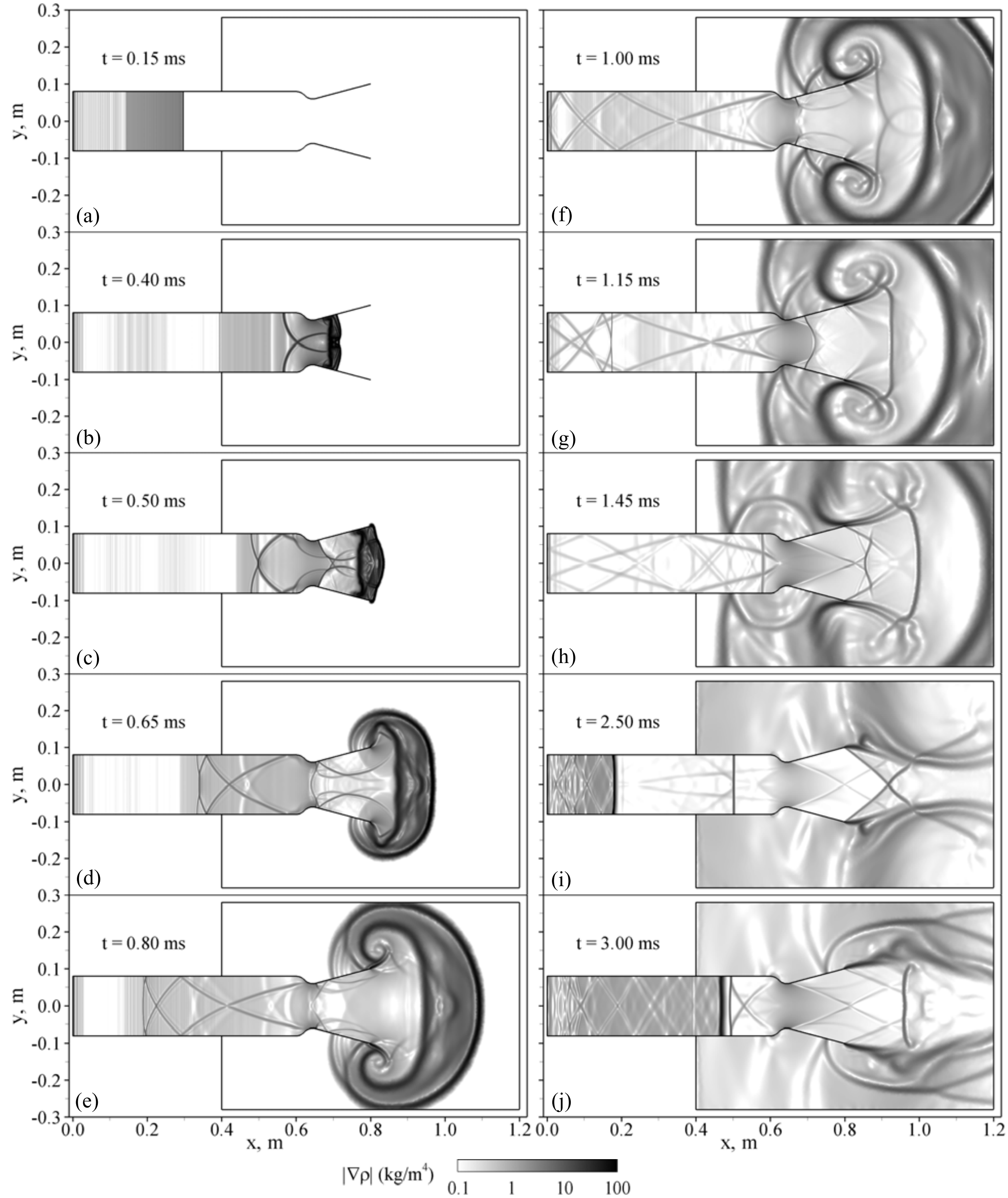

Fig. 4.15 Time evolution of density-gradient field during the first cycle of operation ($\tau_{cycle} = 3$ ms, $\tau_{close} = 2.1$ ms)

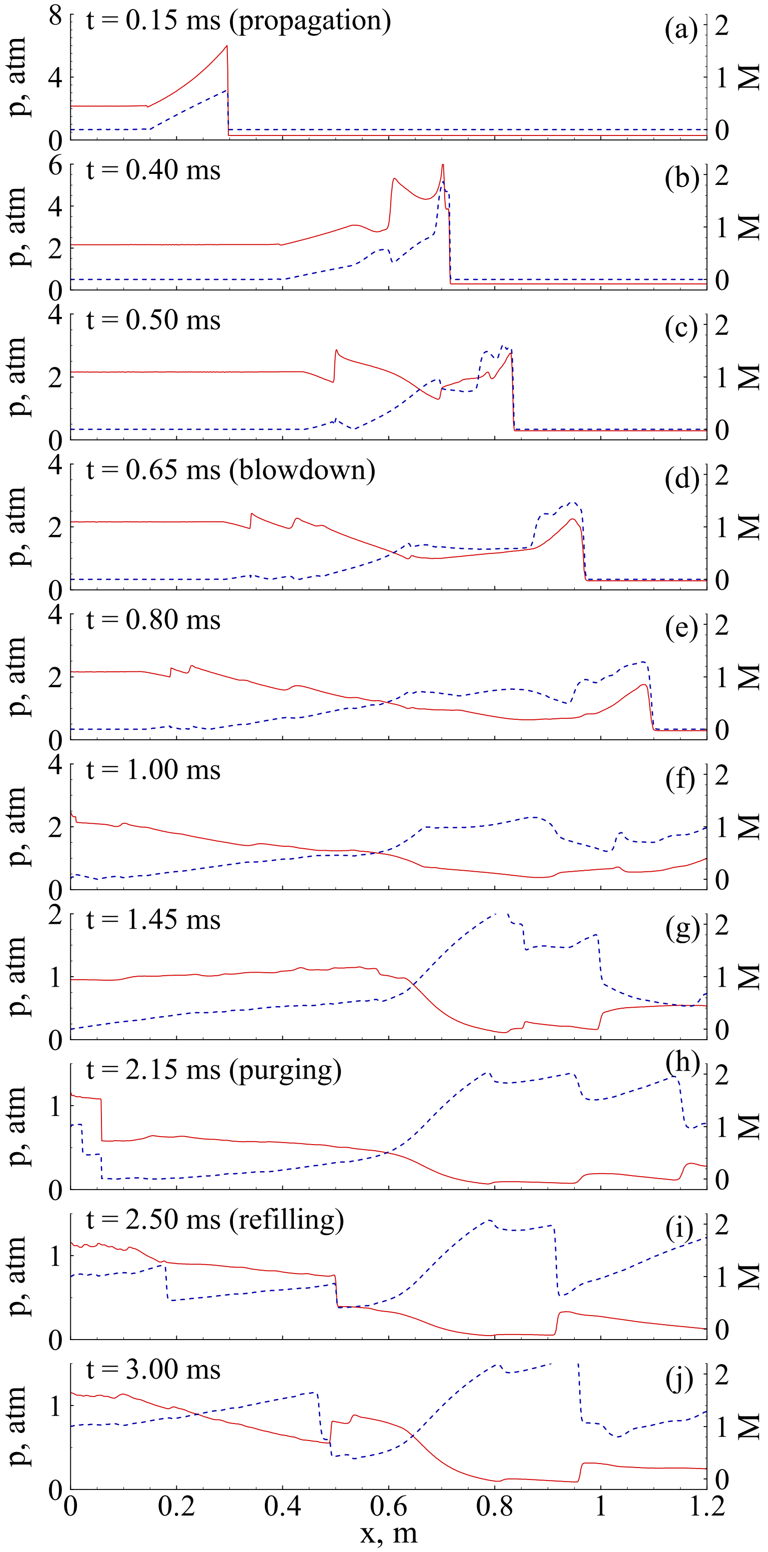

Fig. 4.16 Time evolution of pressure (—) and Mach number (---) distributions along centerline during first cycle of operation ($\tau_{cycle} = 3$ ms, $\tau_{close} = 2.1$ ms)

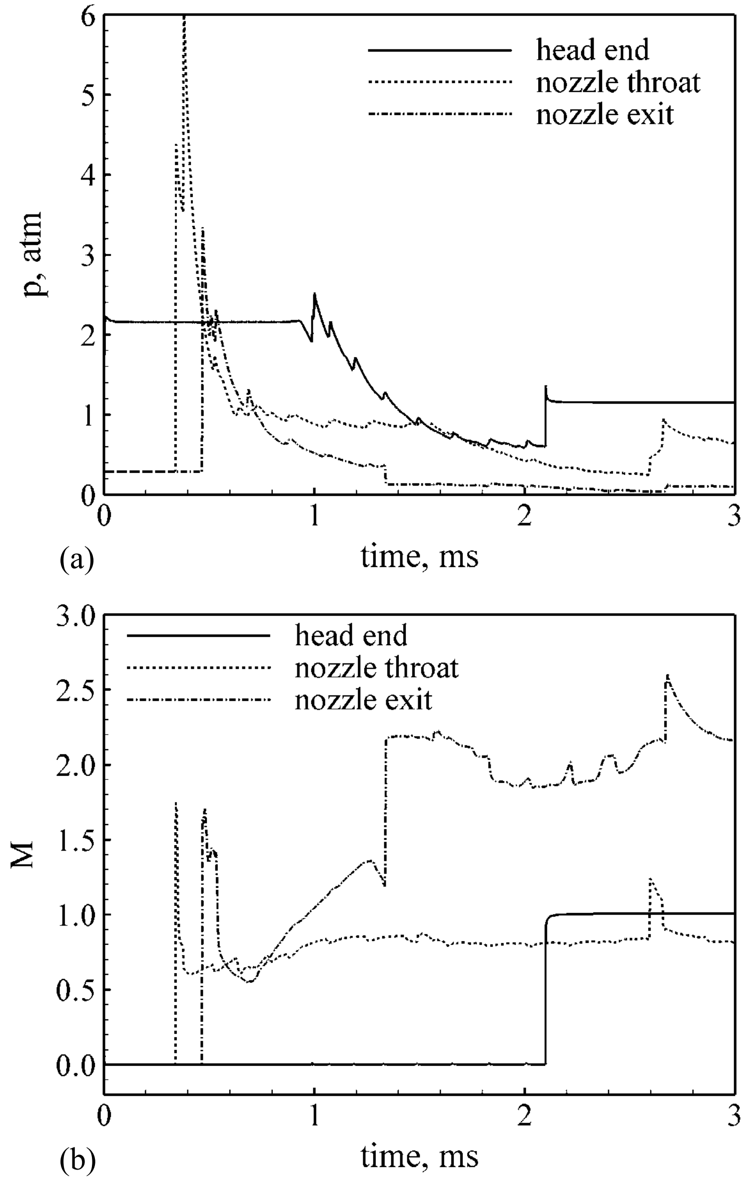

Fig. 4.17 Time histories of (a) pressure and (b) Mach number at midpoints of head end, nozzle throat, and nozzle exit during first cycle of operation ($\tau_{cycle} = 3$ ms, $\tau_{close} = 2.1$ ms)

relation from the CJ point to the uniform region (Fickett and Davis, 2000; Wintenberger et al., 2003). The resultant analytical formulations have been given in Chapter 1 and are summarized again as below.

$$M_D = \sqrt{\frac{\gamma^2 - 1}{2\gamma}\frac{q}{RT_1}} + \sqrt{\frac{\gamma^2 - 1}{2\gamma}\frac{q}{RT_1} + 1}, \quad u_D = M_D\sqrt{\gamma RT_1} \tag{4.20}$$

$$M_2 = \frac{M_D{}^2 - 1}{\gamma M_D{}^2 + 1}, \quad \frac{p_2}{p_1} = \frac{1 + \gamma M_D{}^2}{1 + \gamma}, \quad \frac{T_2}{T_1} = \left(\frac{1 + \gamma M_D{}^2}{(1 + \gamma)M_D}\right)^2 \tag{4.21}$$

$$\frac{p_3}{p_2} = \left(1 - \frac{\gamma - 1}{2}\frac{M_D{}^2 - 1}{\gamma M_D{}^2 + 1}\right)^{\frac{2\gamma}{\gamma - 1}}, \quad \frac{T_3}{T_2} = \left(1 - \frac{\gamma - 1}{2}\frac{M_D{}^2 - 1}{\gamma M_D{}^2 + 1}\right)^2 \tag{4.22}$$

Equation (4.20) yields a detonation wave Mach number of 5.94 and a detonation wave speed of 1956 m/s, which agrees well with the 1950 m/s obtained from the NASA CEA code (McBride and Gordon, 1996). The simulated flow properties at the CJ point and in the uniform region coincide with the corresponding analytical predictions (e.g., deviation of less than 0.1% for the CJ properties and 0.4% for the uniform region properties), as manifested in Table 4.1.

Table 4.1 Flow properties at the CJ point and in the uniform region
(p_1 = 0.29 atm, T_1 = 228 K, γ = 1.29, R = 368.9 J/(kg·K), $q = 2.720\times10^6$ J/kg)

	numerical	analytical
p_2, atm	5.855	5.888
T_2, K	2663	2665
M_2	0.737	0.737
P_3, atm	2.158	2.154
T_3, K	2133	2126
C_3, m/s	1007	1006

At t = 0.15 ms, the detonation wave travels to x = 29.5 cm, and the length of the uniform region becomes 15.0 cm. These two lengths deviate slightly from the following analytical predictions by about 0.6% due to the effect of the detonation initiation process.

$$x_D = u_D \times t = 1956\ \text{m/s} \times 0.15\ \text{ms} = 29.3\ \text{cm} \tag{4.23}$$

$$x_3 = c_3 \times t = 1006\ \text{m/s} \times 0.15\ \text{ms} = 15.1\ \text{cm} \tag{4.24}$$

where c_3 is the sound speed in the uniform region. Generally, the length of the uniform region is about halfway between the detonation wave front and the head end (Fickett and Davis, 2000), as demonstrated by the following relation:

$$\frac{c_3}{u_D} = \frac{\sqrt{\gamma R T_3}}{M_D \sqrt{\gamma R T_1}} = \frac{M_D{}^2 + 1}{2 M_D{}^2} \approx \frac{1}{2} \tag{4.25}$$

The detonation wave continues downstream and reaches the reactant/air interface at the tube exit at t = 0.305 ms. It then degenerates to a non-reacting shock wave (i.e., the primary shock wave) due to the lack of energy support from chemical reaction. Meanwhile, a series of expansion waves are generated and propagate upstream. The primary shock wave proceeds further downstream through the nozzle and reflects off the convergent wall. Its propagation through the nozzle throat resembles the shock diffraction over a convex curved wall (Han and Yin, 1993). At t = 0.40 ms, the primary shock wave has reached the divergent section and is curved due to effect of the expansion waves generated from the curved wall, and the two reflected shock waves have intersected with each other. Along the curved wall, the flow behind the primary shock is locally expanded to supersonic, leading to the formation of two shock waves stemming out from the wall, as can be seen clearly in the enlarged pressure field in Fig. 4.18a. On the other hand, the interaction of the upstream-traveling expansion waves with the downstream-traveling Taylor wave causes a small zero-gradient region, as evidenced by the blank region located at about x = 53 cm from head end in Fig. 4.15b and by the pressure contours in Fig. 4.18a.

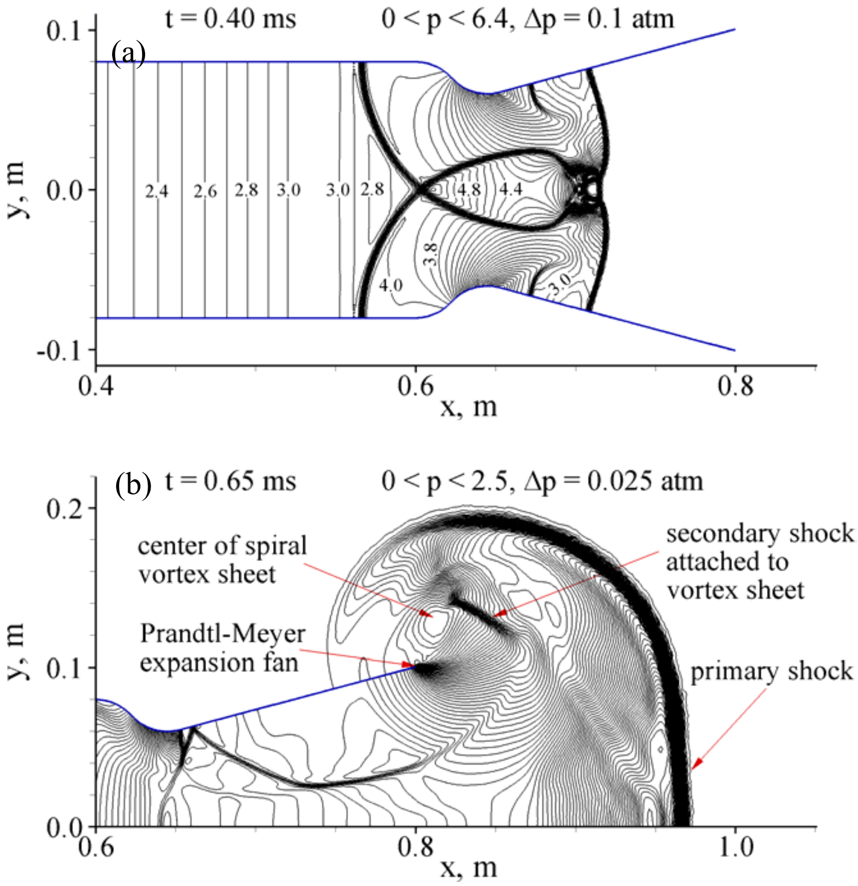

Fig. 4.18 Enlarged views of pressure contours at (a) 0.40 ms and (b) 0.65 ms

At t = 0.50 ms, the primary shock wave arrives at the nozzle exit. The pressure and temperature on the centerline immediately behind the shock wave are 2.76 atm and 527 K, respectively, corresponding to a shock wave Mach number of 2.93, which is much smaller than the original detonation wave Mach number of 5.94. Within the detonation tube, the upstream-traveling expansion waves have passed through the downstream-traveling Taylor wave so that the length of the uniform region begins to decrease. The two reflected shock waves intersect with each other, propagate further upstream, and hit and reflect off the tube walls, leading to more complicated shock wave structures.

At t = 0.65 ms, the primary shock wave has moved out of the nozzle. The shock Mach number is 2.53 at the center and reduces to about 1 near the wall due to strong flow expansion around the edge of nozzle exit. This is consistent with Skews' study (Skews, 1967) on the shock-wave diffraction over a sharp corner, in which the shock Mach number near the wall approaches to 1 for large corner angles. On the other hand, due to the velocity difference between the exhaust and the ambient flow, slip lines (or vortex sheets) are formed and roll up, as can be observed more clearly in the snapshots (e) and (f) of Fig. 4.15. At t = 0.65 ms, the center of the upper spiral vortex sheet is positioned at x = 0.811 m and y = 0.136 m, at which the flow is stationary and has a pressure of as low as 0.18 atm. More quantitative work on the vorticity production in shock diffraction was recently conducted by Sun and Takayama (2003). In the inner region near the edge, the flow accelerates from subsonic to sonic due to expansion waves emanated from the edge, and finally a Prandtl-Meyer expansion fan is formed, as evidenced in Fig. 4.18b. The expanded supersonic flow is terminated by a downstream secondary shock attached to the vortex sheet. It should be noted that although the flow structure resembles that of shock diffraction over a sharp corner (Sun and Takayama, 2003; Skews, 1967; Korobeinikov and Urtiew, 1986; Dyke, 1997), it is complicated by the flow non-uniformity resulting from detonation and contact surface. Within the detonation tube, the downstream shock waves tend to catch up with the upstream shock wave, forming a lambda-shock structure, as displayed in Fig. 4.15d. These shock waves continue upstream and finally lead to a nearly normal leading shock wave (see Fig. 4.15e).

At t = 1.00 ms, part of the primary shock wave has moved out the computational domain. The centers of the spiral vortex sheets move slowly to (0.829 m, ±0.175 m), whereas the pressure further decreases to 0.07 atm. The secondary shocks attached to the vortex sheets have jointed together. The Prandtl-Meyer expansion fans originated from the edges still exist, and the pressure at the nozzle exit plane is about 0.48 atm, higher than the ambient value of 0.29 atm, demonstrating that the nozzle flow remains underexpanded. In the vicinity of the nozzle throat, the sonic region has just grown from near the wall to the entire throat section. The curved sonic line, as evidenced in Fig. 4.14f, starts at the wall slightly upstream of the throat and crosses the nozzle centerline downstream of the throat (Hodge and Koenig, 1995). The Mach number at the midpoint of the nozzle throat is less than unity (see Fig. 4.17b). Along the centerline downstream of the sonic line, the flow is still slightly below sonic and then accelerated to supersonic near the exit plane due to the expansion waves emanated from the edge of the nozzle exit (see Fig. 4.16f). The Mach number at the midpoint of the nozzle exit plane is about 1.05. Inside the detonation tube, the upstream-traveling expansion waves and leading shock wave have reached the head end and been reflected, terminating the head-end pressure plateau that remained for 0.935 ms. The head-end pressure thus decays gradually, followed by an abrupt increase, as displayed in Fig. 4.17a. The zigzag shape of the head-end pressure history during 1 to 2 ms arises from the reflection of the subsequent upstream-traveling expansion waves and shock waves off the head-end.

As the blowdown process continues, the pressure within the tube and nozzle decays. At t = 1.45 ms, the nozzle exit pressure decreases to 0.13 atm at the midpoint and 0.21 atm at the wall, and the nozzle flow has developed to be overexpanded. Also, the Prandtl-Meyer expansion fans disappear and oblique shocks form near the edges. Within the nozzle, the flow downstream of the curved sonic line becomes supersonic, and the Mach number at the midpoint of nozzle exit is about 2.2.

The valve opens at t = 2.10 ms, and the purging process begins. The head-end pressure is about 0.6 atm prior to the valve opening, whereas the total pressure at the combustor entrance is 2.12 atm from the inlet analyses in Chapter 1. As a result of this large pressure difference, a right-running shock wave is established along with a contact surface between the burned and the purged gases, as shown in Figs. 4.14h and 4.15h. The shock wave and the contact surface are located at 0.06 m and 0.02 m from head end at this time instant, respectively. The temperature increases from 370 K to 1916 K across the contact surface, and the Mach number decreases from 1.04 to 0.46. Another contact surface forms between the fresh reactants and the purged air when the refilling process commences 0.1 ms later. The corresponding refilling pressure and velocity are 1.16 atm and 423 m/s, respectively. At t = 2.50 ms, the shock wave and the two contact surfaces travel to 0.5, 0.18, and 0.13 m, respectively. The pressure at the nozzle exit decays to 0.06 atm. The external flow structures bear a close resemblance to those of an overexpanded nozzle flow at steady-state condition (Hodge and Koenig, 1995), e.g., the oblique shocks intersect with each other and reflect off the slip lines (or shear layers) to generate expansion waves, as displayed in Fig. 4.15i. A Mach intersection (Hodge and

Koenig, 1995) of the two oblique shocks may happen as the intersection point moves upstream with a further decay of the nozzle exit pressure.

At the end of the cycle (t = 3.0 ms), the shock wave resulting from the purging process moves out of the nozzle and interacts with the existing waves, further complicating the external flowfield. The fresh reactant fills the tube up to about two-thirds. The pressure of the reactant ranges from 1.16 atm at the head end to 0.60 atm at the leading point, which is significantly higher than the ambient pressure of 0.29 atm. The velocity of the reactant ranges from 430 to 600 m/s, in contrast to the initial stationary condition.

The flow tends to reach steady cyclic condition as the cycle repeats. Figure 4.19 shows the time history of the head-end pressure during the first five cycles. Significant differences between the first and later cycles are observed. Specially, the pressure plateau during the first 0.935 ms does not appear in later cycles because of the rarefaction of waves from the previous cycle. On the other hand, because of the higher pressure of the refilled reactants, the head-end pressure immediately after detonation is higher in later cycles than in the first cycle. Figure 4.20 shows the specific impulse and the filling length of each cycle. The filling length is defined as the length at which the detonation wave catches the leading fresh reactant. Calculation of the specific impulse is given in the next subsection. The specific impulse of the second cycle is much higher than that of the first cycle due to the higher loading density of the reactant during the second cycle. The specific impulse and the filling length reach steady values of 3402 s and 47.5 cm, respectively. In this paper, the relative difference of specific impulse between two continuous cycles being less than 0.1% will be used as the quantitative criterion for reaching steady cyclic operation.

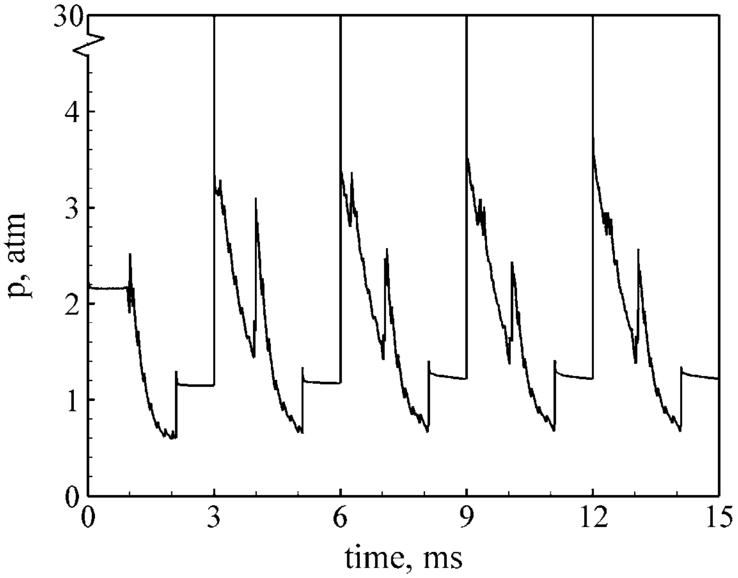

Fig. 4.19 Time history of head-end pressure during first five cycles (τ_{cycle} = 3 ms, τ_{close} = 2.1ms)

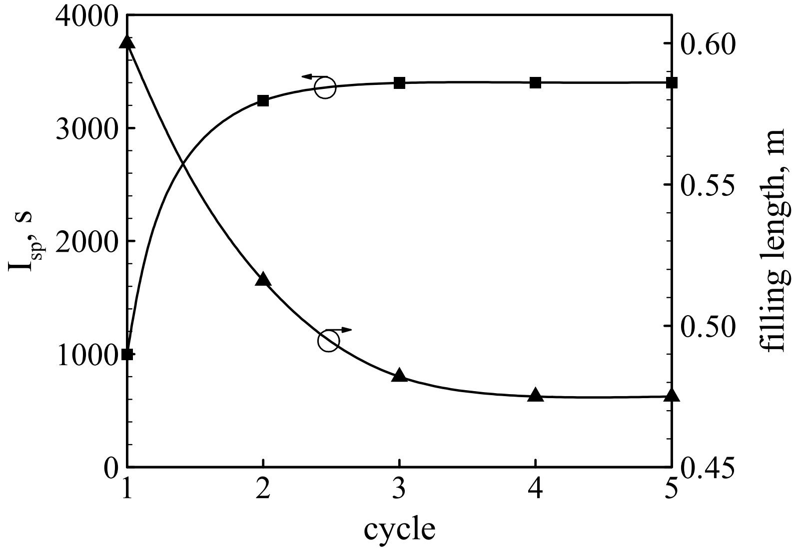

Fig. 4.20 Specific impulse and filling length of first five cycles (τ_{cycle} = 3 ms, τ_{close} = 2.1 ms)

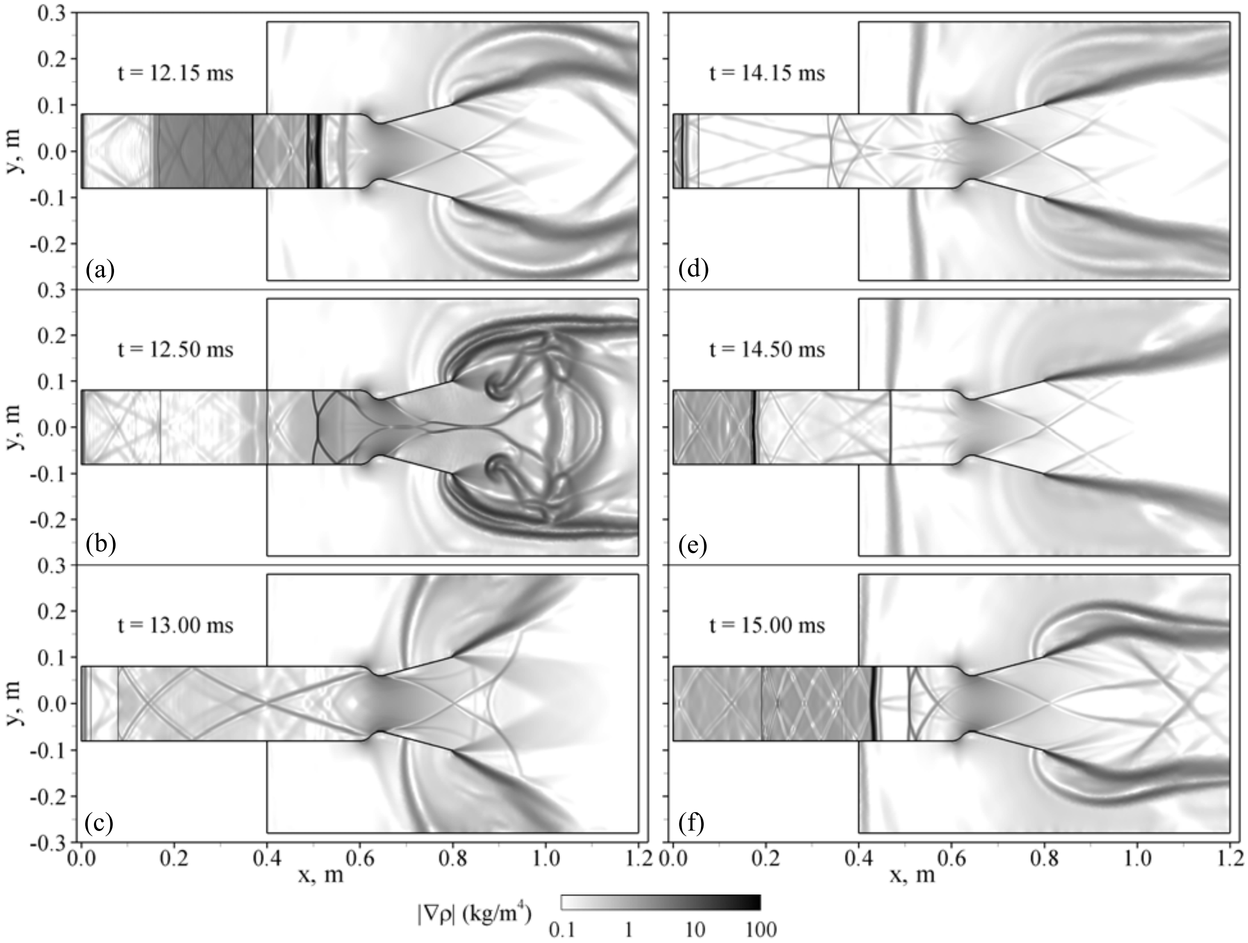

Fig. 4.21 Time evolution of density-gradient field during fifth cycle of operation ($\tau_{cycle} = 3$ ms, $\tau_{close} = 2.1$ ms)

Figure 4.21 shows the time evolution of the density-gradient field during the fifth cycle, at which the steady cyclic operation is reached. Although the time sequence is the same as that of the first cycle, quite different flow patterns are obtained due to the effect of flow non-uniformity arising from the previous cycle. The reactant has already had a speed of about 500 m/s before being burned, the detonation wave thus propagates faster to the tube exit, e.g., the detonation wave front travels 36.8 cm at t = 12.15 ms in contrast to 29.5 cm in the first cycle. In the external region, the pressure level is lower because the flow remains overexpanded during a large amount of the cycle period. From the time history of the pressure at the midpoint of the nozzle exit shown in Fig. 4.22, the flow is overexpanded from 12.0 through 12.3 ms and from 12.9 through 15.0 ms, in contrast to about 1.6 ms of overexpansion during the first cycle. The Mach number at the midpoint of the nozzle exit remains supersonic throughout the whole cycle. From the time evolution of the Mach-number field (not shown), the nozzle is choked during most of the cycle period, thus helping preserve the chamber pressure. The results presented here suggest again that the PDE analysis should be based on multicycle operations.

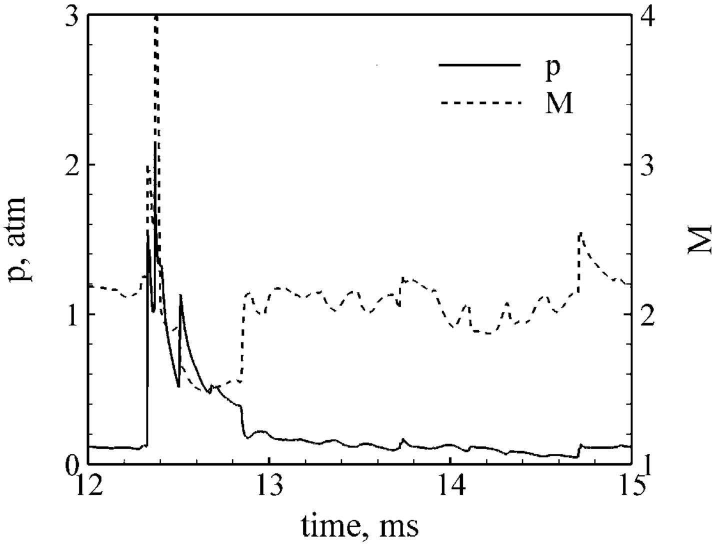

Fig. 4.22 Time histories of pressure and Mach number at midpoint of nozzle exit during fifth cycle of operation ($\tau_{\text{cycle}} = 3$ ms, $\tau_{\text{close}} = 2.1$ms)

4.6.1.1 Effect of Ambient Flow

In the above simulation case, the ambient flow is neglected, i.e., the external flowfield is initially stationary and a non-reflection boundary condition is used. In a real flight condition, however, the ambient flow is not stationary and will interact with the exhaust flow. To consider its effect, a supersonic inflow with a velocity of 636 m/s is applied at the left boundary of the external region (see Fig. 4.11). Figure 4.23 shows the density-gradient field at t = 14.5 ms, which can be compared with Fig. 4.21e for the baseline case. A close-up view of the Mach number contours is shown in Fig. 4.24. In spite of the drastic change of the flow structure in the external region, the flowfield within the detonation tube and nozzle remains nearly the same. This is attributed to the fact that the flow at the nozzle exit plane is supersonic during the whole cycle, and thus the ambient flow effect cannot propagate into the chamber to affect the geodynamics therein. As a result, the specific thrust and specific impulse are unchanged. On the other hand, since the ambient flow modifies the external flowfield, it thus affects the engine drag, which is beyond the scope of this paper. The ambient flow will be treated as stationary for all the other simulation cases.

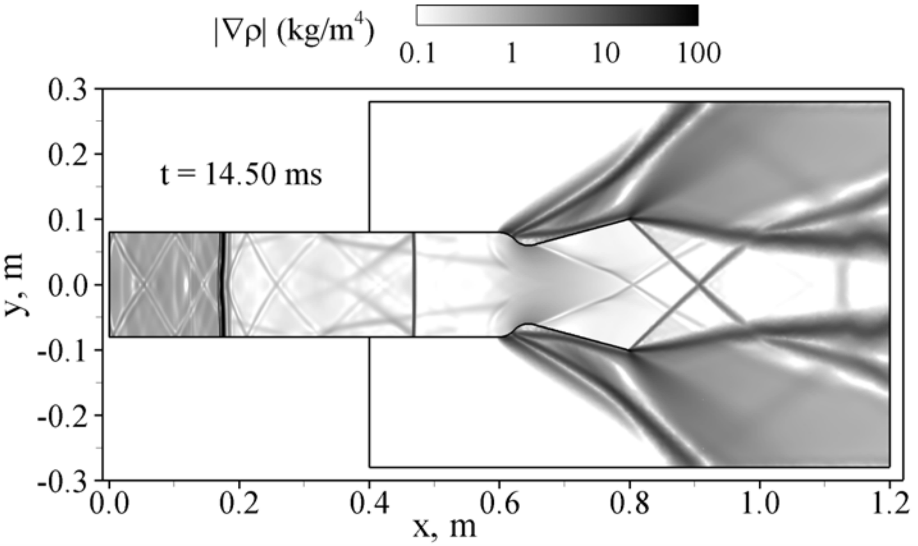

Fig. 4.23 Density-gradient field at t = 14.5 ms, with ambient flow, τ_{cycle} = 3 ms, τ_{close} = 2.1 ms

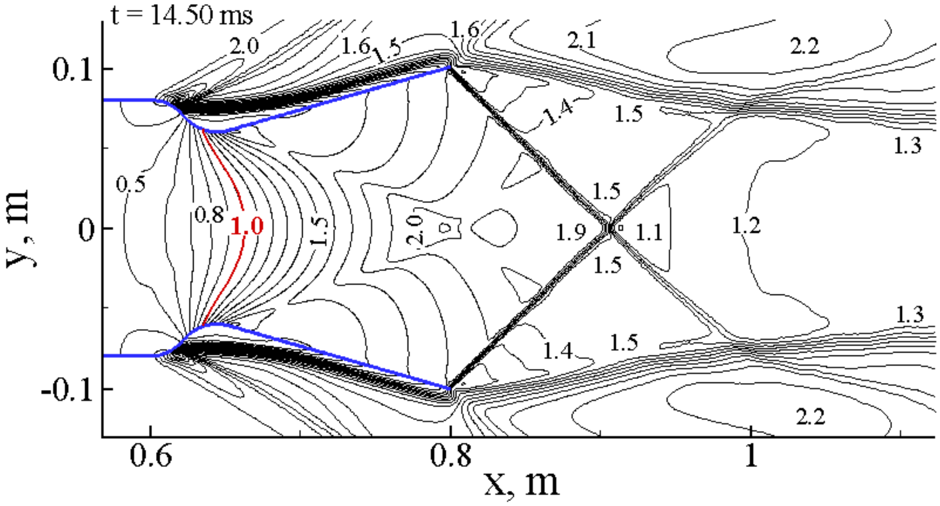

Fig. 4.24 Close-up view of Mach-number contours at t = 14.50 ms, with ambient flow

4.6.2 Propulsive Performance

Figure 4.25 shows the instantaneous axial thrust calculated with Eq. (4.10) by neglecting the last term (i.e., the time-derivative term) during the first five cycles. Initially, the thrust is negative, i.e., −636 N, since the fluid at the engine exit plane is stationary. The exit flow starts at t = 0.47 ms when the primary shock wave moves out of the nozzle, leading to a sudden jump in thrust. This kind of peak exists in each cycle. During the later part of the blowdown stage, the thrust becomes negative due to the low pressure and density at the exit plane. The thrust changes from negative to positive again when the shock resulting from the purging process reaches the exit plane. During a steady periodic cycle, e.g., the fifth cycle, the time duration of negative thrust is about 0.7 ms, that is, from 14.0 to 14.7 ms. With Eqs. (4.12)-(4.14), the cycle-averaged thrust obtained is 862 N, and the specific thrust and specific impulse are 862 m/s and 3402 s, respectively. This specific impulse is much higher than that achieved with only a straight tube. It is noteworthy that the CD nozzle significantly increases the performance because of its effectiveness in preserving the chamber pressure during the blowdown and refilling stages, rather than by thrust generation on the nozzle wall itself. The impulse generated on the nozzle wall can be obtained either by integrating the overpressure force on the wall or by applying momentum balance between the entrance and exit planes of the nozzle. Both are shown in Fig. 4.26. Although they don't coincide with each other at every time instant, the cumulate impulses generated over the fifth cycle are exactly the same, i.e., −0.716 N·s, which provides an essential validation check on the present performance calculations. The negative impulse of nozzle has also been reported by Yungster (2003) for divergent nozzles.

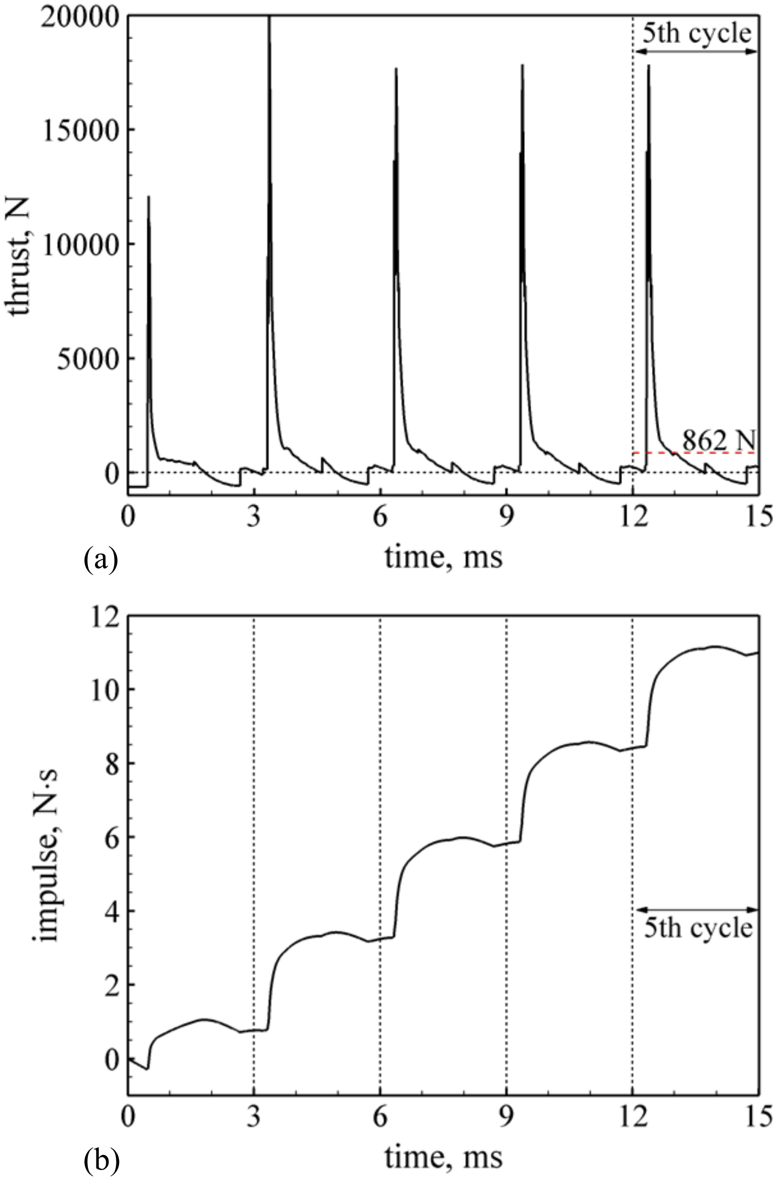

Fig. 4.25 Instantaneous thrust and impulse during first five cycles (τ_{cycle} = 3 ms, τ_{close} = 2.1 ms)

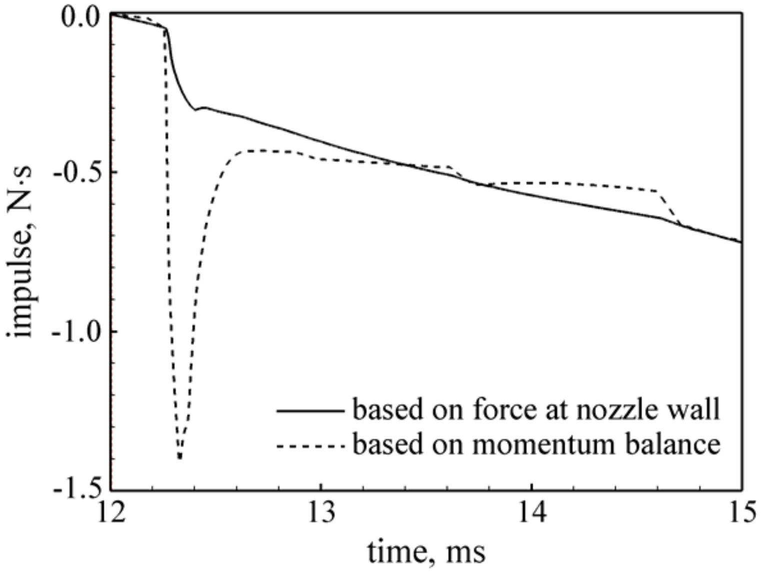

Fig. 4.26 Instantaneous impulse of nozzle during fifth cycle ($\tau_{cycle} = 3$ ms, $\tau_{close} = 2.1$ ms)

4.6.3 Analytical Prediction of Propulsive Performance

Although the CD nozzle increases the propulsive performance significantly, the specific impulse of 3402 s for the baseline case is still below its ramjet counterpart of 3866 s with perfect nozzle flow expansion. It is desirable to develop simple analytical models that can be used to rapidly and reliably predict the PDE performance and to directly compare with the numerical simulation results.

Several analytical models have been proposed in the past and are summarized in Chapter 1. Based on how the impulse is obtained, these models fall into two classes. One employs unsteady gasdynamic analysis to determine the instantaneous pressures and forces acting on the thrust wall and calculate the impulse as the integration of them (Nicholls et al., 1957; Wintenberger et al., 2003). The other obtains the engine impulse by deriving the flow properties at the exit plane (Wu, Ma, and Yang, 2003; Heiser and Pratt, 2002; Talley and Coy, 2002). The analytical model presented here follows the approach of Heiser and Pratt (2002), but takes into account the effects of the refilling velocity and the purging process to provides a more accurate prediction. Figure 4.27 schematically shows the flow path for the analysis. Note that the subscripts ∞, 1, 2, and e represent the states of the freestream, unburned gas, CJ point, and exit plane, respectively. The procedure is detailed as below.

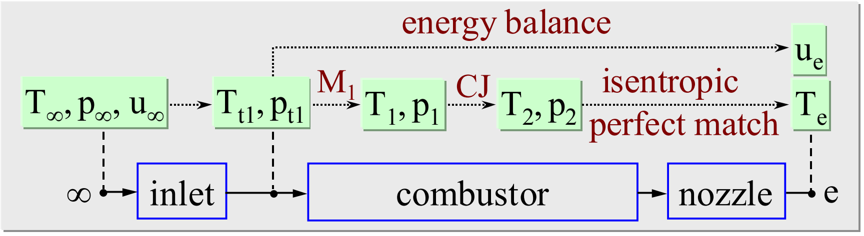

Fig. 4.27 Schematic of flow-path analysis for PDE performance prediction

i. Determine the total temperature T_{t1} and total pressure p_{t1} at the entrance of the combustor from the inlet flow analysis.

ii. Obtain the reactant temperature T_1 and pressure p_1 by assuming a refilling Mach number M_1.

iii. Calculate the CJ temperature T_2 and pressure p_2 using Eqs. (4.20) and (4.21).

iv. Calculate the exit temperature by assuming an isentropic flow expansion from the CJ state to the exit plane with a perfect pressure match:

$$T_e = T_2 (p_\infty / p_2)^{\frac{\gamma-1}{\gamma}} \tag{4.26}$$

v. Deduce the exit velocity by applying the energy balance from the combustor entrance to the engine exit plane:

$$u_e = \sqrt{2\left[q - c_p(T_e - T_{t1})\right]} \tag{4.27}$$

vi. Obtain the specific thrust and specific impulse:

$$F_{sp} = (1+f)u_e - u_\infty, \quad I_{sp} = F_{sp}/(fg) \tag{4.28}$$

If the purging process is further incorporated, the exit temperature can be recalculated based on the following average:

$$T_e = (T_{e1} \cdot \tau_{\text{purge}} + T_{e2} \cdot \tau_{\text{refill}}) / \tau_{\text{open}} \tag{4.29}$$

where T_{e1} and T_{e2} are the temperatures obtained by assuming isentropic flow expansion from the purged-gas state (T_1, p_1) and the CJ state (T_2, p_2) to the exit plane with perfect pressure match, respectively.

$$T_{e1} = T_1(p_\infty / p_1)^{\frac{\gamma-1}{\gamma}}, \;\; T_{e2} = T_2(p_\infty / p_2)^{\frac{\gamma-1}{\gamma}} \tag{4.30}$$

Also, f and q need to be replaced by the overall fuel-to-air mass ratio $\overline{f}$ and the heat addition per unit mass of the mixture of the reactants and purged gas $\overline{q}$, respectively.

$$\overline{f} = f \cdot \tau_{\text{refill}} / \tau_{\text{open}} = f(1-\beta) \tag{4.31}$$

$$\overline{q} = q \cdot \tau_{\text{refill}} / \tau_{\text{open}} = q(1-\beta) \tag{4.32}$$

where β is defined as

$$\beta = \tau_{\text{purge}} / \tau_{\text{open}} \tag{4.33}$$

The specific thrust and specific impulse then become

$$F_{sp} = (1+\overline{f})u_e - u_\infty, \quad I_{sp} = F_{sp}/(\overline{f}g) \tag{4.34}$$

Based on the above analysis, the specific thrust and specific impulse are functions of γ, R, q, f, p_∞, T_{t1}, p_{t1}, M_1, and β. If the current system is to be considered, the first seven parameters are fixed values, that is, $\gamma = 1.290$, $R = 368.9$ J/(kg·K), $q = 2.720\times10^6$ J/kg, $f = 0.0292$ (for stoichiometric H2/air reactants), $p_\infty = 0.29$ atm, $T_{t1} = 428$ K, and $p_{t1} = 2.12$ atm, and M_1 and β are two free parameters. The effects of these two parameters are then considered.

Table 4.2 lists the predicted PDE performance under various M_1 and β. The result from the baseline numerical simulation case, which has an average refilling Mach number of 0.93 and β of 1/9, is also listed for comparison. The first condition represents an ideal one which has zero refilling velocity and no purging process, and has an I_{sp} of 4360 s. Both the specific thrust and specific impulse decrease as M_1 increases. This can be directly explained from the aforementioned analytical formulas. As M_1 increases, T_1 decreases, leading to an increase in M_D, as given by Eq. (4.20). The combination of Eqs. (4.21), (4.26), and (4.27) indicates that T_e increases and u_e decreases as M_D increases. Thus, F_{sp} and I_{sp} decrease. The decrease in performance with the increase of M_1 can also be explained from the entropy point of view, since the entropy rise across the detonation wave is expressed as

$$\begin{aligned}\Delta s = s_2 - s_1 &= c_p \ln\frac{T_2}{T_1} - R\ln\frac{p_2}{p_1}\\ &= c_p \ln\left[\frac{1+\gamma M_D{}^2}{(1+\gamma)M_D{}^2}\left(\frac{1+\gamma M_D{}^2}{1+\gamma}\right)^{\frac{1}{\gamma}}\right] \approx c_p \ln\left[\left(\frac{\gamma}{\gamma+1}\right)^{\frac{\gamma+1}{\gamma}} M_D{}^{\frac{2}{\gamma}}\right]\end{aligned} \tag{4.35}$$

the increase in M_1 leads to increase in M_D and Δs, thus degrading the performance.

Table 4.2 Analytically predicted PDE propulsive performance under various refilling Mach numbers and purge-to-open time ratios

Condition ($p_{t1} = 2.12$ atm, $T_{t1} = 428$ K)	F_{sp}, m/s	I_{sp}, s
(1) $M_1 = 0, \beta = \tau_{\text{purge}}/\tau_{\text{open}} = 0$	1246	4360
(2) $M_1 = 0.93, \beta = 0$	1167	4084
(3) $M_1 = 0, \beta = 1/9$	1150	4527
(4) $M_1 = 0.93, \beta = 1/9$	1075	4235
baseline numerical simulation case	862	3402

Comparison between the first and third conditions of Table 4.2 indicates that F_{sp} decreases and I_{sp} increases with β. The effect of β is quite similar to the partial filling effect for single-pulse operation (Cooper and Shepherd, 2002; Li and Kailasanath, 2002). A larger β translates to a larger air-to-fuel mass ratio. The heat released from combustion thus needs to increase the kinetic energy of more extra air, leading to a decrease in exit velocity. The specific thrust thus decreases. On the other hand, the overall fuel-to-air mass ratio $\bar{f}$, defined by Eq. (4.31), decreases faster than the specific thrust, leading to a increase in specific thrust. The effect of β can be seen more clearly through the Taylor series expansion of F_{sp} and I_{sp} with respect to β.

$$F_{sp} = (1+\bar{f})u_e - u_\infty \approx F_{sp}^0(1 - A\beta) \tag{4.36}$$

$$I_{sp} = F_{sp}/(\bar{f}g) \approx I_{sp}^0[1 + (1-A)\beta] \tag{4.37}$$

where

$$A = \frac{1}{2} \cdot \frac{1 - c_p(T_e^0 - T_{e1})/q}{1 - c_p(T_e^0 - T_{t1})/q} \cdot \frac{u_e^0}{u_e^0 - u_\infty} \tag{4.38}$$

and F_{sp}^0, I_{sp}^0, T_e^0, and u_e^0 denote the specific thrust, specific impulse, exit temperature, and exit velocity at zero purge time, respectively. For the current system, $A \approx 0.7$. Therefore, F_{sp} decreases and I_{sp} increases with β, and since $(1-A)\beta > A\beta$, the relative increase in I_{sp} is less than the relative decrease in F_{sp}. From Table 4.2, when β increases from 0 to 1/9, F_{sp} decreases by 7.7% and I_{sp} increases by 3.8%, which agrees well with the predictions from Eqs. (4.36) and (4.37).

4.6.4 Loss Mechanisms

In addition to the losses in the inlet and manifold mentioned in Chapter 2, there are several losses in the combustor and nozzle of a PDE, including the viscous damping, the loss due to heat transfer to the wall, the loss due to refilling velocity, nozzle expansion loss, flow divergence loss, and internal flow loss. The viscous damping and heat transfer losses will not be considered in the current study. The loss due to refilling velocity has been discussed in Sec. 4.6.3. As the refilling Mach number M_1 increases from 0 to 0.93, the specific impulse decreases by 6.5% from 4527 s to 4235 s, as shown in Table 4.2. The performance discrepancy (about 25%) between the baseline numerical simulation case and the fourth condition given in Table 4.2 is attributed to 1) nozzle expansion loss or pressure-mismatch loss, 2) flow divergence loss, and 3) internal flow loss. These three loss mechanisms are discussed in the following paragraphs.

In conventional steady engines, the nozzle configuration is optimized such that the exit pressure matches with the ambient pressure. This condition, however, does not exist for PDEs due to their unsteady operations. The resultant performance loss, referred to as the nozzle expansion loss, can be estimated through a post-processing analysis. This post-process allows the recorded exhaust flow to be compressed or expanded isentropically to match the ambient pressure and calculates the corresponding ideal specific impulse. For the baseline case, this ideal specific impulse is 3604 s, and the nozzle expansion loss is thus about 6.0%. Figure 4.28 shows the temporal variations of momentum impulse and pressure impulse during a steady periodic cycle for the baseline case. Although the pressure impulse is much smaller than the momentum impulse, it is not zero. As mentioned in Sec. 4.6.1, the nozzle is overexpanded from 12.0 through 12.3 ms and from 12.9 through 15.0 ms, and is underexpanded otherwise. At the end of the cycle, the momentum impulse and pressure impulse are 2.72 and –0.135 N·s, respectively, demonstrating an overall effect of overexpansion of the nozzle flow.

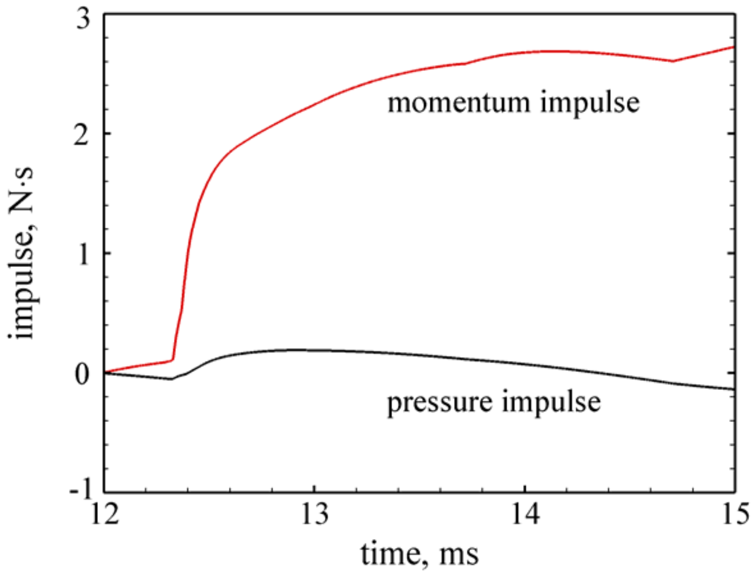

Fig. 4.28 Instantaneous impulse during steady cycle ($\tau_{cycle} = 3$ ms, $\tau_{close} = 2.1$ ms)

The flow divergence loss results from the exhaust velocity vector angularity (Berton, 1991; Mattingly, 1996), and is generally characterized by a nozzle divergence coefficient defined as the ratio of actual axial exhaust momentum to that from an ideal nozzle where all of the exhaust flow is axial. For the current PDE system, the nozzle divergence coefficient can be expressed by

$$\eta_d = \frac{\langle \dot{m}_e u_e \rangle}{\langle \dot{m}_e \tilde{u}_e \rangle} \tag{4.39}$$

where u_e and $\tilde{u}_e$ are defined as

$$u_e = \frac{1}{\dot{m}_e} \int_{S_e} \rho \mathbf{u} \cdot \mathbf{n} u dS \tag{4.40}$$

$$\tilde{u}_e = \frac{1}{\dot{m}_e} \int_{S_e} \rho \mathbf{u} \cdot \mathbf{n} \sqrt{u^2 + v^2} dS \tag{4.41}$$

Equation (4.39) gives rise to a value of 98.7% for the baseline case, which is slightly lower than the analytical value for a steady two-dimensional nozzle flow with a divergence angle of θ =15°:

$$\eta_d = \frac{\sin\theta}{\theta} = 98.9\% \tag{4.42}$$

This means that the flow divergence loss in PDEs is about the same as that in conventional steady engines. The nozzle divergence coefficient directly relates to the loss in gross thrust. The loss in thrust due to flow divergence can be readily obtained after taking into account the freestream momentum,

$$\varepsilon_d = 1 - \frac{\langle \dot{m}_e u_e \rangle - \dot{m}_a u_\infty}{\langle \dot{m}_e \tilde{u}_e \rangle - \dot{m}_a u_\infty} \tag{4.43}$$

which leads to a value of 2.0% for the baseline case.

The internal flow loss is mainly attributed to the shock waves and their interactions within the internal flowfield. In the analytical performance prediction, the flow is assumed to experience an isentropic expansion from the CJ state to the exit plane. However, there exist complicated shock waves within the internal flowfield as described in Sec. 4.6.1. The associated entropy increase and total pressure drop lead to a performance loss. It is formidable to estimate the internal flow loss directly from the flowfield. Nevertheless, since the sum of the nozzle expansion loss, the flow divergence loss, and the internal flow loss is 24.5%, i.e., the deviation of the simulated performance from the analytical prediction (condition 4 in Table 4.2), an internal flow loss of 16.5% can thus be obtained for the baseline case. This large internal flow loss is unique for PDEs and is one of the major disadvantages that degrade the PDE performance. The quantitative values of the various losses discussed above are summarized in Table 4.3 for the baseline case.

Table 4.3 Loss summary for baseline case

loss mechanism	loss in specific impulse [a]
loss due to refilling velocity	8.5%
nozzle expansion loss	6.0%
flow divergence loss	2.0%
internal flow loss	16.5%
total	33%

[a] relative loss based on the baseline numerical result of 3402 s

4.6.5 Effect of Valve Timing

Parametric studies are conducted to investigate the timing effect on the propulsive performance by varying the cycle time τ_{cycle}, valve close-up time τ_{close}, and purge time τ_{purge}. Figure 4.29 shows the effect of τ_{close} on the specific thrust F_{sp} and the specific impulse I_{sp} for three different τ_{cycle}: 2.5, 3 and 4 ms, corresponding to operation frequencies of 400, 333, and 250 Hz, respectively. The purge time τ_{purge} is fixed at 0.1 ms. Similar studies have been conducted in Chapter 3 based on quasi-one-dimensional simulations. When the straight-tube design is compared at the same operating condition, the present system with a choked CD nozzle can indeed substantially improve the engine performance by a margin of 25%.

For each frequency considered herein, the specific thrust increases as τ_{close} decreases. This can be explained as below. For a given τ_{cycle} and τ_{purge}, a smaller τ_{close} brings the following four positive effects. First, the blowdown process is shorter, and the resultant higher chamber pressure during the refilling stage increases the loading density of fresh reactant. Second, the increased refilling period enhances the amount of reactant delivered to the chamber, thus increasing the chamber pressure. Third, the duration of negative thrust is shorter. It has been pointed out in Sec. 4.6.3 that negative thrust may appear at the later part of the blowdown process due to the low-energy level of the gases in the combustor. Figure 4.30 shows the instantaneous thrust and impulse during a steady cycle for three cases with different τ_{close}. The solid line represents the baseline case. When τ_{close} decreases from 2.4 to 1.8 ms, the time duration of negative thrust decreases

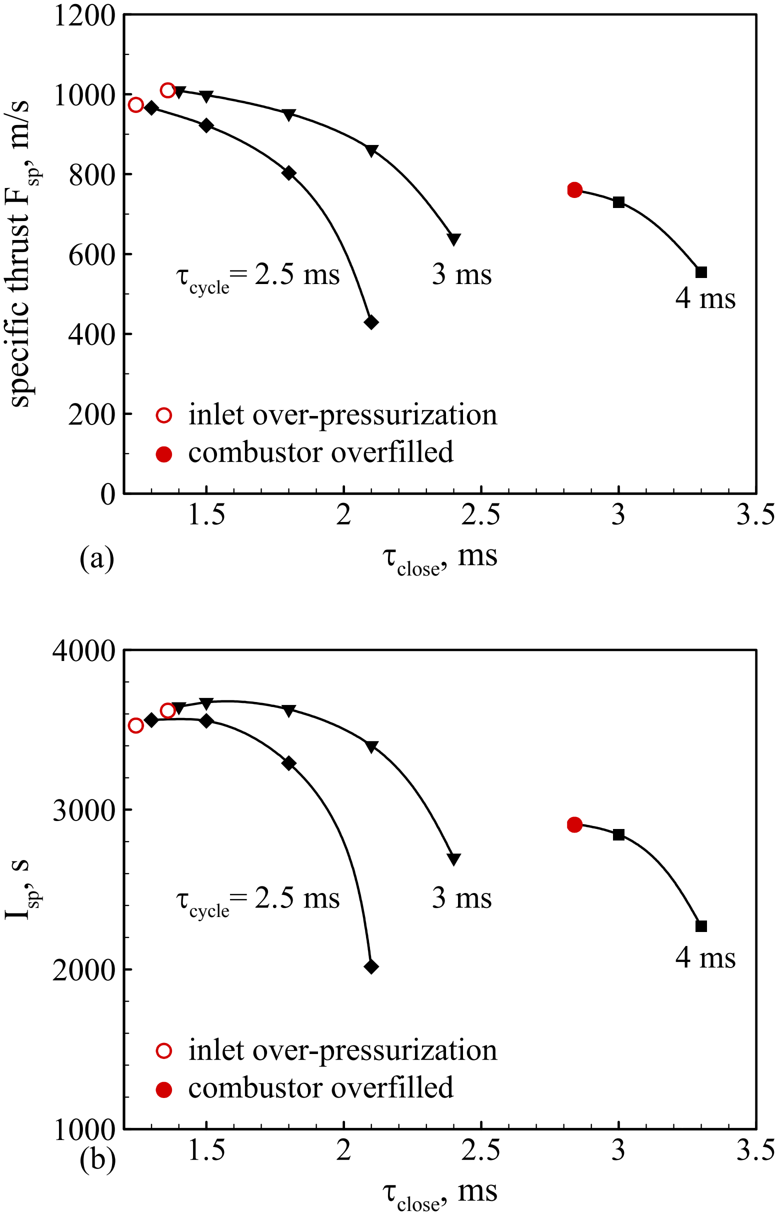

Fig. 4.29 Effect of valve closed time on (a) air-based specific thrust and (b) fuel-based specific impulse at three different operation frequencies; τ_{purge} = 0.1 ms, stoichiometric H_2/air mixture, h = 9.3 km, M_∞ = 2.1.

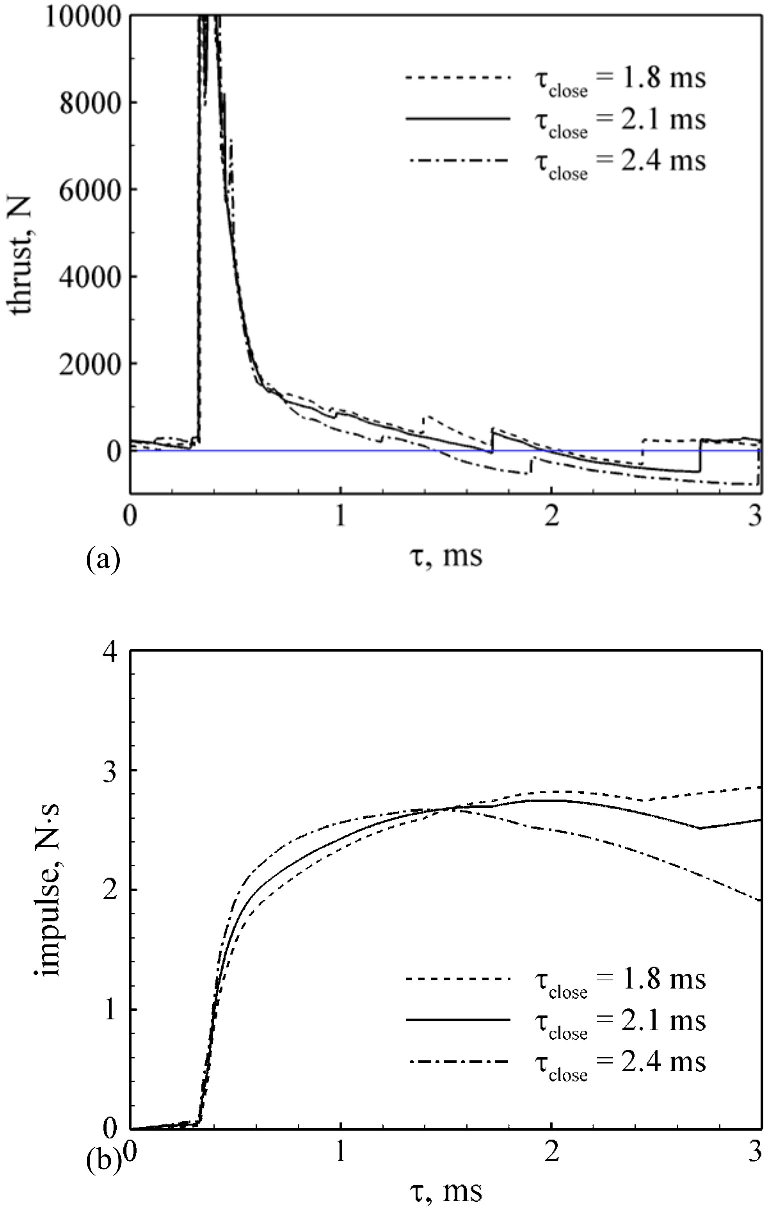

Fig. 4.30 Instantaneous thrust and impulse during a steady cycle, τ_{cycle} = 3 ms, τ_{purge} = 0.1 ms.

from about 1.5 ms to 0.4 ms. Finally, the internal flow loss decreases. For a smaller τ_{close}, the head-end pressure is higher as the valve opens. Correspondingly, the shock resulting from the pressure difference across the valve is weaker. In addition, the reactant temperature T_1 increases, leading to a weaker detonation wave, i.e., the detonation wave number M_D calculated with Eq. (4.20) is smaller. Since the internal flow loss is mainly associated with the shock interactions within the flowfield, it thus decreases as the shock waves weaken. These combined effects make F_{sp} decrease rapidly as τ_{close} increases.

It should be noted, however, the lower bound of τ_{close} is subject to three practical constraints, as mentioned in Chapter 3. The first is concerned with the inlet over-pressurization. The head-end pressure must not exceed the total pressure of the inlet air to allow for purging and refilling when the valve is open. Otherwise, reverse flow may occur and cause engine unstart. This kind of lower bound is denoted by the open circles on the curves of $\tau_{\text{cycle}} = 2.5$ and 3 ms. The second is related to chamber overfilling. The fresh reactant should not flow out of the nozzle to the external region before being burned completely unless afterburning is considered. This kind of lower bound is usually reached in low-frequency operations, as denoted by the full circle on the $\tau_{\text{cycle}} = 4$ ms curve. The third constraint, although commonly satisfied in practical cases, is that τ_{close} should be sufficiently long to cover at least the time required for detonation initiation and propagation throughout the entire chamber. The upper bound of τ_{close} (also the lower bound of τ_{refill}) lies in the requirement that an appropriate amount of fresh reactant be delivered to the chamber to produce thrust.

The effect of τ_{close} on the specific impulse follows the same trend as that of the specific thrust, except for a small range of τ_{close} near its lower bound. The specific impulse and specific thrust satisfy the following relation:

$$I_{sp} = \frac{F_{sp}(1+\tau_{\text{purge}}/\tau_{\text{refill}})}{f\,g} \tag{4.44}$$

As τ_{close} decreases, the factor $(1 + \tau_{\text{purge}/}\tau_{\text{refill}})$ decreases and may override the increase of F_{sp}, consequently leading to a decrease in I_{sp}, as shown in Fig. 4.29b.

Also observed in Fig. 4.29 is the existence of an optimum frequency. For a given τ_{close} and $\tau_{\text{purge},}$ a lower frequency translates to a longer refilling period. As a consequence, a higher chamber pressure can be reached, and the engine performance increases. However, a large refilling time associated with low-frequency operation may cause chamber overfilling and thus degrade the performance. These two conflicting effects result in an optimum frequency. Among the three frequencies considered herein, the 333 Hz (τ_{cycle} = 3 ms) operation offers the best performance margin. The highest specific impulse is 3672 s, slightly lower than its ramjet counterpart of 3866 s with optimum nozzle flow expansion.

The effect of τ_{purge} on the propulsive performance is also studied. Figure 4.31 shows the specific thrust and specific impulse at different τ_{purge} with τ_{cycle} of 3 ms and τ_{close} of 2.1 ms. The full symbols denote the numerical simulation results, and the open ones denote the analytical predictions based on the procedures proposed in Sec. 4.6.3. A performance loss of about 20% (or 25% relative to the numerical results) is observed, similar to that for the baseline case. The specific thrust decreases with τ_{purge}, while the specific impulse increases with $\tau_{purge,}$ which can be explained as follows. For given τ_{cycle} and τ_{close}, a larger τ_{purge} translates to a larger air-to-fuel mass ratio. The heat released from combustion thus needs to increase the kinetic energy of more extra air, leading to a decrease in exit velocity. The decreased τ_{refill} also degrades the specific thrust. Combined, the specific thrust decreases. On the other hand, the factor $(1 + \tau_{purge}/\tau_{refill})$ in Eq. (4.44) increases and overrides the decrease in specific thrust. The specific impulse thus increases. Note that since τ_{open} is fixed (0.9 ms), the effect of τ_{purge} is thus equivalent to that of β discussed in Sec. 4.6.3 based on analytical predictions. The increase of specific impulse is usually at the price of more decrease in specific thrust. In the present study, when τ_{purge} increases from 0 to 0.4 ms, the specific impulse increases about 14%, whereas the specific thrust decreases about 37%.

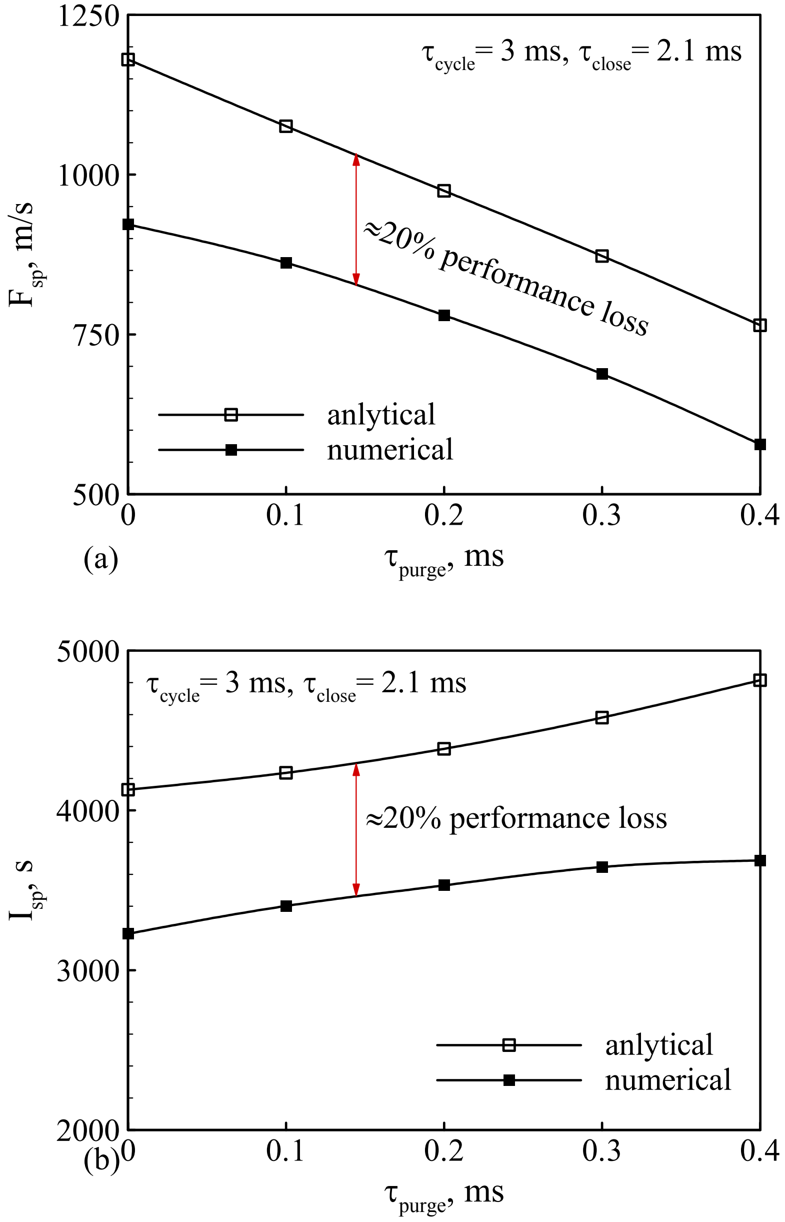

Fig. 4.31 Effect of purging time on (a) air-based specific thrust and (b) fuel-based specific impulse, $\tau_{cycle} = 3$ ms, $\tau_{close} = 2.1$ ms.

4.6.6 Effect of Nozzle Throat and Length

In addition to the operation timing, the nozzle configuration represents another important factor that affects the PDE propulsive performance. In conventional steady engines, the nozzle is optimized by matching the exit pressure to the ambient pressure. This simple criterion, however, is not applicable to PDEs because the intrinsically unsteady pulse detonation process leads to an unsteady pressure field at the exit plane. Both numerical (Cambier and Tegner, 1998; Eidelman and Yang, 1998) and experimental (Daniau et al., 2001; Cooper and Shepherd, 2002) studies on the effect of nozzles on the PDE performance have been reported recently. Most of them, however, were limited to single-pulse operation, and the question of nozzle optimization is far from resolved. In general, the nozzle affects not only the performance through the modification of the gas expansion process, but also the chamber dynamics and is coupled with the operation timing, further compounding the problem. A complete nozzle optimization for PDE thus requires tremendous computation resources. Instead of conducting such an optimization, the main purpose of the present nozzle study is to investigate the qualitative effect of the nozzle configuration on the PDE propulsive performance.

It has been demonstrated in the previous subsections that the CD nozzle significantly increases the performance that can be obtained with only a straight tube. In this subsection, the effect of the CD nozzle configuration in terms of the nozzle length and the throat is further examined. Figure 4.32 shows the four nozzle configurations considered herein. The baseline configuration, as described earlier, has a length of 20 cm and a throat height of 12 cm. In the second configuration, the nozzle length is reduced to 15 cm. The third nozzle has an even smaller length of 12.4 cm, with an exit area equal to that of the tube. The fourth one has a throat height of 9 cm, which is 25% smaller than that of the baseline nozzle.

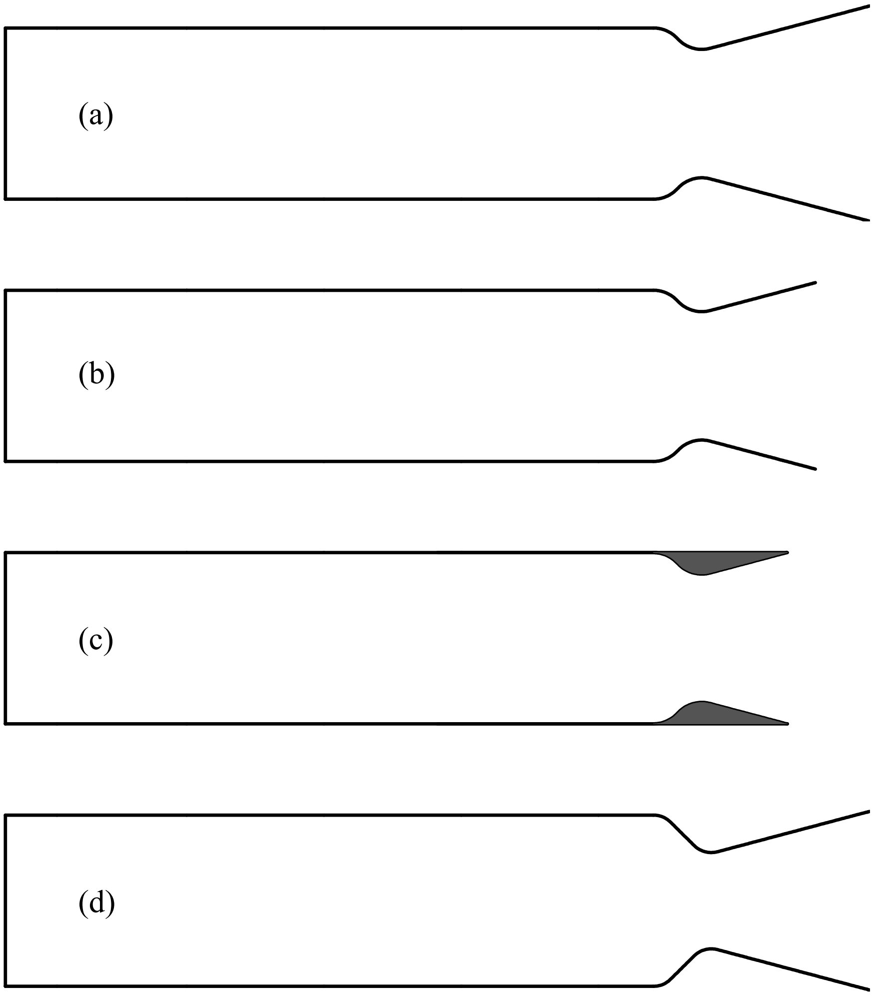

Fig. 4.32 Single-tube PDE configurations (tube length = 60 cm, tube height = 16 cm): (a) baseline case, nozzle length = 20 cm, throat height = 12 cm, (b) nozzle length = 15 cm, (c) nozzle length = 12.4 cm, (d) throat height = 9 cm.

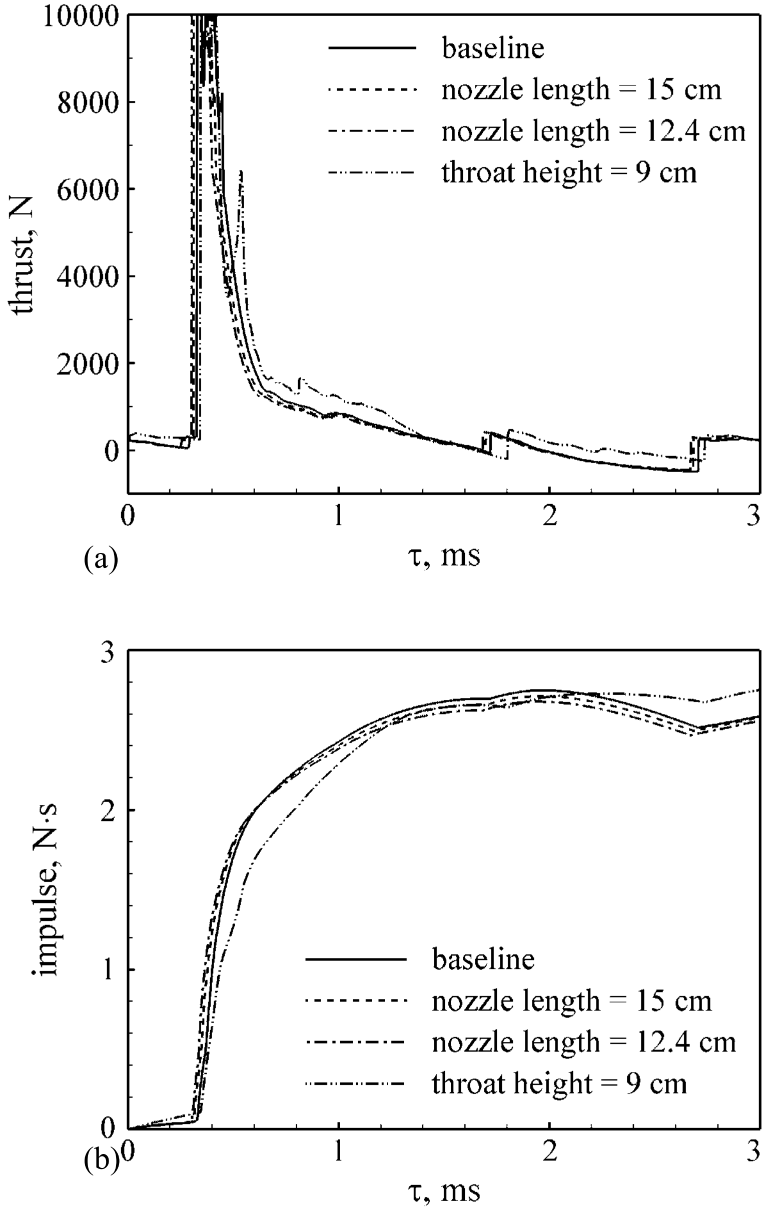

Fig. 4.33 Instantaneous thrust and impulse during steady cycle ($\tau_{cycle} = 3$ ms, $\tau_{close} = 2.1$ ms)

Simulations have been conducted for all the configurations with the same timing: τ_{cycle} of 3 ms, τ_{close} of 2.1 ms, and τ_{purge} of 0.1 ms. Figure 4.33 shows the instantaneous thrust and impulse during a steady cycle. The corresponding performance parameters are listed in Table 4.4. The effect of the nozzle length can be examined from the results of the first three configurations. Both the thrust and impulse curves for these three configurations are very close. Compared to the baseline configuration, the second and third ones have I_{sp} of 0.1% and 1% lower, respectively. Therefore, the nozzle length has a minor effect on the propulsive performance. The pressure impulse shown in Fig. 4.34 demonstrates that the overall effect of the second and third nozzles is underexpansion instead of overexpansion for the baseline nozzle. The underexpansion losses are 6% and 7%, respectively. The nominal perfect-expansion nozzle, in the sense of zero cycle-averaged pressure impulse, thus has a length between 15 cm (second nozzle) and 20 cm (baseline nozzle). Figure 4.35 shows the time history of the head-end pressure during a steady cycle. The first three curves coincide, manifesting the fact that the nozzle length only affects the gas expansion process within the divergent section of nozzle, but not the gasdynamics within the detonation tube.

Table 4.4 Performance comparison among different nozzles

Nozzle	F_{sp}, m/s	I_{sp}, s	imperfect nozzle expansion loss	flow divergence loss
Baseline	862	3402	6%, overexpansion	2.0%
nozzle length = 15 cm	860	3393	6%, underexpansion	2.5%
nozzle length = 12.4 cm	852	3365	7%, underexpansion	2.6%
throat height = 9 cm	917	3597	4%, overexpansion	2.0%

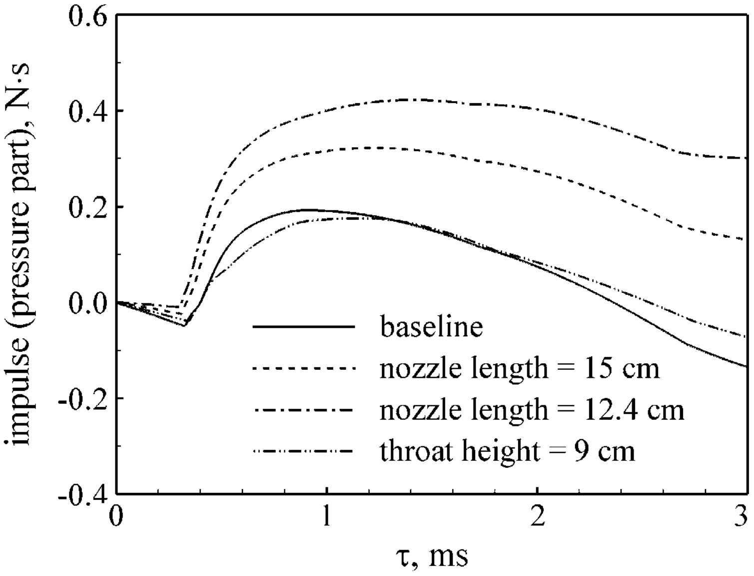

Fig. 4.34 Instantaneous pressure impulse during steady cycle (τ_{cycle} = 3 ms, τ_{close} = 2.1 ms)

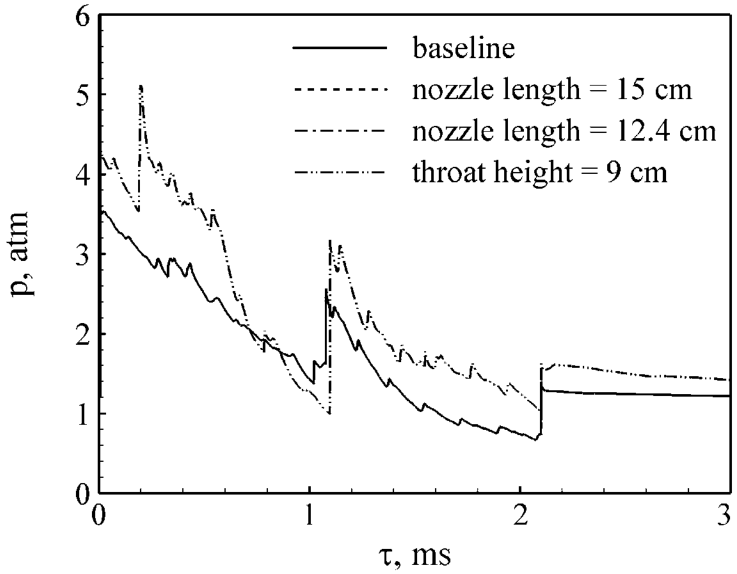

Fig. 4.35 Time history of head-end pressure during steady cycle (τ_{cycle} = 3 ms, τ_{close} = 2.1 ms)

The nozzle throat area, on the other hand, affects both the nozzle expansion process and the flow dynamics within the detonation tube, and thus has a much more significant effect on the performance. The impulse at the end of the cycle for the fourth configuration is apparently higher than the others. The corresponding I_{sp} of 3597 s is 6% higher than that of the baseline configuration, attributed to the following factors. The smaller throat helps preserve the chamber pressure, as evidenced in Fig. 4.35. The refilling pressure for the fourth configuration is about 1.49 atm, higher than the 1.24 atm for the baseline configuration. Consequently, the refilling Mach number of 0.76 is smaller than the 0.93 for the baseline configuration. In addition, the imperfect nozzle expansion loss is reduced, as listed in Table 4.4. All these factors lead to a higher propulsive performance for a smaller throat. Nevertheless, the relation of the propulsive performance and the nozzle throat area is not monotonic. As the nozzle throat becomes exceedingly small, the internal flow loss associated with the shock interactions increases since the shocks reflected off the nozzle convergent wall become stronger. Furthermore, a longer blowdown process may be required to avoid inlet over-pressurization, thus degrading the performance. These two negative effects and the aforementioned positive effects result in the existence of an optimum nozzle throat area.

To find the optimum nozzle throat area requires conducting a large number of simulations because of the coupling between the effects of the nozzle throat and operation timing. A presumptive estimation is that the optimum nozzle may improve the best performance of the baseline nozzle by 6%, that is, the highest I_{sp} of about 3892 s, which is only slightly higher than its ramjet counterpart of 3866 s with perfect nozzle flow expansion. Further improvement of the system design and optimization thus need to be conducted to make the PDEs competitive with other conventional engines. One such improvement is to use multiple detonation tubes, which will be presented in the next Chapter.

Finally, it is noteworthy that the analyses based on single-pulse operation may lead to totally different trends for the nozzle effect. For example, during the first cycle, the overall effect of all four nozzles is underexpansion, and the impulse at the end of the first cycle for the baseline configuration is higher than that for the fourth configuration. A realistic analysis of nozzle effect on PDE performance should thus be based on multicycle instead of single-pulse operations.

4.7 Summary and Conclusions

The thrust chamber dynamics in single-tube airbreathing PDEs with multicycle operations has been studied by means of two-dimensional simulations. The system under consideration includes a supersonic inlet, an air manifold, a rotary valve, a single-tube combustor, and a convergent-divergent nozzle, which is designed for the flight condition at an altitude of 9.3 km and a flight Mach number of 2.1. The combustion and gasdynamics involved in the detonation initiation and propagation, blowdown, purging, and refilling processes are examined in detail. A flow-path based performance prediction model is proposed to estimate the upper performance limit of the current PDE system. The various performance loss mechanisms, such as the imperfect nozzle expansion loss, flow divergence loss, and internal flow loss, are identified. The effects of operation timing, including the cycle time, valve close-up time, and purge time, and nozzle configurations in terms of nozzle length and throat area on the propulsive performance are investigated systematically. The analyses presented in this paper can be effectively utilized to provide guidelines for the PDE design and to identify the various loss mechanisms limiting the PDE performance. A number of important conclusions drawn from the present studies are given as below.

(1) The imperfect nozzle expansion loss resulted from the mismatch between the exit and ambient pressures is unavoidable in PDEs because the intrinsically unsteady pulse detonation process leads to an unsteady pressure field at the exit plane. The internal flow loss is mainly attributed to the shock waves and their interactions within the internal flowfield. These two losses reach 6% and 16.5% for the baseline case, respectively, composing the major factors that degrade the propulsive performance and render the PDE less attractive.

(2) There exists an optimum operation frequency for achieving the best performance margin. At a given frequency and purge time, a smaller valve close-up time increases the performance in most cases. On the other hand, for a given frequency and valve close-up time, a larger purge time decreases the specific thrust and increases the specific impulse.

(3) The nozzle length has a minor effect on the propulsive performance since it only modifies the gas expansion process within the divergent section. The throat area, in contrast, affects both the gas expansion process and the gasdynamics within the chamber, thus exerting a much more significant effect. Among the four nozzle configurations studied herein, the smaller throat improves the performance up to 6%, whereas the nozzle length affects the performance by only 1%. A smaller throat tends to increase the

performance by raising the chamber pressure. However, an exceedingly small throat renders negative effects due to the related longer blowdown process and larger internal flow loss. An optimum throat thus exists.

(4) Significant differences exist between single-pulse and multicycle operations. A realistic analysis of PDE performance should be based on multicycle instead of single-pulse operations.

The best specific impulses obtained for the current PDE system with a stoichiometric hydrogen/air mixture, e.g., 3672 s for the baseline configuration and 3892 s for an optimum nozzle, are only close to or slightly higher than its ramjet counterpart of 3866 s. Further improvement of the design philosophy and optimization of the system configuration and operation timing thus need to be conducted to make the PDEs competitive with conventional engines.

Chapter 5

Two-Dimensional Analyses of Multitube PDEs

Chapter 4 has focused on the thrust chamber dynamics and propulsive performance of single-tube airbreathing PDEs. At a flight altitude of 9.3 km and Mach number of 2.1, the best specific impulse for a baseline configuration with a stoichiometric hydrogen/air system is 3672 s, which is slightly lower than its ramjet counterpart of 3866 s. Further improvements of the system design are thus required to make the PDE competitive with other conventional engines. One of the improvements is to use a combustor consisting of multiple detonation tubes operating sequentially. In principle, this multitube design offers the following advantages:

(1) Delivering air from inlet to multiple detonation tubes reduces the inlet loss associated with the airflow stagnation during the period when none of the tubes are being filled. In a single-tube PDE, this time period takes up a large part of the cycle time and may cause inlet unstart.

(2) Exhaust from multiple detonation tubes discharging into a common nozzle provides a more stable nozzle flow and helps to increase the nozzle exit pressure which would be quite low in a single-tube PDE during the later part of the blowdown process and the purging and refilling processes, and thus improves the nozzle performance.

(3) The detonation wave from one tube can precompress the reactants in other tubes.

(4) The purging and refilling processes are less coupled with the blowdown process, thus leading to a wider range of operation timing.

(5) The overall engine operation frequency is increased, usually by a factor equal to the number of detonation tubes used. Meanwhile, the degree of unsteadiness is reduced.

(6) It provides the potential of fluidic thrust vectoring.

This chapter attempts to develop a comprehensive numerical analysis dealing with the thrust chamber dynamics in multitube PDEs with repetitive operations, to examine the flow interaction among the detonation tubes, and to investigate the effects of operation timing and system geometry on the propulsive performance.

5.1 System Configuration

The system under consideration is shown schematically in Fig. 5.1. It includes a co-axial supersonic inlet with mixed compression, an air manifold, a rotary valve, a combustor consisting of multiple detonation tubes, and a common convergent-divergent (CD) nozzle. This PDE was designed for a flight altitude of 9.3 km and a flight Mach number of 2.1, corresponding to the flight condition of advanced missiles. The static pressure, static temperature, total pressure, and total temperature of the freestream are 0.29 atm, 228 K, 2.65 atm, and 428 K, respectively. The total pressure at the entrance of the combustor is set to 2.12 atm according to the study of the inlet aerodynamics.

The cyclic operation of the PDE is controlled by a valve system located at the entrance of the combustor. The detonation tubes operate sequentially with a fixed time lag between each, as shown schematically in Fig. 5.2 for three detonation tubes. The left ends (head ends) of the tubes are assumed to be fully open or fully closed for simplicity.

The operation sequence of each tube is the same as that for a single-tube PDE, which is controlled by three time periods: the valve close-up period (τ_{close}), the purging period (τ_{purge}), and the refilling period (τ_{refill}). The cycle period of each tube is the sum of the above three periods. It may, however, be different from that for the engine. For clarity, the parameter τ_{cycle} is used to represent the cycle period based on each tube, that is, $\tau_{cycle} = \tau_{close} + \tau_{purge} + \tau_{refill}$.

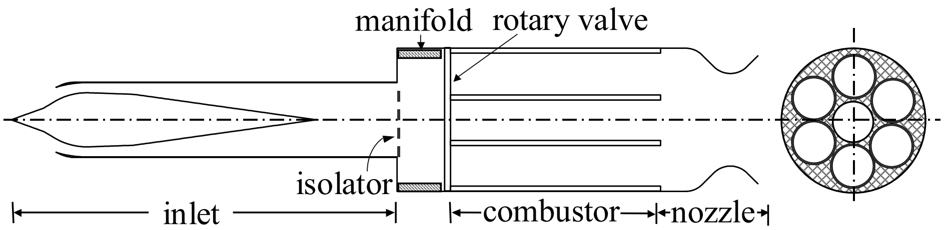

Fig. 5.1 Supersonic airbreathing pulse detonation engine

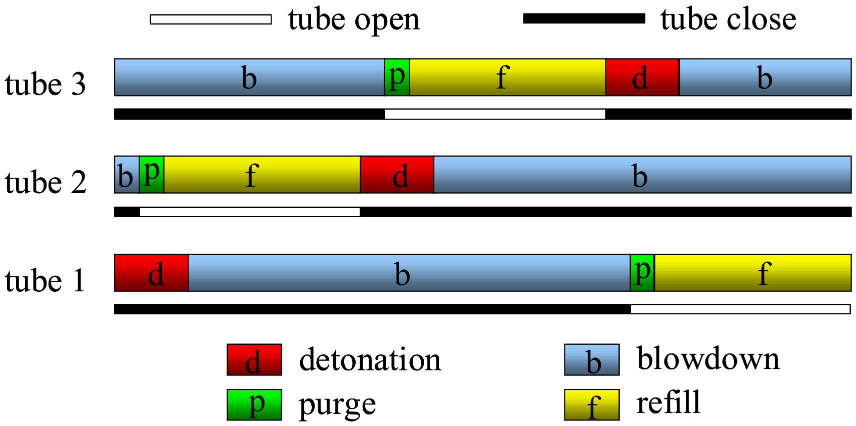

Fig. 5.2 Operation sequence of a triple-tube PDE

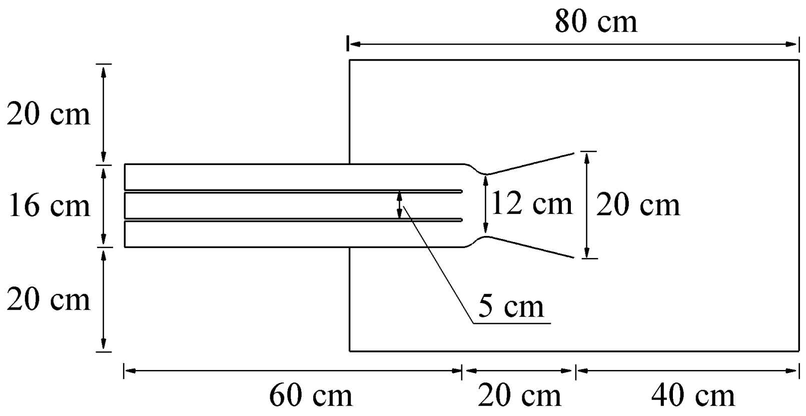

(a) without free volume

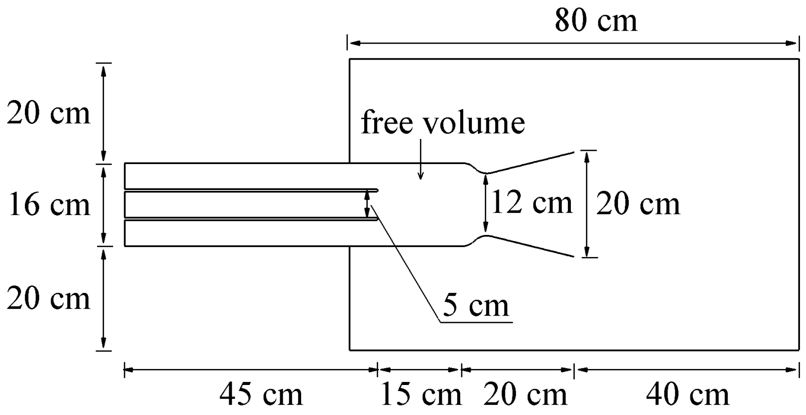

(b) with free volume

Fig. 5.3 Computational domains for multitube PDEs

Practical multitube PDE configurations are three-dimensional. Nevertheless, conducting full three-dimensional simulation of these systems requires tremendous computational resources. The present work thus considers only planar systems to conduct two-dimensional simulations. The resultant flow phenomena and the performance trend are believed to be qualitatively the same as those from the three-dimensional analysis. In addition, the two-dimensional analysis presented here provides direct comparisons with that on single-tube PDEs in Chapter 4.

Figure 5.3 shows the computational domains for the two configurations considered herein. The combustor contains three detonation tubes, each with a height of 5 cm. The tubes are spaced 0.5 cm apart. The nozzle adopts the baseline shape used in Chapter 4, which has a length of 20 cm and a throat height of 12 cm, with a 45° convergent angle and a 15° divergent angle. In the first configuration, the length of the detonation tubes is 60 cm, and the tubes extend to the nozzle entrance. In the second configuration, the length of the detonation tubes decreases to 45 cm, leaving a free volume of 15 cm long between the detonation tubes and the nozzle. The same external region is included in the computational domains for both configurations. The numbers of unstructured grid cells for these two cases are 623254 and 664362, respectively.

5.2 Results and Discussion

A series of simulations are conducted over a wide range of operation parameters for both configurations. The flow evolution, as well as the interactions among the multiple detonation tubes, is first presented in detail for a baseline case, serving as a basis for the further performance analysis and parametric studies. The engine propulsive performance is then obtained, and the various loss mechanisms are identified. Finally, the effects of the valve timing and the system geometry on the propulsive performance are discussed.

5.2.1 Flow Evolution

The baseline case for the first configuration has an operation cycle period (τ_{cycle}) of 3 ms, leading to a 1 ms time lag between tubes. The valve close-up time (τ_{close}), purging time (τ_{purge}), and refilling time (τ_{refill}) are 2.1 ms, 0.1 ms, and 0.8 ms, respectively. The ambient flow is treated as stationary because of its minor effect on the propulsive performance. Figure 5.4 shows the time evolution of the density-gradient field during the first cycle of operation. The corresponding pressure distribution along the centerline of each tube is given in Fig. 5.5, and the time histories of pressure at the midpoint of the head end of each tube in Fig. 5.6.

Initially, the bottom tube is partially (75%) filled with a quiescent stoichiometric hydrogen/air mixture at the ambient pressure (0.29 atm) and temperature (228 K), whereas the other region is filled with the ambient air. Detonation is directly initiated in the bottom tube by a driver gas region spanning 0.2 mm near the head end with a temperature of 2000 K and a pressure of 30 atm. This small amount of driver gas has been demonstrated to have neglectable contribution to the engine impulse in Chapter 4. The detonation wave then propagates downstream at a Chapman-Jouguet (CJ) speed of 1956 m/s, followed by the Taylor wave and a uniform region as have been discussed in Chapter 4. The CJ pressure and temperature are 5.855 atm and 2663 K, respectively, whereas the pressure and temperature of the uniform region are 2.158 atm and 2133 K, respectively. At $t = 0.15$ ms, the detonation wave has traveled approximately one half of the tube length, and the uniform region spreads about halfway between the detonation wave front and the head end, as also demonstrated in Chapter 4. The middle tube is in

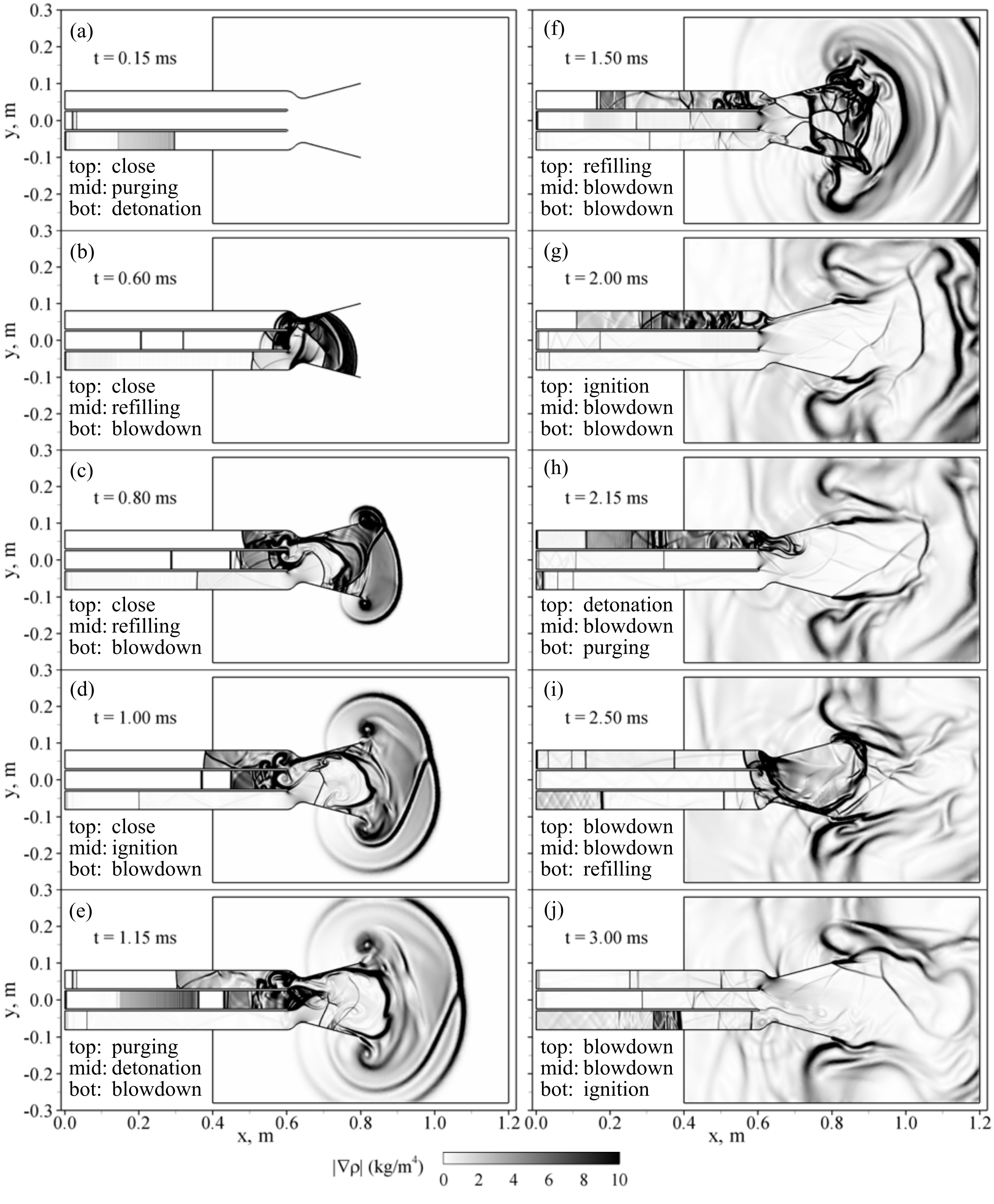

Fig. 5.4 Time evolution of density-gradient field during the first cycle of operation (τ_{cycle} = 3 ms, τ_{close} = 2.1 ms, and τ_{purge} = 0.1 ms)

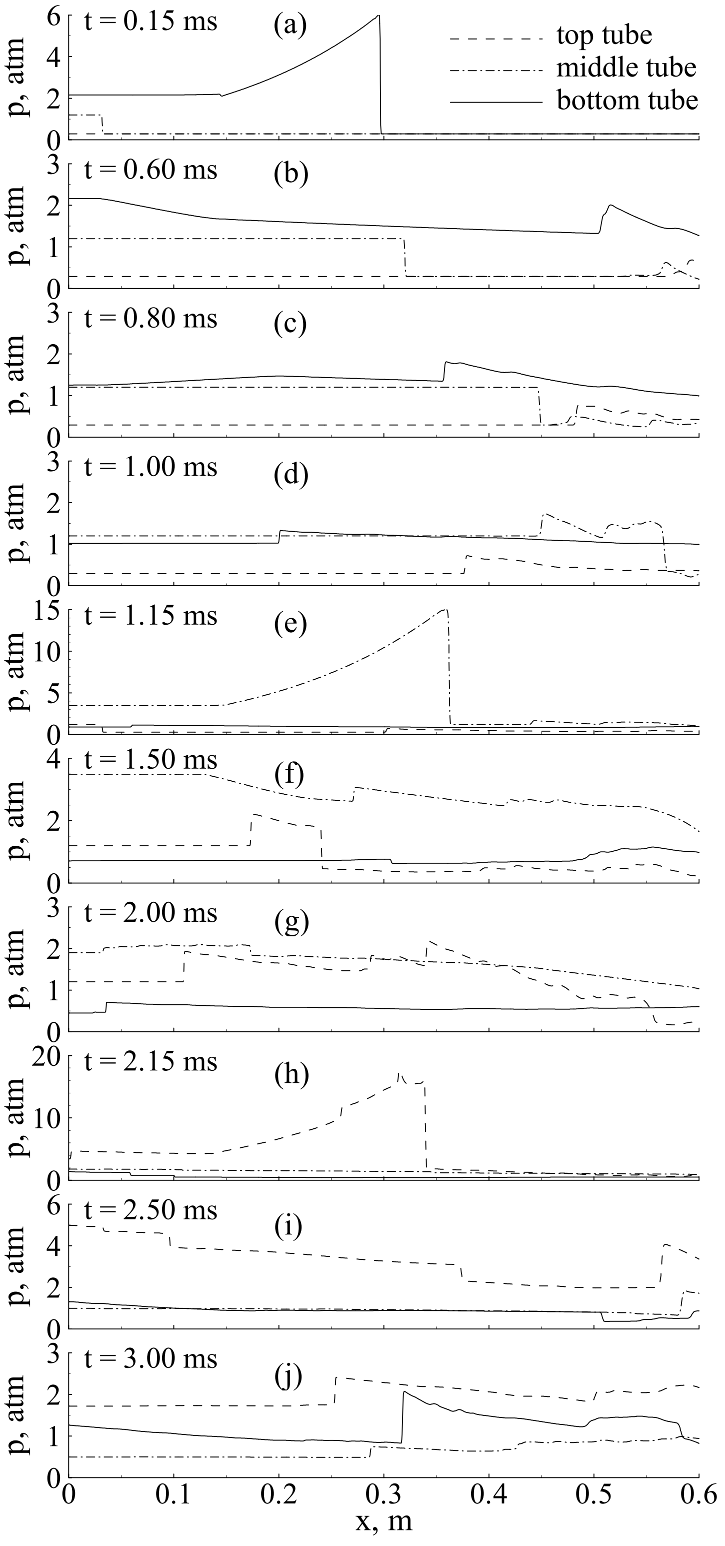

Fig. 5.5 Time evolution of pressure distribution along centerline of each tube during the first cycle of operation ($\tau_{cycle} = 3$ ms, $\tau_{close} = 2.1$ ms, and $\tau_{purge} = 0.1$ ms)

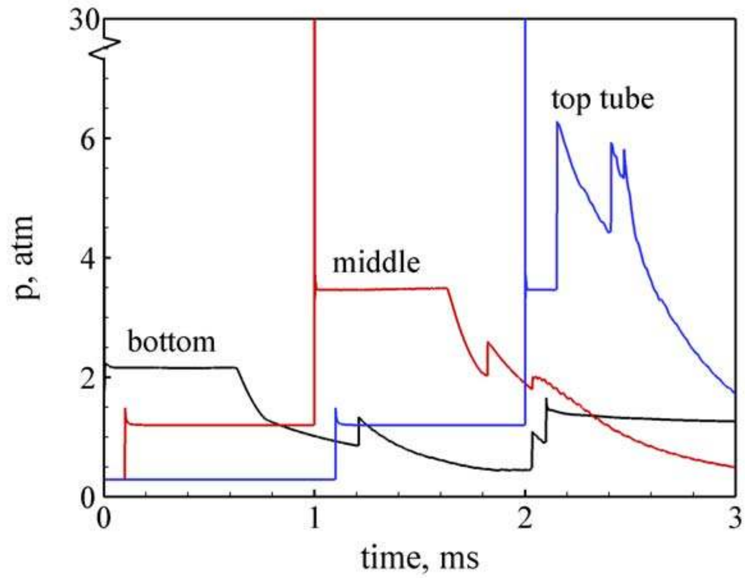

Fig. 5.6 Time histories of pressure at midpoints of head ends of the bottom, middle, and top tubes during the first cycle of operation (τ_{cycle} = 3 ms, τ_{close} = 2.1 ms, and τ_{purge} = 0.1 ms)

the purging stage. The two vertical lines represent the shock wave and the contact surface induced by the pressure difference across the valve as the purging process begins. The pressure and velocity behind the shock wave are 1.20 atm and 411 m/s, respectively.

The detonation wave in the bottom tube reaches the reactant/air interface located at 40 cm from head end at t = 0.20 ms. It then degenerates to a non-reacting shock wave, the primary shock wave. Meanwhile, a series of expansion waves are generated at the interface. The expansion waves propagate both downstream along with the Taylor wave to the tube exit and upstream to the head end. The upstream-traveling expansion waves interact and pass through the Taylor wave and thus reduce the length of the uniform region, as displayed in Fig. 5.5b. The first expansion wave arrives at the head end at t = 0.625 ms, and consequently, the head-end pressure begins to decay gradually. As the expansion waves reflect off the head end, another series of expansion waves form and propagate downstream toward the tube exit, further reducing the pressure in the bottom tube.

The primary shock wave reaches the bottom tube exit at t = 0.380 ms. It then diffracts at the tube exit and reflects from the nozzle walls, causing complex waves propagating upstream into all the three tubes and downstream into the nozzle, as displayed in the snapshot of t = 0.60 ms in Fig. 5.4. A close-up view of these flow developments and the flow interactions among the tubes and nozzle are given in Fig. 5.7. The primary shock wave has been significantly weakened by the expansion waves from the interface before emerging from the bottom tube, e.g., the pressure behind the shock decays to 3.05 atm. Its possibility to initiate detonations in the neighbor tubes is thus avoided. The flow structures related to the diffraction of the shock wave around the upper edge of the bottom tube, such as the Prandtl-Meyer expansion fan, the vortex, and the secondary shock, and the shock reflected from the nozzle wall are all clearly seen in Fig. 5.7b. In Fig. 5.7c, the diffracted and reflected shock waves have propagated into the middle and bottom tubes, respectively, and the pressures behind them are 0.32 and 2.40 atm. On the other hand, the upper part of the leading shock hits the edge connecting the middle and top tubes, whereas the right part propagates in the divergent section of the nozzle. Along the curved wall, the flow behind the leading shock is locally expanded to supersonic, leading to the formation of a shock wave stemming out from the wall, as evidenced in Fig. 5.7c. The upper part of the leading shock then hits (Fig. 5.7d) and reflects off (Fig. 5.7e) the upper wall of the nozzle. In the top tube, the first shock relates to the diffracted part and the second one to the reflected shock from the lower wall of the nozzle. The pressures behind these two shocks are 0.37 and 0.53 atm, respectively. The shock waves established in all the three tubes propagate upstream and elevate the pressure therein (see Figs. 5.5b and 5.5c). In addition, because of the relative low strength, they will not initiate detonations if encountering fresh reactant.

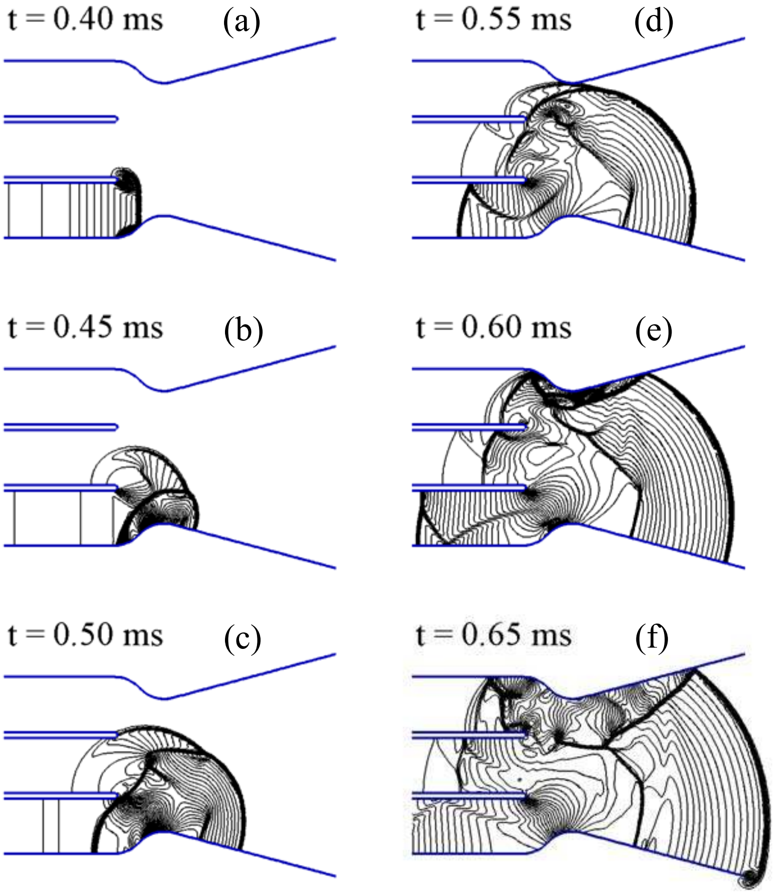

Fig. 5.7 Snapshots of pressure field showing flow interactions among tubes and nozzle during the first cycle ($\tau_{cycle} = 3$ ms, $\tau_{close} = 2.1$ ms, and $\tau_{purge} = 0.1$ ms)

At t = 0.80 ms, the primary shock wave has emerged from the nozzle into the external region. Vortices are formed near the edges of the nozzle exit. Except for the asymmetrical pattern, the external flowfield exhibits quite similar structures to that of the single-tube case. Within the combustor, the reflected shock in the bottom tube propagates toward the head end faster than those in the middle and top tubes, due to the larger sound speed related to the high temperature of the products in the bottom tube. The middle tube is in the refilling stage. The shock wave induced in the purging process travels to the location of 45 cm and is going to meet the upstream-traveling waves induced by the detonation of the bottom tube.

The middle tube ends the refilling process and ignites at t = 1 ms. At this time instant, the purge-induced contact surface locates at x = 37 cm and the leading fresh reactant at x = 32 cm. The purge-induced shock has interacted with the upstream-traveling waves induced by the detonation of the bottom tube. At t = 1.15 ms, the detonation wave in the middle tube reaches x = 37 cm. It is faster than the detonation wave in the bottom tube since the reactant in the middle tube has already had a velocity of about 411 m/s prior to detonation. The top tube undergoes the purging process. At a slightly later time, the detonation wave in the middle tube catches the leading fresh reactant at x = 39 cm and degenerates to a non-reacting shock wave. The resultant shock wave proceeds further downstream and interacts with the waves induced previously by the detonation wave of the bottom tube, causing very complicated flow structures in the nozzle and the external regions, as displayed in Fig. 5.4f. Two Prandtl-Meyer expansion fans are seen at the exit of the middle tube. The top tube is now in the refilling process, with a refilling pressure of 1.20 atm and a refilling velocity of 411 m/s. The interaction of the downstream- and upstream-traveling shock waves leads to a high pressure region with pressure up to 2.2 atm in the top tube, as shown in Fig. 5.5f. This pressure is not high enough to initiate a detonation in the top tube, but may interfere with the refilling process. The refilling process should thus be finished before the upstream-traveling shock wave arrives at the head end. Otherwise, inlet over-pressurization may happen. For the current case, the shock wave propagates toward the head end at a speed of as low as about 126 m/s, and thus permits enough time for the refilling process. It reaches x = 11 cm as the refilling process finishes.

Ignition occurs in the top tube at t = 2 ms while the middle and bottom tubes undergo blowdown process. The aforementioned upstream-traveling shock wave interacts with the detonation wave and Taylor wave and reflects off the head end at about t = 2.15 ms, causing an abrupt raise in head-end pressure, as evidenced in Fig. 5.6. In Fig. 5.4h, the detonation wave has passed through the leading fresh reactant at x = 31.2 cm and degenerated to a non-reacting shock wave. At t = 2.5 ms, the shock wave has moved out of the nozzle to further interact with the local flowfield in the external region. Reflected shock waves can be seen in all the three tubes near their exits. The pressures behind these shocks, from bottom to top, are 0.8, 1.8, and 4.0 atm. The bottom tube is in the refilling stage. The refilling pressure and velocity are 1.30 atm and 380 m/s, respectively.

The bottom tube finishes the refilling process at t = 3.0 ms, the end of the first cycle, whereas the middle and top tubes are in the blowdown process. The leading fresh reactant in the bottom tube reaches x = 35.5 cm. The upstream-traveling shock wave induced by the detonation of the top tube has interacted with the purge-induced shock wave and contact surface and propagated into the fresh reactant, denoted by the pressure jump at about x = 32 cm in Fig. 5.5j.

Comparing with the flow evolution described in Chapter 4 for a single-tube PDE, the current one bears the following characteristics. First, the flowfield exhibits asymmetry and is much more complicated. Second, the expansion pattern of the nozzle is not as apparent as that in the single-tube case, in which the Prandtl-Meyer expansion fan, representing an underexpanded nozzle flow, or the oblique shock wave, representing an overexpanded nozzle flow, can be clearly observed near the nozzle exit during certain periods of the blowdown process. Third, the pressure in a tube is raised not only by the shock waves induced by the detonation wave of this tube but also by the shock waves induced by the detonation waves from other tubes.

The flow tends to attain a steady periodic condition as the cycle repeats. Figure 5.8 shows the specific impulse and the middle tube filling length of each cycle. The specific impulse is calculated based on the momentum balance over a control volume enclosing the entire engine, as detailed in Chapter 4. The filling length is defined as the length at which the detonation wave catches the leading fresh reactant. By using the quantitative criterion proposed in Chapter 4, i.e., the relative deviation in cycle-averaged specific impulses of two continuous cycles being less than 0.1%, the current baseline case reaches steady periodic operation at the fifth cycle. The time evolution of the density-gradient field during this cycle is shown in Fig. 5.9, and the corresponding pressure distribution along the centerline of each tube is given in Fig. 5.10. Quite different flow patterns are obtained due to the effect of flow non-uniformity arising from the previous cycle. The flowfield at t = 15.00 ms is almost the same as that at t = 12.00 ms, verifying again that the steady periodic operation has been reached. The averaged refilling pressures of the bottom, middle, and top tubes are 1.36, 1.16, and 1.24 atm, respectively.

The corresponding refilling Mach numbers are 0.85, 1.0, and 0.94, and the refilling velocities are 361, 440, and 392 m/s, respectively. The filling lengths of the bottom, middle, and top tubes are 39.0, 38.8, and 40.5 cm, respectively, slightly smaller than the 47.5 cm for the single-tube case.

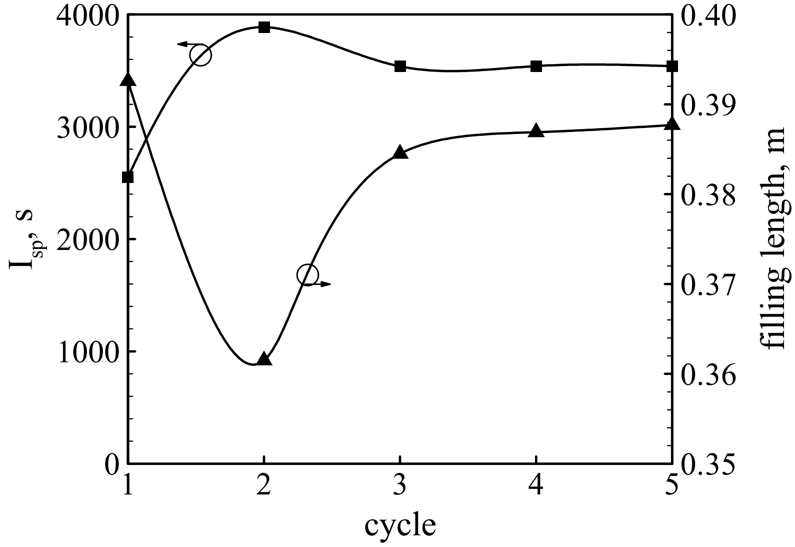

Fig. 5.8 Specific impulse and filling length of the middle tube of the first five cycles ($\tau_{cycle} = 3$ ms, $\tau_{close} = 2.1$ ms, and $\tau_{purge} = 0.1$ ms)

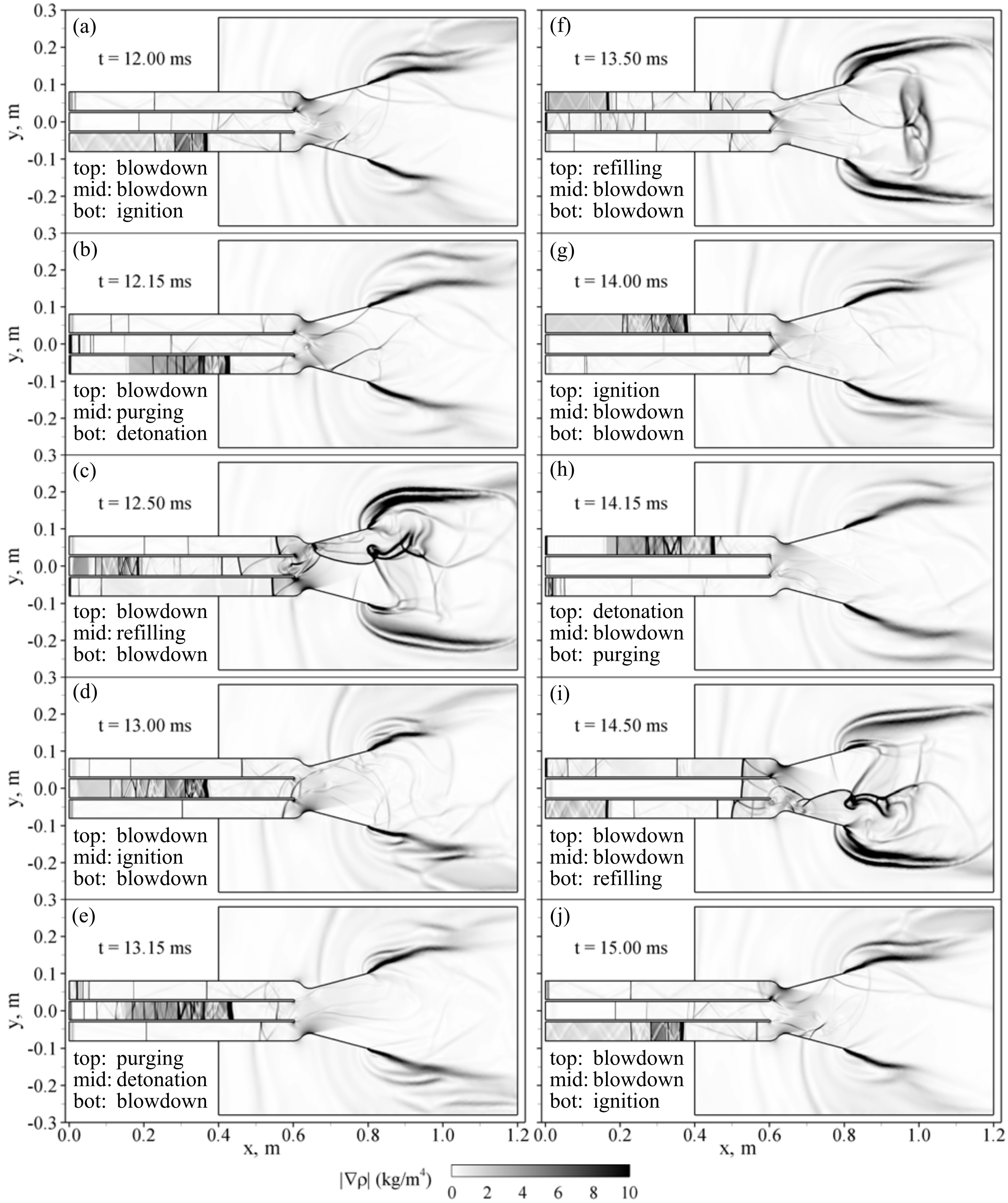

Fig. 5.9 Time evolution of density-gradient field during the fifth cycle of operation ($\tau_{cycle} = 3$ ms, $\tau_{close} = 2.1$ ms, and $\tau_{purge} = 0.1$ ms)

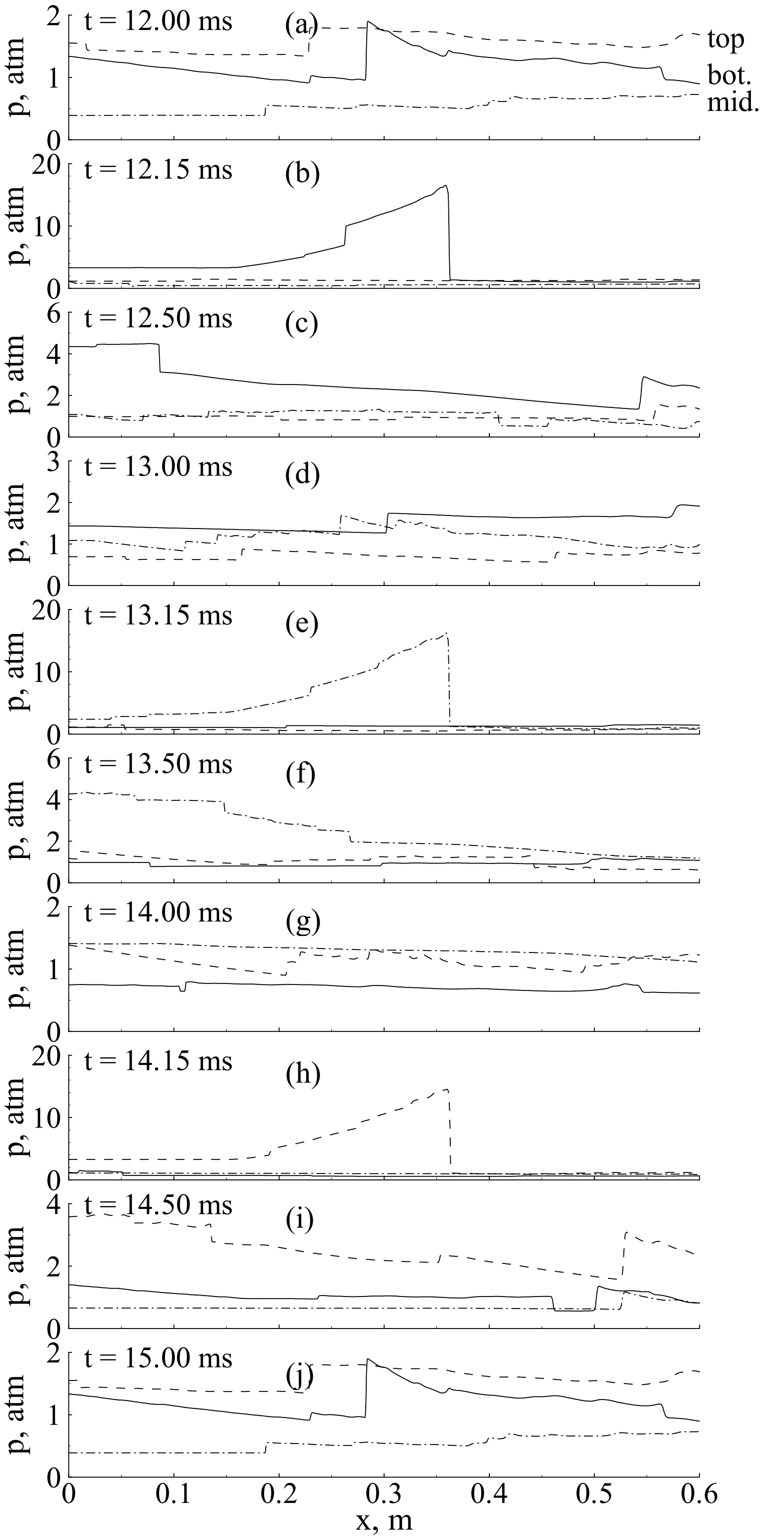

Fig. 5.10 Time evolution of pressure distribution along centerline of each tube during the fifth cycle of operation ($\tau_{cycle} = 3$ ms, $\tau_{close} = 2.1$ ms, and $\tau_{purge} = 0.1$ ms)

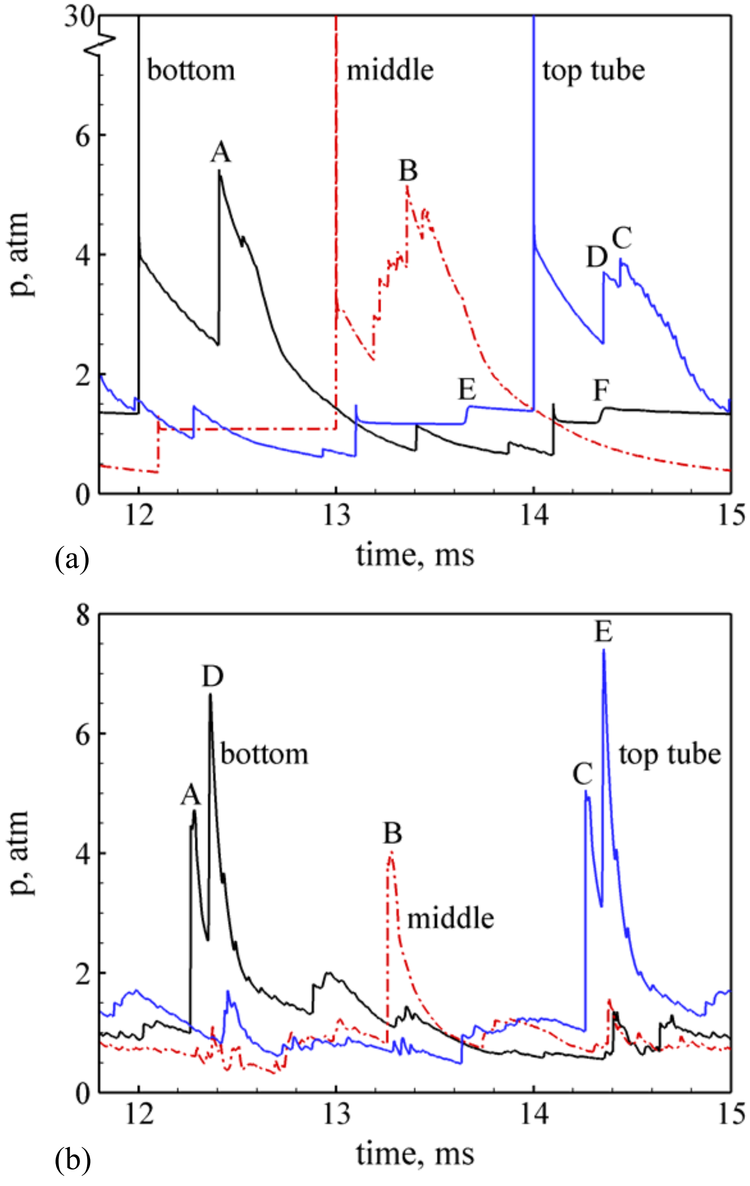

Fig. 5.11 Time histories of pressure at midpoints of (a) head ends and (b) exit of the bottom, middle, and top tubes during the fifth cycle of operation (τ_{cycle} = 3 ms, τ_{close} = 2.1 ms, and τ_{purge} = 0.1 ms)

Figure 5.11 shows the time histories of the pressure at the midpoints of the head end and the exit of each tube, to provide more quantitative inspection on the tube interactions. In Fig. 5.11a, the highest peak on each trace corresponds to the initiation of detonation at the head end. The second peak on the bottom tube trace, point A, indicates the shock wave induced by the detonation of the top tube arriving at the head end. The second peak on the middle tube trace, point B, relates to the arrival of the shock wave induced by the detonation of the bottom tube. This detonation wave also induces a shock wave that propagates into the top tube, interferes with the refilling process, and causes a small jump in the head-end pressure of the top tube, as evidenced by point E. The raised pressure is still less than the total pressure of the incoming gas so that the refilling process continues. The second peak on the top tube trace, point C, results from the detonation wave of the middle tube. Similarly, this detonation wave induces a shock wave in the bottom tube that leads to a small jump in the head-end pressure (point F). The third peak, point D, corresponds to the arrival of the shock wave resulting from the purge-induced shock in the middle tube. This purge-induced shock, however, exhibits little effect on the bottom tube head-end pressure. The reason is that the bottom tube has a supersonic exhaust flow when the purge-induced shock emerges from the middle tube. It is noted that all the aforementioned peak pressures exceed the total pressure of the gas immediately in front of the tubes. They should be thus within the period with valve closed. Otherwise, reverse flow may occur at the entrance of the detonation tubes and engine unstart happens.

In Fig. 5.11b, the first peaks on the three traces, points A, B, and C, correspond to the arrival of the detonation-degenerated shock wave at the tube exit. The second peaks on the traces of the bottom and top tubes, points D and E, correspond to the arrival of the reflected shocks from the nozzle wall. The middle tube, nevertheless, doesn't have this kind of peak because the middle tube exit is farther from the nozzle wall, and a supersonic exhaust flow is developed soon after the detonation-degenerated shock wave emerges from the middle tube.

The flowfield within the common nozzle, as can be seen in Fig. 5.9, is quite different from that of the single-tube PDE. Multiple asymmetrical transverse waves exist within the common nozzle and disorganize the choke pattern which appears in the nozzle of the single-tube PDE during most of the cycle period. The nozzle throat in the multitube PDE seems to play a role less important to the performance than in the single-tube PDE. The complexity of the nozzle flow is also evidenced in Fig. 5.12, in which the time histories of the Mach number at the midpoints of the nozzle throat and exit planes are displayed. In the single-tube PDE, the nozzle is choked during the entire cycle except for a small period during which the detonation-degenerated shock wave sweeps the throat region. The typical choke pattern is represented by a curved sonic line that starts at the wall slightly upstream of the throat and crosses the nozzle centerline downstream of the throat. As a result, the Mach number at the midpoint of the throat is less than unity and remains quite smooth during most time of the cycle as demonstrated in Fig. 5.12a. However, in the multitube PDE, the Mach number at the midpoint of the throat exhibits significant variation and is either larger than or far below unity during a large portion of the cycle. The choke effect of the nozzle throat is thus quite weak. In Fig. 5.12b, the Mach numbers at the midpoint of the nozzle exit plane also display significant difference, such as the three large peaks appearing in the triple-tube trace. Both Mach numbers, however, are larger than unity during the entire cycle.

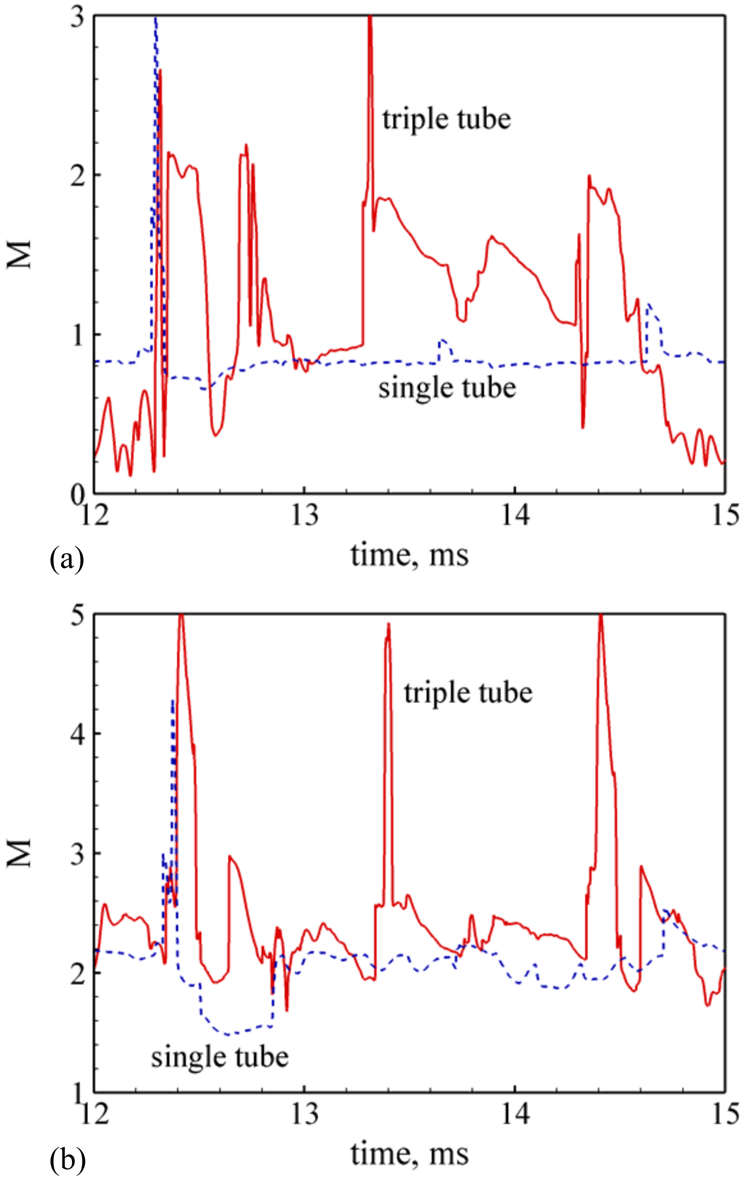

Fig. 5.12 Time histories of Mach number at midpoints of (a) nozzle throat and (b) nozzle exit during the fifth cycle of operation ($\tau_{cycle} = 3$ ms, $\tau_{close} = 2.1$ ms, and $\tau_{purge} = 0.1$ ms)

5.2.2 Propulsive Performance and Loss Mechanisms

Because of the intrinsic unsteady nature of PDEs, their propulsive performance must be calculated appropriately. A detailed description of the performance calculation based on the momentum balance over a control volume enclosing the entire engine has been given in Chapter 4. Figure 5.13 shows the instantaneous thrust in both axial and vertical directions, obtained from Eq. (4.10) by negelecting the last term. The single-tube PDE results are also included for comparison. In Fig. 5.13a, a very high peak up to 15000 N exists for the single-tube PDE, corresponding to the arrival of the primary shock wave at the nozzle exit plane. The deviation of the peak value from the cycle-averaged value represents a quantitative measure of the degree of unsteadiness of the engine thrust. For the triple-tube PDE, the number of peaks increases to three in each cycle, but the peak magnitudes are significantly reduced, e.g., by a factor of about three, rendering a substantial improvement in engine steadiness. The three peaks represent the arrival of the detonation-degenerataed shock waves of the bottom, middle, and top tubes at the nozzle exit plane, respectively. The second peak related to the middle tube is higher because the shock wave from the middle tube experiences less diffraction and reflection than those from the other two tubes. The same reason also leads to a much lower peak related to the middle tube in the lateral thrust (Fig. 5.13b). The increase of the peak number modifies the spectral property of the thrust. Figure 5.14 represents the spectra of the instantaneous axial thrusts. Clearly, the dominant frequency of the single-tube PDE is equal to the tube operation frequency, i.e., 333 Hz. However, that of the triple-tube PDE is increased by three times to 1000 Hz.

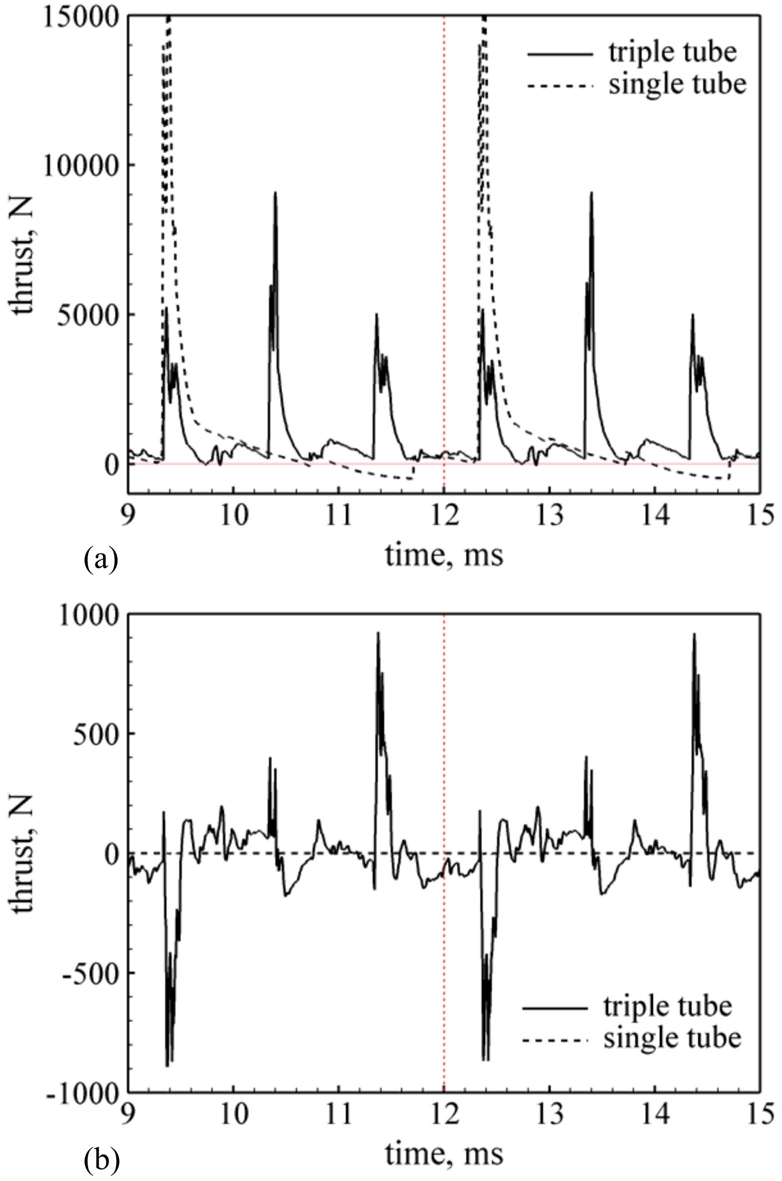

Fig. 5.13 Instantaneous thrust in (a) axial and (b) vertical directions during the fourth and fifth cycles ($\tau_{cycle} = 3$ ms, $\tau_{close} = 2.1$ ms, and $\tau_{purge} = 0.1$ ms)

Also observed in Fig. 5.13a is that the time duration of negative thrust of triple-tube PDE is significantly decreased to nearly zero, whereas that of the single-tube PDE is about 0.7 ms, e.g., from 14.0 to 14.7 ms during the fifth cycle. This is due to the fact that the exhaust flow of low energy level during the later part of the blowdown stage and the refilling stage of a single-tube PDE is avoided in multitube PDE by the sequential operations of the tubes. For exapmle, when one tube is in the later part of the blowdown stage, the other tubes may be in the earlier part of the blowdown stage.

Figure 5.13b demonstrates the existance of a considerable lateral thrust up to 1000 N in the current triple-tube PDE, thereby causing unnecessary vibration of the vehicle. One way to mitigate this problem is to implement tube-pairs. Each tube-pair includes two detonation tubes which are located at symmertic positions and operate synchronously to ensure symmetric operation and consequently eliminates the lateral thrust. In some cases, however, the lateral thrust can also be appropriately utilized for thrust vectoring.

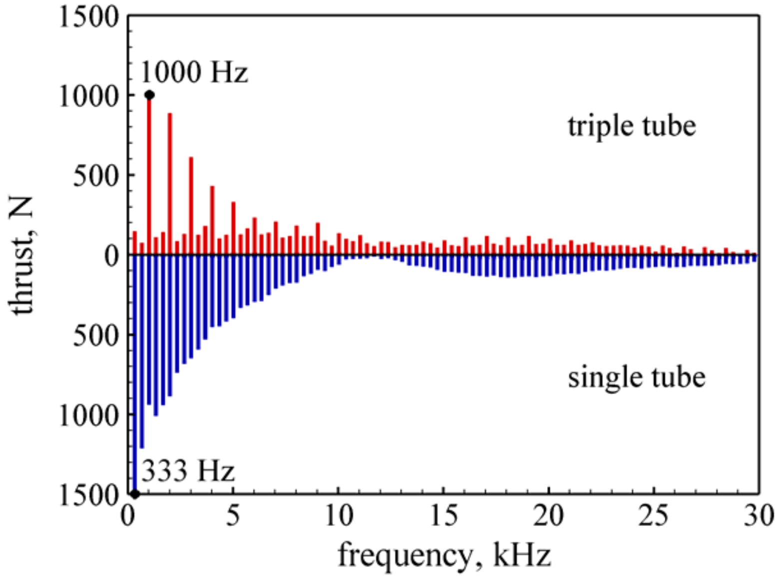

Fig. 5.14 Spectra of periodic instantaneous axial thrusts of single-tube and triple-tube PDEs with operation timing of $\tau_{\text{cycle}} = 3$ ms, $\tau_{\text{close}} = 2.1$ ms, and $\tau_{\text{purge}} = 0.1$ ms

The cycle-averaged specific impulse and specific thrust during a steady periodic cycle, e.g., the fifth cycle, are 3540 s and 895 m/s, respectively. These performance numbers are about 4% higher than those of the baseline single-tube PDE given in Chapter 4. The multitube design thus slightly improves the propulsive performance. To identify the various loss mechanisms, the flow-path based analytical performance prediction model proposed in Chapter 4 is used to predict the upper performance limit. This model requires specifying the refilling Mach number. As mentioned in Sec. III.A, the refilling Mach numbers of the bottom, middle, and top tubes are 0.85, 1.0, and 0.94, respectively. The average is 0.93. Interestingly, it is just the same as that for the baseline single-tube PDE. The corresponding upper limit of the specific impulse is thus 4235 s. Comparing the simulated specific impulse to this upper limit, a performance loss of about 19.6% is obtained. This performance loss includes the imperfect nozzle expansion loss, the flow divergence loss, and the internal flow loss. Based on the calculation methods provided in Chapter 4, the three losses for the current baseline triple-tube PDE are 3%, 2.3%, and 14.3%, respectively. Compared to the baseline single-tube PDE, the nozzle expansion loss is significantly reduced, the internal flow loss is slightly reduced, and the flow divergence loss remains about the same. The 4% increase in propulsive performance of the triple-tube PDE thus comes from the reduction of the imperfect nozzle expansion loss and the internal flow loss.

Figure 5.15 shows the instantaneous pressure thrust and impulse during a steady periodic cycle. The single-tube results are also included for comparison. In conventional steady engines with optimized nozzle, the exit pressure is equal to the ambient pressure, and the pressure thrust is thus zero. For unsteady engines such as PDE, the closer the pressure thrust to zero, the less the imperfect nozzle expansion loss. It is clear in Fig. 5.15a that the pressure thrust of the triple-tube PDE remains closer to zero than that of the single-tube PDE, demonstrating a reduction in the imperfect nozzle expansion loss. The cumulative pressure impulse over the cycle is less than zero, as can be seen in Fig. 5.15b, indicating the overall effect of the nozzle flow is overexpansion.

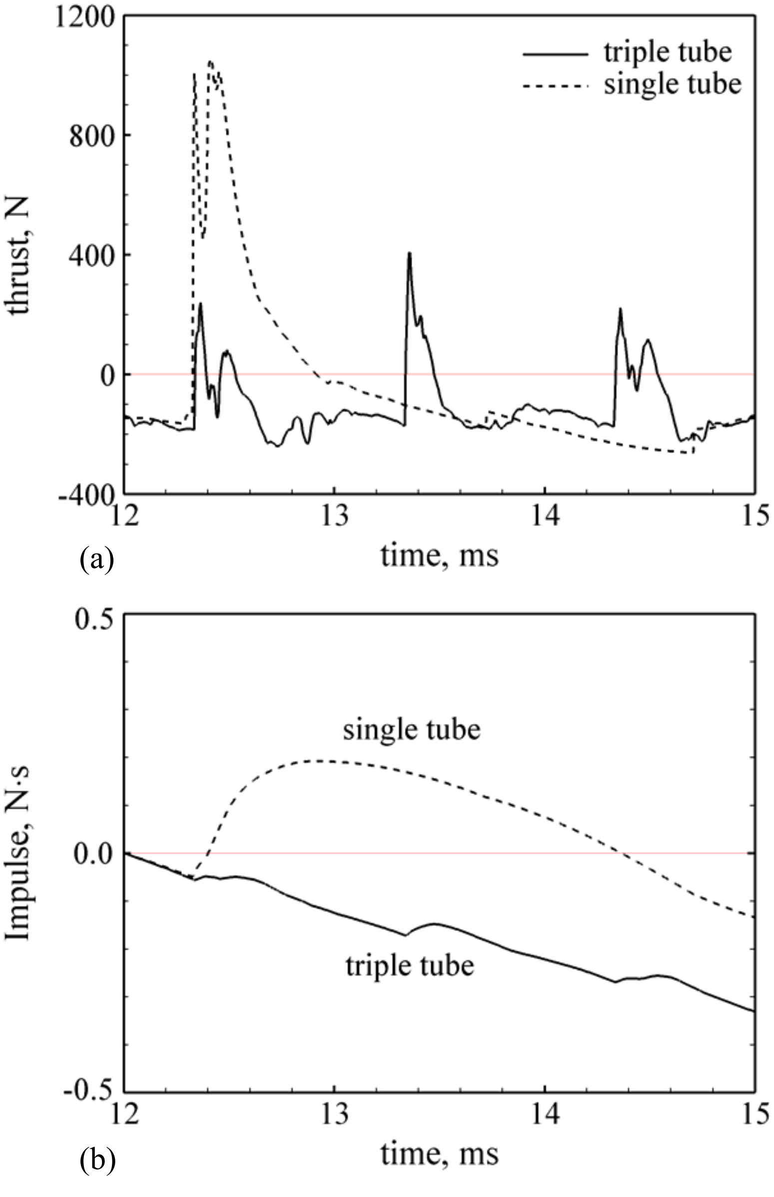

Fig. 5.15 Instantaneous pressure thrust and impulse during the fifth cycle ($\tau_{cycle} = 3$ ms, $\tau_{close} = 2.1$ ms, and $\tau_{purge} = 0.1$ ms)

The flow divergence loss results from the exhaust velocity vector angularity. Figure 5.16 compares the velocity profiles at the nozzle exit plane during a steady periodic cycle between the triple- and single-tube PDEs. The asymmetric pattern of the triple-tube results are clearly observed. However, the velocities from both cases are very close, leading to almost the same flow divergence losses.

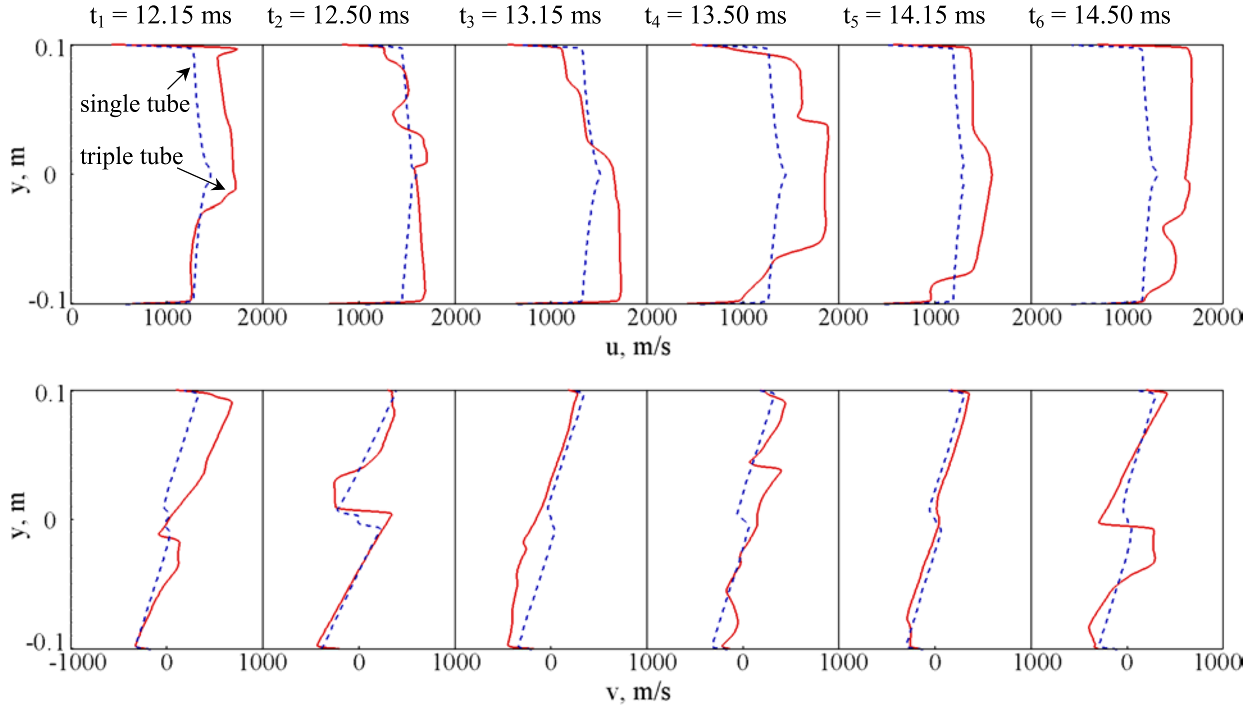

Fig. 5.16 Axial and vertical velocity profiles at nozzle exit plane during the fifth cycle of operation ($\tau_{cycle} = 3$ ms, $\tau_{close} = 2.1$ ms, and $\tau_{purge} = 0.1$ ms)

The internal flow loss is mainly attributed to the shock waves and their interactions within the internal flowfield. In spite of the much more complicated shock interactions within the multitube PDE flowfield, the strengths of the shock waves related to the diffraction around the tube exit and the reflection from the nozzle wall are relatively smaller than the strength of the shock wave related to the reflection from the nozzle wall in the single-tube PDE, leading to a slightly smaller internal flow loss.

5.2.3 Effect of Valve Timing

A parametric study is conducted to investigate the timing effect on the propulsive performance by varying the cycle time τ_{cycle} and the valve close-up time τ_{close}. The purge time τ_{purge} is fixed at 0.1 ms. Figure 5.17 shows the effects of τ_{close} on the specific thrust F_{sp} and the specific impulse I_{sp} for two τ_{cycle}: 3 ms and 4 ms. The single-tube results are also included for comparison. Clearly, the multitube design helps improve the propulsive performance.

The specific thrust increases as τ_{close} decreases for each frequency considered herein. The explanation of this trend for single-tube PDEs presented in Chapter 4 also applies here. Briefly, for a given τ_{cycle} and τ_{purge}, a smaller τ_{close} leads to higher loading density of fresh reactant, a larger amount of reactant delivered to the chamber, a shorter period of negative thrust, and less internal flow loss, and thus results in a higher specific thrust. The lower bound of τ_{close} is subjected to three practical constraints as mentioned in Chapter 4.

For single-tube PDEs, it has been demonstrated in Chapter 4 that there exists an optimum frequency for a given configuration, which is attributed to the following two conflicting effects: 1) more reactants can be recharged into the detonation tube at a lower cycle frequency and 2) an exceedingly large refilling time associated with a low-frequency operation may cause chamber overfilling and thus degrade the performance. A similar conclusion is found for multitube PDEs. Figure 5.17b indicates that the lower frequency of 250 Hz ($\tau_{cycle} = 4$ ms) offers not only a wide operating range but also higher performance than the higher frequency of 333 Hz ($\tau_{cycle} = 3$ ms). The optimum frequency is thus less than 333 Hz. However, further parametric studies are needed to determine this.

A comparison between the triple-tube and single-tube results demonstrates the superiority of the multitube design. For the 333 Hz operation, the triple-tube PDE has performances of about 4% to 5% higher than those of single-tube PDEs. For the 250 Hz operation, the triple-tube PDE possesses both a wider operation range and higher performance. The lower bound of τ_{close} related to the combustor overfilling in the single-tube PDE doesn't appear in the triple-tube PDE. Instead, the performance increases as τ_{close} decreases until the lower bound related to the inlet over-pressurization is reached. This is attributed to the fact that in the multitube PDE, the pressure in a detonation tube within the refilling process can be raised by the detonation-degenerated shock waves from other tubes, as discussed in Sec. 5.2.1. In contrast, the chamber pressure during the refilling process of the single-tube PDE may be quite low, especially for cases with very long blowdown process, thus resulting in high refilling velocity and chamber overfilling. The highest specific impulse obtained for the current design is 3870 s, at an operation timing with τ_{cycle} of 4 ms and τ_{close} of 1.8 ms. This performance number slightly exceeds its ramjet counterpart of 3866 s with optimum nozzle flow expansion and can be further improved by optimizing the operation timing.

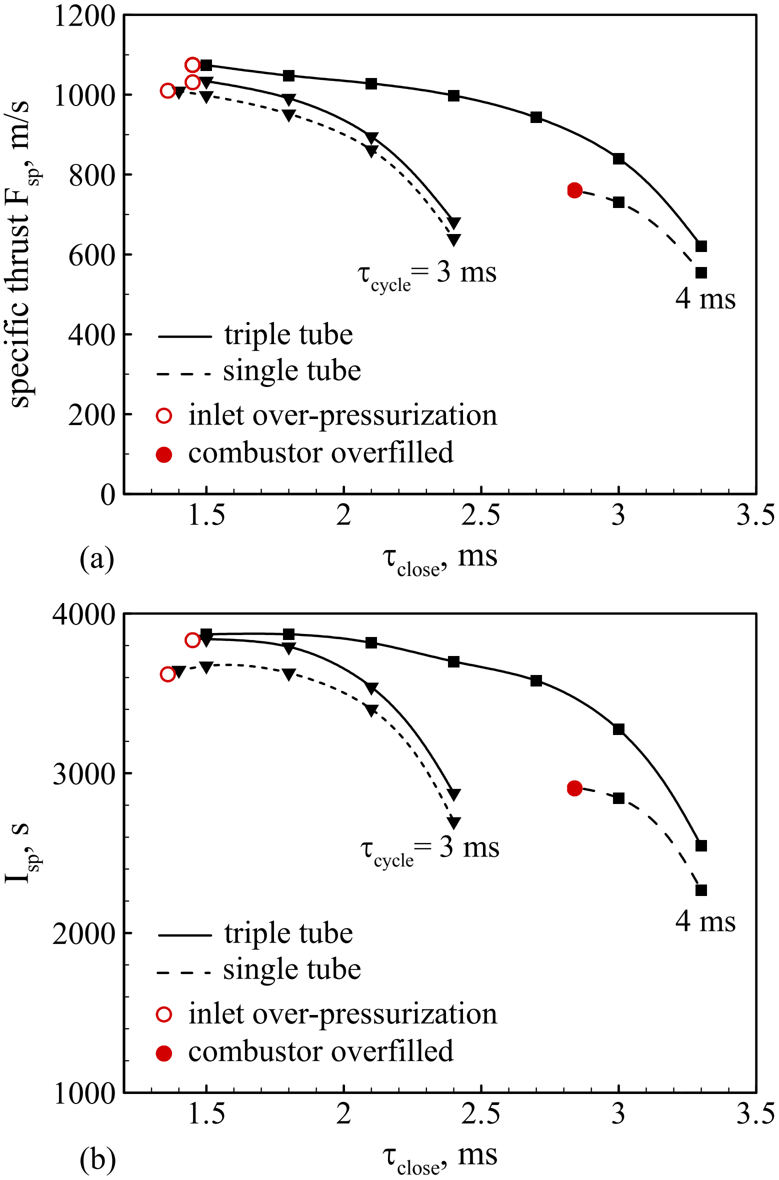

Fig. 5.17 Effect of valve close-up time on (a) air-based specific thrust and (b) fuel-based specific impulse; $\tau_{purge} = 0.1$ ms, stoichiometric H_2/air mixture, h = 9.3 km, $M_\infty = 2.1$.

5.2.4 Effect of System Geometry

In addition to the operation timing, the system geometry represents another important factor that affects both the flow dynamics and the propulsive performance of a multitube PDE. The system geometry includes many independent variables, such as tube length, nozzle length, nozzle throat and exit areas, and so on. Generally, the study of the geometrical effect requires much effort due to the need to regenerate the computational grid. In Chapter 4 for single-tube PDEs, the effect of the CD nozzle configuration has been investigated by varying the nozzle length and throat area. In this chapter, the effect of a free volume located between the multiple tubes and the common nozzle, as depicted in Fig. 5.3, is considered. The purpose of adding such a free volume is to provide a buffer region to smooth the flowfield and improve the operation steadiness.

Figure 5.18 shows the time evolution of the density-gradient field during the fifth cycle. The operation timing remains identical to that for the baseline case. The refilling lengths for the bottom, middle, and top tubes are 33.6, 44.3, and 34.8 cm, respectively. The averaged refilling Mach numbers are 0.88, 1.0, and 0.99, respectively. The flowfield characteristics within the detonation tubes and the external region are quite similar in nature to those without free volume. Within the free volume, however, the flow exhibits very complicated structures. In addition to the diffraction and reflection of the shock waves from the three detonation tubes, the interactions of the supersonic exhaust flow from the detonation tubes with the subsonic flow within the corner regions near the conjunction of the combustor and the convergent nozzle wall lead to the formation of standing-like shock waves. These shock waves may be quite strong. For example, the shock wave located at the middle of the free volume has a pressure ratio of as high as 5.

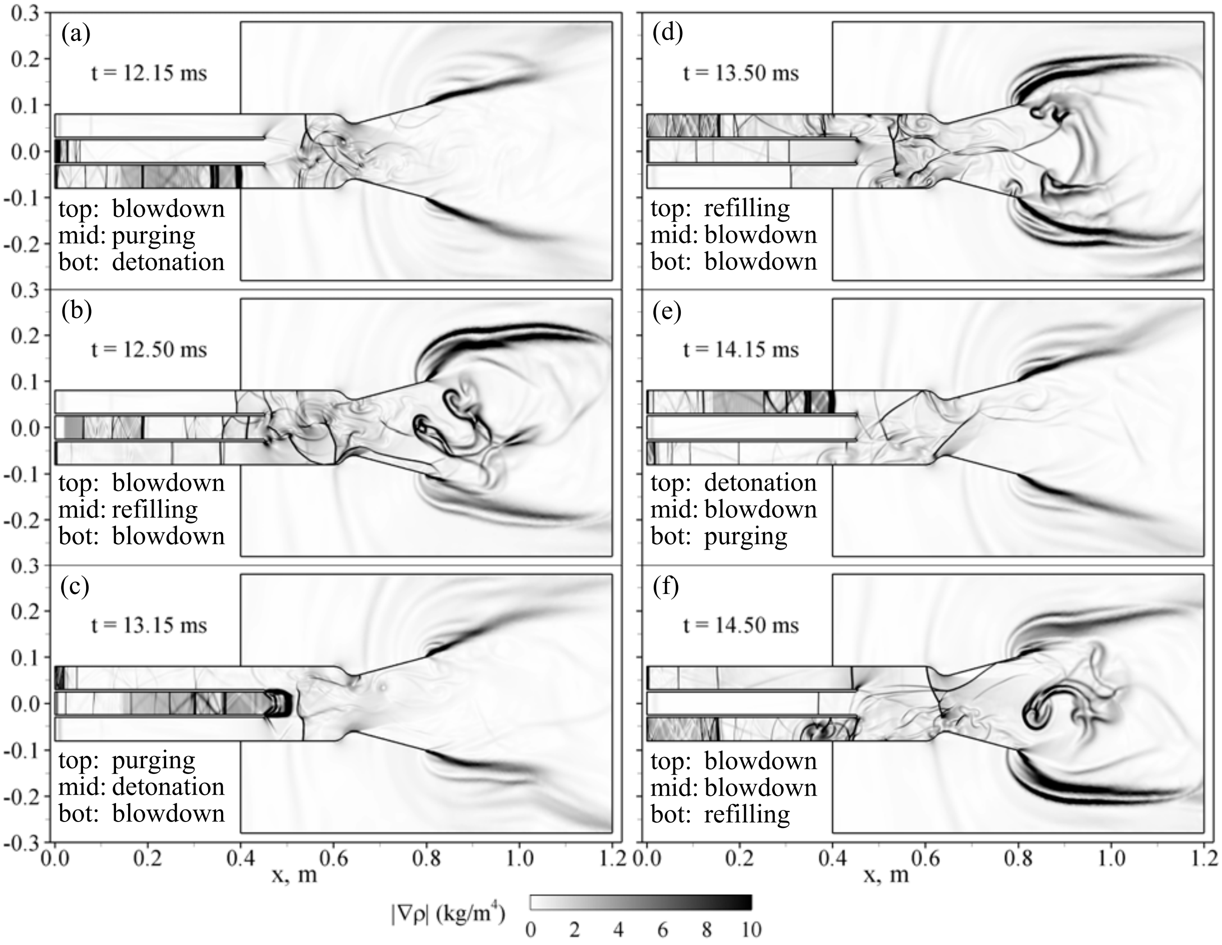

Fig. 5.18 Time evolution of density-gradient field during the fifth cycle of operation ($\tau_{cycle} = 3$ ms, $\tau_{close} = 2.1$ ms, and $\tau_{purge} = 0.1$ ms), with free volume

These shock waves represent certain internal flow loss and have no contribution to raise the detonation tube pressure. Only those shock waves that propagate back into the tubes have such contribution. The interactions of the exhaust flows and the corner zones also result in the formation of recirculation zones, as evidenced in Fig. 5.19, in which two large and one small recirculation zones between the bottom tube exit, and the upper corner and one large recirculation zone between the bottom tube exit and lower corner zone can be clearly seen. This kind of flow structure further increases the internal flow loss and is thus detrimental to the propulsive performance. A plug nozzle may be a better candidate for multitube PDE since it permits certain tube interactions through moving shock waves within the detonation tubes while keeping away the standing-like shock waves from the internal flowfield.

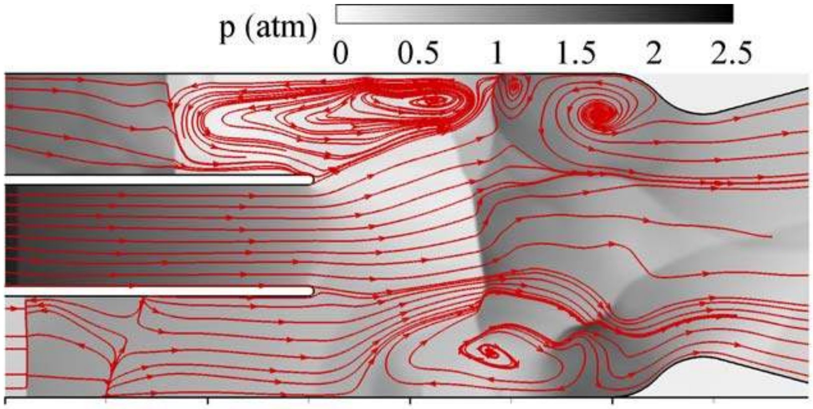

Fig. 5.19 Pressure contours and streamlines at t = 13.50 ms (τ_{cycle} = 3 ms, τ_{close} = 2.1 ms, and τ_{purge} = 0.1 ms), with free volume

Fig. 5.20 shows the instantaneous axial thrust during a steady periodic cycle for both configurations. The second peak related to the middle tube detonation is slightly reduced with the addition of the free volume, while the first and third peaks related to the other two tubes remain the same. Therefore, the improvement in operation steadiness by the free volume is very limited.

The specific impulse and specific thrust are 3372 s and 855 m/s, respectively. These values are lower than those without free volume and are even lower than those of the single-tube PDE, demonstrating a negative effect of the free volume on the propulsive performance. The performance losses are identified similarly as in Sec. III.B. The average refilling Mach number is 0.96, slightly larger than that without free volume. The imperfect nozzle expansion loss, flow divergence loss, and internal flow loss are 2.2%, 2.3%, and 15.5%, respectively. The free volume thus reduces the imperfect nozzle expansion loss. However, it leads to a significant increase in the internal flow loss, mainly due to the complicated shock waves and the recirculation zones within the free volume as aforementioned.

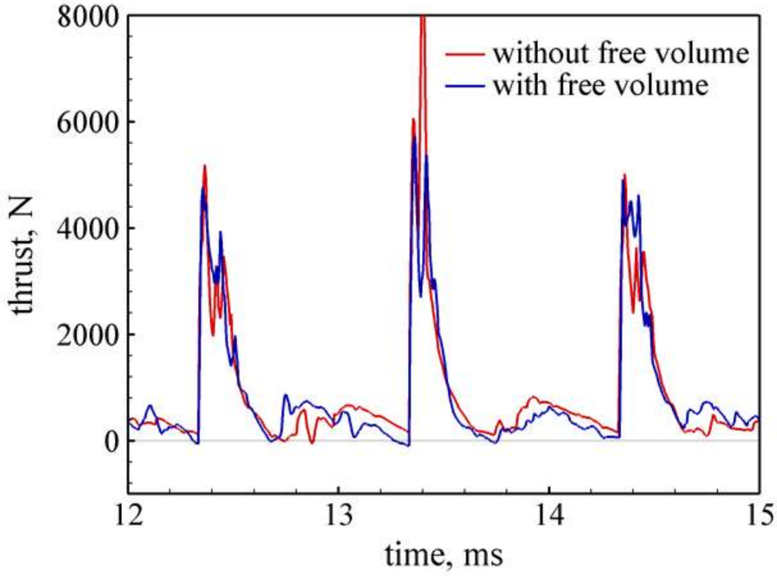

Fig. 5.20 Instantaneous axial thrust during the fifth cycle (τ_{cycle} = 3 ms, τ_{close} = 2.1 ms, and τ_{purge} = 0.1 ms)

5.3 Summary and Conclusions

The thrust chamber dynamics and propulsive performance of multitube airbreathing PDEs with repetitive operations were studied by means of two-dimensional numerical simulations. The system under consideration includes a supersonic inlet, an air manifold, a rotary valve, a triple-tube combustor, and a convergent-divergent nozzle, which is designed for a flight altitude of 9.3 km and a flight Mach number of 2.1. The flow evolution and tube interactions were studied in detail and the various loss mechanisms were identified. The effects of operating timing such as the cycle time and the valve close-up time were investigated systematically. Similar trends as those for single-tube PDEs were found. There exists an optimum frequency, and at a given frequency, a smaller valve close-up time increases the performance in most cases. Comparison with the single-tube results also demonstrates that the multitube design improves the engine performance in terms of specific impulse, operation steadiness, and timing range. The effect of the system geometry was partially assessed by considering a free volume between the detonation tubes and the common nozzle. Results indicate that the free volume helps to reduce the imperfect nozzle expansion loss and improve the engine steadiness. However, it also induces more complicated shock waves and increases the internal flow loss. The overall effect is a decrease in the propulsive performance.

The highest specific impulse obtained for the current triple-tube PDE is 3870 s at an operation frequency of 250 Hz. It exceeds its ramjet counterpart of 3866 s with perfect nozzle flow expansion and can be further improved by optimizing the operation timing and the system geometry. However, it should be also noted that some loss mechanisms not considered in the present analysis, such as the energy required for detonation initiation and the flow losses associated with the inlet isolator, rotary valve, and air distributor, may render the PDE less attractive. These losses should be counted in the future to provide more accurate comparison between PDEs and conventional engines.

The flow evolution and the system geometry effect analyses suggest that the benefit of the convergent-divergent nozzle for a multitube PDE is not as apparent as that for a single-tube PDE. A plug nozzle may be a better candidate for multitube PDE than the internal flow nozzles since it permits certain tube interactions through the moving shock waves induced by the detonations in the neighboring tubes to raise the chamber pressure while avoiding the standing-like shock waves within the internal flowfield that are detrimental to performance.

Chapter 6

Summary and Future Work

6.1 Summary

The present work studied the flow dynamics and system performance of airbreathing pulse detonation engines (PDEs) with a stoichiometric hydrogen/air mixture. The system under consideration includes a supersonic inlet, an air manifold, a rotary valve, a single-tube or multitube combustor, and a convergent-divergent (CD) nozzle, which is designed for the flight condition with a flight altitude of 9.3 km and a flight Mach number of 2.1.

Axisymmetric two-dimensional simulations are first conducted for a mixed-compression supersonic inlet to investigate the steady-state inlet flow dynamics and the response of the inlet shock system to downstream disturbances. Two different back pressures (2.1 atm and 2.2 atm) are carefully chosen such that the inlet operates at a supercritical condition to provide a sufficient shock stability margin. The response of the inlet shock system to downstream disturbances is studied by imposing periodic pressure oscillations at the exit plane. A wide range of fluctuation frequency and amplitude are investigated. Important phenomena of concern include oscillations of mass flow rate, pressure recovery, flow distribution, and terminal shock displacement. In general, the acoustic response of the inlet flow increases with increasing amplitude of the imposed oscillation, but decreases with the frequency.

A quasi-one-dimensional Euler code is then established based on the recently developed Space-Time CE/SE method, which circumvents the deficiencies of existing numerical methods for treating detonation waves and shock discontinuities, to study the flow dynamics and propulsive performance of an airbreathing PDE with a CD nozzle. The chemical kinetics is simulated using a simple one-progress variable model calibrated with the NASA CEA code. The flow dynamics is clearly depicted through numerically obtained x-t diagrams for both the first and the steady periodic cycles. Parametric studies are conducted by varying the cycle time (or frequency) and valve close-up time. Four operation frequencies (200 Hz, 250 Hz, 333 Hz, and 400 Hz) are considered. At a given frequency and purge time, a smaller valve close-up time (or a longer refilling time) increases the performance in most cases. The lower bound of the valve close-up time is subject to the constraints associated with inlet over-pressurization and combustion overfilling. The results also demonstrate the existence of an optimum frequency for a given engine configuration and flight condition.

Two-dimensional analyses are carried out for single-tube PDEs with or without CD nozzles under multicycle operation in order to provide more detailed flow dynamics and more accurate performance predictions. The two-dimensional code is efficiently parallelized by implementing the message-passing-interface (MPI) library and a domain decomposition technique. The resultant code is executed on an in-house cluster using 64 CPUs. A flow-path based performance prediction model is proposed to estimate the upper performance limit of the current PDE system. The various performance loss mechanisms, such as the imperfect nozzle expansion loss, flow divergence loss, and internal flow loss, are identified. The internal flow loss, which is mainly associated with the shock interactions within the chamber, is one of the major factors that degrade the performance of the current PDE system. The effects of operation timing including the cycle time or frequency, valve close-up time, and purge time on the propulsive performance are comprehensively studied. Results manifest the existence of an optimum operation frequency for achieving the best performance margin. At a given frequency and purge time, a smaller valve close-up time increases the performance in most cases. On the other hand, for a given frequency and valve close-up time, a larger purge time decreases the specific thrust and increases the specific impulse. The effects of nozzle configurations in terms of nozzle length and throat area on the propulsive performance are also examined. The throat area affects both the nozzle expansion process and the flow dynamics within the chamber, thus exerting a much more significant effect than the nozzle length. A smaller throat tends to increase the performance by raising the chamber pressure. However, an exceedingly small throat renders negative effects due to the related longer blowdown process and larger internal flow loss.

Finally, multitube airbreathing PDEs with repetitive operations are studied by means of two-dimensional simulations. The combustor consists of three detonation tubes. The flow evolution and tube interactions are carefully examined and the various loss mechanisms are identified. The effects of operating timing such as the cycle time and the valve close-up time were investigated systematically. Similar trends as those for single-tube PDEs were found. Comparison with the single-tube results demonstrates that the multitube design improves the engine performance in terms of specific impulse, operation steadiness, and timing range. The effect of the system geometry is partially assessed by considering a free volume between the detonation tubes and the common nozzle. Results indicate that the free volume helps to reduce the imperfect nozzle expansion loss and improve the engine steadiness. However, it also induces more complicated shock waves and increases the internal flow loss. The overall effect is a decrease in the propulsive performance.

6.2 Major Contributions and Conclusions

(1) A two-dimensional, reacting, unstructured-grid-based code is developed based on the Space-Time CE/SE method and is efficiently parallelized with the implementation of the MPI library and the domain decomposition technique.

(2) The acoustic response of the inlet flow increases with increasing amplitude of the imposed oscillation, but decreases with the frequency.

(3) For a given PDE configuration and flight condition, an optimum cycle frequency exists for achieving the best performance.

(4) For a given frequency and purge time, a longer refilling period increases the specific thrust of PDEs considered herein.

(5) A convergent-divergent (CD) nozzle can increase the propulsive performance that can be obtained with only a straight tube by up to 25%.

(6) The length of the CD nozzle has a minor effect on the performance whereas the throat area may modify the performance by up to 6%.

(7) A performance prediction model is proposed. The propulsive performances of PDEs are about 20% lower than the predictions from this model, which is attributed to

three losses: the divergence loss, the imperfect nozzle expansion loss, and the internal flow loss.

(8) The internal flow loss, which is mainly associated with the shock waves and their interactions within the internal flowfield, is the major factor that degrades the PDE propulsive performance.

(9) The multitube design slightly improves the propulsive performance of a single-tube PDE.

(10) The highest specific impulse obtained for the current triple-tube PDE is 3870 s at an operation frequency of 250 Hz, which slightly exceeds its ramjet counterpart of 3866 s with perfect nozzle flow expansion.

6.3 Recommendation for Future Work

The present inlet analysis relies on imposing periodic sinusoid pressure oscillations at the exit plane to investigate the response of the inlet shock system to downstream disturbances. Other types of oscillations may be considered to more accurately represent the disturbance from the pulsed detonation process. On the other hand, the current study didn't consider the flow dynamics within the acoustic cavity that connects the inlet and the combustor. The interaction between the inlet, acoustic cavity, and combustor should also be addressed.

In the current numerical simulations, the detonation is initiated directly by a small spark region which has neglectable effect on the performance. However, in most experiments, the detonation is initiated through a deflagration-to-detonation-transition

(DDT) process. It might be useful to incorporate this DDT process into numerical simulations so that more detailed comparisons with experiments could be made.

The present nozzle studies indicate that the convergent-divergent (CD) nozzle can significantly increase the propulsive performance of single-tube PDEs. The effect of the length and throat area of the CD nozzle is investigated. Other shape parameters such as the convergent and divergent angles could be studied in the future to aid the PDE nozzle design.

The multitube design is found to be able to improve the propulsive performance of a single-tube PDE. Further research can be conducted to investigate the effect of the number of detonation tubes and their relative positions on the flow dynamics and system performance.

The multitube PDE studies also reveal that the benefit of the CD nozzle for a multitube PDE is not as significant as that for a single-tube PDE. A plug nozzle may be a better candidate for multitube PDEs than the internal flow nozzles since it permits certain tube interactions through the moving shock waves induced by the detonations in the neighboring tubes to raise the chamber pressure while avoiding the standing-like shock waves within the internal flowfield that are detrimental to performance. This conjecture needs to be approved through further studies on plug nozzles for multitube PDEs.

Appendix A

Thermodynamic Cycle Efficiencies of Brayton, Humphrey, and Ideal PDE Cycles

Figure A.1 shows the temperature-entropy diagram for the Brayton, Humphrey, and ideal PDE cycles.

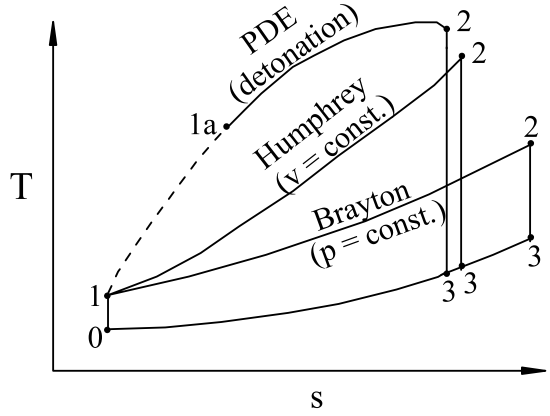

Fig. A.1 Temperature-entropy diagram

The Brayton cycle consists of an isotropic compression process (0-1), a constant-pressure heat addition process (1-2), an isotropic expansion process (2-3), and a constant-pressure cooling process (3-0). The Humphrey cycle is similar to the Brayton cycle except that the constant-pressure heat addition process (1-2) in the Brayton cycle is replaced by a constant-volume heat addition process. In the ideal PDE cycle (Heiser and Pratt, 2002), the heat addition process is modeled by a detonation process (1-1a-2), in which state 2 is the CJ state. The thermodynamic cycle efficiency η is defined as the ratio of the external work done by the cycle to the amount of thermal energy added by the heat addition process, that is,

$$\eta = 1 - \frac{q_{rej}}{q} \tag{A.1}$$

where q is the heat added during the heat addition process, and q_{rej} is the heat released to the surroundings during the cooling process. The expressions of η for the Brayton, Humphrey, and ideal PDE cycles are derived in the following subsections with the assumption of constant gas properties.

A.1 Brayton cycle

For a Brayton cycle,

$$\eta = 1 - \frac{q_{rej}}{q} = 1 - \frac{h_3 - h_0}{h_2 - h_1} = 1 - \frac{c_p (T_3 - T_0)}{c_p (T_2 - T_1)} = 1 - \frac{T_0}{T_1} \cdot \frac{T_3 / T_0 - 1}{T_2 / T_1 - 1} \tag{A.2}$$

and

$$\frac{T_3}{T_0} = \frac{T_3}{T_2} \cdot \frac{T_2}{T_1} \cdot \frac{T_1}{T_0} = \left(\frac{p_3}{p_2} \right)^{\frac{\gamma - 1}{\gamma}} \cdot \frac{T_2}{T_1} \cdot \left(\frac{p_1}{p_0} \right)^{\frac{\gamma - 1}{\gamma}} = \frac{T_2}{T_1} \tag{A.3}$$

Therefore,

$$\eta = 1 - \frac{T_0}{T_1} \tag{A.4}$$

A.2 Humphrey cycle

For a Humphrey cycle,

$$\eta = 1 - \frac{q_{rej}}{q} = 1 - \frac{h_3 - h_0}{e_2 - e_1} = 1 - \frac{c_p(T_3 - T_0)}{c_v(T_2 - T_1)} = 1 - \gamma \frac{T_0}{T_1} \cdot \frac{T_3/T_0 - 1}{T_2/T_1 - 1} \tag{A.5}$$

and

$$\begin{aligned} \frac{T_3}{T_0} &= \frac{T_3}{T_2} \cdot \frac{T_2}{T_1} \cdot \frac{T_1}{T_0} = \left(\frac{p_3}{p_2}\right)^{\frac{\gamma-1}{\gamma}} \cdot \frac{T_2}{T_1} \cdot \frac{T_1}{T_0} \\ &= \left(\frac{p_0}{p_1} \cdot \frac{p_1}{p_2}\right)^{\frac{\gamma-1}{\gamma}} \cdot \frac{T_2}{T_1} \cdot \frac{T_1}{T_0} = \frac{T_0}{T_1} \cdot \left(\frac{T_1}{T_2}\right)^{\frac{\gamma-1}{\gamma}} \cdot \frac{T_2}{T_1} \cdot \frac{T_1}{T_0} = \left(\frac{T_2}{T_1}\right)^{\frac{1}{\gamma}} \end{aligned} \tag{A.6}$$

Therefore,

$$\eta = 1 - \gamma \frac{T_0}{T_1} \cdot \frac{(T_2/T_1)^{1/\gamma} - 1}{T_2/T_1 - 1} \tag{A.7}$$

On the other hand, since

$$q = c_v(T_2 - T_1) = c_p(T_2 - T_1)/\gamma \tag{A.8}$$

then η can also be expressed as:

$$\eta = 1 - \frac{T_0}{T_1} \cdot \frac{(1 + \gamma \tilde{q})^{1/\gamma} - 1}{\tilde{q}} \tag{A.9}$$

where

$$\tilde{q} \equiv q/(c_p T_1) \tag{A.10}$$

A.3 Ideal PDE cycle

For an ideal PDE cycle,

$$\eta = 1 - \frac{q_{rej}}{q} = 1 - \frac{c_p(T_3 - T_0)}{q} = 1 - \frac{T_0}{T_1} \cdot \frac{T_3/T_0 - 1}{q/(c_p T_1)} = 1 - \frac{T_0}{T_1} \cdot \frac{T_3/T_0 - 1}{\tilde{q}} \tag{A.11}$$

The temperature ratio T_3/T_0 can be derived as follows:

$$\frac{T_3}{T_0} = \frac{T_3}{T_2} \cdot \frac{T_2}{T_1} \cdot \frac{T_1}{T_0} \tag{A.12}$$

$$\frac{T_3}{T_2} = \left(\frac{p_3}{p_2}\right)^{\frac{\gamma-1}{\gamma}} = \left(\frac{p_0}{p_1} \cdot \frac{p_1}{p_2}\right)^{\frac{\gamma-1}{\gamma}} = \frac{T_0}{T_1} \cdot \left(\frac{p_2}{p_1}\right)^{-\frac{\gamma-1}{\gamma}} \tag{A.13}$$

The property variations across the detonation wave have been derived in Chapter 1:

$$\frac{p_2}{p_1} = \frac{1 + \gamma M_D{}^2}{1 + \gamma}, \quad \frac{T_2}{T_1} = \left(\frac{1 + \gamma M_D{}^2}{(1 + \gamma) M_D}\right)^2 \tag{A.14}$$

where the detonation wave Mach number M_D is determined from:

$$M_D = \sqrt{\frac{\gamma^2 - 1}{2\gamma} \frac{q}{R T_1}} + \sqrt{\frac{\gamma^2 - 1}{2\gamma} \frac{q}{R T_1} + 1} = \sqrt{\frac{\gamma + 1}{2} \tilde{q}} + \sqrt{\frac{\gamma + 1}{2} \tilde{q} + 1} \tag{A.15}$$

Substitution of Eqs. (A.13) and (A.14) into Eq. (A.12) leads to

$$\frac{T_3}{T_0} = \frac{1}{M_D{}^2} \left(\frac{1 + \gamma M_D{}^2}{1 + \gamma}\right)^{\frac{\gamma+1}{\gamma}} \tag{A.16}$$

Therefore, the ideal PDE thermodynamic cycle efficiency is

$$\eta = 1 - \frac{T_0}{T_1} \cdot \frac{\frac{1}{M_D{}^2} \left(\frac{1 + \gamma M_D{}^2}{1 + \gamma}\right)^{(\gamma+1)/\gamma} - 1}{\tilde{q}} \tag{A.17}$$

Appendix B

Jacobian Matrices for Quasi-One- and Two-Dimensional Systems

B.1 Quasi-One-Dimensional System

The Jacobian matrices $A \equiv \dfrac{\partial \mathbf{E}}{\partial \mathbf{Q}}$ and $D \equiv \dfrac{\partial \mathbf{H}}{\partial \mathbf{Q}}$ are

$$A = \begin{bmatrix} 0 & 1 & 0 & 0 \\ \frac{1}{2}[(\gamma-3)u^2] & -(\gamma-3)u & \gamma-1 & -(\gamma-1)q \\ \begin{array}{c} -u(e_t + p/\rho) \\ +(\gamma-1)u^3/2 \end{array} & \begin{array}{c} e_t + p/\rho \\ -(\gamma-1)u^2 \end{array} & \gamma u & -(\gamma-1)qu \\ -uZ & Z & 0 & u \end{bmatrix} \tag{B.1}$$

$$D = -\frac{1}{A}\frac{dA}{dx}\begin{bmatrix} 0 & 1 & 0 & 0 \\ -u^2 & 2u & 0 & 0 \\ A_{31} & A_{32} & A_{33} & A_{34} \\ -uZ & Z & 0 & u \end{bmatrix} + \begin{bmatrix} 0 & 0 & 0 & 0 \\ 0 & 0 & 0 & 0 \\ 0 & 0 & 0 & 0 \\ d_{41} & d_{42} & d_{43} & d_{44} \end{bmatrix} \tag{B.2}$$

where A in Eq. (B.2) represents the area, and

$$\begin{aligned} d_{41} &= -d_{43}[e_t - u^2 - qZ] \\ d_{42} &= -d_{43}u \\ d_{43} &= (\gamma-1)h_4 E_a \rho / p^2 \\ d_{44} &= -d_{43}q - K\exp(-E_a \rho / p) \end{aligned} \tag{B.3}$$

B.2 Two-Dimensional System

Jacobian matrices $A \equiv \dfrac{\partial \mathbf{E}}{\partial \mathbf{Q}}$, $B \equiv \dfrac{\partial \mathbf{F}}{\partial \mathbf{Q}}$, and $D \equiv \dfrac{\partial \mathbf{H}}{\partial \mathbf{Q}}$ are

$$A = \begin{bmatrix} 0 & 1 & 0 & 0 & 0 \\ \frac{1}{2}[(\gamma-3)u^2+(\gamma-1)v^2] & -(\gamma-3)u & -(\gamma-1)v & \gamma-1 & -(\gamma-1)q \\ -uv & v & u & 0 & 0 \\ \begin{matrix} -u(e_t+p/\rho) \\ +(\gamma-1)u(u^2+v^2)/2 \end{matrix} & \begin{matrix} e_t+p/\rho \\ -(\gamma-1)u^2 \end{matrix} & -(\gamma-1)uv & \gamma u & -(\gamma-1)qu \\ -uZ & Z & 0 & 0 & u \end{bmatrix} \quad \text{(B.4)}$$

$$B = \begin{bmatrix} 0 & 0 & 1 & 0 & 0 \\ -uv & v & u & 0 & 0 \\ \frac{1}{2}[(\gamma-3)v^2+(\gamma-1)u^2] & -(\gamma-1)u & -(\gamma-3)v & \gamma-1 & -(\gamma-1)q \\ \begin{matrix} -v(e_t+p/\rho) \\ +(\gamma-1)v(u^2+v^2)/2 \end{matrix} & -(\gamma-1)uv & \begin{matrix} e_t+p/\rho \\ -(\gamma-1)v^2 \end{matrix} & \gamma v & -(\gamma-1)qv \\ -vZ & 0 & Z & 0 & v \end{bmatrix} \quad \text{(B.5)}$$

$$D = \begin{bmatrix} 0 & 0 & 0 & 0 & 0 \\ 0 & 0 & 0 & 0 & 0 \\ 0 & 0 & 0 & 0 & 0 \\ 0 & 0 & 0 & 0 & 0 \\ d_{51} & d_{52} & d_{53} & d_{54} & d_{55} \end{bmatrix} \tag{B.6}$$

where

$$\begin{aligned} d_{51} &= -d_{54}[e_t - (u^2 + v^2) - qZ] \\ d_{52} &= -d_{54}u \\ d_{53} &= -d_{54}v \\ d_{54} &= (\gamma - 1)h_5 E_a \rho / p^2 \\ d_{55} &= -d_{54}q - K\exp(-E_a \rho / p) \end{aligned} \tag{B.7}$$

Appendix C

Procedures of Building x-t Diagram

The common way to obtain the x-t diagram is the Lagrangian approach, in which a number of points are placed in the flowfield and move at characteristic velocities u, $u+c$, and $u-c$. A major drawback of this approach is the large cumulative error during the tracing process. In addition, special handling is needed when the points move out of the computational domain.

In this thesis, an Euler approach was proposed. The basic idea of this approach is that the characteristic lines are equivalent to the streamlines in the (x, t) plane with a characteristic velocity in the x direction and a unit velocity in the t direction. For example, since

$$dx/dt = u\,,\quad dt/dt = 1 \tag{C.1}$$

the characteristic lines of $dx/dt = u$ are equivalent to the streamlines in the (x, t) plane with velocity (u, 1). The x-t diagram is constructed based on the following procedures:

1) At each time step, output the following information to a file at every i_{skip} (for example, i_{skip} = 10) grid points: x, t, u, $u+c$, $u-c$, 1.d0.
2) Use Tecplot to draw streamlines in the (x, t) plane with velocities of (u, 1), ($u+c$, 1), and ($u-c$, 1). Several trials may be needed in placing the streamlines to determine the Taylor wave, the contact surfaces, the detonation wave front, and so forth.

Appendix D

Space-Time CE/SE Method for Two-Dimensional Problems

A two-dimensional, unstructured triangular mesh Euler solver for non-reacting flows based on the space-time conservation element and solution element (CE/SE) method has been developed by Wang and Chang (1999). The ideas and solution procedure are similar to those for one-dimensional problems described in Sec. 3.1.2. For the purpose of completeness, this appendix describes the space-time CE/SE method, including the basic solution procedure, the extended scheme, and source term handling for two-dimensional problems.

D.1 Governing Equations and Their Integral Form

For clarity, the two-dimensional governing equations without source term is first considered, which is expressed in a vector form as below:

$$\frac{\partial Q}{\partial t}+\frac{\partial E}{\partial x}+\frac{\partial F}{\partial y}=0 \tag{D.1}$$

where Q is the dependent variable vector, E and F are convective flux vectors. The governing equations with source term will be considered in Sec. D.5.

Let $x_1 = x$, $x_2 = y$, $x_3 = t$ be the coordinates of a three-dimensional Euclidean space E_3. Then the integral form of Eq. (D.1) in space-time E_3 is

$$\oint_{S(V)} \mathbf{h}\cdot d\mathbf{s}=0 \tag{D.2}$$

where $\mathbf{h} = (E, F, Q)$ is the flux vector in E_3, $S(V)$ the boundary of an arbitrary space-time region V in E_3, and $d\mathbf{s}$ the surface vector of an infinitesimal surface in E_3.

D.2 Triangular Mesh, Conservation Element, and Solution Element

The present 2-D CE/SE solver is constructed for an unstructured triangular mesh. Figure D.1 shows an arbitrary triangular cell ($\Delta V_1V_2V_3$) and its three neighbor cells. Points C, C_1, C_2, and C_3, as marked by the circles in Fig. D.1, are the centroids of the center cell and the three neighbor cells, respectively. The centroids of the neighbor cells and the vertices of the center cell form a hexagon ($C_1V_3C_2V_1C_3V_2$). The centroid of this hexagon, point S, is referred to as the solution point of the center cell. Each cell is associated with a unique solution point (marked by cross in Fig. D.1) at which the dependent variable vector and its spatial derivatives are defined and solved. In general the solution points don't coincide with the cell centroids except for the uniform mesh. The hexagon $C_1V_3C_2V_1C_3V_2$ is composed of three quadrilaterals: $C_1V_3CV_2$, $C_2V_1CV_3$, and $C_3V_2CV_1$. The centroids of these three quadrilaterals are E_1, E_2, and E_3, respectively.

The conservation element and solution element associated with cell j at the nth time level are shown schematically in Fig. D.2. The superscripts (') and ('') are used to denote the $n-1$ and $n+1$th time levels, respectively. The conservation element CE(j, n) is defined by the hexagonal cylinder $C_1V_3C_2V_1C_3V_2C_1'V_3'C_2'V_1'C_3'V_2'$. It is composed of three sub-CEs: $CE_r(j, n)$, $r = 1,2,3$. Each sub-CE is a quadrilateral cylinder in the E_3-space. The solution element SE(j, n) is the union of three vertical plane segments and a horizontal plane segment.

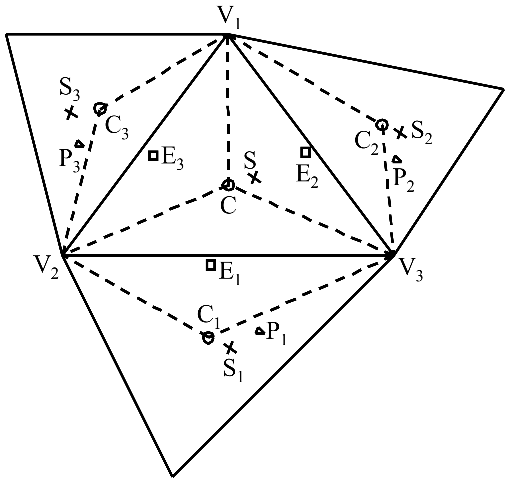

Fig. D.1 A triangular cell and its three neighbours

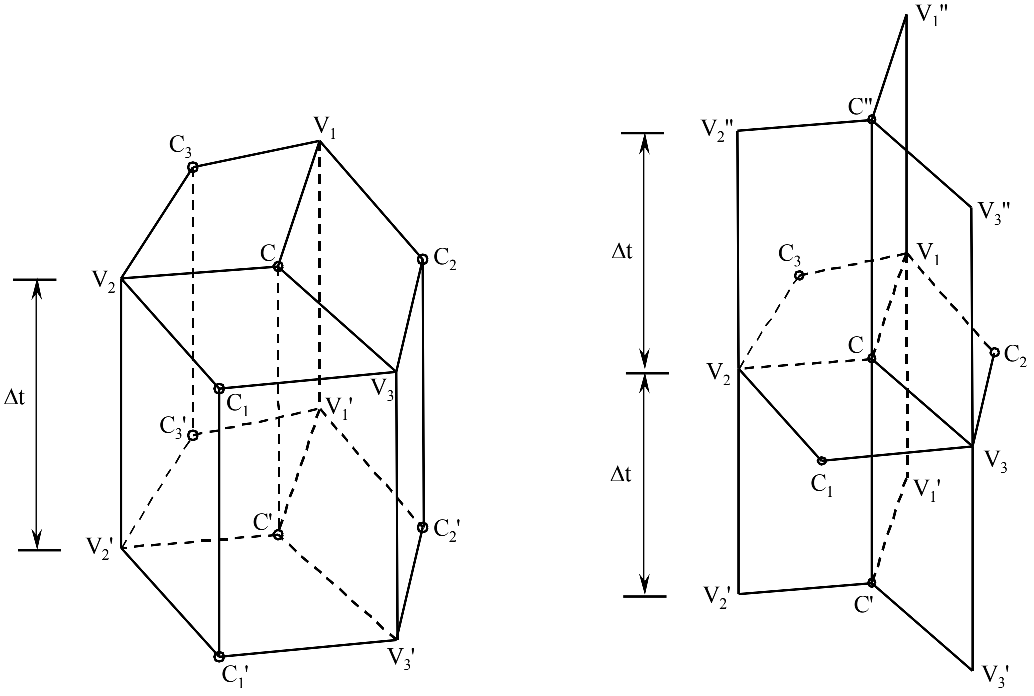

(a) conservation element CE(j, n)

(b) solution element SE(j, n)

Fig. D.2 Schematic of CE and SE associated with solution point (j, n)

D.3 Basic Solution Procedure

For any point $(x, y, t) \in \mathrm{SE}(j, n)$, let $Q(x, y, t)$, $E(x, y, t)$, and $F(x, y, t)$, respectively, be approximated by $Q^*(x, y, t; j, n)$, $E^*(x, y, t; j, n)$, and $F^*(x, y, t; j, n)$ through the following first-order Taylor's expansions,

$$Q^*(x,y,t;j,n) = Q_j^n + (Q_x)_j^n(x - x_j) + (Q_y)_j^n(y - y_j) + (Q_t)_j^n(t - t^n) \tag{D.3}$$

$$E^*(x,y,t;j,n) = E_j^n + (E_x)_j^n(x - x_j) + (E_y)_j^n(y - y_j) + (E_t)_j^n(t - t^n) \tag{D.4}$$

$$F^*(x,y,t;j,n) = F_j^n + (F_x)_j^n(x - x_j) + (F_y)_j^n(y - y_j) + (F_t)_j^n(t - t^n) \tag{D.5}$$

where the label $(\,)_j^n$ denotes the corresponding quantities evaluated at solution point (j, n) whose coordinate is (x_j, y_j, t^n). Also note that E_j^n and F_j^n are functions only of Q_j^n, and that $(E_x)_j^n$, $(E_y)_j^n$, $(E_t)_j^n$, $(F_x)_j^n$, $(F_y)_j^n$, and $(F_t)_j^n$ are functions of Q_j^n, $(Q_x)_j^n$, $(Q_y)_j^n$, and $(Q_t)_j^n$:

$$E_j^n = A_j^n Q_j^n, \quad (E_x)_j^n = A_j^n (Q_x)_j^n, \quad (E_y)_j^n = A_j^n (Q_y)_j^n, \quad (E_t)_j^n = A_j^n (Q_t)_j^n \tag{D.6}$$

$$F_j^n = B_j^n Q_j^n, \quad (F_x)_j^n = B_j^n (Q_x)_j^n, \quad (F_y)_j^n = B_j^n (Q_y)_j^n, \quad (F_t)_j^n = B_j^n (Q_t)_j^n \tag{D.7}$$

where $A \equiv \dfrac{\partial E}{\partial Q}$ and $B \equiv \dfrac{\partial F}{\partial Q}$ are the Jacobian matrices of the convective flux vectors E and F, respectively.

Moreover, let Q^*, E^*, and F^* satisfy the differential governing equation at the solution point (j, n),

$$\frac{\partial Q^*}{\partial t} + \frac{\partial E^*}{\partial x} + \frac{\partial F^*}{\partial y} = 0 \tag{D.8}$$

The following relation can be obtained,

$$(Q_t)_j^n = -(E_x)_j^n - (F_y)_j^n = -(AQ_x + BQ_y)_j^n \tag{D.9}$$

which means that $(Q_t)_j^n$ is a function of Q_j^n, $(Q_x)_j^n$, and $(Q_y)_j^n$. Therefore, there are three sets of unknown variables at solution point (*j*, *n*), i.e., Q_j^n, $(Q_x)_j^n$, and $(Q_y)_j^n$. These unknowns can be solved from the following three flux conservation equations:

$$\oint_{S(CE_r(j,n))} \mathbf{h}^* \cdot d\mathbf{s} = 0, \quad r = 1,2,3 \tag{D.10}$$

where $\mathbf{h}^* = (E^*, F^*, Q^*)$. Details of the solving procedure are given below.

For each CE$_r$(*j*, *n*) there are six faces, as indicated in Fig. D.2. Let $\mathbf{S}_j^{(r)}$ and $\mathbf{S}_j^{(r,b)}$, respectively, denote the surface vectors of the top and bottom faces, and $\mathbf{S}_j^{(r,i)}$, i = 1,2,3,4, denote the surface vectors of the four lateral faces, with i = 1 and 2 for the two lateral faces associated with point C$_r$, and i = 3 and 4 for the two lateral faces associated with point C. All these surface vectors are knowns defined by the geometires. For example, the six surface vectors for CE$_1$(*j*, *n*) are:

$$\mathbf{S}_j^{(1)} = S_j^{(1)} \ (0,\ 0,\ 1) \tag{D.11}$$

$$\mathbf{S}_j^{(1,b)} = S_j^{(1)} \ (0,\ 0,\ -1) \tag{D.12}$$

$$\mathbf{S}_j^{(1,1)} = (S_{jx}^{(1,1)},\ S_{jy}^{(1,1)},\ 0) = \Delta t\ (-y_j^{V_2} + y_j^{C_1},\ x_j^{V_2} - x_j^{C_1},\ 0) \tag{D.13}$$

$$\mathbf{S}_j^{(1,2)} = (S_{jx}^{(1,2)},\ S_{jy}^{(1,2)},\ 0) = \Delta t\ (y_j^{V_3} - y_j^{C_1},\ -x_j^{V_3} + x_j^{C_1},\ 0) \tag{D.14}$$

$$\mathbf{S}_j^{(1,3)} = (S_{jx}^{(1,3)},\ S_{jy}^{(1,3)},\ 0) = \Delta t\ (y_j^{V_2} - y_j^{C},\ -x_j^{V_2} + x_j^{C},\ 0) \tag{D.15}$$

$$\mathbf{S}_j^{(1,4)} = (S_{jx}^{(1,4)},\ S_{jy}^{(1,4)},\ 0) = \Delta t\ (-y_j^{V_3} + y_j^{C},\ x_j^{V_3} - x_j^{C},\ 0) \tag{D.16}$$

On the other hand, because $\mathbf{h}^*$ is linear in *x*, *y*, and *t* within each SE, the flux of $\mathbf{h}^*$ leaving CE$_r$(*j*, *n*) through any one of the six faces is equal to the product of the vector $\mathbf{h}^*$

evaluated at the centroid of the face and the surface vector of that face. Let point F$_{\text{ri}}$ (i = 1,2,3,4) denotes the centroid of the ith lateral face of CE$_r$(j, n). Then the flux conservation equation (D.10) can be expressed out as

$$Q^{*E_r} S_j^{(r)} - Q^{*E_r^{'}} S_j^{(r)} + \sum_{i=1}^{4} (E^{*F_{ri}} S_{jx}^{(r,i)} + F^{*F_{ri}} S_{jx}^{(r,i)}) = 0, \quad r = 1,2,3 \tag{D.17}$$

where

$$Q^{*E_r} = Q_j^n + (Q_x)_j^n (x_j^{E_r} - x_j) + (Q_y)_j^n (y_j^{E_r} - y_j) \tag{D.18}$$

$$Q^{*E_r^{'}} = Q_{j_r}^{n-1} + (Q_x)_{j_r}^{n-1} (x_j^{E_r} - x_{j_r}) + (Q_y)_{j_r}^{n-1} (y_j^{E_r} - y_{j_r}) \tag{D.19}$$

$$E^{*F_{ri}} = E_j^n + (E_x)_j^n (x_j^{F_{ri}} - x_j) + (E_y)_j^n (y_j^{F_{ri}} - y_j) - (E_t)_j^n \Delta t / 2, \quad i = 3,4 \tag{D.20}$$

$$F^{*F_{ri}} = F_j^n + (F_x)_j^n (x_j^{F_{ri}} - x_j) + (F_y)_j^n (y_j^{F_{ri}} - y_j) - (F_t)_j^n \Delta t / 2, \quad i = 3,4 \tag{D.21}$$

$$E^{*F_{ri}} = E_{j_r}^{n-1} + (E_x)_{j_r}^{n-1} (x_j^{F_{ri}} - x_{j_r}) + (E_y)_{j_r}^{n-1} (y_j^{F_{ri}} - y_{j_r}) + (E_t)_{j_r}^{n-1} \Delta t / 2, \quad i = 1,2 \tag{D.22}$$

$$F^{*F_{ri}} = F_{j_r}^{n-1} + (F_x)_{j_r}^{n-1} (x_j^{F_{ri}} - x_{j_r}) + (F_y)_{j_r}^{n-1} (y_j^{F_{ri}} - y_{j_r}) + (F_t)_{j_r}^{n-1} \Delta t / 2, \quad i = 1,2 \tag{D.23}$$

Here the index j_r represents cell j's rth neighbor with point C$_r$ as its centroid. Using Eqs. (D.6) and (D.7), Eq. (D.17) can be further expressed in terms of Q, Q_x, and Q_y as

$$(L_r \cdot Q + L_r^x \cdot Q_x + L_r^y \cdot Q_y)_j^n = (R_r \cdot Q + R_r^x \cdot Q_x + R_r^y \cdot Q_y)_{j_r}^{n-1}, \quad r = 1,2,3 \tag{D.24}$$

where

$$L_r = S_j^{(r)} \cdot I + (K^{(r,3)} + K^{(r,4)}) \tag{D.25}$$

$$L_r^x = (x_j^{E_r} - x_j) S_j^{(r)} \cdot I + \sum_{i=3}^{4} (x_j^{F_{ri}} - x_j) K^{(r,i)} + \frac{\Delta t}{2} (K^{(r,3)} + K^{(r,4)}) \cdot A \tag{D.26}$$

$$L_r^y = (y_j^{E_r} - y_j) S_j^{(r)} \cdot I + \sum_{i=3}^{4} (y_j^{F_{ri}} - y_j) K^{(r,i)} + \frac{\Delta t}{2} (K^{(r,3)} + K^{(r,4)}) \cdot B \tag{D.27}$$

$$R_r = S_j^{(r)} \cdot I - (K^{(r,1)} + K^{(r,2)}) \tag{D.28}$$

$$R_r^x = (x_j^{E_r} - x_{j_r}) S_j^{(r)} \cdot I - \sum_{i=1}^{2} (x_j^{F_{ri}} - x_{j_r}) K^{(r,i)} + \frac{\Delta t}{2} (K^{(r,1)} + K^{(r,2)}) \cdot A \tag{D.29}$$

$$R_r^y = (y_j^{E_r} - y_{j_r}) S_j^{(r)} \cdot I - \sum_{i=1}^{2} (y_j^{F_{ri}} - y_{j_r}) K^{(r,i)} + \frac{\Delta t}{2} (K^{(r,1)} + K^{(r,2)}) \cdot B \tag{D.30}$$

and $K^{(r,i)}$ is defined as:

$$K^{(r,i)} = A_{j_r}^{n-1} S_{jx}^{(r,i)} + B_{j_r}^{n-1} S_{jy}^{(r,i)}, \quad i = 1,2 \tag{D.31}$$

$$K^{(r,i)} = A_j^n S_{jx}^{(r,i)} + B_j^n S_{jy}^{(r,i)}, \quad i = 3,4 \tag{D.32}$$

It is easy to prove that,

$$L_1 + L_2 + L_3 = (S_j^{(1)} + S_j^{(2)} + S_j^{(3)}) \cdot I + \sum_{r=1}^{3} (K^{(r,3)} + K^{(r,4)}) = S_j \cdot I \tag{D.33}$$

$$L_1^x + L_2^x + L_3^x = 0 \tag{D.34}$$

$$L_1^y + L_2^y + L_3^y = 0 \tag{D.35}$$

The dependent variable vector Q_j^n can be solved by summing Eq. (D.24) over r = 1,2,3,

$$Q_j^n = \frac{1}{S_j} \sum_{r=1}^{3} (R_r \cdot Q + R_r^x \cdot Q_x + R_r^y \cdot Q_y)_{j_r}^{n-1} \tag{D.36}$$

And the spatial derivatives $(Q_x)_j^n$ and $(Q_y)_j^n$ can then be obtained as:

$$\begin{pmatrix} (Q_x)_j^n \\ (Q_y)_j^n \end{pmatrix} = \begin{pmatrix} L_1^x & L_1^y \\ L_2^x & L_2^y \end{pmatrix}^{-1} \cdot \begin{pmatrix} RHS_1 - L_1 \cdot Q_j^n \\ RHS_2 - L_2 \cdot Q_j^n \end{pmatrix} \tag{D.37}$$

where

$$RHS_r = (R_r \cdot Q + R_r^x \cdot Q_x + R_r^y \cdot Q_y)_{j_r}^{n-1} \tag{D.38}$$

D.4 The Extended Scheme

The basic solution procedure is usually referred to as the Euler *a* scheme (Wang and Chang, 1999) which needs no free parameter and has nearly no numerical dissipation. This *a* scheme, however, is not equipped to suppress numerical wiggles that generally appear within the region with large gradient or discontinuity. Moreover, it is not computationally efficient since a large part of the computation time is spent on calculating the derivatives of the mesh variable (Q_x and Q_y) as indicated by Eq. (D.37). As remedies for these deficiencies, several extended schemes, such as the Euler a-ε and a-ε-α-β schemes were then proposed (Chang, 1995; Wang and Chang, 1999). In this thesis, only one parameter, α, was introduced to control the numerical dissipation. This scheme, as described in the following paragraphs, is a special case of the a-ε-α-β scheme with $\varepsilon = 1/2$ and $\beta = 1$ (Wang and Chang, 1999). Several remarks on the parameters ε, α, and β were given by Chang et al. (1999).

To proceed, some geometry-related preliminaries are first introduced. Let ϕ be a linear function of *x* and *y* in a spatial plane $P_1P_2P_3$, and ϕ_1, ϕ_2, and ϕ_3 be the function values at point P_1, P_2, and P_3, respectively, then

$$\phi_1 - \phi_3 = (x_1 - x_3)\phi_x + (y_1 - y_3)\phi_y \qquad \text{(D.39)}$$

$$\phi_2 - \phi_3 = (x_2 - x_3)\phi_x + (y_2 - y_3)\phi_y \qquad \text{(D.40)}$$

The partial derivatives ϕ_x and ϕ_y can thus be solved as:

$$\phi_x = \Delta_x / \Delta \qquad \text{(D.41)}$$

$$\phi_y = \Delta_y / \Delta \qquad \text{(D.42)}$$

where

$$\Delta = \begin{vmatrix} x_1 - x_3 & y_1 - y_3 \\ x_2 - x_3 & y_2 - y_3 \end{vmatrix} \tag{D.43}$$

$$\Delta_x = \begin{vmatrix} \phi_1 - \phi_3 & y_1 - y_3 \\ \phi_2 - \phi_3 & y_2 - y_3 \end{vmatrix} \tag{D.44}$$

$$\Delta_y = \begin{vmatrix} x_1 - x_3 & \phi_1 - \phi_3 \\ x_2 - x_3 & \phi_2 - \phi_3 \end{vmatrix} \tag{D.45}$$

With the above preliminaries, construct plane $\mathrm{P_1P_2P_3}$ so that the solution point S is its centroid. The spatial coordinates of point $\mathrm{P_r}$ are

$$x^{\mathrm{P_r}} = x_{j_r} + (x_j - \frac{1}{3}\sum_{r=1}^{3} x_{j_r}) \tag{D.46}$$

$$y^{\mathrm{P_r}} = y_{j_r} + (y_j - \frac{1}{3}\sum_{r=1}^{3} y_{j_r}) \tag{D.47}$$

The variable Q at point $\mathrm{P_r}$ is evaluated as

$$\begin{aligned} Q^{\mathrm{P_r}} &= Q^*(x^{\mathrm{P_r}}, y^{\mathrm{P_r}}, t^n; j_r, n-1) \\ &= Q_{j_r}^{n-1} + (Q_x)_{j_r}^{n-1}(x^{\mathrm{P_r}} - x_{j_r}) + (Q_y)_{j_r}^{n-1}(y^{\mathrm{P_r}} - y_{j_r}) + (Q_t)_{j_r}^{n-1} \cdot \frac{1}{2}\Delta t \end{aligned} \tag{D.48}$$

Let planes #1, 2 and 3, respectively, be the planes containing $\mathrm{SP_2P_3}$, $\mathrm{SP_3P_1}$ and $\mathrm{SP_1P_2}$, then Q_x, and Q_y on plane #r can be evaluated as

$$(Q_x^{(r)})_j{}^n = \Delta_x^{(r)} \big/ \Delta^{(r)} \tag{D.49}$$

$$(Q_y^{(r)})_j{}^n = \Delta_y^{(r)} \big/ \Delta^{(r)} \tag{D.50}$$

where

$$\Delta^{(1)} = \begin{vmatrix} x^{\mathrm{P_2}} - x_j & y^{P_2} - y_j \\ x^{\mathrm{P_3}} - x_j & y^{P_3} - y_j \end{vmatrix} \tag{D.51}$$

$$\Delta_x^{(1)} = \begin{vmatrix} Q^{\mathrm{P}_2} - Q_j^{\ n} & y^{P_2} - y_j \\ Q^{\mathrm{P}_2} - Q_j^{\ n} & y^{P_3} - y_j \end{vmatrix} \tag{D.52}$$

$$\Delta_y^{(1)} = \begin{vmatrix} x^{\mathrm{P}_2} - x_j & Q^{\mathrm{P}_2} - Q_j^{\ n} \\ x^{\mathrm{P}_3} - x_j & Q^{\mathrm{P}_3} - Q_j^{\ n} \end{vmatrix} \tag{D.53}$$

and $\Delta^{(r)}$, $\Delta_x^{(r)}$, and $\Delta_y^{(r)}$ ($r = 2,3$) are defined by replacing the points P$_2$ and P$_3$ in the above equations with P$_3$ and P$_1$, and P$_1$ and P$_2$, respectively.

With these $Q_x^{(r)}$ and $Q_y^{(r)}$ available, Q_x and Q_y can be obtained through a simple arrange,

$$(Q_x)_j^{\ n} = \frac{1}{3}\sum_{r=1}^{3}(Q_x^{(r)})_j^{\ n} \tag{D.54}$$

$$(Q_y)_j^{\ n} = \frac{1}{3}\sum_{r=1}^{3}(Q_y^{(r)})_j^{\ n} \tag{D.55}$$

Alternatively, this simple average can be further improved by the following weighted average:

$$(Q_x)_j^n = \left.\frac{(\theta_2\theta_3)^\alpha Q_x^{(1)} + (\theta_3\theta_1)^\alpha Q_x^{(2)} + (\theta_1\theta_2)^\alpha Q_x^{(3)}}{(\theta_2\theta_3)^\alpha + (\theta_3\theta_1)^\alpha + (\theta_1\theta_2)^\alpha}\right|_j^n \tag{D.56}$$

$$(Q_y)_j^n = \left.\frac{(\theta_2\theta_3)^\alpha Q_y^{(1)} + (\theta_3\theta_1)^\alpha Q_y^{(2)} + (\theta_1\theta_2)^\alpha Q_y^{(3)}}{(\theta_2\theta_3)^\alpha + (\theta_3\theta_1)^\alpha + (\theta_1\theta_2)^\alpha}\right|_j^n \tag{D.57}$$

where

$$(\theta_r)_j^n = \sqrt{[(Q_x^{(r)})_j^n]^2 + [(Q_y^{(r)})_j^n]^2} \tag{D.58}$$

and α $(\alpha \geq 0)$ is an adjustable constant to control the numerical dissipation and usually chosen to be 1 or 2. Note that to avoid dividing by zero in Eqs. (D.56) and (D.57), a small positive number such as 10^{-60} may be added to the denominators.

The *a-ε-α-β* scheme proposed by Wang and Chang (1999) solves the spatial derivatives as follows:

$$Q_x = Q_x^a + 2\varepsilon(Q_x^c - Q_x^a) + \beta(Q_x^w - Q_x^c) \qquad \text{(D.59)}$$

$$Q_y = Q_y^a + 2\varepsilon(Q_y^c - Q_y^a) + \beta(Q_y^w - Q_y^c) \qquad \text{(D.60)}$$

where the superscript *a*, *c* and *w*, respectively, denote the spatial derivatives obtained by the basic solution procedure with Eq. (D.37), the simple average with Eqs. (D.54) and (D.55), and the weighted average with Eqs (D.56) and (D.57). The stability condition for the *a-ε-α-β* scheme is

$$0 \leq \varepsilon \leq 1, \quad \beta \geq 0, \quad \alpha \geq 0, \quad \text{and} \quad CFL \leq 1 \qquad \text{(D.61)}$$

D.5 Source Term Treatment

The two-dimensional governing equations with source term is expressed as:

$$\frac{\partial Q}{\partial t} + \frac{\partial E}{\partial x} + \frac{\partial F}{\partial y} = H \qquad \text{(D.62)}$$

where *Q* is the dependent variable vector, *E* and *F* are convective flux vectors, and *H* the source term vector. The integral form in space-time E_3 is

$$\oint_{S(V)} \mathbf{h} \cdot d\mathbf{s} = \int_V H dV \qquad \text{(D.63)}$$

where dV is an infinitesimal volume in E_3.

The solution procedure is similar to that without source term. Only a few equations need to be updated. Let Q^*, E^*, F^*, and H satisfy the differential governing equation at the solution point (j, n),

$$\frac{\partial Q^*}{\partial t}+\frac{\partial E^*}{\partial x}+\frac{\partial F^*}{\partial y}=H_j^n \tag{D.64}$$

get a updated version of Eq. (D.9),

$$(Q_t)_j^n = H_j^n-(E_x)_j^n-(F_y)_j^n=-(AQ_x+BQ_y-DQ)_j^n \tag{D.65}$$

In addition, the flux conservation equation, Eq. (D.10), is updated by

$$\oint_{S(CE_r(j,n))}\mathbf{h}^*\cdot d\mathbf{s}=\int_{V(CE_r(j,n))}HdV, \quad r=1,2,3 \tag{D.66}$$

The basic solution procedure for the dependent variable Q slightly differs depends on whether the source term is treated explicitly of implicitly. In general, the explicit treatment is used for non-stiff source term while the implicit treatment is used for stiff source term.

D.5.1 Explicit Treatment of Source Term

If the source term is treated explicitly such that,

$$\int_{V(CE_r(j,n))}HdV = H_{j_r}^{n-1}S_j^{(r)}\Delta t, \quad r=1,2,3 \tag{D.67}$$

then the dependent variable Q is solved as

$$Q_j^n=\frac{1}{S_j}\sum_{r=1}^{3}(R_r\cdot Q+R_r^x\cdot Q_x+R_r^y\cdot Q_y)_{j_r}^{n-1} \tag{D.68}$$

where R_r^x and R_r^y, respectively, take the same formulations given by Eqs. (D.29) and (D.30), and R_r is updated from Eq. (D.28) as

$$R_r = \left[S_j^{(r)} \cdot I - (K^{(r,1)} + K^{(r,2)})\right] + \Delta t\left[S_j^{(r)} \cdot I - (K^{(r,1)} + K^{(r,2)})D_{j_r}^{n-1}/2\right] \tag{D.69}$$

D.5.2 Implicit Treatment of Source Term

If the source term is treated implicitly such that,

$$\int_{V(CE_r(j,n))} HdV = H_j^n S_j^{(r)} \Delta t, \quad r = 1,2,3 \tag{D.70}$$

then the dependent variable Q is solved from

$$Q_j^n = \frac{1}{S_j}\sum_{r=1}^{3}(R_r \cdot Q + R_r^x \cdot Q_x + R_r^y \cdot Q_y)_{j_r}^{n-1} + \Delta t D_j^n Q_j^n \tag{D.71}$$

Here R_r^x and R_r^y, respectively, take the same formulations given by Eqs. (D.29) and (D.30), and R_r is defined as

$$R_r = \left[S_j^{(r)} \cdot I - (K^{(r,1)} + K^{(r,2)})\right] - \Delta t\left[(K^{(r,1)} + K^{(r,2)})D_{j_r}^{n-1}/2\right] \tag{D.72}$$

Equation (D.71) can be solved either with fully implicit approach, such as the Newton-Raphson iteration technique, or with linearized implicit approach which solves the following linearized equation:

$$(I - \Delta t D_j^{n-1})Q_j^n = RHS \tag{D.73}$$

where

$$RHS = \frac{1}{S_j}\sum_{r=1}^{3}(R_r \cdot Q + R_r^x \cdot Q_x + R_r^y \cdot Q_y)_{j_r}^{n-1} \tag{D.74}$$

For extremely stiff source term such as those arising from chemical reactions, the conventional fractional-step technique (Oran and Boris, 2001) may be employed. This technique has been incorporated into the CE/SE scheme recently by Wu et al. (2000) and Im et al. (2002) for detonation problems. In this technique, Eq. (D.71) is modified as

$$Q_j^n = RHS + \frac{\Delta t}{N} \sum_{m=1}^{N} (DQ)_j^{(m)} \tag{D.75}$$

where N is the number of sub-time steps within Δt. The above equation can be solved using the following procedure.

$$\begin{aligned}
&Q_j^{(1)} = RHS + \frac{\Delta t}{N}(DQ)_j^{(1)} \\
&Q_j^{(2)} = Q_j^{(1)} + \frac{\Delta t}{N}(DQ)_j^{(2)} \\
&\vdots \\
&Q_j^{(N-1)} = Q_j^{(N-2)} + \frac{\Delta t}{N}(DQ)_j^{(N-1)} \\
&Q_j^n = Q_j^{(N-1)} + \frac{\Delta t}{N}(DQ)_j^n
\end{aligned} \tag{D.76}$$

The Newton-Raphson iteration technique may be employed in each sub-time step.

Appendix E

Reflecting Boundary Conditions on an Inviscid Solid Wall

This appendix describes the numerical reflecting boundary conditions on an inviscid solid wall for the CE/SE method. The followings are adopted from Wang and Chang (1999) with minor modifications.

Consider a boundary cell ΔABC that has an edge located on the solid wall, as shown in Fig. E.1. The solid wall is aligned with an angle of θ from the x-axis. The ghost cell ΔABD is a mirror image of the boundary cell ΔABC with respect to the wall. The solution points of both cells are marked by cross. Assuming that the index of the boundary cell ΔABC is j, the index of the ghost cell will be set as $-j$.

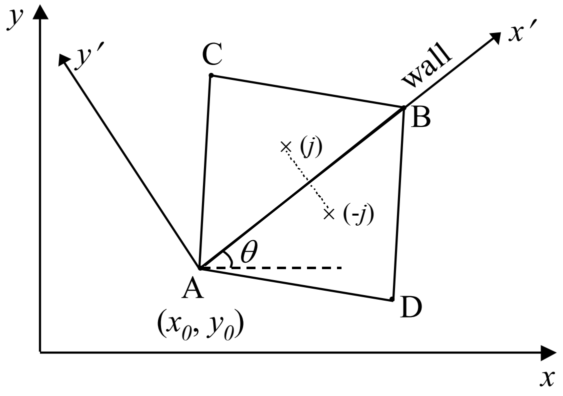

Fig. E.1 A boundary cell and its mirror image with respect to the solid wall

To proceed, a new spatial coordinate system x'-y' is introduced. Let the origin of the x'-y' coordinate system, point A, be the point (x_0, y_0) in the x-y coordinate system. These two coordinate systems then satisfy:

$$x - x_0 = x'\cos\theta - y'\sin\theta \qquad \text{(E.1)}$$

$$y - y_0 = x' \sin\theta + y' \cos\theta \tag{E.2}$$

which can be written in a matrix form:

$$\begin{bmatrix} x - x_0 \\ y - y_0 \end{bmatrix} = T \begin{bmatrix} x' \\ y' \end{bmatrix} \tag{E.3}$$

where

$$T = \begin{bmatrix} \cos\theta & -\sin\theta \\ \sin\theta & \cos\theta \end{bmatrix} \tag{E.4}$$

The inverse of matrix T is

$$T^{-1} = \begin{bmatrix} \cos\theta & \sin\theta \\ -\sin\theta & \cos\theta \end{bmatrix} \tag{E.5}$$

Let Q' denotes the dependant variable in the x'-y' coordinate system for the two-dimensional Euler equations with one species equation,

$$Q' = [q_1', q_2', q_3', q_4', q_5']^T \tag{E.6}$$

The slip solid wall boundary conditions are then constructed by assuming that, at any time, the flowfields within the boundary cell (ΔABC) and the ghost cell (ΔABD) are mirror images of each other in the x'-y' coordinate system. That is,

for the dependant variables,

$$(q_i')_{-j} = (q_i')_j, \quad i = 1,2,4,5 \tag{E.7}$$

$$(q_i')_{-j} = -(q_i')_j, \quad i = 3 \tag{E.8}$$

for the spatial derivatives,

$$\left(\frac{\partial q_i'}{\partial x'}\right)_{-j} = \left(\frac{\partial q_i'}{\partial x'}\right)_j, \quad \left(\frac{\partial q_i'}{\partial y'}\right)_{-j} = -\left(\frac{\partial q_i'}{\partial y'}\right)_j, \quad i = 1,2,4,5 \tag{E.9}$$

$$\left(\frac{\partial q_i'}{\partial x'}\right)_{-j} = -\left(\frac{\partial q_i'}{\partial x'}\right)_j, \quad \left(\frac{\partial q_i'}{\partial y'}\right)_{-j} = \left(\frac{\partial q_i'}{\partial y'}\right)_j, \quad i = 3 \tag{E.10}$$

In order to obtain the expressions in the *x*-*y* coordinate system, the relation between Q and Q' and between their spatial derivatives need to be derived first. It can be proved that,

$$q_i' = q_i, \quad i = 1,4,5 \tag{E.11}$$

$$\begin{bmatrix} q_2' \\ q_3' \end{bmatrix} = T^{-1} \begin{bmatrix} q_2 \\ q_3 \end{bmatrix} \tag{E.12}$$

and

$$\begin{bmatrix} \dfrac{\partial q_i'}{\partial x'} \\ \dfrac{\partial q_i'}{\partial y'} \end{bmatrix} = T^{-1} \begin{bmatrix} \dfrac{\partial q_i}{\partial x} \\ \dfrac{\partial q_i}{\partial y} \end{bmatrix}, \quad i = 1,4,5 \tag{E.13}$$

$$\begin{bmatrix} \dfrac{\partial q_2'}{\partial x'} & \dfrac{\partial q_3'}{\partial x'} \\ \dfrac{\partial q_2'}{\partial y'} & \dfrac{\partial q_3'}{\partial y'} \end{bmatrix} = T^{-1} \begin{bmatrix} \dfrac{\partial q_2}{\partial x} & \dfrac{\partial q_3}{\partial x} \\ \dfrac{\partial q_2}{\partial y} & \dfrac{\partial q_3}{\partial y} \end{bmatrix} \tag{E.14}$$

With these relations available, the slip wall boundary conditions can then be expressed as:

for Q,

$$(q_i)_{-j} = (q_i)_j, \quad i = 1,4,5 \tag{E.15}$$

$$\begin{bmatrix} q_2 \\ q_3 \end{bmatrix}_{-j} = M \begin{bmatrix} q_2 \\ q_3 \end{bmatrix}_j \tag{E.16}$$

for Q_x and Q_y,

$$\begin{bmatrix} \dfrac{\partial q_i}{\partial x} \\ \dfrac{\partial q_i}{\partial y} \end{bmatrix}_{-j} = M \begin{bmatrix} \dfrac{\partial q_i}{\partial x} \\ \dfrac{\partial q_i}{\partial y} \end{bmatrix}_{j}, \quad i = 1,4,5 \tag{E.17}$$

$$\begin{bmatrix} \dfrac{\partial q_2}{\partial x} & \dfrac{\partial q_3}{\partial x} \\ \dfrac{\partial q_2}{\partial y} & \dfrac{\partial q_3}{\partial y} \end{bmatrix}_{-j} = M \begin{bmatrix} \dfrac{\partial q_2}{\partial x} & \dfrac{\partial q_3}{\partial x} \\ \dfrac{\partial q_2}{\partial y} & \dfrac{\partial q_3}{\partial y} \end{bmatrix}_{j} M \tag{E.18}$$

where

$$M \equiv T \begin{bmatrix} 1 & 0 \\ 0 & -1 \end{bmatrix} T^{-1} = \begin{bmatrix} \cos 2\theta & \sin 2\theta \\ \sin 2\theta & -\cos 2\theta \end{bmatrix} \tag{E.19}$$

Appendix F

Determination of the Time Instant of the Arrival of the First Rarefaction Wave on the Head End

Figure F.1 schematically shows the *x*-*t* diagram for detonation wave propagation through a constant-area tube. The detonation wave is initiated at the head end ($x = 0$) and propagates downstream, followed by the Taylor wave and a uniform region. As the detonation wave arrives at the tube exit ($x = L$), a series of rarefaction waves are generated and propagate upstream. The first rarefaction wave arrives at the head end at time t_B, which can be obtained analytically. The analysis detailed below basically follows that given by Wintenberger et al. (2003).

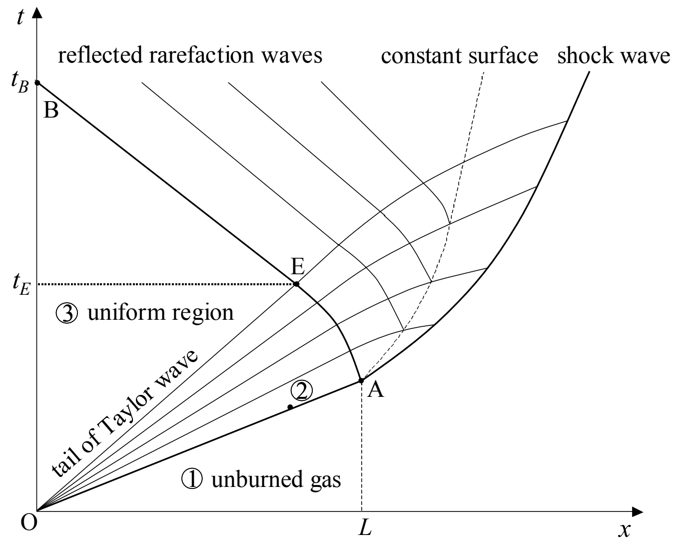

Fig. F.1 Space-time diagram for detonation wave propagation

Within the Taylor wave region (region OAE), the Riemann invariant relation along the characteristic line from state 3 to the point (x, t) gives

$$0-\frac{2}{\gamma-1}c_3=u-\frac{2}{\gamma-1}c \tag{F.1}$$

where u and c are the velocity and sound speed at point (x, t), respectively. Since the forward characteristic lines are straight, the relationship between x and t can be represented by

$$\frac{x}{t}=u+c \tag{F.2}$$

Combination of the above two equations leads to the following solutions of u and c:

$$\frac{u}{c_3}=\frac{2}{\gamma+1}\cdot\frac{x}{c_3 t}-\frac{2}{\gamma+1} \tag{F.3}$$

$$\frac{c}{c_3}=\frac{\gamma-1}{\gamma+1}\cdot\frac{x}{c_3 t}+\frac{2}{\gamma+1} \tag{F.4}$$

And as given in Eq. (1.27), c_3 can be related to u_D as

$$c_3=\frac{{M_D}^2+1}{2{M_D}^2}\cdot u_D \tag{F.5}$$

On the other hand, portion AE of the first reflected rarefaction wave can be described by

$$\frac{dx}{dt}=u-c \tag{F.6}$$

Substituting Eqs. (F.3), (F.4), and (F.5) into the above equation leads to the following ordinary differential equation:

$$\frac{dx}{dt}+\frac{\gamma-3}{\gamma+1}\cdot\frac{x}{t}+\frac{2({M_D}^2+1)}{(\gamma+1){M_D}^2}\cdot u_D=0 \tag{F.7}$$

With the initial condition:

$$x = L \quad \text{at} \quad t = L/u_D \tag{F.8}$$

the solution to Eq. (F.7) can be obtained:

$$x(t) = u_D t \cdot \left[-\frac{{M_D}^2 + 1}{(\gamma - 1){M_D}^2} + \frac{\gamma {M_D}^2 + 1}{(\gamma - 1){M_D}^2} \cdot \left(\frac{L}{u_D t} \right)^{\frac{2(\gamma-1)}{\gamma+1}} \right] \tag{F.9}$$

Considering that point E is the intersection of OE and AE, thus,

$$c_3 t_E = x(t_E) = u_D t_E \cdot \left[-\frac{{M_D}^2 + 1}{(\gamma - 1){M_D}^2} + \frac{\gamma {M_D}^2 + 1}{(\gamma - 1){M_D}^2} \cdot \left(\frac{L}{u_D t_E} \right)^{\frac{2(\gamma-1)}{\gamma+1}} \right] \tag{F.10}$$

Solving for t_E,

$$t_E = \frac{L}{u_D} \cdot \left[\frac{2(\gamma {M_D}^2 + 1)}{(\gamma + 1)({M_D}^2 + 1)} \right]^{\frac{\gamma+1}{2(\gamma-1)}} \tag{F.11}$$

Since the characteristic line OE and EB have the same wave speed magnitude c_3, t_B and t_E satisfy the following relation:

$$t_B = 2 t_E \tag{F.12}$$

Therefore,

$$t_B = \frac{2L}{u_D} \cdot \left[\frac{2(\gamma {M_D}^2 + 1)}{(\gamma + 1)({M_D}^2 + 1)} \right]^{\frac{\gamma+1}{2(\gamma-1)}} \tag{F.13}$$

In addition, to obtain the α used in Wintenberger et al. (2003), let

$$t_B = \frac{L}{u_D} + \alpha \cdot \frac{L}{c_3} \tag{F.14}$$

then it can be derived that,

$$\alpha = \frac{1}{2}(1+\frac{1}{{M_D}^2})\cdot\left\{2\left[\frac{2(\gamma {M_D}^2+1)}{(\gamma+1)({M_D}^2+1)}\right]^{\frac{\gamma+1}{2(\gamma-1)}}-1\right\} \tag{F.15}$$

which is equivalent to but simpler than Eq. (20) in Wintenberger et al. (2003).

Considering that ${M_D}^2 \gg 1$, Eqs. (F.13) and (F.15) can be further simplified with the following approximation:

$$t_B \approx \frac{2L}{u_D}\left[\frac{2\gamma}{\gamma+1}\right]^{\frac{\gamma+1}{2(\gamma-1)}} \tag{F.16}$$

$$\alpha \approx \frac{1}{2}\left[2(\frac{2r}{r+1})^{\frac{r+1}{2(r-1)}}-1\right] \tag{F.17}$$

Note that Eq. (F.16) was also given by Zitoun and Desbordes (1999).

Bibliography

Aarnio, M.J., Hinkey, J.B., and Bussing, T.R.A., "Multiple Cycle Detonation Experiments during the Development of a Pulse Detonation Engine," AIAA Paper 1996-3263, July 1996.

Allgood, D., Gutmark, E., and Katta, V., "Effects of Exit Geometry on the Performance of a Pulse Detonation Engine," AIAA Paper 2002-0616, January 2002.

Belegundu, A.D., and Chandrupatla T.R., *Optimization Concepts and Applications in Engineering*, Prentice-Hall, Inc., New Jersey, 1999.

Benedick, W., Guirao, C., Knystautas, R., and Lee, J.H.S., "Critical Charge for Direct Initiation of Detonation in Gaseous Fuel/Air Mixtures," *Dynamics of Explosions*, Edited by Bowen, J.R. and Leyer, J.C., Vol. 106, Progress in Astronautics and Aeronautics, AIAA, New York, 1986, pp. 181-202.

Berton, J.J., "Divergence Thrust Loss Calculations for Convergent-Divergent Nozzles: Extensions to the Classical Case," NASA TM-105176, 1991.

Bratkovich, T.E., and Bussing, T.R.A., "A Pulse Detonation Engine Performance Model," AIAA Paper 1995-3155, July 1995.

Broda, J.C., Conrad, C., Pal, S., Woodward, R.D., and Santoro, R.J., "Experimental Results on Air-Breathing Pulse Detonation Studies," *Proceedings of 11th Annual Symposium on Propulsion,* Propulsion Engineering Research Center, Pennsylvania State University, State College, PA, October 1999.

Brophy, C.M. and Netzer, D.W., "Effects of Ignition Characteristics and Geometry on the Performance of a JP-10/O2 Fueled Pulse Detonation Engine," AIAA Paper 1999-2635, June 1999.

Brophy, C.M., Netzer, D.W., and Forster, L.D., "Detonation Studies of JP-10 with Oxygen and Air for Pulse Detonation Engine Development," AIAA Paper 1998-4003, July 1998.

Brophy, C.M., Sinibaldi, J.O., and Damphousse, P., "Initiator Performance for Liquid-Fueled Pulse Detonation Engines," AIAA Paper 2002-0472, January 2002.

Brophy, C.M., Werner, L.S., and Sinibaldi, J.O., "Performance Characterization of a Valveless Pulse Detonation Engine," AIAA Paper 2003-1344, January 2003.

Bussing, T.R.A. and Pappas, G., "An Introduction to Pulse Detonation Engines," AIAA Paper 1994-0263, January 1994.

Bussing, T.R.A. and Pappas, G., "Pulse Detonation Engine Theory and Concepts," *Developments in High-Speed-Vehicle Propulsion Systems*, Edited by Murthy, S.N.B. and Curran, E.T., Vol. 165, Progress in Astronautics and Aeronautics, AIAA, Reston, VA, 1996, pp. 421-472.

Bussing, T.R.A., "A Rotary Valve Multiple Pulse Detonation Engine (RVMPDE)," AIAA Paper 1995-2577, July 1995.

Bussing, T.R.A., Hinkey, J.B., and Kaye, L., "Pulse Detonation Engine Preliminary Design Considerations," AIAA Paper 1994-3220, June 1994.

Cambier, J.L., and Adelman, H.G., "Preliminary Numerical Simulations of a Pulsed Detonation Wave Engine," AIAA Paper 1988-2960, July 1988.

Cambier, J.L. and Tegner, J.K, "Strategies for Pulsed Detonation Engine Performance Optimization," *Journal of Propulsion and Power*, Vol. 14, No. 4, 1998, pp. 489-498.

Chang, S.C., "The Method of Space-Time Conservation Element and Solution Element - A New Approach for Solving the Navier-Stokes and Euler Equations," *Journal of Computational Physics*, Vol. 119, No. 2, 1995, pp. 295-324.

Chang, S.C., Loh, C.Y., Yu, S.T., Himansu, A., Wang, X.Y., Jorgenson, P., "Robust and Simple Non-Reflecting Boundary Conditions for the Space-Time Conservation Element and Solution Element Method," AIAA Paper 1997-2077, June-July, 1997.

Chang, S.C., Wang, X.Y., and Chow, C.Y., "The Space-Time Conservation Element and Solution Element: A New High Resolution and Genuinely Multidimensional Paradigm for Solving Conservation Laws," *Journal of Computational Physics*, Vol. 156, No. 1, 1999, pp. 89-136.

Chang, S.C., Wu, Y.H., Wang, X.Y., and Yang, V., "Local Mesh Refinement in Space-Time Conservation Element and Solution Element Method," *Proceedings of 1st International Conference on Computational Fluid Dynamics*, Springer-Verlag, Berlin, 2000.

Cooper, M. and Shepherd, J.E., "The Effect of Nozzles and Extensions on Detonation Tube Performance," AIAA Paper 2002-3628, July 2002.

Cooper, M., Jackson, S., Austin, J., Wintenberger, E., and Shepherd, J.E., "Direct Experimental Impulse Measurements for Detonation and Deflagrations," *Journal of Propulsion and Power*, Vol. 18, No. 5, 2002, pp. 1033-1041.

Culick, F. E. C. and Rogers, T., "The Response of Normal Shocks in Diffusers," *AIAA Journal*, Vol. 21, No. 10, 1983, pp. 1382-1390.

Daniau, D., Zitoun, R., Couquet, C., and Desbordes, D., "Effects of Nozzles of Different Length and Shape on the Propulsion Performance of Pulsed Detonation Engines," *High Speed Deflagration and Detonation, Fundamentals and Control*, Edited by Roy, G., Frolov, S., Netzer, D., and Borisov, A., ELEX-KM Publishers, Moscow, Russia, 2001, pp. 251-262.

Desbordes, D., "Transmission of Overdriven plane detonations: Critical Diameter as a Function of Cell Regularity and Size," *Dynamics of Reactive Systems Part I: Flames; Part II: Homogeneous Combustion and Applications*, Edited by Kuhl, A.L., Bowen, J.R., and Borisov, A.A., Vol. 114, Progress in Astronautics and Aeronautics, AIAA, New York, 1988, pp.170-185.

Dunlap, R., Brehm, R.L., and Nicholls, J.A., "A Preliminary Study of the Application of Steady State Detonative Combustion of a Reaction Engine," *Jet Propulsion*, Vol. 28, No. 7, 1958, pp. 451-456.

Dyke, M.V., *An Album of Fluid Motion*, The Parabolic Press, Stanford, CA, 1997, pp. 145-148.

Ebrahimi, H.B. and Merkle, C.L., "A Numerical Simulation of a Pulse Detonation Engine with Hydrogen Fuels," *Journal of Propulsion and Power*, Vol. 18, No. 5, 2002, pp. 1042-1048.

Ebrahimi, H.B., Mohanraj, R., and Merkle, C.L., "Modeling of Multi-Tube Pulse Detonation Engine Operation," AIAA Paper 2001-3813, July 2001.

Ebrahimi, H.B., Mohanraj, R., and Merkle, C.L., "Multilevel Analysis of Pulsed Detonation Engines," *Journal of Propulsion and Power*, Vol. 18, No. 2, 2002, pp. 225-232.

Ebrahimi, H.B. and Merkle, C.L., "Optimization of Multitube Pulse Detonation Engine Configuration," AIAA Paper 2002-4228, July 2002.

Ebrahimi, H.B., Malo-Molina, F.J., and Merkle, C.L., "Numerical Investigation of Multi-Tube Pulse Detonation," AIAA Paper 2003-0718, January 2003.

Eidelman, S. and Yang, X., "Analysis of the Pulse Detonation Engine Efficiency," AIAA Paper 1998-3877, July 1998.

Eidelman, S., Grossman, W., and Lottati, I., "Air-Breathing Pulsed Detonation Engine Concept; A Numerical Study," AIAA Paper 1990-2420, July 1990.

Eidelman, S., Grossman, W., and Lottati, I., "Review of Propulsion Applications and Numerical Simulations of The Pulse Detonation Engine Concept," *Journal of Propulsion and Power*, Vol. 7, No. 6, 1991, pp. 857-865.

Falempin, F., Bouchaud, D., Forrat, B., Desbordes, D., and Daniau, E., "Pulsed Detonation Engine: Possible Application to Low Cost Tactical Missile and to Space Launcher," AIAA Paper 2001-3815, July 2001.

Farinaccio, R., Harris, P., Stowe, R.A., and Akbar, R., "Multi-Pulse Detonation Experiments with Propane-Oxygen," AIAA Paper 2002-4070, July 2002.

Fickett, W., and Davis, W.C., *Detonation Theory and Experiment*, Dover Publications, New York, 2000.

Fong K.K., and Nalim M.R., "Gas Dynamics Limits and Optimization of Pulsed Detonation Static Thrust," AIAA Paper 2000-3471, July 2000.

Frankey, B., Schauer, F., Bradley, R., and Hoke, J., "Evaluation of a Hybrid-Piston Pulsed Detonation Engine," AIAA Paper 2002-0474, January 2002.

Glassman, I., *Combustion*, Third Edition, Chapter 5, Academic Press, CA, 1996.

Goddard, R.H., "Rotating Valve for Multiple Resonance Combustion Chambers," U.S. Patent 2515644, July 18, 1950.

Green, J. E., "Interactions between Shock Waves and Turbulent Boundary Layers," *Progress in Aerospace Sciences*, Vol. 11, 1970, pp. 235-340.

Han, Z.Y. and Yin, X.Z., *Shock Dynamics*, Kluwer Academic Publishers/Science Press, 1993, pp. 50-63.

Harris, P.G., Farinaccio, R., and Stowe, R.A., "The Effect of DDT Distance on Impulse in a Detonation Tube," AIAA Paper 2001-3467, July 2001.

Harten, A., "High Resolution Schemes for Hypersonic Conservation Laws," *Journal of Computational Physics*, Vol. 49, No. 3, 1983, pp. 357-393.

Heiser, W.H. and Pratt, D.T., "Thermodynamic Cycle Analysis of Pulse Detonation Engines," *Journal of Propulsion and Power*, Vol. 18, No. 1, 2002, pp. 68-76.

Helman, D., Shreeve, R.P., and Eidelman, S., "Detonation Pulse Engine," AIAA Paper 1986-1683, June 1986.

Hinkey, J.B., Bussing T.R.A., and Kaye, L., "Shock Tube Experiments for the Development of a Hydrogen-Fueled Pulse Detonation Engine," AIAA Paper 1995-2578, July 1995.

Hinkey, J.B., Williams, J.T., Henderson, S.E., and Bussing, T.R.A., "Rotary-Valved, Multiple-Cycle, Pulse Detonation Engine Experimental Demonstration," AIAA Paper 1997-2746, July 1997.

Hodge, B.K. and Koenig, K., *Compressible Fluid Dynamics with Personal Computer Applications*, Prentice Hall, Englewood Cliffs, New Jersey, 1995, pp. 98-99, p. 187, pp. 467-486.

Hoffman, N., “Reaction Propulsion by Intermittent Detonative Combustion,” Ministry of Supply, Volkenrode Translation, 1940.

Im, K.S., Yu, S.T., Kim, C.K., Chang, S.C., and Jorgenson, P.C.E., “Application of the CE/SE Method to Detonation with Realistic Finite-Rate Chemistry,” AIAA Paper 2002-1020, January 2002.

Kailasanath, K., Patnaik, G., and Li, C., “Computational Studies of Pulse Detonation Engines: A Status Report,” AIAA Paper 1999-2634, June 1999.

Kailasanath, K., “Review of Propulsion Applications of Detonation Waves,” *AIAA Journal*, Vol. 38, No. 9, 2000, pp. 1698-1708.

Kailasanath, K., “A Review of PDE Research – Performance Estimates,” AIAA Paper 2001-0474, January 2001.

Kailasanath, K., “A Review of Research on Pulse Detonation Engine Nozzles,” AIAA Paper 2001-3932, July 2001.

Kailasanath, K., “Recent Developments in the Research on Pulse Detonation Engines,” AIAA Paper 2002-0470, January 2002.

Kailasanath, K., “Recent Developments in the Research on Pulse Detonation Engines,” *AIAA Journal*, Vol. 41, No. 2, 2003, pp. 145-159.

Karypis, G. and Kumar, V., “Multilevel K-Way Partitioning Scheme for Irregular Graphs,” *Journal of Parallel and Distributed Computing*, Vol. 48, No. 1, 1998, pp. 96-129.

Kawai, S. and Fujiwara, T., “Numerical Analysis of 1st and 2nd Cycles of Oxyhydrogen PDE,” AIAA Paper 2002-0929, January 2002.

Kentfield, J.A.C., “The Fundamentals of Idealized Air-Breathing Pulse-Detonation Engines,” *Journal of Propulsion and Power*, Vol. 18, No. 1, 2002, pp. 77-83.

Knystautas, R., Lee, J.H.S., Moen, I., and Wagner, H.G., “Direct Initiation of Spherical Detonation by a Hot Turbulent Gas Jet,” *Proceedings of 17th International Symposium on Combustion*, The Combustion Institute, Pittsburgh, 1979, pp. 1235-1245.

Korobeinikov, V.P., and Urtiew, P.A. (English-Edition Editor), *Unsteady Interaction of Shock and Detonation Waves in Gases*, Hemisphere Publishing Corporation, 1986, Chapter 6, pp. 80-96.

Korovin, L.N., Losev, A., Ruban, S.G., and Smekhov, G.D., "Combustion of Natural Gas in a Commercial Detonation Reactor," *Fizika Gor. Vzryva*, Vol. 17, No. 3, 1981, p. 86. (cited in Eidelman et al., 1991)

Krzycki, L.J., "Performance Characteristics of an Intermittent-Detonation Device," U.S. Naval Ordnance Test Station, China Lake, CA, NAVWEPS Report 7655, 1962.

Kuo, K., *Principles of Combustion*, Chapter 4, John Wiley and Sons, 1986.

Lee, J.H.S., "Dynamic Parameters of Gaseous Detonations," *Annual Review of Fluid Mechanics*, Vol. 16, 1984, pp. 311-336.

Lee, J.H.S. and Moen, I.O., "The Mechanism of Transition from Deflagration to Detonation in Vapor Cloud Explosions," *Progress in Energy and Combustion Science*, Vol. 6, 1980, pp. 359-389.

Lee, S.Y., Conrad, C., Watts, J., Woodward, R., Pal, S., and Santoro, R.J., "Deflagration to Detonation Transition Study Using Simultaneous Schlieren and OH PLIF Images," AIAA Paper 2000-3217, July 2000.

Li, C., and Kailasanath, K., "A Numerical Study of Reactive Flows in Pulse Detonation Engines," AIAA Paper 2001-3933, July 2001.

Li, C., and Kailasanath, K., "Performance Analysis of Pulse Detonation Engines with Partial Fuel Filling," AIAA Paper 2002-0610, January 2002.

Li, C., Kailasanath, K., and Patnaik, G., "A Numerical Study of Flow Field Evolution in a Pulsed Detonation Engine," AIAA Paper 2000-0314, January 2000.

Lieberman, D.H., Parkin, K.L., and Shepherd, J.E., "Detonation Initiation by a Hot Turbulent Jet for Use in Pulse Detonation Engines," AIAA Paper 2002-3909, July 2002.

Litchford, R.J., "Development of a Gas-Fed Pulse Detonation Research Engine," AIAA Paper 2001-3814, July 2001.

Lynch, E.D. and Edelman, R.B., "Analysis of the Pulse Detonation Wave Engine," *Developments in High-Speed-Vehicle Propulsion Systems*, Edited by Murthy, S.N.B. and Curran, E.T., Vol. 165, Progress in Astronautics and Aeronautics, AIAA, Reston, VA, 1996, pp. 473-516.

Ma, F.H., Choi, J.Y., Wu, Y.H., and Yang, V., "Modeling of Multitube Pulse Detonation Engine Dynamics," *Confined Detonations and Pulse Detonation Engines,* Edited by Roy, G., Frolov, S., Santoro, R., and Tsyganov, S., Torus Press, Moscow, Russia, 2003, pp. 233-248.

Mattingly, J.D., *Elements of Gas Turbine Propulsion*, McGraw-Hill, 1996, p. 805.

McBride, B.J. and Gordon, S., "Computer Program for Calculation of Complex Chemical Equilibrium Compositions and Applications," NASA Reference Publication 1311, June 1996.

McManus, K., Furlong, E., Leyva, I., and Sanderson, S., "MEMS-Based Pulse Detonation Engine for Small-Scale Propulsion Applications," AIAA Paper 2001-3469, July 2001.

Meyer, T.R., Hoke, J.L., Brown, M.S., Gord, J.R., and Schauer, F.R., "Experimental Study of Deflagration Enhancement Techniques in a H2/Air Pulsed-Detonation Engine," AIAA Paper 2002-3720, July 2002.

Meyers, J.M., Lu, F.K., and Wilson, D.R., "Performance Enhancements on a Pulsed Detonation Engine," AIAA Paper 2003-1173, January 2003.

Mohanraj, R., and Merkle, C.L., "A Numerical Study of Pulse Detonation Engine Performance," AIAA Paper 2000-0315, January 2000.

Nicholls, J.A., Wilkinson, H.R., and Morrison, R.B., "Intermittent Detonation as a Thrust-Producing Mechanism," *Jet Propulsion*, Vol. 27, No. 5, 1957, pp. 534-541.

Oh, J. Y., "Numerical Study of Steady and Oscillatory Flow Structures in an Axisymmetric Supersonic Inlet," Ph.D. Thesis, Department of Mechanical Engineering, The Pennsylvania State University, University Park, PA, August 1994.

Oran, E.S., and Boris, J.P., "Numerical Simulation of Reactive Flow," Second Edition, Cambridge University Press, 2001, p. 405.

Oppenheim, A.K., Manson, N., and Wagner, H.G., "Recent Progress in Detonation Research," *AIAA Journal*, Vol. 1, No. 10, 1963, pp. 2243-2252.

Rasheed, A., Tangirala, V., Pinard, P.F., Dean, A.J., "Experimental and Numerical Investigations of Ejectors for PDE Applications," AIAA Paper 2003-4971, July 2003.

Roache, P.J., "Quantification of Uncertainty in Computational Fluid Dynamics," *Annual Review of Fluid Mechanics*, Vol. 29, 1997, pp. 126-160.

Rodi, W., "Experience with Two-Layer Models Combining the k-ε Model with a One-Equation Model Near the Wall," AIAA Paper 1991-0216, January 1991.

Sanders, S.T., Jenkins, T.P., and Hanson, R.K., “Diode Laser Sensor System for Multi-Parameter Measurements in Pulse Detonation Engine Flows,” AIAA Paper 2000-3593, July 2000.

Santoro, R.J., Lee, S.Y., Conrad, C., Brumberg, J., Saretto, S., Pal, S., and Woodward, R.D., “DDT Studies for Multicycle PDE Applications,” *Confined Detonations and Pulse Detonation Engines,* Edited by Roy, G., Frolov, S., Santoro, R.J., and Tsyganov, S., Torus Press, Moscow, Russia, 2003, pp. 259-270.

Schauer, F., Stutrud, J., and Bradley, R., “AFRL’s In-House Research Pulse Detonation Engine,” *Proceedings of 11th Annual Symposium on Propulsion*, Propulsion Engineering Research Center, Pennsylvania State University, State College, PA, October 1999.

Schauer, F., Stutrud, J., and Bradley, R., “Detonation Initiation Studies and Performance Results for Pulsed Detonation Engine Applications,” AIAA Paper 2001-1129, January 2001.

Schauer, F., Stutrud, J., Bradley, R., and Katta, V., “AFRL/PRSC Pulse Detonation Engine Research Program,” *Proceedings of 12th Annual Symposium on Propulsion*, Propulsion Engineering Research Center, Ohio Aerospace Institute, Cleveland, OH, October 2000.

Seddon, J. and Goldsmith, E.L., *Intake Aerodynamics*, Second Edition, Blackwell Science, Oxford, 1999, p. 137.

Shchelkin, K.I., *Soviet Journal of Technical Physics*, Vol. 10, 1940, pp. 823-827.

Shehadeh, R., Saretto, S., Lee, S.Y., Pal, S., and Santoro, R.J., “Experimental Study of a Pulse Detonation Engine Ejector,” AIAA Paper 2003-4972, July 2003.

Shepherd, J.E., Pintgen, F., Austin, J.M., and Eckett, C.A., “The Structure of the Detonation Front in Gases,” AIAA Paper 2002-0773, January 2002.

Shimo, M., Meyer, S.E., Heister, S.D., Weng, C.S., Ji, J., and Gore, J.P., “An Experimental and Computational Study of Pulsed Detonations in a Single Tube,” AIAA Paper 2002-3716, July 2002.

Sinibaldi, J.O., Brophy, C.M., and Robinson, L.J.P., “Ignition Effects on Deflagration-to-Detonation Transition Distance in Gaseous Mixtures,” AIAA Paper 2000-3590, July 2000.

Sinibaldi, J.O., Brophy, C.M., Li, C., and Kailasanath, K., “Initiator Detonation Diffraction Studies in Pulsed Detonation Engines,” AIAA Paper 2001-3466, July 2001.

Skews, B.W., “The Perturbed Region Behind a Diffracting Shock Wave,” *Journal of Fluid Mechanics*, Vol. 29, No. 4, 1967, pp. 705-719.

Skews, B.W., “The Shape of a Diffracting Shock Wave,” *Journal of Fluid Mechanics*, Vol. 29, No. 2, 1967, pp. 297-305.

Smirnov, V.N. and Boichenko, A.P., “Transition from Deflagration to Detonation in Gasoline-Air Mixtures,” *Fizika Gor. Vzryva*, Vol. 22, No. 2, 1986, pp. 65-67. (Cited in Eidelman et al., 1991)

Spapart, P. R., “Direct Simulation of a Turbulent Boundary Layer up to $Re_\theta = 1410$,” *Journal of Fluid Mechanics*, Vol. 187, pp. 61-98, 1988.

Strehlow, P.A., *Fundamentals of Combustion*, Chapter 9, International Textbook Company, 1968.

Sterling, J., Ghorbanian, K., Humphrey, J., and Sobota, T., “Enhanced Combustion Pulsejet Engines for Mach 0 to 3 Applications,” AIAA Paper 1996-2687, July 1996.

Sterling, J., Ghorbanian, K., Humphrey, J., and Sobota, T., “Numerical Investigations of Pulse Detonation Wave Engines,” AIAA Paper 1995-2479, July 1995.

Stuessy W.S. and Wilson, D.R., “Experimental Investigation of an Annual Multi-Cycle Pulsed Detonation Wave Engine,” AIAA Paper 1996-0346, January 1996.

Sun, M., and Takayama, K., “Vorticity Production in Shock Diffraction,” *Journal of Fluid Mechanics*, Vol. 478, 2003, pp. 237-256.

Talley, D.G. and Coy, E.B., “Constant Volume Limit of Pulsed Propulsion for a Constant γ Ideal Gas,” *Journal of Propulsion and Power*, Vol. 18, No. 2, 2002, pp. 400-406.

Taylor, G.I., “The Dynamics of the Combustion Products Behind Plane and Spherical Detonation Fronts in Explosives,” *Proceedings of the Royal Society of London, Series A: Mathematical and Physical Sciences*, Vol. 200, 1950, pp. 235-247.

Taylor, G. I. and Maccoll, J. W., “The Air Pressure on a Cone Moving at High Speed,” *Proceedings of the Royal Society of London, Series A: Mathematical and Physical Sciences*, Vol. 139, 1929, p. 496.

Tew, D.E., “Ideal Polytropic Ramjet Performance,” *Proceedings of 11th Annual Symposium on Propulsion*, Propulsion Engineering Research Center, Pennsylvania State University, State College, PA, October 1999.

Wang, X.Y. and Chang, S.C, “A 2D Non-Splitting Unstructured Triangular Mesh Euler Solver Based on the Space-Time Conservation Element and Solution Element Method,” *Computational Fluid Dynamic Journal*, Vol. 8, No. 2, 1999, pp. 309-325.

Watson, W. R. and Myers, M. K., “Inflow-Outflow Boundary Conditions for Two-Dimensional Acoustic Waves in Channels with Flow,” *AIAA Journal*, Vol. 29, No. 9, 1991, pp. 1383-1389.

Watts, J., Conrad, C., Lee, S.Y., Woodward, R.D., Pal, S., Santoro, R.J., “Fundamental Studies of the DDT Process in Pulse Detonation Engines Based on Single/Multi-Cycle Operation,” *Proceedings of 12th Annual Symposium on Propulsion*, Propulsion Engineering Research Center, Ohio Aerospace Institute, Cleveland, OH, October 2000.

White, F.M., *Viscous Fluid Flow*, McGraw Hill Book Co., New York, 1974.

Wintenberger, E., Austin, J.M., Cooper, M., Jackson, S., and Shepherd, J.E., “An Analytical Model for the Impulse of a Single-Cycle Pulse Detonation Engine,” *Journal of Propulsion and Power*, Vol. 19, No. 1, 2003, pp. 22-38.

Wu, Y.H., “System Performance and Thermodynamic Cycle Analysis of Air-Breathing Pulse Detonation Engines,” Ph.D. Thesis, Department of Mechanical and Nuclear Engineering, The Pennsylvania State University, University Park, PA, May 2002.

Wu, Y.H., Ma, F.H., and Yang, V., “System Performance and Thermodynamic Cycle Analysis of Airbreathing Pulse Detonation Engines,” *Journal of Propulsion and Power*, Vol. 19, No. 4, 2003, pp. 556-567.

Wu, Y.H., Yang, V., and Chang, S.C., “Numerical Simulation of Chemically Reacting Flows with Detailed Kinetics Using the Space-Time Method,” *Proceedings of 1st International Conference on Computational Fluid Dynamics*, Springer-Verlag, Berlin, 2000, pp. 207-212.

Yang, V. and Cappuccio, M., “Supersonic Inlet Design for Missiles,” Research Report, Department of Mechanical Engineering, the Pennsylvania State University, University Park, PA, 1990.

Yang, V. and Culick, F.E.C., “Analysis of Unsteady Inviscid Diffuser Flow with a Shock Wave,” *Journal of Propulsion and Power*, Vol. 1, 1985, pp. 222-228.

Yee, H. C., “A Class of High-Resolution Explicit and Implicit Shock-Capturing Methods,” Lecture Series for Computational Fluid Dynamics, von Karman Institute for Fluid Dynamics, March 6-10, 1989, Rhode-St-Genese, Belgium; NASA TM-101088, 1989.

Yu, S.T. and Chang, S.C., “Treatment of Stiff Source Terms in Conservation Laws by the Method of Space-Time Conservation Element and Solution Element,” AIAA Paper 1997-0435, January 1997.

Yungster, S. and Perkins, H.D., “Multiple-Cycle Simulation of a Pulse Detonation Engine Ejector,” AIAA Paper 2002-3630, July 2002.

Yungster, S., “Analysis of Nozzle Effects on Pulse Detonation Engine Performance,” AIAA Paper 2003-1316, January 2003.

Zhang, Z.C., Yu, S.T., and Chang, S.C., “A Space-Time Conservation Element and Solution Element Method for Solving the Two- and Three-Dimensional Unsteady Euler Equations Using Quadrilateral and Hexahedral Meshes,” *Journal of Computational Physics*, Vol. 175, No. 1, 2002, pp. 168-199.

Zitoun, R., and Desbordes, D., “Propulsive Performance of Pulsed Detonations,” *Combustion Science and Technology*, Vol. 144, 1999, pp. 93-114.

Vita

Fuhua Ma was born in Hubei, China. He received his B.S. degree in Mechanical Engineering from the University of Science and Technology of China in 1996, and his M.S. degree in 1999. He started his Ph.D. study in the Department of Mechanical Engineering at the Pennsylvania State University from August 1999, focusing on the modeling and simulation of pulse detonation engines.